



HAL
open science

Retinal waves : theory, numerics, experiments

Theodora Karvouniari

► **To cite this version:**

Theodora Karvouniari. Retinal waves : theory, numerics, experiments. Bioinformatics [q-bio.QM]. COMUE Université Côte d'Azur (2015 - 2019), 2018. English. NNT : 2018AZUR4014 . tel-01818522

HAL Id: tel-01818522

<https://theses.hal.science/tel-01818522>

Submitted on 19 Jun 2018

HAL is a multi-disciplinary open access archive for the deposit and dissemination of scientific research documents, whether they are published or not. The documents may come from teaching and research institutions in France or abroad, or from public or private research centers.

L'archive ouverte pluridisciplinaire **HAL**, est destinée au dépôt et à la diffusion de documents scientifiques de niveau recherche, publiés ou non, émanant des établissements d'enseignement et de recherche français ou étrangers, des laboratoires publics ou privés.

THÈSE DE DOCTORAT

Les ondes rétiniennes: théorie,
numérique, expériences

Dora KARVOUNIARI

Inria, équipe Biovision

**Présentée en vue de l'obtention
du grade de docteur en Informatique
de Inria, UCA**

Dirigée par : Bruno Cessac

Soutenue le : 15 mars 2018

Devant le jury, composé de :

Stephen Eglen, Reader, Cambridge University,
Rapporteur

Evelyne Sernagor, Reader, University of
Newcastle, Rapporteur

Mathieu Desroches, Chercheur CR1, Inria,
Examineur

Olivier Marre, Chercheur CR2, Institut de la
Vision, Examineur

Konstantina Nikita, Professeur, NTUA,
Examineur

Elisabeth Pecou, Professeur, UCA, Examineur

Z. Jimmy Zhou, Professeur, Yale University,
Examineur

Bruno Cessac, Chercheur DR2, Inria, Directeur
de thèse

Doctoral School Sciences et Technologies de l'Information et de la Communication
Research Center Inria Sophia Antipolis - Méditerranée

PhD Thesis

Submitted in partial fulfillment of the requirements for the degree of doctor
of the Université Côte d'Azur

Specialized in: *Informatics*

by

Dora Karvouniari

Retinal waves: theory, numerics, experiments

Directed by:

Bruno Cessac, Research Director, Université Côte d'Azur, Inria

To be defended on March 15th 2018 in front of the jury composed by:

Reviewers	Stephen EGMEN	Reader, Cambridge University, UK
	Evelyne SERNAGOR	Reader, University of Newcastle, UK
Examiners	Mathieu DESROCHES	Researcher CR1, Université Côte d'Azur, Inria, France
	Olivier MARRE	Researcher CR2, Vision Institute, INSERM, France
	Konstantina NIKITA	Professor, National Technical University of Athens, Greece
	Elisabeth PECOU	Professor, Université Côte d'Azur, France
	Z. Jimmy ZHOU	Professor, Yale University, USA
Supervisor	Bruno CESSAC	Research Director DR2, Université Côte d'Azur, Inria, France

Mots-clés
rétiniennes

biophysique, modélisation, simulation, bifurcations, ondes

Résumé (1700 caractères maximum espaces compris)

Les ondes rétiniennes sont des bursts spontanées d'activité se propageant dans la rétine en développement, jouant un rôle fondamental dans le façonnage du système visuel et des circuits rétiniens. Ils disparaissent complètement à la maturation. Comprendre comment les ondes rétiniennes sont initiées et se propagent dans la rétine pourrait nous permettre de concevoir des protocoles pour déclencher de telles ondes rétiniennes dans la rétine adulte, s'attendant à réintroduire une certaine plasticité dans le tissu rétinien et les projections dans le cerveau. Dans ma thèse, je me suis concentré sur un stade spécifique de développement des ondes, appelé stade II, induit par des cellules spécifiques (SAC) et médiée par le neurotransmetteur acétylcholine. Les SAC immatures présentent un comportement d'éclatement spontané dû aux mécanismes cellulaires intrinsèques, qui disparaissent complètement lors de la maturation. En outre, les SAC immatures sont connectés par des connexions excitatrices, conduisant à des poussées d'activité en propagation. L'esprit général de ce travail de thèse est de proposer un modèle pour les ondes rétiniennes (i) suffisamment proche de la biophysique pour expliquer et proposer des expériences et (ii) suffisamment bien posé mathématiquement pour analyser sa dynamique sur des paramètres biophysiques variables. Dans ce contexte, nous avons voulu élucider les mécanismes qui font éclater les SAC immatures et comment les ondes rétiniennes commencent, se propagent et s'arrêtent. Nous avons proposé un modèle mathématique, fondé sur la biophysique, et à travers la théorie des bifurcations, nous expliquons les mécanismes cellulaires sous-jacents possibles des ondes rétiniennes, en soulignant les paramètres biophysiques pertinents contrôlant la propagation et la disparition des ondes. En plus de cela, nous avons analysé comment l'évolution de la conductance cholinergique due à la maturation des récepteurs nicotiques modifie considérablement les caractéristiques de l'onde rétinienne. En particulier, il existe un intervalle très étroit de conductance de l'acétylcholine où la taille des ondes rétiniennes obéit à une distribution de loi de puissance, suggérant un mécanisme spécifique (homéostatique) stabilisant temporairement le réseau SAC dans cette gamme spécifique. En résumé, les résultats de cette thèse sont principalement théoriques, mais ils conduisent également à des prédictions expérimentales directement liées à la biologie.

Keywords

biophysics, modeling, simulations, bifurcations, retinal waves

Abstract (maximum 1700 prints including spaces)

Retinal waves are spontaneous bursts of activity propagating in the developing retina, playing a fundamental role in shaping the visual system and retinal circuitry. They disappear completely upon maturation. Understanding how retinal waves are initiated and propagate in the retina could enable us to design protocols to trigger such retinal waves in the adult retina, expecting to reintroduce some plasticity in the retinal tissue and the projections in the brain. In my thesis, I have focused on a specific stage of development of waves, called stage II, induced by specific cells (SACs) and mediated by the neurotransmitter acetylcholine. Immature SACs exhibit a spontaneous bursting behavior due to intrinsic cellular mechanisms, which disappears completely upon maturation. Also, immature SACs are connected by excitatory connections, leading to propagating bursts of activity. The general spirit of this thesis work, is to propose a model for retinal waves (i) sufficiently close to biophysics to explain and propose experiments and (ii) sufficiently well posed mathematically to analyse its dynamics upon varying biophysical parameters. In this context, we wanted to elucidate the mechanisms causing immature SACs to burst and how retinal waves start, propagate and stop. We proposed a mathematical model, grounded on biophysics, and through bifurcations theory we explain the possible underlying cellular mechanisms of retinal waves, highlighting the relevant biophysical parameters controlling waves propagation and disparition. On top of that, we analyzed how the evolution of cholinergic conductance due to the maturation of nicotinic receptors dramatically changes the retinal wave characteristics. Especially, there is a very narrow interval of acetylcholine conductance where retinal waves size obey a power law distribution, suggesting a specific (homeostatic) mechanism stabilizing temporarily the SACs network in this specific range. To sum up, this thesis results are mainly theoretical, but they also lead to experimental predictions directly linked to biology.

Ithaka

”As you set out for Ithaka
hope the voyage is a long one,
full of adventure, full of discovery.
Laistrygonians and Cyclops,
angry Poseidon don’t be afraid of them:
you’ll never find things like that on your way
as long as you keep your thoughts raised high,
as long as a rare excitement
stirs your spirit and your body.
Laistrygonians and Cyclops,
wild Poseidon you won’t encounter them
unless you bring them along inside your soul,
unless your soul sets them up in front of you.
Hope the voyage is a long one.
May there be many a summer morning when,
with what pleasure, what joy,
you come into harbors seen for the first time;
may you stop at Phoenician trading stations
to buy fine things,
mother of pearl and coral, amber and ebony,
sensual perfume of every kind
as many sensual perfumes as you can;
and may you visit many Egyptian cities
to gather stores of knowledge from their scholars.
Keep Ithaka always in your mind.
Arriving there is what you are destined for.
But do not hurry the journey at all.
Better if it lasts for years,
so you are old by the time you reach the island,
wealthy with all you have gained on the way,
not expecting Ithaka to make you rich.
Ithaka gave you the marvelous journey.
Without her you would not have set out.
She has nothing left to give you now.
And if you find her poor, Ithaka won’t have fooled you.
Wise as you will have become, so full of experience,
you will have understood by then what these Ithakas mean.” - **C.P. Cavafy**

Acknowledgements

Pursuing a PhD is a long journey, a life-changing experience that transformed my way of thinking, helping me evolve as a scientist but also as a person. There are times during a thesis where your limits and strength are tested, making you question everything. For sure it is a bumpy ride full of battles, but it is also a wonderful one, a trip that I will always carry with me, thanks to the amazing people I met with who I shared some of the best years of my life.

First of all, I would like to thank my advisor Bruno Cessac, for being the best mentor one could ask during these years. Bruno is passionate about science but he is also passionate about supporting his students in every possible way, so for me he has been a supervisor, a mentor, a coach, a psychologist and also a good friend. I will always cherish these years working together, guiding and helping me in order to achieve the thesis I have dreamt of. He has been beyond any doubt a role model for me, as a scientist and as a person, and I will always appreciate deeply his constant support and care.

I was also extremely lucky to work with amazing collaborators, leading experts in many fields. I thank Lionel Gil, for his help, the extremely interesting discussions where he would always speak "the voice of physics" and his restless spirit making me to push forward my theoretical point of view. I would like also to thank Olivier Marre, who has been giving me precious advice and guidance challenging me with his sharp spirit and observations, on neuroscience and how to work at the interface of mathematics and biology. Olivier, along with Serge Picaud, helped me realise one of my dreams for this thesis, as I was able towards the end to conduct experiments that our theoretical work predicted. For this opportunity I will be always grateful to them.

I would like to deeply thank Evelyne Sernagor, for being a pure inspiration for me. Evelyne is an incredible woman, and as her expertise in the domaine of retinal waves is world class, I consider myself highly privileged to have had her insight over the years. I will be forever grateful for her immediate and thoughtful responses to our biological questions, our enlightening discussions and her invaluable help. Also, I was glad to have her as a reviewer in my thesis, where her remarks are very educational and enriching.

I would also like to thank Stephen Eglén, for accepting to be a reviewer for my thesis and for his high-quality insightful report. My deepest gratitude goes also to the rest of the jury members: Mathieu Desroches, Konstantina Nikita, Elisabeth Pecou and Z. Jimmy Zhou for accepting to participate in my thesis defense and for their valuable insights as experts in various domains.

On the personal side, I was blessed with amazing friends and colleagues throughout the years in France all of whom made this experience unforgettable. Nikos and Katerina were the friends I chose for family, and the level of closeness we reached makes me

always feel like home when I am around them. Loukas and Katt showed me how it is to have older siblings- I always call them uncles from America though. George, the only member of our Physics UoA clan in Cote d'Azur, showed me how a person can care about everything and nothing at the same time, with his pure child heart and his sharp intellect. Akis, is my awesome cool friend, a point of reference and I know he is the one I can always count on. Pavlos, who is never wrong and does always the right thing in the most effortless way.

Last year, while I thought that life gave me enough close friends already, I met Jenny, without who, my last year of PhD would not be as awesome, being always there for me discussing all our troubles away everyday, caring as well as laughing our hearts out.

Nice now feels like home because of all my beloved friends: Christos, Konstantinos, Stefano, Milica, Alex, Teo, Penny, Pantelis, Stelios, Stelios, Bountouris, Maria, TTT, Konstantinos, Selma, Marco, Francois, Joss, Alicia and many more. I thank you all for those amazing years we shared.

In order to evolve we should never forget where we come from. For that, I am grateful to have the constant support and unconditional love of my mom, dad and two sisters Natasa and Ioanna, and my childhood friends Despina and Marieta, for all the endeavours I have embarked to in my life. However far, we are always connected through the deepest roots.

Last but most importantly, I thank my fiance, Panos, without whom, I can not imagine how my life would be. He always believes in me, even when I don't and his limitless love makes me feel invincible. I really thank him for being the wind underneath my wings and the force that is always with me.

Contents

1	Introduction	7
1.1	Introduction to the visual system	7
1.1.1	Visual system and structure	7
1.1.2	The retina and its structure	8
1.1.3	Starburst Amacrine Cells	8
1.2	From neurons to neural networks	10
	Synapses.	10
	Connectivity.	11
1.3	Retinal waves	11
1.3.1	General mechanism of stage II retinal waves	12
1.4	Modeling stage II retinal waves	14
1.4.1	State of the art	14
1.4.2	What is this thesis about?	15
1.4.3	Methods and tools used in this thesis	17
	Bifurcations theory.	17
	Numerical simulations.	17
2	Modeling the bursting activity of individual immature SACs	19
2.1	The Morris-Lecal model	19
2.2	A biophysical model for bursting immature SACs	20
2.3	Deriving sAHP dynamics	22
	Saturated calmodulin production.	22
	Binding of calmodulin to SK terminals.	23
	Calcium concentration	23
	Calcium concentration dynamics.	23
2.3.1	Full set of equations for the single SAC dynamics	25
2.4	Rescaled equations and Multi-time scale analysis	25
2.5	Parameters value and auxiliary functions	25
	Units.	25
	Calibrating parameters from experiments	26
	Auxiliary functions.	26
	Parameters.	26
2.6	Comparison with existing models	26
2.7	Bifurcations analysis	28
	Slow-fast analysis.	28
	Dynamical changes with respect to parameters variations.	28
	Dynamically driven bursting.	29
	Robustness with respect to parameters variations.	33

2.7.1	Variations of the bursting frequency depend on potassium and calcium conductances.	33
2.8	Characterizing the effect of noise on the bursting activity	37
2.9	Explaining the wide range of interburst intervals (IBI) across species by a unique mechanism	39
2.9.1	How do the average interburst depend on the parameter V_L	40
2.10	The role of the fast potassium conductance in bursting activity	42
2.11	Exploring the role of the potassium conductance in the loss of SACs excitability upon maturation	43
2.12	A conjecture on the role of the KV_3 channels in the loss of SACs excitability upon maturation	47
2.13	Discussion	47
	The role of inhibition	48
	Pharmacological control.	48
	The role of bursting in the spatial structure of SAC	48
3	The cholinergic coupling: a 1-dimensional study	49
3.1	Modeling cholinergic coupling	49
3.1.1	Cholinergic receptors	49
	Nicotinic acetylcholine receptors (nAChRs)	50
3.1.2	Full set of equations	52
	Parameters.	52
3.1.3	Tuning the parameters to fit experiments for acetylcholine dynamics	52
3.1.4	Bursting periods of immature SACs as a function of their biophysical parameters	52
	The role of sAHP on bursting characteristics	52
	The role of cholinergic coupling on bursting characteristics	55
3.2	Bursting of an isolated cell and acetylcholine production.	55
	Rest state	55
	Acetylcholine concentration dynamics.	57
	Acetylcholine concentration in the rest state.	57
	Ach concentration during a burst.	57
	Ach concentration just after a burst.	58
	Ach concentration during the hyperpolarization phase.	58
	Numerical checks.	58
3.3	Bursting of 2 coupled cells.	59
	Cells interaction.	59
	Fitting the Ach profile.	59
	The delay between bursts of cell 1 and cell 2.	60
	Burst bifurcation.	61
	Piecewise linear approximation for U	62
	Average Ach current in the rising phase.	63
	Time of the next burst.	63
	Calcium burst.	64
3.3.1	Remarks on how the waves propagate and stop	64
	Analytic characterization of the propagation in a 1-dimensional chain.	64

3.4	Coupled Bursters in 1D (ring)	65
3.4.1	Characterizing the dynamically driven bursting scenario in 1D	66
3.4.2	Characterizing the noise driven bursting scenario in 1D	67
3.5	How do SACs synchronize upon cholinergic coupling?	73
3.5.1	Mechanism for two bursting cells synchronization	73
	Synchronization and coupled oscillators.	73
	Synchronization in the dynamically driven bursting cells.	74
	Synchronization in the noise driven bursting cells.	76
3.6	What is the probability that one cell induces bursting to its neighbour?	76
3.6.1	Fluctuations about the rest state.	76
3.6.2	Ornstein-Uhlenbeck solution.	77
3.6.3	Bursting bifurcation.	77
3.7	Conclusion and Discussion	77
	How identical cells can display variability in behaviour.	78
4	Modeling and simulating stage II Retinal waves in 2D	79
4.1	Modeling a network of SACs	79
4.1.1	Network structure	79
4.2	How waves are generated in the developing retina? A proposed mechanism for waves triggering	80
4.2.1	Scenario 1: Noise induced triggering.	80
4.2.2	Scenario 2: Dynamically driven triggering.	82
4.3	How do waves propagate?	82
4.3.1	Propagation in a medium without friction	83
4.3.2	Propagation in a medium with an sAHP landscape	86
	Analytic characterization of the wave propagation in a sAHP profile.	91
	Example: $R^4(x, y) = \alpha\rho$,	92
4.4	Distribution of waves near the critical point.	92
	One wave.	93
	Non direct interaction between waves.	93
4.5	Modeling the dynamical changes occurring within stage II retinal waves	97
4.5.1	How does the cholinergic conductance evolves during development?	97
4.5.2	Different spatiotemporal patterns emerge within stage II retinal waves	98
4.5.3	Spatial Correlations reveal a characteristic size for stage II waves	100
4.6	Characterizing the SACs population activity and the features of retinal waves	100
4.6.1	Possible phase transition on the population firing rate	100
4.6.2	Distribution of waves size and duration, Power laws, Criticality	101
	Waves statistical features	101
4.7	Pattern formation in the dynamically driven bursting regime	102
4.8	Conclusion and Discussion	105
5	Towards a mesoscopic approach to analyse retinal waves	109
5.1	Transport equation	110
5.1.1	Model and variables rescaling	110
5.1.2	Reduced dynamics	111

	Fast dynamics of V, N	111
	Slow variables	112
	Medium scale variables	112
5.1.3	Equation of transport for Ach	112
	Approximations	112
	Ach production on the lower branch.	113
	Ach production on the upper branch.	113
	Thresholding.	113
	Variable Γ	113
	Piecewise linear approximation.	114
	Laplacian approximation.	114
	Singular diffusion.	114
	Current.	115
5.2	Discussion	115
	Single neuron dynamics in the presence of a tunable sAHP and Ach currents	115
6	Confronting our model to experimental recordings	119
6.1	The role of potassium channels in waves characteristics	119
6.2	Exploring the effect of the cholinergic transmission on the spatio-temporal patterns of stage II retinal waves	125
	Objective of the experiment.	125
	Pharmacology.	125
	Tissue preparation.	125
	Recordings of retinal waves with MEA of 256 electrodes	125
	Analysis of the MEA recordings	125
6.2.1	The effect of hexametonium in early stage II retinal waves	126
6.2.2	The effect of atropine in early stage II retinal waves	129
6.2.3	Power laws and criticality in experimental recordings of retinal waves	133
6.3	Conclusion and Discussion	134
7	Conclusions and Perspectives	137
7.1	Reflecting on possible theoretical extensions	137
	Synaptic coupling versus volume diffusion.	137
	The role of variability in SACs on waves generation.	138
	Extending our model towards a generic dynamical system for retinal waves	139
7.2	Can we use retinal waves to restore plasticity in pathological retinas?	139

Chapter 1

Introduction

In the natural world, all complex phenomena follow the laws of physics and for centuries physicists translate these physical rules in mathematical formalisms. For each physical system, one can try to decompose it to its parts and understand how these parts are connected to each other. Then, one can extract information, on which are the underlying mechanisms, explaining what we observe. Imagine now, trying to understand something as complex as a network of electrically active biological cells in our eyes, which are connected to each other by highly complex mechanisms, working together to manifest a collective activity, which helps in fact the shaping of the visual system during development. All biological processes involved in this system, are simply too complex to be translated to a mathematical model that could be analysed. But what if we could find a simpler system, that has similar physical principles to our network of cells, and use it as an analogy in order to write down our equations. And so did Hodgkin and Huxley thought, that the electrical behaviour of a nerve, if we take into account only currents flowing in and out of a cell membrane, would be really similar to a classical electric circuit; and so they wrote their famous equations based on this idea [59]. Since then, mathematical modeling in biology and neuroscience has been vastly developed and used to understand the principles that govern neural networks. In this thesis, we are going to use the same approach, in order to describe mathematically how specific cells in the retina of the eye, exhibit propagating electrical activity in the process of shaping the visual system during development. In the following, as an introduction, we discuss the necessary elements for the reader, in order to smoothly follow the ideas of this work.

1.1 Introduction to the visual system

1.1.1 Visual system and structure

The visual system is part of the central nervous system and its main function is to process visual information. Although its functionality seems effortless, it carries out complex tasks including the reception of light and the formation of visual representations, the identification and categorization of visual objects, computing distances to and between objects and guiding body movements in relation to the environment. The visual system includes basically the eyes, the optic nerve up to the Lateral Geniculate Nucleus (LGN) and the visual cortex. The neural signals, initially processed by the retina, travel via the axons of the ganglion cells through the optic nerves, dividing and

partially crossing over into the optic chiasm and then traveling via the optic tracts to the lateral geniculate nucleus (LGN). From the LGN, the signals continue to the primary visual cortex, where further visual processing takes place.

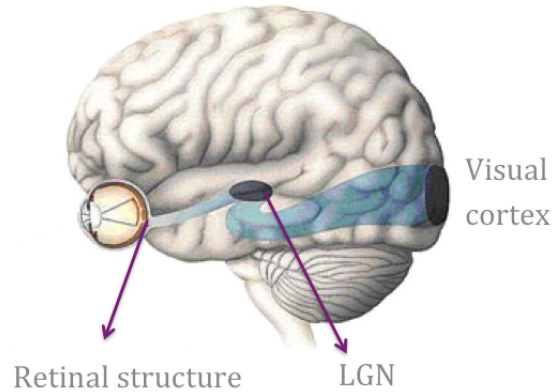


Figure 1.1: **The visual system's structure.** A textbook representation of the visual system composed of the retina, the LGN and the visual cortex.

1.1.2 The retina and its structure

The retina is a light-sensitive tissue at the back of the eye that covers about 65 percent of its interior surface. In the middle of the retina is a small dimple called the fovea. It is the center of the eye's sharpest vision and the location of most color perception. Moreover, retina is 0.5mm thick and it is composed of three layers of cell bodies and two layers of synapses.

Photosensitive cells, called photoreceptors (rods and cones), convert the incident light into electric pulses (spikes). A radial section of a portion of the retina reveals that the photoreceptors lie outermost in the retina against the pigment epithelium (see Fig 1.2). Light must, therefore, travel through the thickness of the retina before striking and activating the rods and cones. Subsequently the absorption of photons by the visual pigment of the photoreceptors is translated first into a biochemical message and then an electrical message that can stimulate all the adjacent neurons of the retina. The input from multiple photoreceptors is integrated and regulated by horizontal cells which are laterally interconnecting neurons with their cell bodies in the inner nuclear layer of the retina. Next, bipolar cells, existing between photoreceptors and ganglion cells, act directly or indirectly, to transmit signals from the photoreceptors to the ganglion cells. Amacrine cells are interneurons in the retina that are responsible for 70 per cent of input to retinal ganglion cells also. Ganglion cells (RGC), are the output neurons of the retina, and lie innermost in the retina, closest to the lens and front of the eye. Ganglion cells axons form the optic nerve, that carries the optic signal to the visual cortex.

1.1.3 Starburst Amacrine Cells

Starburst amacrine cells (SACs) are a subtype of retinal amacrine cells primarily identified by the characteristic star-like shape of their dendritic arbor [28]. SACs have two

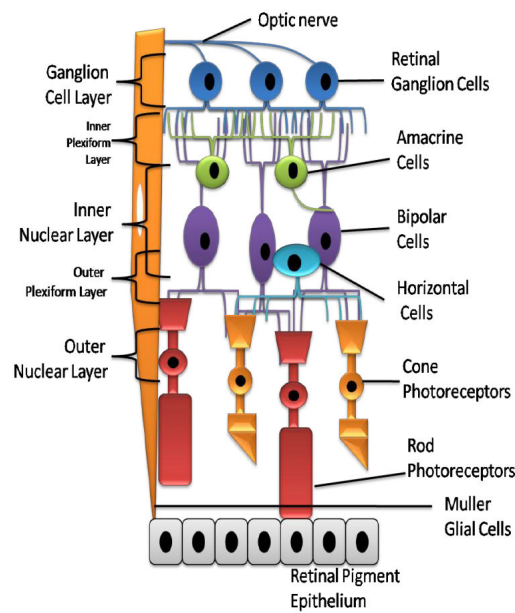


Figure 1.2: **Retinal structure** A textbook representation of the layered structure of the retina showing the different cell types: photoreceptors, bipolars, amacrines, horizontal, ganglion cells [19].

main functional roles are: i) their participation in the direction selectivity feature [6] and ii) generate spontaneous propagating activity in the developing retina [63]. SACs involvement in the direction selectivity feature in the retina computation, is explained by their morphological characteristics, such as the specific dendritic radial shape and a desymmetrised distribution of excitatory and inhibitory connections along the dendritic arbors [4, 60]. Also SACs, within the adult mammalian retina provide the critical inhibition that underlies the receptive field properties of direction-selective ganglion cells (DSGCs) [25].

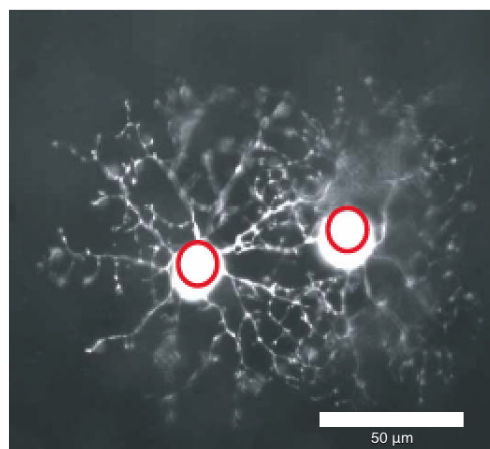


Figure 1.3: **Starburst amacrine cells.** We clearly see their special shape of their dendritic arboring [63]

SACs, in the developing retina, exhibit autonomous rhythmic spontaneous activity, which generates propagating waves across the retina, called retinal waves, responsible to shape the visual pathways. SACs are the only cells in the retina that have been shown to release two neurotransmitters, acetylcholine and GABA [62]. In fact, SACs form a transient excitatory network, coupled by mutual cholinergic connections, generating retinal waves. A detailed biophysical modeling of the spontaneous activity of SACs leading to propagating waves in the developing retina, is analyzed in detail in this thesis.

1.2 From neurons to neural networks

The overwhelming capacity of the retina to convert complex visual scenes into spike trains that send information to the visual cortex are largely due to its layered structure and to dynamical interactions between neurons in the retina. As a consequence and although it is very important to study the physiology and structure of individual neurons, in order to fully comprehend the functionality of the retina we need to study the system as a network, which processes the information via collective activity. Let us first though describe the components of a neural network in general.

Synapses. Synapses are functional connections between neurons, or between neurons and other types of cells. A typical neuron may have several thousand synapses, although there are some types that make far fewer. Most synapses connect axons to dendrites, but there are also other types of connections, including axon-to-cell-body, axon-to-axon, and dendrite-to-dendrite. Synapses are generally too small to be recognizable using a light microscope except at points where the membranes of two cells appear to touch, but their cellular elements can be visualized clearly using an electron microscope. Chemical synapses are specialized junctions through which cells of the nervous system signal to one another and to non-neuronal cells such as muscles or glands 1.5. Chemical synapses allow the neurons of the central nervous system to form interconnected neural circuits. They are thus crucial to the biological computations that underlie perception and thought. They also provide the means through which the nervous system connects to and controls the other systems of the body. Chemical synapses pass information directionally from a presynaptic cell to a postsynaptic cell and are therefore asymmetric in structure and function. The presynaptic terminal, or synaptic button, is a specialized area within the axon of the presynaptic cell that contains neurotransmitters enclosed in small membrane-bound spheres called synaptic vesicles. Synaptic vesicles are docked at the presynaptic plasma membrane at regions called active zones. Electrical synapses are mechanical and electrically conductive links between two adjacent neurons that are formed at a narrow gap between the pre- and postsynaptic neurons known as gap junctions. At gap junctions, such cells approach within about $3.5nm$ of each other, a much shorter distance than the 20 to $40nm$ distance that separates cells at a chemical synapse. In many animals, electrical synapse-based systems co-exist with chemical synapses.

Compared to chemical synapses, electrical synapses conduct nerve impulses faster, but, unlike chemical synapses, they lack gain since the signal in the postsynaptic neuron, is the same or smaller than that of the originating neuron. Electrical synapses are often found in parts of the neural systems that require the fastest possible response,

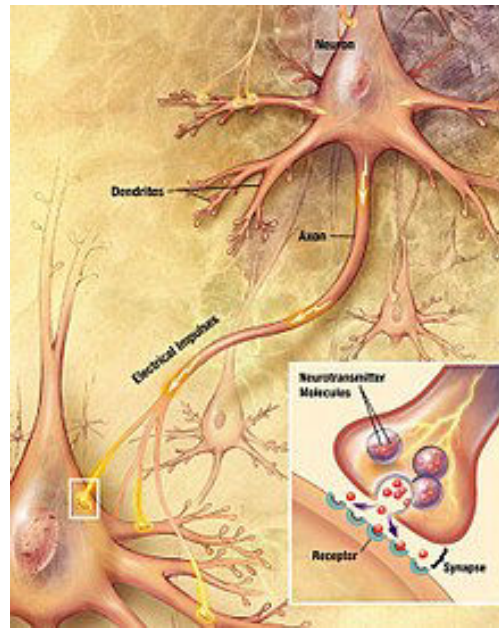


Figure 1.4: **Chemical Synapse** An artistic representation of a chemical synapse (source Wikipedia).

such as defensive reflexes. An important characteristic of electrical synapses is that, most of the time, they are bidirectional. However, some gap junctions do restrict communication to only one direction [28].

Connectivity. The connections between neurons are made with chemical synapses and electrical gap junctions. One principle by which neurons work is neural summation, i.e. potentials at the post synaptic membrane sum up in the cell body. If the depolarization of the neuron at the axon goes above threshold an action potential will occur that travels down the axon to the terminal endings to transmit a signal to other neurons. Excitatory and inhibitory synaptic transmission is realized mostly by inhibitory postsynaptic potentials and excitatory postsynaptic potentials. On the electrophysiological level, there are various phenomena which alter the response characteristics of individual synapses, (such as synaptic plasticity) and individual neurons, (intrinsic plasticity). Connections display temporal and spatial characteristics. Temporal characteristics refer to the continuously modified activity-dependent efficacy of synaptic transmission. It has been observed in several studies that the synaptic efficacy of this transmission can undergo short-term increase, called facilitation or decrease, according to the activity of the presynaptic neuron. The induction of long-term changes in synaptic efficacy, by long-term potentiation (LTP) or depression (LTD), depends strongly on the relative timing of the onset of the excitatory postsynaptic potential and the postsynaptic action potential.

1.3 Retinal waves

Long before the retina is responsive to light, in early development wave activity is observed. The so called retinal waves, observed in many vertebrate species - chicks

[31], ferrets [36], mice [53], turtles [55], macaques [69] etc. are spontaneous bursts of activity propagating in the developing retina and playing a fundamental role in shaping the visual system and retinal circuitry. They emerge due to the conjunction of intrinsic single-cell properties (excitability and long refractoriness) and network interactions [63]. In the developing retina, waves evolve during three consecutive stages, mainly characterized by different types of synaptic transmission. Stage I waves are mediated by gap junctions, travelling both horizontally across the RGC layer and vertically across the thickness of the retina, several days before synapse formation [56]. They are believed to play a role in the formation of the retinal circuitry but they are not yet fully understood [56]. Stage II waves are elicited by SACs through acetylcholine connections and propagate laterally across the retina. Also, their propagation speed is much slower than Stage I waves, they occur less frequently and their wave initiation points and trajectories are highly random [36, 56]. Functionally, they are found to refine the retinotopic mapping, which is the mapping of the visual input from the retina to the brain. In the next phase, stage III retinal waves switch their control from cholinergic to glutamatergic input [15], from the bipolar cells. These late waves are more localized, propagate vertically and disappear when vision is functional.

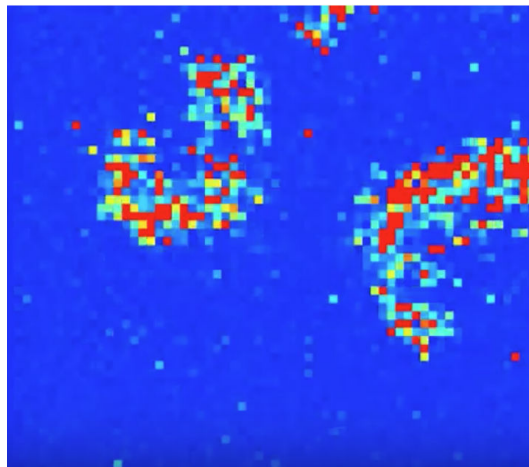


Figure 1.5: **Stage II retinal waves.** An experimental recording of stage II retinal waves in mice, measuring the local voltage, showing propagating activity [53].

1.3.1 General mechanism of stage II retinal waves

In the work of Zheng et al. [63], which is a benchmark on establishing the cellular mechanisms underlying stage II retinal waves, they conclude that in order to generate these waves, there are 3 necessary conditions (see Fig 1.6). The details of these conditions are developed throughout this thesis.

- (i) Fast repetitive bursts of spikes;
- (ii) Prolonged refractoriness through slow AfterHyperpolarisations (sAHP)
- (iii) Synchronization via cholinergic connections of SACs

The fast repetitive firing is needed as a source of depolarization for wave initiation given that there is no external input (e.g. from visual stimulation in the early

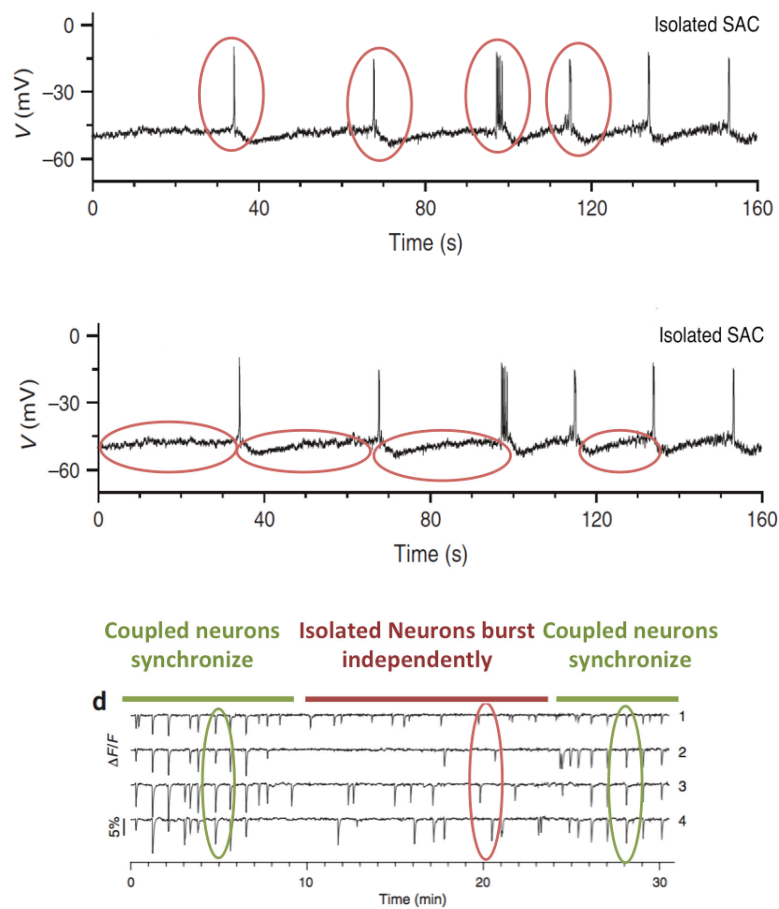


Figure 1.6: **Illustrating the 3 necessary conditions to generate stage II retinal waves.** *Top and Middle.* Patch clamp recording of an isolated SAC exhibiting bursting activity. In red, we mark the two components of bursting. *Bottom.* Calcium imaging to show that acetylcholine synchronizes the network of SACs. All figures are from the work of [63].

retina). Thus, there must be some intrinsic mechanism by which neurons become active. As it is shown in [63], SACs exhibit fast oscillations due to their intrinsic cellular mechanisms, mainly controlled by voltage gated Ca^{+2} channels. Second, the long refractoriness of SACs, is needed to limit the spatial extent of waves and dictate the minimum interval between them. Finally, mutual cholinergic excitation, is essential for the synchronisation of SACs. When the multiple bursts occur in a neighbourhood of a neuron, SACs are synchronized, and they trigger a wave.

1.4 Modeling stage II retinal waves

The prevalence of retinal waves, observed in many different species and at different developmental stages, suggests that they are generated by generic collective and non linear mechanisms that still need to be unravelled. Developing mathematical models constitute a way to extract these underlying mechanisms. This strategy has been applied over the last twenty years, essentially for stage II, which are the most well studied waves.

1.4.1 State of the art

We briefly mention here previous models [34, 38, 54, 12], close to the spirit of the present thesis. For an extended review, see [50, 51].

Hennig et al. [54] model is, up to now the most elaborated model of stage II retinal waves with respect to biophysics. Especially, it capture the basis of the sAHP dynamics and reproduces prominent statistical characteristics of waves experimentally observed in mice. As our own model is inspired by [54], we will widely comment it in the thesis. In this introduction we shortly expose our main criticism: (i) the equations are not strictly bound to experimental findings and several parameter values are not biophysically justified. This holds for the other existing models [34, 38, 12]; (ii) this model requires an exogeneous shot noise current in order to induce the bursting activity triggering wave propagation: without this noise neurons stay at rest and it is not possible to reproduce the spontaneous depolarization and bursting observed in [63]. The same type of "artificial" source of spontaneous depolarization is used by [34, 38, 12] as well. Moreover, the noise level needs to be fine tuned so as to reproduce experimental curves for waves size distribution; (iii) they do not provide a mathematical analysis of their model. As we discuss in this thesis, such analysis is useful to unravel generic mechanisms for waves generation, propagation and shaping. Later, a dynamical system of a reaction diffusion type for stage II waves has been proposed by Lansdell et al. [12]. Their model is based on Hennig et al.'s with several important modifications: (i) The sAHP current is modeled in a less biophysical way; (ii) synaptic interactions are modeled by acetylcholine diffusion in a continuous medium in contrast to [54] where they use synaptic interactions. As in Hennig et al. model, SACs are at rest in spontaneous activity and waves triggering requires a exogeneous noise. The authors perform a limited mathematical analysis.

The models [34, 38, 54] have compared their numerical results with experimental data and showed that they are able to reproduce some characteristics of retinal waves such as the waves sizes, duration, speeds and frequency. However, these models, are mostly able to reproduce already existing experimental results and not really predict new ones. Their approaches mainly lie on capturing phenomenologically the features of

waves and do not model in detail the underlying biophysical mechanisms responsible for retinal waves generation.

1.4.2 What is this thesis about?

Having discussed the criticism of the state of the art, we have to say that the best model is the one that answers one's questions and no single model can answer all of them. In other words, all models have their limitations as they are constructed so as to answer specific questions. So, in contrast to these existing models, our approach is based on the detailed biophysical modeling of the cellular mechanisms of the spontaneous activity in immature SACs, addressing questions directly accessible and linked to pharmacological manipulations on retinal waves.

On theoretical grounds, it is natural to seek generic mechanisms (typically non linear instabilities) generating such waves and to extract from this analysis a few canonical parameters (e.g. conductances, characteristic times, reversal potentials etc.) controlling the generation of retinal waves as well as their characteristics. However, a conventional nonlinear analysis based on spatially extended dynamical systems would not be entirely appropriate to deal with the specific structure of the retina: discrete medium, specific connectivity via amacrine cells and electrical synapses, spiking ganglion cells, conductances adaptation. Neurons are non linear systems producing a wide repertoire of dynamical activity, intrinsic, in response to a stimulus or due to change in physiological properties (e.g. conductances). They are connected in a complex way, because the graph of connectivity itself is complex, and evolve in time (synaptic plasticity), but also because the connectivity mechanism are themselves non linear, involving delays and memory. It's also a multiscale problem, for the molecular scale to brain scale, from microseconds to years. As a consequence, the mathematical study of neuronal network is progressing slowly. Although there exist efficient methods to study theoretically extended neuronal networks in the cortex (mean-field, neural field, Fokker-Planck equation), the equivalent studies do not exist, to our best knowledge, in the retina. This work is an attempt to propose such an analysis, taking into account the specific characteristics of the retina (here amacrine cells and cholinergic coupling). An adaptation of the standard non linear analysis to these constraints is therefore done, integrating chemical synapses and a thorough mathematical analysis of their dynamics. Our constructed set of equations constitutes therefore a solid basis to analyze non linear generation of waves in a neuronal network.

Using our model, we are able to answer several questions both on the single neuron as well as the network level. The detailed modeling of individual SACs dynamics as autonomous, rhythmic bursters and the mathematical analysis of our dynamical system using bifurcations theory, helps us identify the key parameters which control bursting in immature SACs. We propose a mathematical model, grounded on biophysics, which enables us to reproduce the bursting activity of SACs and to propose a plausible, generic and robust, mechanism that generates it. Based on a bifurcations analysis we exhibit a few biophysical parameters, especially regulating calcium and potassium activity, controlling bursting. We propose a testable experimental prediction on the role of voltage-dependent potassium channels on the excitability properties of SACs and on the evolution of this excitability along development. We also propose an explanation on how SACs across different species can exhibit a large variability in their bursting

periods, as observed experimentally, yet based on a simple, unique, mechanism. Extending the single neuron dynamics, we model in detail the mutual cholinergic synaptic connections between SACs, ending up exploring the mechanisms of SACs synchronization. We make a thorough analytic and numerical analysis to characterize how waves start, propagate and stop, providing analytic conditions that define the waves dynamics. We also provide an extension of our modeling towards a mesoscopic approach to study the propagation of waves in another spatial scale, that of acetylcholine. Finally, we confront our model to experiments, performed by our collaborators, in order to validate our theoretical findings on the role of potassium channels and the cholinergic coupling on waves. Also, we use these experimental data to validate our predicted link to critical systems via power law manifestations for the waves characteristics.

Taken together, with this research we answer to the following questions with respect to our understanding of how retina works during development. Which is the biophysical mechanism that generates sustained periodically bursting in immature SACs and which are the parameters that control it? How can we link the biophysical parameters of our model directly with experimental measures, creating a framework where experiments can be reproduced by our model and our predictions could be tested experimentally? What is the mechanism underlying the loss of SACs excitability upon maturation? Is the mechanism of waves generation universal accross species given their variability in their characteristics? How do SACs synchronize in order to produce propagating waves? How do waves propagate and what is the type of their propagation? How do waves stop? How do the characteristics of waves depend on the biophysical parameters of their model and what can we predict for the network's state? Is the network of SACs in a critical state and if so, what are the consequences of criticality on waves?

This work has possible future outcomes with respect to retina therapy as well. Understanding how retinal waves are initiated and propagate in the retina could enable us to define protocols to trigger such retinal waves in the in vivo adult retina. Inducing such waves is expected to reintroduce some plasticity in the retinal tissue and the projections in the brain. This induced plasticity could have important therapeutic applications to treat patients or stimulate regeneration of retinal ganglion cell axons following optic nerve crush.

The structure of the thesis is organized as follows: in Chapter 2, we study the dynamics of a single SAC and we propose a mathematical model, grounded on biophysics, which enables us to reproduce the bursting activity of SACs and to propose a plausible, generic and robust, mechanism that generates it. Based on a bifurcations analysis we exhibit a few biophysical parameters, especially regulating calcium and potassium activity, controlling bursting. In Chapter 3, we model the cholinergic connections and address mainly the questions "*How do waves start?*" and "*How bursting cells synchronize?*" in a 1-dimensional study. In Chapter 4, we perform the 2-dimensional study of retinal waves, characterizing the waves propagations as well as their statistical characteristics. In Chapter 5, we provide a derivation of a transport equation to study the spatiotemporal dynamics on a mesoscopic scale. In Chapter 6, we confront some of our theoretical findings to experiments. Finally, in Chapter 7, we conclude the thesis and give our perspectives for future extensions of this work.

1.4.3 Methods and tools used in this thesis

Bifurcations theory. Many systems evolving in time are described by differential equations. Although it is tempting to try and find an analytic solution for these equations, this is, in most cases not possible. Dynamical system theory is a branch of mathematics/physics, attempting to describe the behaviour of these solutions, without having an explicit representation of them. This is a powerful method, initiated by Poincaré with a lot of applications in mathematics, physics, biology, chemistry, engineering, economics, and medicine. The mathematical study of changes in the qualitative behaviour of a set of non-linear equations, upon the continuous smooth variation of the parameters values, is called bifurcations theory. A bifurcation occurs when a dramatic sudden change in the behaviour of the dynamical system is caused by the small smooth change made to a parameter values [73]. In other words, there exist certain points, acting as 'thresholds', at which the dynamics change abruptly, called bifurcation points. Bifurcations theory, provide us with tools to study the behaviour of complex dynamical systems depending on key parameters, using geometrical arguments, overcoming the difficulty to have direct solutions. It is a powerful tool, that helps us understand in depth how complex systems behave, allowing us to make predictions and extract mechanisms for the modeled systems. The name "bifurcation" was first introduced by Henri Poincaré in 1885 in the first paper in mathematics showing such a behavior [74].

Numerical simulations. In this work we use numerical methods done mostly in Python (we also use the Brian2 simulator [22] and MATLAB (we use the bifurcations software MATCONT [58]), but also methods programmed in C in order to simulate our model, perform bifurcations analysis and also characterize waves.

Chapter 2

Modeling the bursting activity of individual immature SACs

Stage II retinal waves, are triggered by a transient network of neurons called Starburst Amacrine Cells (SACs) showing a bursting activity which disappears upon further maturation. The underlying mechanisms of the spontaneous bursting and the transient excitability of immature SACs are not completely clear yet. While several models have tried to reproduce retinal waves, none of them is able to mimic the rhythmic autonomous bursting of individual SACs and understand how these cells change their intrinsic properties during development. Here, we propose a mathematical model, grounded on biophysics, which enables us to reproduce the bursting activity of SACs and to propose a plausible, generic and robust, mechanism that generates it. Based on a bifurcations analysis we exhibit a few biophysical parameters, especially regulating calcium and potassium activity, controlling bursting. We propose a testable experimental prediction on the role of voltage-dependent potassium channels on the excitability properties of SACs and on the evolution of this excitability along development. We also propose an explanation on how SACs across different species can exhibit a large variability in their bursting periods, as observed experimentally, yet based on a simple, unique, mechanism. As we discuss, these observations in the cellular level, have a deep impact on the retinal waves description.

This material is the subject of a paper '*A biophysical model explains the spontaneous bursting activity in the developing retina*', D. Karvouniari, L. Gil, O. Marre, S. Picaud, B. Cessac, currently under review in *Nature Scientific Reports*, [1].

2.1 The Morris-Lecar model

The Morris-Lecar model [13], is a conductance based model, and a simplified version of the Hodgkin-Huxley equations [59], since it does not describe the fast dynamics of sodium. The Morris-Lecar equations are particularly useful for modelling fast-spiking neurons, such as the pyramidal neurons of the neocortex. Morris-Lecar-type models may prove useful for studying scaling phenomena, such as showing how neural oscillators and oscillatory networks change as the cells grow during development. Finally, the Morris-Lecar model neuron has been applied to modeling networks of coupled neural oscillators. Here the simple but realistic parameterization allows one to describe collective oscillations which depend on the inter-neuron coupling. A model employing

Morris-Lecar oscillators of different frequencies has been used to explain quite complex bursting phenomena of coupled neurons. All the above characteristics of the Morris-Lecar equations, make them the suitable candidate to model to describe the dynamics of autonomous bursters, such as immature SACs. Evidently, the basic Morris-Lecar model, as it is two dimensional, is not sufficient to model SACs dynamics, whose activity is generated by more complex currents. However, it is possible to extend Morris-Lecar equations by adding the additional currents involved in SACs bursting, as we will show in the following,

2.2 A biophysical model for bursting immature SACs

In the case of immature SACs, the two key biophysical mechanisms associated with the emergence of spontaneous bursting during early development are [63]:

- (i) fast repetitive bursts of spikes mainly controlled by voltage-gated Ca^{+2} channels;
- (ii) prolonged AHPs modulating fast oscillations, controlled by Ca^{+2} -gated K^{+} channels.

Concerning (i), the fast repetitive firing during the active phase of bursting generally results from the competition between a depolarizing and a hyperpolarizing current. Experiments in [63] on specifying the ionic channels involved in the spontaneous bursting of immature SACs, suggest voltage-gated Ca^{+2} channels for the depolarizing component. Note that [63] have shown that voltage-gated Na^{+} channels do not participate in the bursting mechanism of immature SACs (bursting activity of SACs was not altered upon tetrodotoxin -TTX- application), thus, dynamics of Na^{+} channels will not be considered in our modeling. The ionic channels related to the hyperpolarizing component of SACs bursting have not yet been identified experimentally. In this work, we propose *fast* voltage-gated K^{+} channels play this role. This point is further developed in the following.

Concerning (ii), the long refractoriness in-between consecutive bursts is controlled by a slow After Hyper-Polarization (sAHP) K^{+} current, I_{sAHP} . It was observed by [63] that I_{sAHP} is mediated by Ca^{+2} -gated K^{+} channels, and that it resembles the sAHP observed by Abel et al. [11], generated by specific channels called *SK*. Following these tracks we propose a modeling of "SK"-like channel (as named in [63]) based on [54] for the structure of the equations and [44] for the calcium dynamics. The mechanism of the opening of Ca^{+2} -gated ionic channels is analyzed in detail in the supporting information section. In order to simplify the cascade of chemical reactions taking place while opening the sAHP channels, we approximate the channel dynamics by reducing the process into two discrete steps: a) Four ions of Ca^{+2} bind to a second messenger protein called calmodulin, forming a saturated calmodulin complex, CaM; b) CaM binds to each of the four intracellular subunits of the channel to open it (see Fig 2.1). This process is mapped to our model through three variables: 1) the variable C which models the intracellular calcium concentration and mainly controls the gating variables of the sAHP channels, 2) the variable S which models the fraction of the saturated calmodulin and 3) the variable R which models the fraction of bounded terminals. This gating mechanism is sketched in Fig 2.1.

From these observations, we model SACs activity with a conductance based model of the Morris-Lecar type [13] with additional currents featuring (i), (ii). The model involves 5 variables whose evolution is controlled by a set of non-linear differential equations (see Eq (2.2)-(2.8)): $V(t)$, the local membrane potential, $N(t)$, the gating variable for fast voltage-gated K^+ channels, $R(t)$ and $S(t)$, the gating variables for slow Ca^{2+} -gated K^+ channels and $C(t)$, the intracellular Ca^{2+} concentration. All parameters values and the auxiliary functions involved are found in Methods.

The membrane voltage $V(t)$ obeys:

$$C_m \frac{dV}{dt} = I_L(V) + I_C(V) + I_K(V, N) + I_{sAHP}(V, R) + \sigma \xi_t, \quad (2.1)$$

where C_m is the membrane capacitance, $I_L = -g_L(V - V_L)$ is the leak current, with g_L leak conductance and V_L leak reversal potential. ξ_t is a white noise whose amplitude is controlled by σ . The terms I_C and I_K , respectively corresponding to Ca^{+2} and K^+ currents, are generating the fast Ca^{+2} oscillations. These currents are described by a Morris-Lecar model [13] where the voltage-gated Ca^{+2} current is:

$$I_C(V) = -g_C M_\infty(V)(V - V_C). \quad (2.2)$$

$g_C M_\infty(V)$ is the voltage dependent conductance of the Ca^{+2} channel (see Eq (2.21) in Methods).

The fast voltage-gated K^+ channel is modeled as:

$$I_K(V, N) = -g_K N(V - V_K). \quad (2.3)$$

where the evolution of the fast voltage-gated K^+ channel gating variable $N(t)$ is modeled as:

$$\tau_N \frac{dN}{dt} = \Lambda(V)(N_\infty(V) - N), \quad (2.4)$$

$\Lambda(V)$ and $N_\infty(V)$ are given by Eq (2.22), (2.23) in Methods. Note that equations (2.1) - (2.4) with $I_{sAHP} = 0$ and $\sigma = 0$, correspond to the Morris-Lecar model with a fast variable N .

The sAHP current takes the form:

$$I_{sAHP}(V, R) = -g_{sAHP} R^4 (V - V_K), \quad (2.5)$$

where g_{sAHP} is the maximum sAHP conductance. Indeed, 4 bound terminals are needed to open a Ca^{+2} -gated K^+ channel, thus the corresponding conductance is $g_{sAHP} R^4$, involving a fourth order nonlinearity.

Now, we model the gating mechanism of the Ca^{+2} gated K^+ channels as follows. The gating variable $R(t)$:

$$\tau_R \frac{dR}{dt} = \alpha_R S(1 - R) - R, \quad (2.6)$$

the fraction of saturated calmodulin concentration $S(t)$;

$$\tau_S \frac{dS}{dt} = \alpha_S C^4(1 - S) - S, \quad (2.7)$$

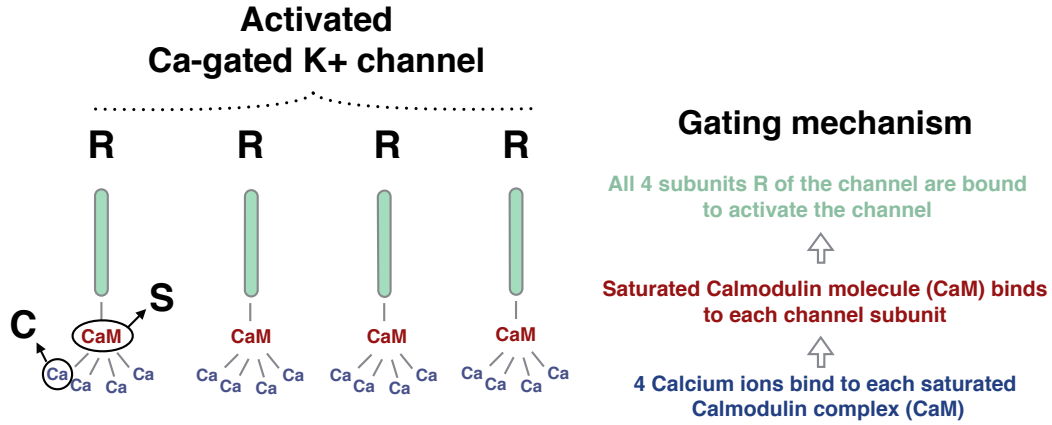


Figure 2.1: **Schematic representation of the modeling of the gating mechanism of Ca^{+2} -gated K^+ channels.** The correspondence between the channel's activation steps and the modeling state variables R, S, C is also indicated.

and the intracellular calcium concentration $C(t)$;

$$\tau_C \frac{dC}{dt} = -\frac{\alpha_C}{H_X} C + C_0 - \delta_C g_C M_\infty(V)(V - V_C). \quad (2.8)$$

The derivation of the equations (2.6), (2.7), (2.8) is fully justified in Methods.

2.3 Deriving sAHP dynamics

To our best knowledge, the ionic channels type involved in sAHP for immature stage II SAC is not precisely known. However, Zheng et al. argue in [63] that these channels could share characteristics with SK channels, thoroughly studied for pyramidal neurons by Abel et al in [11]. On this basis we modeled SK channels dynamics. SK channels have four subunits associating to form a tetramer. The SK channel gating mechanism is controlled by intracellular calcium levels. The precise mechanism is: (i) calcium binds to the protein calmodulin forming the complex CaM where 4 ions Ca^{2+} are fixed to calmodulin; (ii) CaM binds to a SK channel terminal to open it; (iii) 4 terminals must be open to let the SK channel open. We now model these different steps.

Saturated calmodulin production. The set of kinetic equations leading to CaM formation is widely described in M. Graupner's work [43, 44]. This is a cascade of equations that we summarize in one kinetic equation, from free calmodulin, M , to the saturated one, CaM .

Let us call k_{ass} ($M^{-4}s^{-1}$) and k_{diss} (s^{-1}) respectively association and dissociation constants of calmodulin. Set $K_d^4 = \frac{k_{diss}}{k_{ass}}$. If we call $M_0 = [M] + [CaM]$ the total calmodulin concentration, and $S = \frac{[CaM]}{M_0}$ the fraction of saturated calmodulin, we have $\frac{[M]}{M_0} = 1 - S$ and we obtain a kinetic equation:

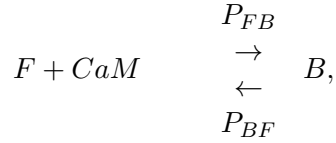
$$\frac{dS}{dt} = k_{ass} C^4 (1 - S) - k_{diss} S.$$

where C is the intracellular calcium concentration. Setting $\tau_S = \frac{1}{k_{diss}}$ and $\alpha_S = \frac{k_{ass}}{k_{diss}} = \frac{1}{K_d^4}$ we arrive at:

$$\tau_S \frac{dS}{dt} = \alpha_S C^4 (1 - S) - S. \quad (2.9)$$

Note equation (2.7) has a similar form to the one proposed by Hennig et al. in [54]. However, in their model our term C^4 is replaced by $\frac{C^4}{K_d^4 + C^4}$ which is hardly interpretable in terms of kinetics.

Binding of calmodulin to SK terminals. This corresponds to a reaction:



where F is the density of free terminals, B the density of bounded terminals, P_{FB} (P_{BF}) the transition rate from free to bound (bound to free).

Calling R the fraction of bounded terminals, $\tau_R = \frac{1}{P_{BF}}$, $\alpha_R = \frac{P_{FB}}{P_{BF}}$ we end up with a kinetic equation:

$$\tau_R \frac{dR}{dt} = \alpha_R S (1 - R) - R = \alpha_R S - (1 + \alpha_R S) R. \quad (2.10)$$

Equation (2.6), is similar to Eq (3) in [54] ($\tau_R \frac{dR}{dt} = (\alpha C + S)(1 - R) - R$), with a remarkable difference: in our model there is no direct dependence on calcium concentration whereas the term αC in [54] corresponds to a direct binding of Ca^2 to a terminal. Note that, taking the quite large value of the parameter α (2400) considered by these authors, their equation is essentially equivalent to $\tau_R \frac{dR}{dt} = \alpha C (1 - R) - R = \alpha C - (1 + \alpha C) R$ with a steady state $R = \frac{\alpha C}{1 + \alpha C}$ very close to 1 whenever αC is quite larger than 1. In this case, S plays essentially no role.

Finally, since R is the probability that a terminal is open and since 4 terminals must be open to let the SK channel open, the sAHP conductance is $g_{sAHP} R^4$.

Calcium concentration Both variables R and S are driven by intracellular Ca^2 concentration dynamics, given by:

$$\tau_C \frac{dC}{dt} = -\frac{\alpha_C}{H_X} C + C_0 - \delta_C g_C M_\infty(V)(V - V_C) \quad (2.11)$$

Equation (2.11) is a linear approximation of a more complex equation ((2.14) below). This equation is similar to Hennig et al (Eq (5)) with two notable differences: (1) We have added a rest concentration C_0 avoiding unphysical situations where C can become negative; (2) the value of parameters are different.

Calcium concentration dynamics. The calcium current crossing a membrane section results from the opening of gates in ionic channels. Following [43] the equation for Ca concentration is (adapted with our notations):

$$\frac{dC}{dt} = \frac{G}{n_{Ca} F} \left[\frac{I_C}{S} - J_X(C) - J_p(C) + L \right] \frac{1}{1 + \frac{dC a_{bound}}{dC}}. \quad (2.12)$$

Here $G = \frac{S}{V} = 6 \mu m^{-1} = 6 \times 10^5 dm^{-1}$ is the surface to volume ratio that accounts for the localisation of the channels at the surface of the membrane, $n_{Ca} = 2$ is the calcium valence and $F = 96500 C mol^{-1}$ is the Faraday number. $\frac{dCa_{bound}}{dC}$ corresponds to a quasi-steady-state approximation for the calcium buffering where the bound calcium concentration (on calmodulin) Ca_{bound} is adapted instantaneously to the free calcium concentration C at each time. Since we have no way to estimate $\frac{dCa_{bound}}{dC}$ we shall consider it is a constant and set $\frac{1}{1 + \frac{dCa_{bound}}{dC}} \equiv K_{bound}$. To alleviate notations we set:

$$r = \frac{G K_{bound}}{n_{Ca} F}. \quad (2.13)$$

The first term in Eq (2.12), $r \frac{I_C}{S}$ corresponds to an increase of internal Ca^{2+} concentration upon calcium influx (current $I_C(V)$) generated by spikes or, in experiments, by voltage clamp. As $V_{Ca} = 50mV$ this current is positive unless $V > V_{Ca}$.

The second term is $-rJ_X(C)$, where

$$J_X(C) = \rho_X I_X \frac{C}{H_X + C},$$

is the efflux current density through sodium-calcium exchanger (NCX). It corresponds to an outward through NCX exchangers, contributing to restoring the initial Ca concentration. Here, ρ_X is the surface density of the NCX membrane proteins. We take $\rho_X = 100 \mu m^{-2} = 10^{12} dm^{-2}$ (from [44]). $I_X = 4.8 \times 10^{-19} C ms^{-1} = 4.8 \times 10^{-16} C s^{-1}$ is the maximum ionic flux through a single NCX channel. This corresponds to 3 + charges ($1.5 Ca^{2+}$) per ms ; $H_X = 1.8 \mu M = 1.8 \times 10^{-6} M$ is the half activation concentration [43].

Also, in (2.12), $J_p(C)$ is the current density of Ca pumps. We shall neglect this term from now on. Finally, L is the leakage surface current density representing the residual conductivity of the plasma membrane. We have not been able to find its value in the literature.

To summarize Eq (2.12) becomes:

$$\frac{dC}{dt} = r \left[\frac{I_C}{S} - \rho_X I_X \frac{C}{H_X + C} + L \right]. \quad (2.14)$$

We also assume that NCX current term is approximated by a linear term. This is valid if one assumes that calcium concentration $C \ll H_X$ which is the case in our simulations.

In order to match (2.14) with the form (2.11) ((2.8) in the text), we set:

$$\frac{\alpha_{Ca}}{\tau_{Ca}} = r \rho_X I_X; \quad (2.15)$$

$$\frac{\delta_{Ca}}{\tau_{Ca}} = \frac{r}{S}; \quad (2.16)$$

$$\frac{C_0}{\tau_{Ca}} = rL. \quad (2.17)$$

$$(2.18)$$

2.3.1 Full set of equations for the single SAC dynamics

To summarize, the full set of equations in our model with the 5 state variables V, N, C, S, R is the following:

$$\left\{ \begin{array}{l} C_m \frac{dV}{dt} = -g_L(V - V_L) - g_C M_\infty(V)(V - V_C) - g_K N(V - V_K) - g_{sAHP} R^4(V - V_K) \\ \tau_N \frac{dN}{dt} = \Lambda(V)(N_\infty(V) - N) \\ \tau_C \frac{dC}{dt} = -\frac{\alpha_C}{H_X} C + C_0 - \delta_C g_C(V)(V - V_C) \\ \tau_S \frac{dS}{dt} = \alpha_S(1 - S)C^4 - S \\ \tau_R \frac{dR}{dt} = \alpha_R S(1 - R) - R \end{array} \right. \quad (2.19)$$

2.4 Rescaled equations and Multi-time scale analysis

The dynamical system (2.19) has 3 characteristic times: fast variables V, N (of order ms); medium C (of order s); slow R, S (of order $10 s$), fixed by the characteristic times given in the Table 2.1. In order to make explicit these time-scales separation we set $\tilde{g}_X = \frac{g_X}{|g_L|}$ for conductances ($X = C, K, sAHP$); $\tau = \frac{C_m}{g_L}$; $\tilde{t} = \frac{t}{\tau}$; $\tilde{\tau}_X = \frac{\tau_X}{\tau}$, where $X = N, C, R, S$. This gives:

$$\left\{ \begin{array}{l} \tau_L \frac{dV}{d\tilde{t}} = -\tilde{g}_L(V - V_L) - \tilde{g}_C M_\infty(V)(V - V_C) - \tilde{g}_K N(V - V_K) - \tilde{g}_{sAHP} R^4(V - V_K) \\ \tau_N \frac{dN}{d\tilde{t}} = \Lambda(V)(N_\infty(V) - N) \\ \tau_C \frac{dC}{d\tilde{t}} = -\frac{H_X}{\alpha_C} C + C_0 - \delta_C g_C M_\infty(V)(V - V_C) \\ \tau_S \frac{dS}{d\tilde{t}} = \alpha_S(1 - S)C^4 - S \\ \tau_R \frac{dR}{d\tilde{t}} = \alpha_R S(1 - R) - R \end{array} \right.$$

On the fast time scale, one uses the approximation $\frac{1}{\tau_X} = 0$, $X = C, S, R$, and the variables C, S, R are constant. So, fast dynamics reduces to a Morris-Lecar model (here with a fast variable N) in the presence of an additional current $I_{ext} = I_{sAHP}$ (constant):

$$\left\{ \begin{array}{l} C_m \frac{dV}{d\tilde{t}} = -g_L(V - V_L) - g_C M_\infty(V)(V - V_C) - g_K N(V - V_K) + I_{ext}; \\ \tau_N \frac{dN}{d\tilde{t}} = \Lambda(V)(N_\infty(V) - N). \end{array} \right. \quad (2.20)$$

2.5 Parameters value and auxiliary functions

Units. In all the thesis, physical quantities are expressed in the units displayed in table 2.1. Having integrated over all the surface of the membrane we omit the surface units.

Calibrating parameters from experiments All parameters values are calibrated with respect to biophysics, found in the literature or fitted from experimental curves in [11], [62] and [63]. Morris-Lecar tuning parameters V_1 , V_2 , V_3 , V_4 were calibrated (see Fig 2.11), so as to reproduce the experiment of [63] (Fig 4a), where the authors investigate the ionic mechanisms of the fast oscillations. Note that the bursting regime is robust to (small) variations of these parameters (results not shown). We tuned the sAHP parameters taking into account the analogy with SK channels studied in [11] (fit not shown). Also, we note that the intensity of sAHP observed by Abel et al. in pyramidal neurons (of order 150 pA) is quite bigger than in stage II SAC. In our model, this means a lower sAHP conductance g_{sAHP} ($g_{sAHP} = 2$ nS).

Physical quantity	Dimension
Time	ms
Potential	mV
Capacitance	pF
Current	pA
Conductance	nS
Concentrations	nM

Table 2.1: Dimensions of physical quantities used in the thesis.

Auxiliary functions. The dimensionless auxiliary functions involved in the dynamical equations appearing in the model definition are:

$$M_\infty(V) = \frac{1}{2} \left[1 + \tanh\left(\frac{V - V_1}{V_2}\right) \right], \quad (2.21)$$

$$\Lambda(V) = \cosh\left(\frac{V - V_3}{2V_4}\right), \quad (2.22)$$

$$N_\infty(V) = \frac{1}{2} \left[1 + \tanh\left(\frac{V - V_3}{V_4}\right) \right], \quad (2.23)$$

Parameters. The parameters used in the model are displayed in Table 3.1.

2.6 Comparison with existing models

In this section we shortly revisit models of SACs activity in the stage II and compare them to our model, ([34, 38, 54, 30, 12], for a review see [50, 51]). We would first like to remark that all models we know are devoted to describe wave activity and do not focus on thoroughly describing individual SACs dynamics. Especially, none of the models we know describe the biophysical mechanisms of SACs bursting activity and the role played by biophysical parameters. Instead the focus was more on having a relatively simple description of the cell activity with a minimal set of tunable parameters (a notable example is Butts et al model[34] which has two free parameters governing the waves properties).

The closest model to ours has been proposed by M. Hennig and collaborators [54] (referred as Hennig model) (see also the extension by Ford and Feller and the recent

Parameter	Physical value
C_m	$22 pF$
g_L	$2 nS$
g_C	$[3 : 20] nS$
g_K	$[1, 20] nS$
g_{sAHP}	$2 nS$
V_L	$[-72, -70] mV$
V_C	$50 mV$
V_K	$-90 mV$
V_1	$-20 mV$
V_2	$20 mV$
V_3	$-25 mV$
V_4	$7 mV$
τ_N	$5 ms$
τ_R	$8300 ms$
τ_S	$8300 ms$
τ_C	$2000 ms$
δ_C	10.503 $nM pA^{-1}$
α_S	$\frac{1}{200^4} nM^{-4}$
α_C	$4865 nM$
α_R	4.25
H_X	$1800 nM$
C_0	$88 nM$

Table 2.2: Range of values for the parameters used in the thesis.

paper of Xu et al. [9]). Actually, our model has been widely inspired by this work with several notable differences. As exposed in the Methods section our biophysical analysis of sAHP dynamics leads to equations and parameters values departing from Hennig model. Additionally, Hennig model does not consider a fast potassium dynamics and there is no fast oscillation. The mechanism that mimics SACs bursting is a switch from low membrane potential level to high one. This switch is determined by an exogeneous shot noise i.e. a voltage dependent rate modulated Poisson process with a slow decay. This activity is maintained long enough so that sAHP can be activated, enabling the cell to return to rest. In our model shot noise is not necessary to trigger activity. Instead, a cell can spontaneously switch to the bursting state, where it stays until the sAHP produced by its activity leads it back to the rest state. By spontaneous we mean literally happening or done in a sudden way, without any planning or without being forced/without premeditation. In our model this sudden switch is a bifurcation induced by the mere cells dynamics. The presence of a fast (Brownian) noise facilitates this transition, but, there is no need for a shot noise. The cell stays in the bursting state by its mere dynamics, even when it is isolated.

A similar modeling holds in Lansdell et al. model [12]. It is ruled as well by an excitable Morris Lecar model with a slow potassium variable linked to sAHP. There is no fast potassium. Here too cells do not burst. As in Hennig the cell activity is

triggered by a random excitatory current and maintained by network dynamics.

Although Hennig or Lansdell model are based on differential equations with many parameters, none of these authors made a bifurcation analysis of their model. We did it and we found that there is no bifurcation in a neighbourhood of the parameters value they choose. In this sense, our model is in strong contrast with previous studies. This is precisely because cells are close to a bifurcation point that they are able to exhibit the wide repertoire of dynamics we have presented in close agreement with experimental findings.

2.7 Bifurcations analysis

Slow-fast analysis. Bursting is an alternation between a rest state and repetitive firing, often modulated by slow voltage- or Ca^{+2} -dependent processes [49]. As we show in our model, the joint fast dynamics of Ca^{+2} and K^+ channels generates fast oscillations while the slow AHP, mediated by Ca^{+2} gated K^+ channels, modulates slow oscillations, [63]. The conjunction of these two mechanisms generate bursting as we now explain.

For this, we use a slow-fast time scale analysis. The variable V, N evolve with a fast time scale of the order of a few milliseconds under the influence of the slow current I_{sAHP} whose conductance is driven by slow variables C, S, R (time scale - several seconds). Due to this time scales separation, it is relevant to make a bifurcation analysis of the fast Morris-Lecar V, N dynamics, in the presence of a constant external current I_{ext} used as a bifurcation parameter and mimicking the sAHP current (see Methods). Doing so we neglect the fast variation of I_{sAHP} induced by the fast variations of V in the term $V - V_K$ (see eq. 2.5). A justification of this approximation is seen in Fig 2.3)

Dynamical changes with respect to parameters variations. Our reasoning relies therefore on a thorough analysis of the bifurcations structure in the fast Morris-Lecar dynamics. There exist remarkable bifurcations numerical studies of the standard Morris-Lecar model (see for example [7]), but to our best knowledge there are not such analyses with our range of parameters and fast potassium dynamics. In [7], the ratio between the time scale $\tau_L = \frac{C}{g_L}$ of V and τ_N and the time scale of N (τ_N) is about $\sim \frac{1}{2000}$, while in our fast potassium dynamical case, it is about 2. This has a strong impact on dynamics. Therefore, the bifurcations results presented here (Fig. 2.5, 2.6, 2.7) are novel. The dynamics of our model involves many parameters and it is important to study how it behaves when varying certain of them. This allows to identify drastic changes when crossing critical values (bifurcations), as well as to check the robustness of the behavior described in this chapter with respect to parameters variations. In order to do so, we selected the relevant parameters according to the following reasoning.

We distinguished two classes of parameters. The first one consists of parameters constraining the Morris-Lecar dynamics, namely V_1, V_2, V_3, V_4 . We verified the robustness of the scenario described in this chapter when varying these parameters. Especially, V_3 is the half activation potential of the fast potassium channels, playing a central role in SACS excitability as shown later in the text (see Fig 2.12).

The second class is the set of parameters constrained by biophysics (such as C_m, g_L , etc). Most of them have been fixed based on the biophysical literature and are not

considered to vary. Here, we choose to study the variation of 4 parameters: I_{ext} because it features sAHP; g_K and g_C because, as we show later in this chapter, their variations allows us to reproduce experimental facts that have not been reproduced before by any model and to propose a conjecture on the role of the potassium conductance during development. Finally, we also vary V_L , the leak potential. Although a variation δV_L of V_L is identical to adding a constant external current $g_L \delta V_L$, this variable allows us to easily switch between two different regimes of bursting scenarios discussed below. Both scenarios could be possible as retinal waves are concerned, as argued in the conclusion. In addition, V_L provides an easy control on the bursting period as shown below. We insist that varying this parameter was used here as a modeling facility.

Dynamically driven bursting. We now illustrate how bursting takes place. We consider an example with $g_K = 10$ nS, $g_C = 12$ nS and $V_L = -70$ mV and discuss later the robustness of this scenario to parameters variations. Using the time scale separation we perform a bifurcations analysis of the fast V, N dynamics, in the presence of a constant external current I_{ext} used as a bifurcation parameter, mimicking the effect of the sAHP current. The bifurcations diagram is represented in Fig 2.2 (drawn using MATCONT [58]), where we have explored a wide range of variation of I_{ext} , (-100 to $+300$ pA). We also show the numerical solution of the full system, projected onto the bifurcation diagram of the fast subsystem, zooming to our regime of interest (see Fig 2.3).

When $I_{ext} < I_{H_c} \sim -5.83$ pA, there is a stable rest state (lower red branch in Fig 2.3), where $V_{rest} \in [-70, -60]$ mV, coexisting with two unstable fixed points (middle and upper branch). For $I_{ext} = I_{H_c}$ there is an homoclinic bifurcation giving rise to a stable limit cycle. In the range $I_{ext} \in [I_{H_c}, I_{SN_1}]$, where $I_{SN_1} \sim -3.7$ pA, the stable rest state (lower branch) coexists then with a stable limit cycle, corresponding to fast oscillations, and an unstable fixed point (middle branch). When $I_{ext} = I_{SN_1}$ the stable rest state coalesces with the middle unstable branch and both disappear with a saddle-node bifurcation (SN_1). For $I_{ext} > I_{SN_1}$ the dynamics has only attractor, the limit cycle, corresponding to fast oscillations. This cycle eventually disappears by a Hopf bifurcation at $I_{ext} = 250$ pA. However, this value of external current is quite beyond the range of plausible values during the bursting activity of SACs.

From this bifurcation analysis we see that the cell is firing rapidly (limit cycle) in the absence of an external current. Being in a high voltage state, Ca^{2+} loads, leading to a rise of sAHP current. This corresponds, in the bifurcation diagram, to a motion toward negative current values. This motion goes on until the cell reaches the homoclinic bifurcation where rapid firing stop. I_{sAHP} is high now, leading to the hyperpolarization phase. Then, because voltage is low, $[Ca^{2+}]$ decreases and I_{sAHP} drops down. Eventually, SAC crosses the SN_1 bifurcation point and starts firing again. This is illustrated in Fig. 2.3. Here, red and black lines correspond to stable and unstable fixed points and green line represent the amplitude of the limit cycle. The blue trace is the trajectory of a burst in the plane ($I_{ext} = I_{sAHP}, V$). In this scenario, cells burst therefore periodically, with a frequency controlled by the characteristic times τ_R, τ_S of variables R and S respectively. From a dynamical systems perspective, there are two important bifurcations associated with bursting: a) bifurcation of the rest state that leads repetitive firing and b) bifurcation of a spiking attractor that leads to a rest state [49]. There are two possible types of bifurcations linked to such type of behavior (i) Homoclinic saddle-node bifurcation and (ii) Hopf bifurcation. We have

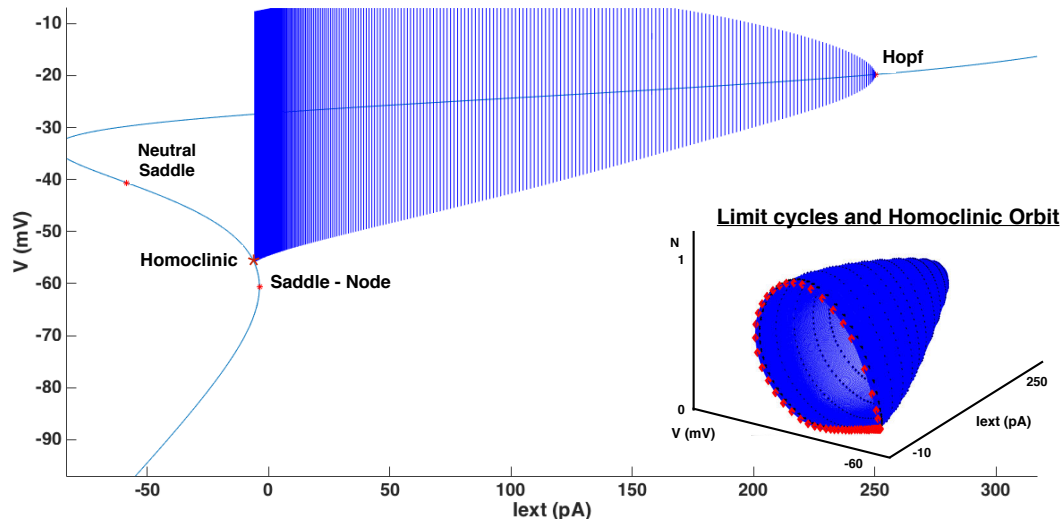


Figure 2.2: **Bifurcation diagram of the fast dynamics** (Eq (2.20) in supporting information section S2) **when the constant current I_{ext} is varied in a wide range.** *Red:* Stable fixed points. *Dashed-dot line:* Neutral saddle points. *Dashed line:* Unstable fixed points. SN stands for Saddle-Node bifurcation. For further references on this terminology see [45]. **Inset.** 3D diagram of the variables V, N and the parameter I_{ext} . *Blue* Evolution of the limit cycles. *Red.* Homoclinic orbit. Bursting stops by an homoclinisation of the limit cycle.

therefore shown that (i) holds in our case. The first bifurcation associated with the breaking of the rest state is the saddle-node bifurcation. The "spiking attractor", here the limit cycle, is created by an homoclinisation. According to the classification of bursting made by Izhikevich in [49], this corresponds to a "square-wave" point-cycle planar burster.

Noise induced bursting. This scenario drastically changes upon the effect of a sufficiently large negative current. As discussed above we model this effect by a change of the leak reversal potential V_L . A small variation δV_L of V_L amounts to adding a constant current $g_L \delta V_L$ to the dynamics (2.1) of V . So, somewhat the variation of V_L is redundant with the variation of I_{ext} . Nevertheless, the resulting bifurcation analysis (not shown) reveals an interesting point. There is a critical value $V_{L_{SN_1}} = -71.85$ mV such that, for $V_L < V_{L_{SN_1}}$, there is saddle-node bifurcation giving rise to a stable rest state V_{rest} for $I_{ext} = 0$ coexisting with a saddle and a stable periodic orbit (see also Fig 2.5). This is in perfect agreement with the bifurcation diagram Fig 2.2. The SN1 bifurcation in Fig 2.2 arises for $I_{SN_1} = -3.7$ pA. This corresponds to $\delta V_L = \frac{I_{SN_1}}{g_L} = -1.85$ mV thus to $V_{L_{SN_1}} = -70 - 1.85$ mV. Hence, for $V_L < V_{L_{SN_1}}$, there are two fixed points: V_{rest} , which is stable, and V_u which is unstable. They collide for $V_L = V_{L_{SN_1}}$ and for $V_L > V_{L_{SN_1}}$ periodic bursting takes place.

This observation has a strong consequence on bursting. Indeed, when $V_L < V_{L_{SN_1}}$, the cell is in a rest state in the absence of external current and it cannot switch to rapid firing. This is the situation for the deterministic dynamics. However, in the presence of noise, sufficiently close to the bifurcation point (depending on the noise amplitude) the random fluctuations around the rest state leads eventually the cell into the rapid

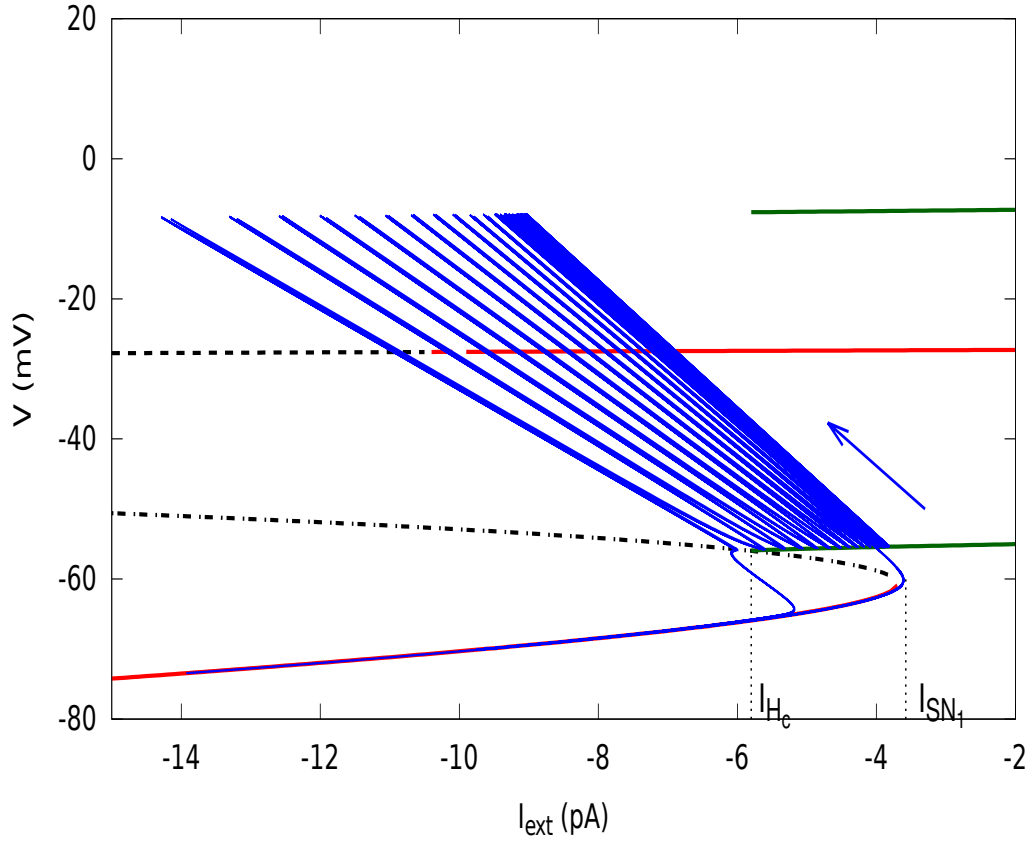


Figure 2.3: **Bifurcation diagram of the full dynamics.** The plot shows a representation of bursting in the plane $I_{ext} - V$ in relation with the bifurcation diagram of figure 2.2. Red lines correspond to stable fixed points, dashed lines to unstable fixed points, green lines are the extremal values of voltage fast oscillations. We observe the trajectory of a burst in the plane ($I_{sAHP} \equiv I_{ext}, V$) (blue). The blue arrow indicates the direction of the flow. In the fast oscillations regime V is varying periodically, with a fast period, inducing a fast variation of the term $V - V_K$ in the sAHP current, explaining the diagonal motion. Despite these fast oscillations one sees that the bifurcation is driven by the slow motion on the branches obtained from the bifurcation analysis assuming a constant current. The conductance $g_{sAHP}R^4$ is varying slowly, with the time scale of R , explaining the slow leftwise shift of the trajectory until the homoclinic bifurcation point is reached.

firing regime where the mechanism generating sAHP holds similarly to Fig 2.3 (data not shown).

We are therefore able to capture both the noise driven and the dynamically driven bursting regimes in a single, unifying model. In the presence of noise the dynamically driven bursting regime still exists but the period has now random fluctuations. In fact, the noise smooths the transition between those 2 regimes (see the heat maps in Fig. 2.8).

To summarize, our analysis shows that SACS are, in this range of parameters, periodic bursters where the period can fluctuate due to noise. We have not been able to find, in the experimental literature, indications about which regime corresponds to real SACS. Maybe both are possible, depending on the different species. Nevertheless, for *both* proposed scenarii the biophysical mechanism for the triggering of bursting is the same and it is sketched in Fig 2.4.

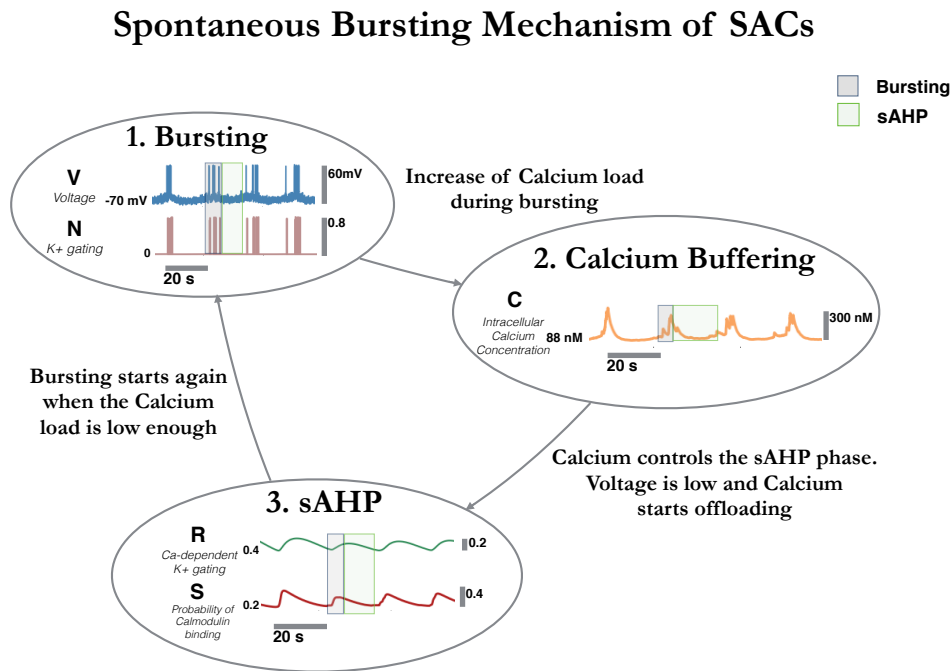


Figure 2.4: **Biophysical mechanism for the sustained spontaneous oscillations of immature SACS.** 1. Fast spiking occurs due to the competition between voltage gated Ca^{+2} (excitatory current) and K^+ channels (inhibitory current). 2. Calcium load increases during the rapid firing phase while the voltage is in a high voltage state. This leads to a slow increase of sAHP. When sAHP is large enough there is a sharp decay of the voltage (bifurcation) and the hyperpolarisation phase of the cell starts. As voltage is low, the calcium load starts to slowly decrease. 3. During the slow offloading calcium stage we observe a refractory phase. The decrease of calcium concentration induces a slow decay of the sAHP. When calcium is small enough rapid firing starts again via a new bifurcation.

To our best knowledge this is the first model able to provide a mechanism to account for the repetitive firing of SACS, which is the condition under which calcium controls the after-hyperpolarization phase.

Robustness with respect to parameters variations. We now study the robustness of this analysis to variations of our main parameters. As, later in the chapter, we discuss the effects of varying the potassium conductance, we first show the effect of varying I_{ext} and g_K , and then, the effect of varying g_C and g_K . We have used different software (MATCONT [58], PyCont [29]) and we were not able to get all bifurcations with them (especially homoclinic bifurcations). So we obtained the bifurcations diagram by a direct inspection of the phases portraits with respect to parameters variations. The points shown in the bifurcation maps are sampling points whereas continuous lines correspond to fit. We note that Hopf and Saddle Node bifurcations were obtained identically using the bifurcations analysis software quoted above.

In Fig 2.5 we have drawn the bifurcation map in the plane I_{ext}, g_K for $V_L = -72$ mV. Note that the corresponding bifurcation diagram for $V_L = -70$ mV is deduced from this one by shifting all curves 4 pA left-wise (not shown).

The vertical line SN (Saddle-Node) stands at $I_{ext} = 0.3$ pA so that, in the absence of external current, the cell is in region *B* where a stable rest state coexists with a stable limit cycle. As argued above, the transition to fast oscillations is made by noise (noise induced bursting). In contrast, for $V_L = -70$ mV, the SN lines stands at -3.7 pA. Therefore, in the absence of external current, the cell is now in region *D* where only fast oscillations take place. In both cases, an increase of sAHP drives the cell in the region *A* where fast oscillations stop. Note that the sAHP current $g_{sAHP}R^4(V - V_K)$ is of order -10 pA for $g_{sAHP} = 2$ nS, enough to drive the cell in the region *A*.

As bursting is a competition between calcium and potassium dynamics we have also checked the structure of bifurcations when varying the calcium conductance g_C and the potassium conductance g_K around the values we have fixed in our model. The resulting bifurcations diagrams are drawn in Fig 2.6 and 2.7. Here we show the bifurcations diagrams for two values of V_L because they are quite different: $V_L = -72$ mV (noise induced bursting) and $V_L = -70$ mV (dynamically driven bursting). In the noise induced bursting regime there is a region (*D* in the figure 2.6), delimited by two homoclinic bifurcations lines, where the cell is bistable without fast oscillations. This region does no exist for $V_L = -70$ mV.

2.7.1 Variations of the bursting frequency depend on potassium and calcium conductances.

To complete our analysis, we show in Fig 2.8 the variation of the inter-burst interval (τ_{IBI}) as a function of calcium and potassium conductance. We observe two important facts useful for the interpretation of experimental results discussed below. First, although bursting takes place only in region *D* of the bifurcations maps 2.7 and 2.6 for the deterministic case, noise ($\sigma = 4pA ms^{1/2}$) allows bursting in region *C* as well, close to the frontier with region *D*. Second, the interburst increases when approaching the border of region *D*. With $V_L = -70$ mV it can increase up to 2 minutes, whereas, for $V_L = -72$ mV it can increase to quite bigger values (several minutes). This corresponds to the yellow region in Fig 2.6. The irregular shape of this region, alternation between yellow and black regions is due to our numerical procedure. We generate 20 trajectories of duration 2000 s and count the number of bursts in each trajectory.

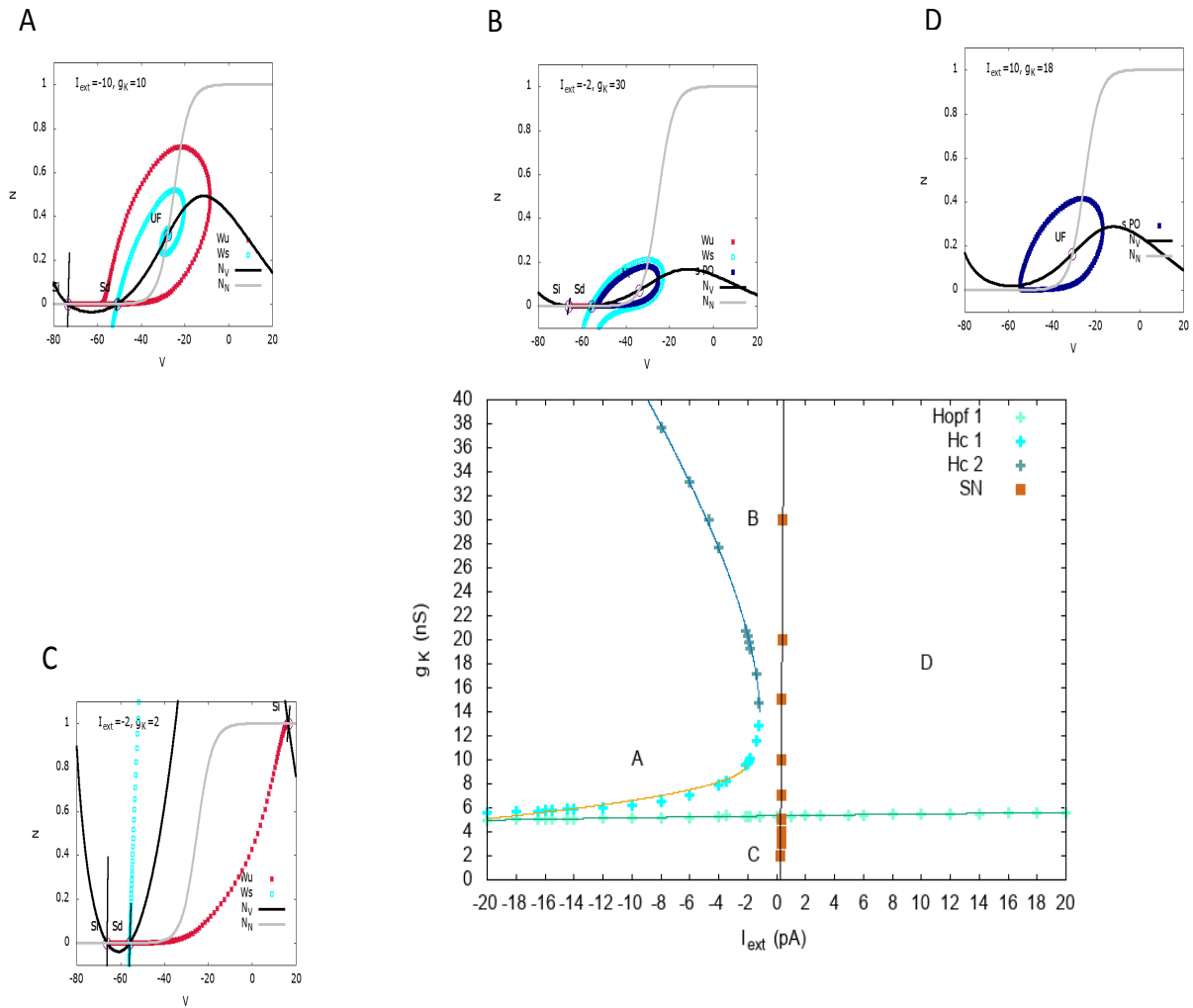


Figure 2.5: **Bifurcations diagram as a function of I_{ext} , g_K for $V_L = -72$ mV.** In the bottom right, the bifurcations map is plotted. Points are sampling points obtained by a direct inspection of the phase portrait whereas continuous lines correspond to fit. "Hc" means "homoclinic bifurcation" and "SN" stands for "saddle-node". The capital letters A, B, C, D, E inside correspond to the typical phase portraits surrounding the bifurcation map. In these phase portraits, continuous lines correspond to nullclines. 'Si' stands for 'Sink', 'Sd' for 'Saddle', 'SF' for 'Stable Focus' and 'UF' for 'Unstable Focus'. Sink and Focus correspond to stable rest state: a small perturbation about this state decay exponentially fast. On the opposite, saddle and unstable focus are unstable. For Saddle we show the stable and unstable directions (black lines) as well as the stable (red) and unstable (cyan) manifolds W_s, W_u . 'SPO' means 'Stable Periodic Orbit'. It corresponds to fast oscillations, plotted in dark blue. The value of $I_{ext}(pA), g_K(nS)$ are indicated top left. In region A, there is a low voltage stable state. In region B, a stable state with low voltage coexists with a limit cycle (fast oscillations) separated by an unstable state. When the cell is in the low voltage state, a large enough perturbation (e.g. noise or other cells action) leads it to fast oscillations. In region C, two stable states, one with low voltage and one with high voltage, coexist separated by an unstable point. In region D, the cell only exhibits a fast oscillations regime, reached whatever the initial condition. Finally, in region E, there is a stable state with high voltage. When varying parameters, continuous change occurs in the interior of a region (e.g. the period of oscillations continuously varies), whereas crossing the bifurcation lines leads to abrupt changes.

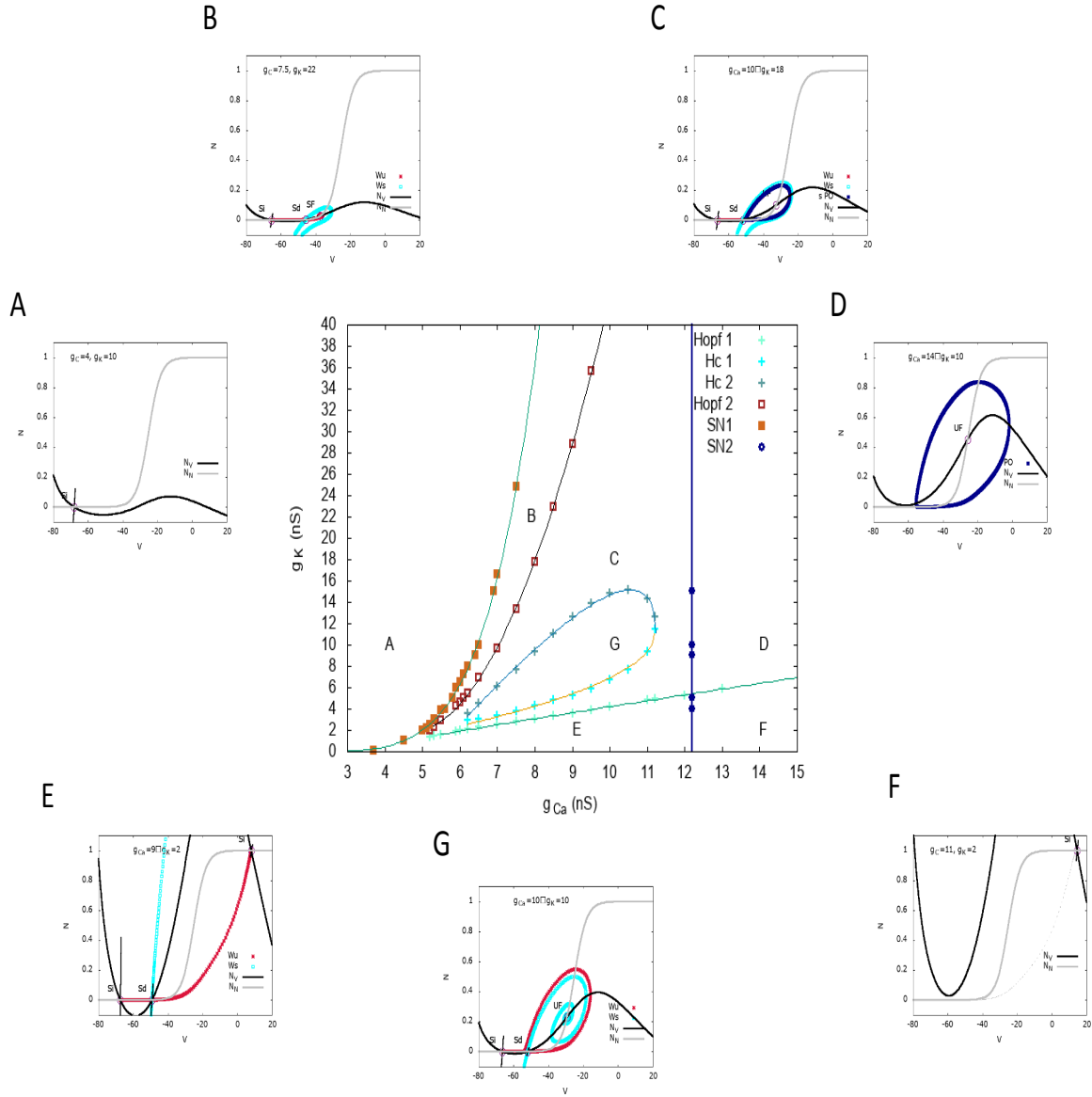


Figure 2.6: **Bifurcations diagram** as a function of g_{Ca} , g_K for $V_L = -72$ mV. Same representation as Fig 2.5. In region A, there is a unique stable rest states with low voltage. In region B two stable rest state with low voltage coexist separated by an unstable point; hence dynamics is bistable. In region C, a stable rest state with low voltage coexists with a limit cycle (fast oscillations) separated by an unstable state. When the cell is in the low voltage rest state, a large enough perturbation leads it to fast oscillations. In region D the cell only exhibits a fast oscillations regime, reached whatever the initial condition. In region E two stable rest states, one with low voltage and one with high voltage, coexist separated by an unstable point. Region F has only one high voltage stable rest state. Finally, in region G, there is a low voltage rest stable state.

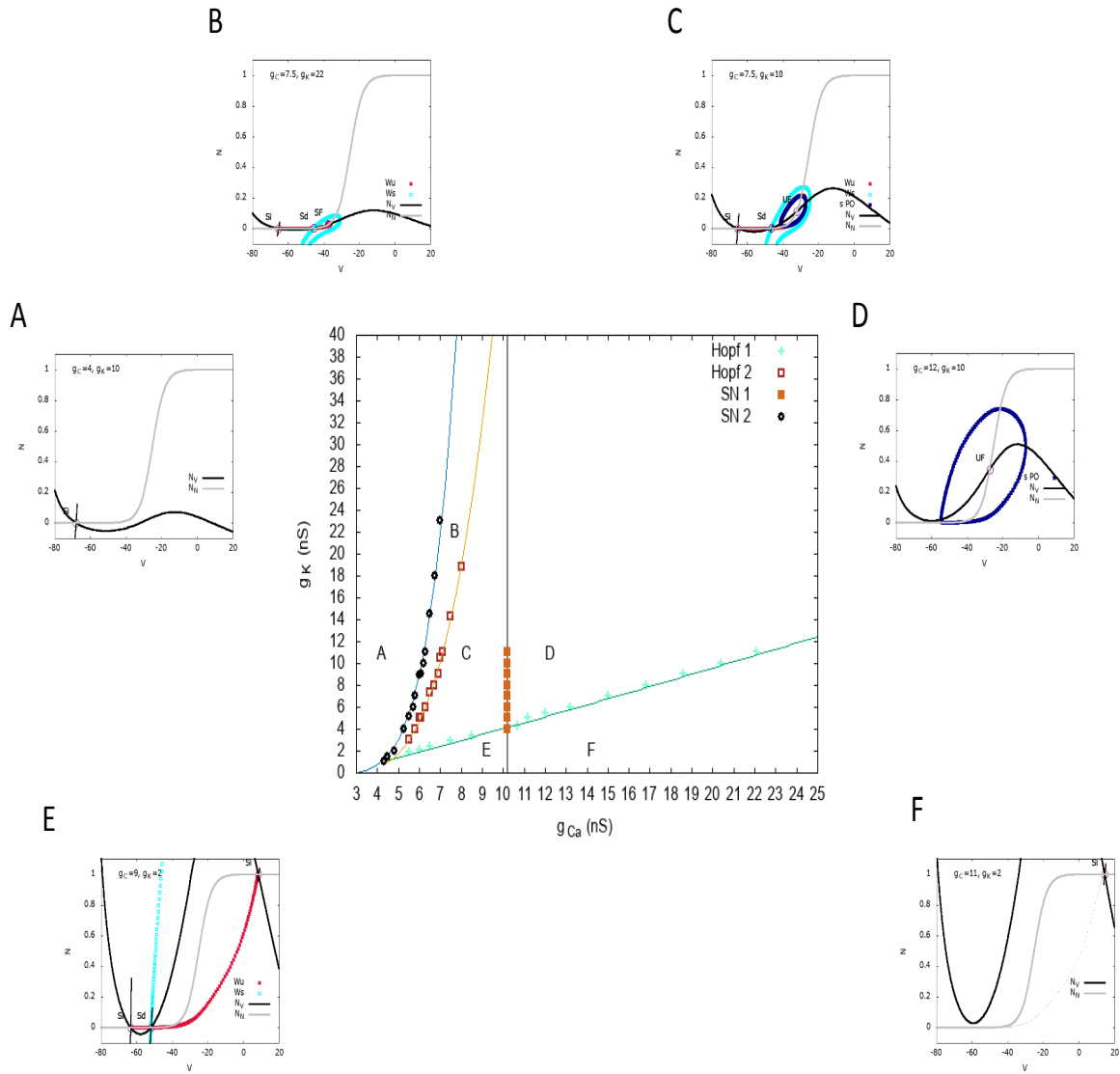


Figure 2.7: **Bifurcations diagram** as a function of g_C , g_K for $V_L = -70$ mV. Same representation as Fig 2.5 and same comments.

In addition, we consider that a period of high calcium activity has to last at least 1 second to be considered as a burst. In our simulation, when going far from the frontier between region C and D, we observe that this sampling is not sufficient; we have rare bursts giving poor statistics, and, in some cases (black regions in-between yellow ones), we observe no burst in the sample.

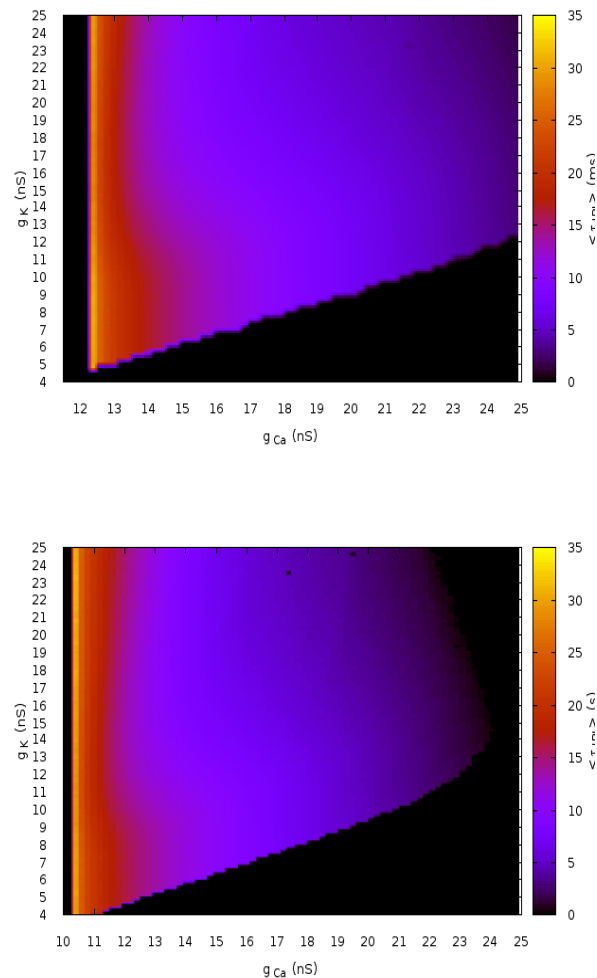


Figure 2.8: **Heat map of the interburst period as a function of g_C and g_K .** We sample g_C, g_K on a grid with resolution 0.25 nS. For each point, we generate 20 trajectories of duration 2000 s and count the number of bursts in each trajectory. A period of high calcium activity has to last at least 1 second to be considered as a burst. The heat map show the average value of τ_{IBI} in color log scale. Top: $V_L = -72$ mV (noise induced bursting with $\sigma = 4$); Bottom: $V_L = -70$ mV (dynamically driven bursting).

2.8 Characterizing the effect of noise on the bursting activity

At this point, it is important to characterize the effect of noise on the bursting dynamics of SACs. In [63], recordings show that the bursting periods of SACs are not regular

and have a certain probability distribution. We mimic this effect as a Brownian noise, added to the dynamics of the voltage V (see Eq (2.1)). This can be interpreted as fluctuations in ionic currents due to the random opening of ionic channels. We observe that the bursting period distribution depends on the level of noise σ . For small σ , dynamics has fluctuations around the deterministic trajectory with little effects during the bursting phase. In contrast, low additive noise during the slow (after-hyperpolarization) dynamics, is enough to accelerate (or delay) the start of a burst. For higher values of σ the bursting period of cells decreases dramatically. As shown in Fig 2.9 the presence of noise has also a drastic impact on the shape of the interbursts intervals distribution. Note that we define an interburst interval numerically by a simple thresholding method, which is controlled by a suitable Ca^{+2} concentration threshold (here 150 nM).

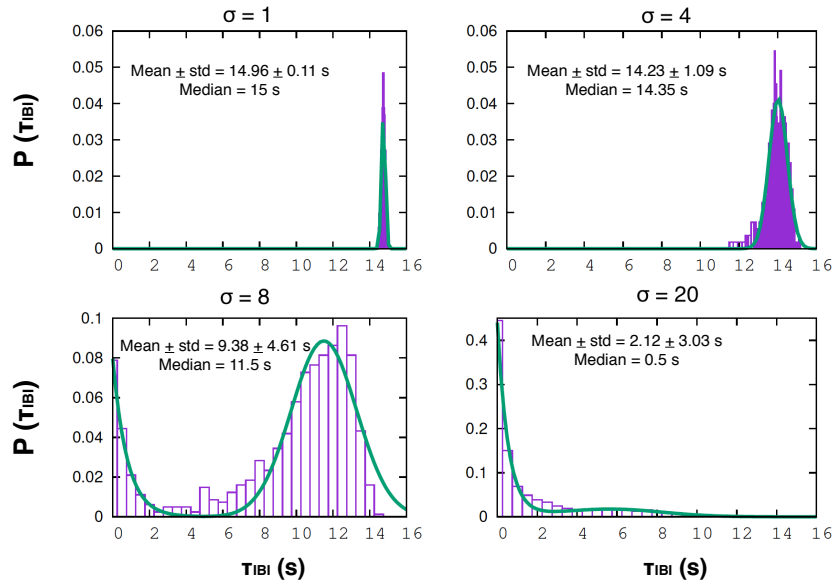


Figure 2.9: **Histogram of bursting periods for different noise levels.** We show the distribution of interburst interval distribution τ_{IBI} with different levels of noise. *Top left:* $\sigma = 1 \text{ pA ms}^{1/2}$. *Top right:* $\sigma = 4 \text{ pA ms}^{1/2}$. *Bottom left:* $\sigma = 8 \text{ pA ms}^{1/2}$. *Bottom right:* $\sigma = 20 \text{ pA ms}^{1/2}$. Green curves correspond to fit either by a Gaussian (top), or a linear combination of a Gaussian and a decaying exponential (bottom).

Experimentally, maybe due to the lack of sufficiently large samples in [63], the exact shape of the distribution of the interburst intervals is not sharply defined. Therefore, the comparison with our theoretical results is difficult. However, the experimental distribution obtained by these authors is definitely not exponential. As we observe an exponential distribution for large enough σ values, Fig 2.9, this remark provides us with an upper bound on the level of noise which should be no greater than $8 \text{ pA ms}^{1/2}$.

2.9 Explaining the wide range of interburst intervals (IBI) across species by a unique mechanism

Spontaneous bursting activity in immature SACs has been consistently observed across various species i.e. mice, rabbits, chicks, turtles, macaques etc., although, the measured mean interburst interval (τ_{IBI}) strongly varies [55, 53, 36, 31]. This experimental observation raises the question whether there exists a single underlying mechanism which could explain such variability across species, instead of possibly several corresponding mechanisms for each different species. This variability could be due to distinct involved mechanisms, but bifurcations theory provides another explanation. Indeed bursting involves a saddle-node bifurcation and interburst is known to be sensitive to parameter variations near this bifurcation [35]. This is actually what is shown in the heat maps, Fig 2.8. The IBI increases when approaching the Saddle Node line.

Obviously, there are several parameters that we could vary. Here, to illustrate our point and the sensitivity of the τ_{IBI} in the model, we vary the leak potential V_L . This parameter can easily be varied in experiments (by e.g. changing the chloride concentration) but our main point is not here. It is simply to show that we can explain the wide variability of τ_{IBI} across species with a single model and a single parameter.

As we show in Fig 2.10 the variation of V_L around the normal physiological conditions of the rest membrane potential ($\sim -70mV$) induces strong variations in τ_{IBI} . The variations are compatible with the variations observed across species although we do not claim here that the variations across species *are due* to a variation of V_L . It would nevertheless be interesting to see how τ_{IBI} changes upon a variation of the chloride concentration. We observe that τ_{IBI} increases monotonously as V_L decreases, following a hyperbola whose form has been derived analytically (see Methods and Fig 2.10, blue trace). As shown in the paper [35], hyperbola is one the 2 possibilities, corresponding to the case where the noise amplitude is small compare to the excitability. We also observe a sharp transition from a bursting to a non-bursting regime, where $\tau_{IBI} = 0$, which corresponds to the loss of SACs excitability.

Based on the shape of our theoretical curve, we show that τ_{IBI} exhibits a *strong asymptotic behavior* around a very narrow regime of the rest potential ($V_L = -70 mV$, $\delta V_L \sim 2 mV$). This means that depending on slight variations of physiological conditions ($\delta V_L \sim 2 mV$) a SAC could exhibit very variable bursting periods, explaining how different species exhibit variability in τ_{IBI} of immature SACs. The analytic form of the function $\tau_{IBI}(V_L)$ is the following (see Methods for detailed derivation):

$$\tau_{IBI} = \begin{cases} 0, & V_L \leq V_{L_c}; \\ \frac{K}{\sqrt{V_L - V_{L_c}}}, & V_L > V_{L_c}; \end{cases} \quad (2.24)$$

(where $K = 0.93 \text{ s mV}^{\frac{1}{2}}$ and $V_{L_c} = -72.5 mV$, for $\sigma = 4 pA ms^{1/2}$, $g_K = 10$, $g_C = 12 nS$). The value K, V_{L_c} are obtained from fit. Note that for $V_L \leq V_{L_c}$ τ_{IBI} is not defined because neurons do not burst anymore. We set it to zero by convention (black color).

To compare with experimental results, we show in the same figure τ_{IBI} for different species as found in the literature. We have not been able to find τ_{IBI} for turtles and chicks. We found the mean interwave intervals τ_{IWI} instead. In order to extrapolate to τ_{IBI} in these cases, we used a common constant scaling factor of 3, based on the ratio between τ_{IBI} and τ_{IWI} for rabbits and mice found in [63] and [37] respectively.

Besides this narrow regime a decrease of V_L results in a sharp disappearance of bursting activity, which means that bursting activity stops after a limit value of V_L . As exposed above, decreasing V_L is equivalent to add a constant negative current in the model. In real SACs, this inhibitory current could correspond to a change in the intrinsic inhibitory ionic currents of individual SAC or to external inhibitory inputs from other layers of the retina upon maturation. These two factors should drive the disappearance of bursting activity and subsequently the loss of SACs excitability. On the other hand, an increase of V_L leads to a gradual decrease of τ_{IBI} towards zero, meaning that in this regime of parameters, SACs tend to burst repeatedly, without a refractory period. This scenario is not observed under normal physiological conditions, but could be tested experimentally by varying V_L pharmacologically.

Finally, in the experimental paper [71], it is found that the bursting period increases upon maturation (experiment in P1-P2 rabbit SAC). In light of the present model-driven analysis, this could be linked to a change of intrinsic properties of SACs during development although it is not clear to us how synaptic inhibition acts on the disappearance of bursting activity of immature SAC across species.

Taken together, the hyperbolic behavior observed near a saddle-node bifurcation provides a generic mechanism explaining the wide variation across species of τ_{IBI} upon a tiny variation of a physiological parameter suggesting that bursting activity in immature SACs share a common mechanism across species. Obviously, we have no guarantee that this variation is, in real SACs, induced by a variation of the leak potential V_L . But what matters here is that this wide variation of period is expected near a saddle-node bifurcation when imposing an external current, no matter which biophysical mechanism effectively drives this current and which parameter controls it.

2.9.1 How do the average interburst depend on the parameter V_L .

In this section we analyze how the interburst interval τ_{IBI} depends on the leak potential V_L . In particular, we justify Eq (2.24). We vary the leak potential V_L around the value $V_L = -70$ mV, value for which the bifurcation diagram in Fig 2.2, 2.3 has been drawn. We note δV_L this variation which corresponds to adding, in Eq (2.20), a constant current $I_L = g_L \delta V_L$, positive or negative, playing the role of the external current in the abscissa of the bifurcation diagram.

As explained in the text there are two distinct regimes where the interburst interval τ_{IBI} is constrained by different factors. In the noise induced bursting regime ($V_L < V_{L_{SN_1}}$) bursting is induced by noise. When the SAC is in the rest state, the random fluctuations around this state can lead it into the oscillatory regime where the mechanism generating sAHP holds similarly to Fig 2.4, with an important difference: at the end of the cycle, when I_{sAHP} reaches its minimum, the SAC stays at rest. The stochastic dynamics around the rest state is described, with a good approximation, by a Ornstein-Uhlenbeck process (upon neglecting the non linearities coming from g_C and g_K , which are small in this range of membrane potential). Therefore, fluctuations of V are Gaussian with a mean V_{rest} and a variance proportional to σ , the noise intensity. Thus, the probability to cross the bifurcation threshold and enter into the bursting regime can be easily computed. This is a sigmoid with a slope proportional to $\frac{1}{\sigma}$. As a consequence, bursting can take place when $V_L < V_{L_{SN_1}}$, because of noise, but the probability to burst decreases rapidly when V_L decreases, after a threshold value

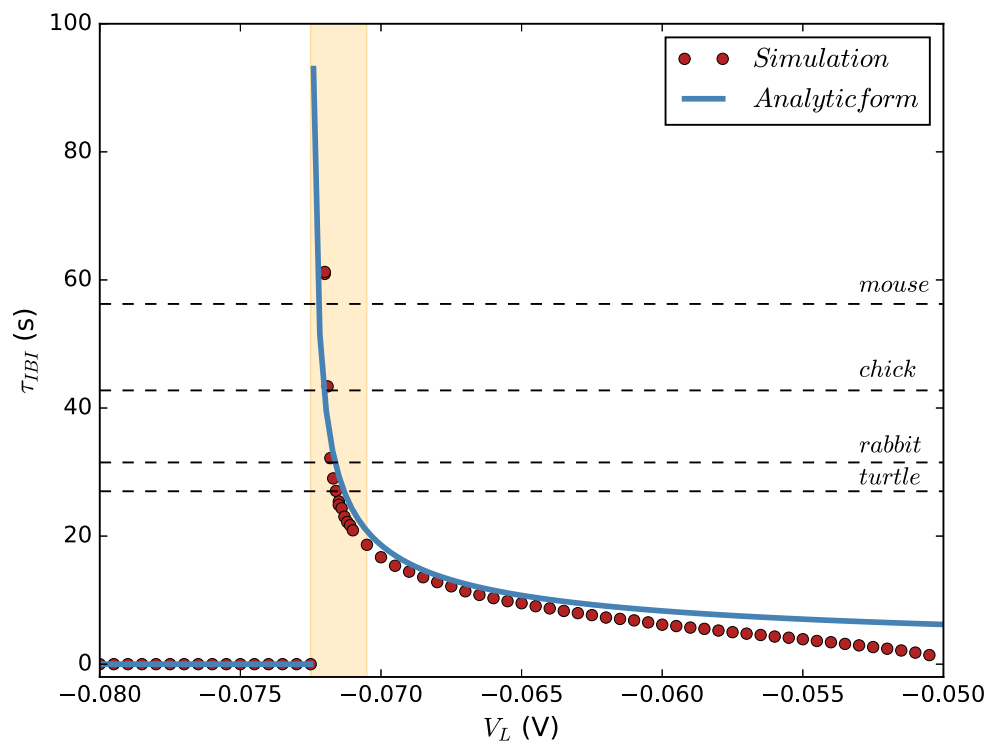


Figure 2.10: **The behavior of the bursting period near a saddle-node bifurcation explains variability across species.** *Red:* Computing the dependence of τ_{IBI} upon the variation of V_L with our model. *Blue:* A 2 parameters fit of the simulated data with the curve $\frac{K}{2\sqrt{V_L - V_{Lc}}}$ for $V_L > -72mV$. Note that this fit does not hold true away from the asymptote. (see Methods). *Red:* Values of experimentally measured interburst intervals for different species mapped to our results (see text).

$V_{L_c} \equiv V_{L_c}(\sigma)$ depending on σ . Formally, the bifurcation value $V_{L_{SN_1}}$ is shifted to V_{L_c} , explaining this term in Eq (2.24). For $V_L < V_{L_c}$ the probability to induce bursting by noise is so small that we consider it vanishes. Here τ_{IBI} is not defined anymore but we set it to zero in Eq (2.24) by convention.

In the dynamically driven bursting regime ($V_L > V_{L_{SN_1}}$), τ_{IBI} is constrained by two times: (i) the time t_1 to get in a neighborhood of the bifurcation point V_{SN_1} in Fig 2.3 where bursting starts (essentially determined by the sAHP) and (ii) the time t_2 to leave this neighborhood. When V_L is quite larger than $V_{L_{SN_1}}$, τ_{IBI} is largely dominated by t_1 . Here, τ_{IBI} decreases slowly as V_L increases. Indeed, the higher V_L the higher the positive current I_L and the more neurons are prone to bursting. When V_L becomes too large, I_{sAHP} is not enough to stop the oscillatory phase and $\tau_{IBI} = 0$. Close to $V_{L_{SN_1}}$, we can use the normal form of the saddle-node bifurcation for the variable V : $\frac{dV}{dt} = -(V_{L_{SN_1}} - V_L) + (V - V_s)^2$ where V_s is the rest state at the bifurcation point. In this approximation, the rest state, existing only when $V_L < V_{L_{SN_1}}$, is approximated by $V_{rest} \sim V_s - \sqrt{V_{L_{SN_1}} - V_L}$. The linear stability of this point is described by the linearized equation $\frac{dx}{dt} = -2x\sqrt{V_{L_{SN_1}} - V_L}$ where x is a small perturbation around V_{rest} . This equation has a characteristic time $\frac{1}{2\sqrt{V_{L_{SN_1}} - V_L}}$ which diverges as $V_L \rightarrow V_{L_{SN_1}}$ from below. When $V_L > \sim V_{L_{SN_1}}$ the normal form still holds but there is no fixed point anymore. Nevertheless, around the point where bursting starts the flow has a very small amplitude. As a consequence, the time to leave a neighborhood of this point is also of order $\frac{1}{2\sqrt{V_L - V_{L_{SN_1}}}}$. In this case τ_{IBI} is largely dominated by the time t_2 to leave the neighborhood of the transition point where bursting starts. In the absence of noise, we have thus $\tau_{IBI} = \frac{K}{\sqrt{V_L - V_{L_{SN_1}}}}$ for $V_L > V_{L_{SN_1}}$. With noise the threshold value $V_{L_{SN_1}}$ is shifted to V_{L_c} as explained above. This fully justifies Eq (2.24).

2.10 The role of the fast potassium conductance in bursting activity

We now address in further detail the potential role of the fast voltage-gated potassium channels used in our model to produce bursting (see also the work of E. Marder and collaborators, in a different context [8]). Zheng et al. [63] propose that the ionic channels mainly involved in the bursting activity of SACs during early development are voltage-gated Ca^{+2} channels. In this work the hyperpolarizing current involved is not characterized and these authors don't mention potassium channels before the end where they perform experiments with TEA (see below for more details). We proposed above fast voltage-gated K^+ channels as a source of fast inhibition necessary for the active phase of bursting of SACs. We now justify this claim based on several experiments made by Zheng et al., interpreted in the context of our bifurcations analysis.

We first show (Fig 2.11) how our model accurately reproduces a key experiment of [63]. Here, the authors artificially control the triggering of fast oscillations by applying a short current pulse (150 pA for 60 ms) to individual immature SACs. Also, upon the pharmacological application of Cd^{+2} , which blocks all Ca^{+2} related channels (voltage-gated Ca^{+2} and sAHP), they show that no oscillatory activity is triggered upon stimulation, but only a raise in the plateau of the level of the voltage. The

corresponding figure of their experiment in the paper [63] has been reproduced in Fig 2.11A (with the kind authorization of the authors). As shown in Fig 2.11 B, we are able to reproduce reliably this result using the fast K^+ channels described in Eq (2.3). Particularly, we are able to simulate the emergence of fast oscillations during a short current pulse, with an AHP phase after the end of the pulse (see green curve in Fig 2.11 B).

This is interpreted as follows from the bifurcations diagram Fig 2.5. In the absence of an external current the cell is in region B so it is in a rest state (recall that the vertical line of SN stands at $I_{ext} = 0.3$ pA). A pulse of current of 150 pA drives the cell in region D where it fast spikes. Removing the current pulse drives back the cell in region B but now the cell is on the limit cycle where it displays fast oscillations. Then sAHP takes place eventually leading the cell back to the rest state. This scenario holds for $V_L = -72$ mV. In order to have the same for $V_L = -70$ mV one needs to clamp the voltage so as to maintain the cell in the rest state. There is no mention of clamping in Zheng et al. paper which is a pity as it would have allowed us to decide in which regime (dynamically driven bursting or noise induced bursting) SACs were in their experiment. We emulate as well the disappearance of the oscillations observed by these authors, upon blocking all Ca^{+2} related channels (voltage-gated Ca^{+2} and sAHP), setting, in our model, the corresponding conductances to zero (see orange curve in Fig 2.11 B). We found that no oscillations are exhibited without the presence of the fast K^+ current ($g_K = 0$), only a rise from the rest state in the voltage plateau during the current pulse, illustrating that the depolarizing current (voltage-gated Ca^{+2} channels) is not sufficient to produce spontaneous bursting activity.

These observations support therefore our proposition that the hyperpolarizing component of the fast oscillations observed in immature SACs are driven by fast voltage-gated K^+ channels.

2.11 Exploring the role of the potassium conductance in the loss of SACs excitability upon maturation

SACs in the retina of vertebrates lose their ability to spontaneously burst once they reach a certain stage of development - different for each species. This transient excitability is a key process in the developing retina and the shaping of the visual system. It is not yet clear which physiological properties of SACs change upon maturation causing the abrupt change from autonomous bursting to rest state. So far, to our best knowledge, no experiment has studied in detail the biophysical properties of immature SACs at the level of each ionic channels involved during this window of development. However, there are some indirect experimental implications which help us extrapolate a possible scenario on how SACs change their properties upon maturation. In [4] Ozaita et al show that mature SACs not only stop bursting but also cannot be depolarized beyond $-20mV$. A specific type of inhibitory voltage gated K^+ channels, Kv_3 , is responsible for this property, providing an electric shunt to SACs somas. In the contrary, in the developing retina, SACs are autonomous bursters, depolarised beyond mature SACs ($\sim -5mV$) [63]. Therefore, upon maturation, the characteristics of voltage gated K^+ channels evolve, leading to a drastic change in SACs activity. In our model, these observations can be reproduced by the variation of two parameters; i) the conductance g_K and ii) the half-activation potential V_3 of the voltage gated K^+

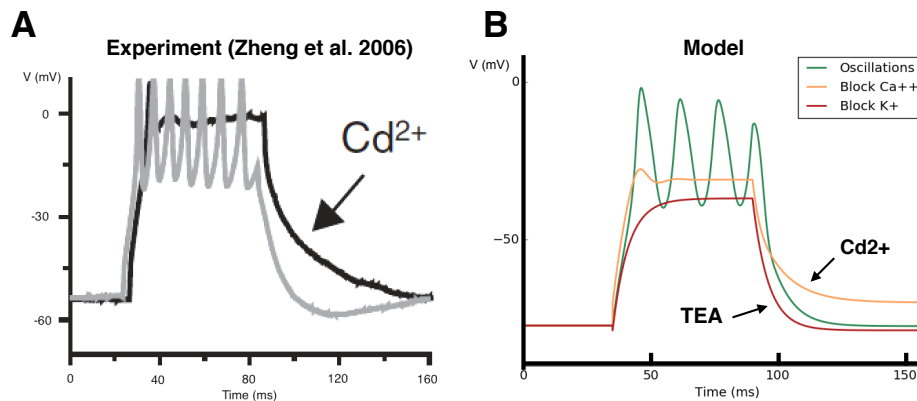


Figure 2.11: **Modeling the cellular mechanisms generating bursting activity in immature SACs.** **A.** Experimental investigation of the cellular mechanisms involved in bursting activity by [63]. *Gray*: Fast sub-threshold oscillations and subsequent AHP generated by a short pulse of current of amplitude 150 pA and duration 60 ms. *Black*: Blocking of all Ca^{+2} related channels by Cd^{+2} . No oscillations are exhibited. **B.** Simulating the experimental conditions of [63] *Green*: Reproducing fast sub-threshold oscillations and subsequent AHP emulating the experiment of [63]. Application of a current step pulse of 150 pA for 60ms. *Orange*: Oscillations disappear when Ca^{+2} related conductances are set to zero. *Red*: Blocking the oscillations upon setting the voltage-gated K^+ conductance to zero.

channels. The variation of the conductance g_K accounts for a change in the expression of the channels upon maturation whereas the variation of V_3 mimics the change in the level of depolarization in SACs.

On this basis, we reproduce with the model an experiment by Zheng et al. 2006 [63]. The results of their experiment are shown in Fig 2.13, left column (with the kind authorization of the authors), whereas the model results are presented in Fig 2.13, right column. Our results are based on a bifurcations analysis of the model in the plane $V_3 - g_K$, which reveals a wide region of parameters where bursting takes place. In Fig 2.12 we show, on the left, the bifurcation diagram in the plane V_3, g_K and on the right, a heat map, similar to Fig 2.8. This map makes easier the interpretation of Zheng et al experiment which mainly addresses the following questions.

- *How does SACs autonomous bursting stop?* Zheng et al. consider first isolated SACs (all synaptic connections are inactivated with a pharmacological cocktail). While SACs are bursting spontaneously (i.e. without the influence of the other cells) at P4 (first row, left in Fig 2.13), this spontaneous activity disappears at P6 (second row, left). We can easily reproduce this observation (Fig 2.13, first and second row, right) by moving from region C in the bifurcation diagram to another region. A simple transition to region A is obtained by decreasing the half-activation potential V_3 of the fast K^+ channels, leading to the saturation of SACs depolarization below $-20mV$ observed in mature SACs. A concomitant variation of g_K is also possible leading to stop bursting as well. To illustrate this scenario, we set $g_K = 14$ and $V_3 = -35mV$ as an indicative example (see Fig 2.13).

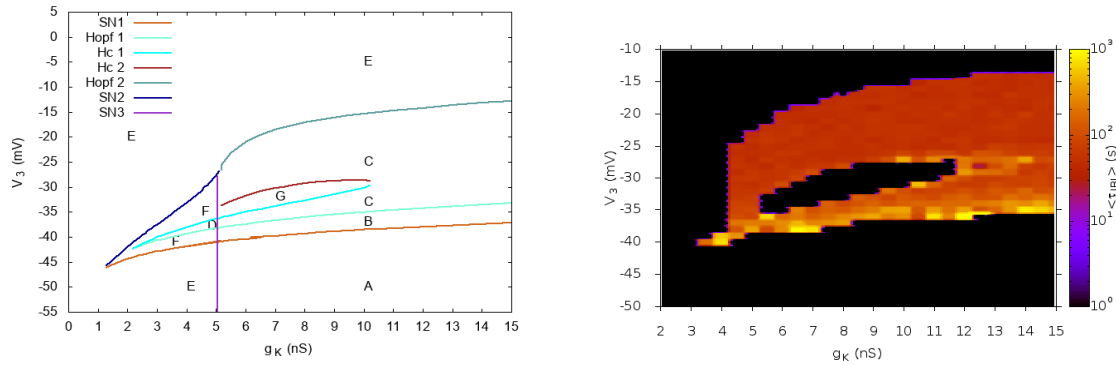


Figure 2.12: **Bifurcation diagram and heat map of τ_{IBI} in the plane $V_3 - g_K$.** Left. The bifurcation diagram uses the same representation as Fig. 2.5, 2.6, 2.7. In region A, there is a stable fixed point with low voltage. In B, 2 stable fixed points with low voltage coexist with a saddle-point. In C a stable fixed point with low voltage coincides with a stable periodic orbit giving rise to fast oscillations. In region D there are 4 fixed points (2 stable, 2 unstable) and a limit cycle. In region E there is a stable fixed point with low voltage and a stable fixed point whose position depends on g_K and V_3 . In region F there are five fixed points, 2 stables. Region G contains 2 stable fixed point (a sink and a focus) separated by an unstable fixed point. Bursting takes place in regions C and D. Right. Heat map of the τ_{IBI} . Same representation as Fig 2.8. We sampled the plane g_K, V_3 with a step of 0.5 nS on the g_K axis and 1 mV on the V_3 axis, explaining the irregular shape of the border. We show the τ_{IBI} is logarithmic scale.

- *How can bursting be restored in further mature SACs?* Zheng et al. show that bursting activity can be re-initiated pharmacologically in P8 (stage III) and P22 retinas with chemical agents upon i) blocking all synaptic connections (gap junctions, cholinergic, gabaergic and glutamatergic synapses), especially inhibition and ii) decreasing the conductance of the fast inhibitory K^+ channels. This suggests that upon maturation, bursting is in fact suppressed by alterations in the intrinsic properties of individual SACs. Particularly, in the same preparation (P8 isolated SACs), the authors apply a voltage-gated K^+ channel blocker tetraethylammonium (TEA), which results in restoring bursting activity in isolated mature SACs (Fig 2.13, third row, left). A potential type of potassium channels involved is the TEA (tetraethylammonium)-sensitive K^+ of the Kv_3 family. Therefore, this experiment emphasizes once again the potential role of fast potassium channels and especially the Kv_3 family. We mimic the blocking of these channels in our model by decreasing the conductance g_K . When g_K is small enough, we reproduce the bursting restoration (Fig 2.13, third row, right). This example corresponds, in the heat map, to a motion from $(g_K, V_3) = (14, -40)$ (region B) to $(g_K, V_3) = (4.5, -30)$ (region C). Note that the chosen value $V_3 = -35$ mV allows us to fix the maximal depolarization to -20 mV, the value observed by Ozaita et al. [4] for further mature SACs. Remark that the lower branch of the heat map 2.12 (region between G and B in the bifurcation map) corresponds to interburst intervals of the order of 8 – 16 min, so according to SACs recording not to a biophysically plausible bursting regime.
- *How can bursting be restored in adult SACs?* Upon further maturation, Zheng et al. show that the restoration of bursting in P22 SACs (late stage III-before eye-

opening) depends on the interplay between the change of the intrinsic properties of K^+ channels strong inhibition (TEA application) and blocking the strong inhibitory (gabaergic) input induced by other amacrine cells at this phase (Fig 2.13, fourth and fifth row, left). Neither of these conditions suffice alone for the bursting restoration. To model the gabaergic inhibitory input to SAC at P22 coupled SACs we add a constant external current $I_{ext} = -10$ pA whereas the effect of TEA is modeled by decreasing the g_K conductance. This conductance is not set to 0 because TEA blocks only one subtype of kv_3 channels while there exist several of them (see below) in the developing retina. The whole operation has the effect of suppressing bursting (red trace top) and corresponds moving from region B to region A in Fig. 2.5. Bursting re-initiation is obtained by setting back the current I_{ext} to zero.

Along these lines, we have been able to reproduce the effects of the pharmacological manipulation performed by Zheng et al. at the three separate ages; P4, P8 and P22 in Fig 2.13.

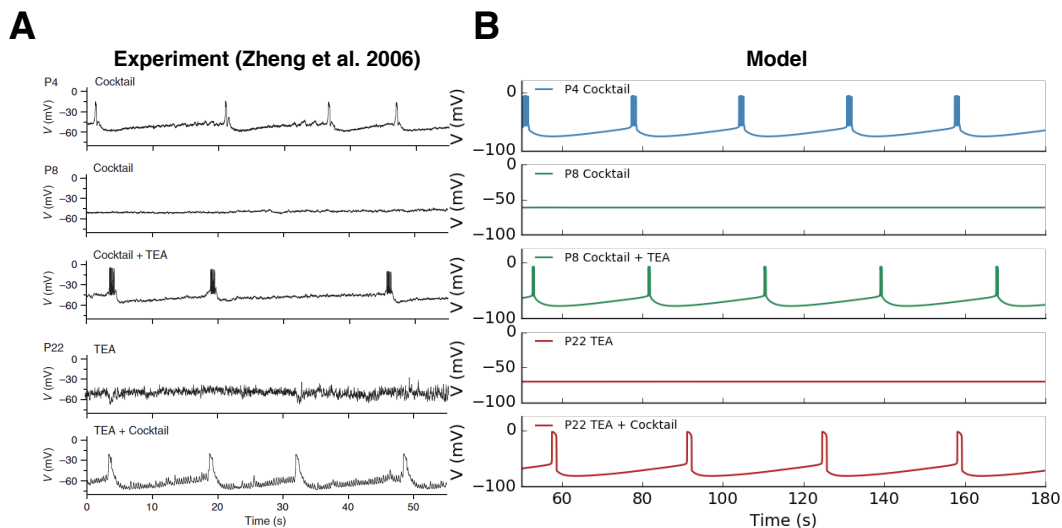


Figure 2.13: **A. Pharmacological manipulations made by [63] in order to restore bursting activity in rabbit SACs at different ages. B. Varying the potassium conductance g_K and the half-activation potential V_3 changes the excitability of SACs in our model.** *Blue:* Modeling the bursting activity of isolated P4 SAC, $g_K = 10nS, V_3 = -25mV$. *Green top:* Modeling P8 isolated SACs where we see no bursting activity, $g_K = 14nS, V_3 = -35mV$. *Green bottom:* Decreasing $g_K = 4.5nS, V_3 = -35mV$ we restore oscillations. *Red top:* Modeling P22 coupled SAC where there is no bursting activity upon treatment with TEA. A constant external current $I_{ext} = -10pA$ is applied to coarsely mimic the gabaergic inhibitory input to SAC at this stage of development. To account for the TEA application we take a lower value of K^+ conductance $g_K = 4.5nS$ ($V_3 = -35$). *Red bottom:* Restoration of bursting at P22 by removing all inhibitory synaptic connections, $I_{ext} = 0pA$. Removing inhibition from mature amacrine circuitry, along with blocking a sub-family of K^+ channels with TEA, is enough to re-initiate bursting activity. The values proposed here for V_3, g_K are only indicative. Also, note that we reproduce with our model the results of [63] with both of the proposed bursting scenarios, but here we only show the dynamically driven one.

2.12 A conjecture on the role of the KV_3 channels in the loss of SACs excitability upon maturation

Taken together, we predict that bursting occurs in immature SACs, during a certain age window while fast potassium channels are under-expressed. Upon development, we make the hypothesis that potassium channels increase their expression and spontaneous bursting stops when the inhibitory K^+ dominate the dynamics over the excitatory Ca^{+2} channels. Also, we suggest that upon maturation, the half activation potential V_3 decreases in order to provide a saturation in mature SACs activity as shown in [4]. This theoretical prediction could be experimentally tested, by following the expression of the fast K^+ channels in SACs during development and showing a potential increase of their activity along maturation. Moreover, we propose that the fast voltage gated K^+ channels involved is the Kv_3 family. More specifically, two subtypes of fast voltage gated K^+ channels have been identified [52, 4], both belonging to the kv_3 family: i) I_K , delayed rectifier currents, sensitive to TEA (tetraethylammonium) emitted by subunits $Kv_3.1$ and $Kv_3.2$ and ii) I_A A-type currents, sensitive to 4-aminopyridine (4AP), emitted by subunits $Kv_3.3$ and $Kv_3.4$ [52] which are not sensitive to TEA. The apparition and evolution of such channels in SACs during development has not been studied yet. However, in the experiment of [63], the application of TEA in *immature* SACs (rabbit $\sim P8$) was crucial to the reinitiation of bursting activity. This finding implies that, during development TEA sensitive K^+ channels are already expressed in SACs. On this basis, we propose that the specific type of K^+ channels responsible for the spontaneous bursting activity during development and eventually its loss upon maturation, is the I_K rectifier currents of the $Kv_3.1$ and $Kv_3.2$ subtype.

To conclude, we propose that, during early development ($< P6$), kv_3 channels are under-expressed, allowing a competition between inhibition (K^+) and excitation (Ca^{+2}), leading SACs to burst (see Fig 2.13, blue trace). Upon maturation, the expression of these channels could evolve increasingly, leading to stronger inhibition, dominating fully the competition of inhibitory/excitatory channels, by suppressing oscillations completely. Therefore, we suggest that the evolution of the expression of fast Kv_3 channels could be part of the transient process that leads to a complete loss of excitability of mature SAC. Our theoretical results indicate that the level of the expression of Kv_3 channels could increase gradually upon maturation, which essentially means that the conductance of these channels would increase as well as other physiological properties of the channels such as kinetics parameters like the half-activation potential (fixing the characteristic activation sigmoid of the channel). This type of experiment could elucidate the exact role of Kv_3 channels in the intrinsic properties of the excitability of SACs.

2.13 Discussion

In this chapter we have proposed a model for spontaneous bursting of SACs, one of the key ingredients for the initiation of stage II retinal waves. This leads us to propose several conjectures and possible experiments, directly inspired from the model analysis. We would like now to develop other aspects, not considered in the main text.

The role of inhibition Spontaneous bursting activity in immature SAC has been observed consistently across species i.e. mice, rabbits, chicks etc., but with different characteristic bursting periods. In Fig. 2.10, we show the relationship of the average bursting period τ_{IBI} with respect to the value of the leak potential V_L in our model, which could be translated on how an effective inhibition affects the characteristics of the bursting activity and even stops it completely. The source of such an inhibition could be linked either with intrinsic cell transient properties or inhibitory inputs from other layers of the retina (i.e. bipolar cells) upon maturation. As a result, we believe it would be worth investigating experimentally, if our theoretical result in Fig. 2.10 could be reproduced.

Pharmacological control. Although this model has many parameters, bifurcations analysis allows us to highlight several of them, g_C , g_K , V_3 and V_L , controlling important aspects of dynamics, in direct links with experiments. Varying those parameters have a deep impact on SACs dynamics as shown e.g. in Fig 2.13. This is possible via a pharmacological control (e.g. TEA to vary K conductance, Cd to vary Ca conductance, chlorid concentration to vary V_L ...). It would be interesting to try and confirm experimentally our bifurcations diagram with such experiments. In addition, this study opens the possibility that mature SACs are still potential bursters. Then, by a suitable pharmacological treatment, guided by the bifurcations analysis, they could start to burst in mature retinas. Would this restore waves as well, knowing that the structure of mature retinas is quite different from stage II ? A wave activity has been recently produced in mature mice retinas [20]. g_K and g_C could allow the control and arousal of retinal waves in adults. This deserves however further investigations.

The role of bursting in the spatial structure of SAC Mature SACs are found to be responsible for the direction selectivity feature in the retina computation. Especially, SAC have specific morphological characteristics such as a specific dendritic radial shape and a desymmetrised distribution of excitatory and inhibitory connections along the dendritic arbors, which explain as well their functionality linked to direction selectivity[4]. An interesting question to ask would be what is the role of bursting during development in the shaping of such special morphological characteristics of mature SAC and how the inhomeogeneity in SACs structure is shaped.

Chapter 3

The cholinergic coupling: a 1-dimensional study

In [63], the second prerequisite for the emergence of retinal waves, in addition to intrinsic bursting activity and long hyperpolarisation, is cells synchrony. In the following, we address mainly the questions "*How do waves start?*" and "*How bursting cells synchronize?*" helping to push a step further towards answering these questions from a theoretical point of view. Since bursting activity is an intrinsic property of each cell, it is interesting to explore first how two such cells behave when connected by nonlinear (here cholinergic) coupling. The utter goal of this approach is to study how SACs are able to opportunistically synchronize leading to propagating patterns in a 1D network. This work has been done in close collaboration with Lionel Gil, INPHYNI, UCA, France. Also for the model design we collaborated with O. Marre and S. Picaud, Vision Institute. These results have been partially published in [3, 2]. Also, this material is the subject of a paper *Spontaneous emergence of spatio-temporal structure in the early retina* which is currently under preparation for submission.

3.1 Modeling cholinergic coupling

At this point we extend the individual SACs model Eq (2.19) by adding a synaptic term to the equation of the voltage depending on the evolution of the concentration of the neurotransmitter acetylcholine A . It is shown in early experiments [55] that during stage II retinal waves, the dominant mechanism of synaptic transmission is cholinergic.

3.1.1 Cholinergic receptors

An acetylcholine (ACh) receptor (AChR) responds to the binding of acetylcholine and is classified into two major types according to its sensitivity to different molecules; i) muscarinic (mAChR) and ii) nicotinic (nAChR) acetylcholine receptors. During early retinal waves (stage II), nicotinic receptors are responsible for the mutual excitation between SACs and therefore waves propagation, whereas nAChRs have no effect on late waves. On the contrary, muscarinic receptors, control late spontaneous waves (stage III) and have no effect during early retinal waves [15]. Since, our model describes stage II retinal waves, we focus on the modelling of the biophysics of nAChRs.

Nicotinic acetylcholine receptors (nAChRs) respond to the neurotransmitter acetylcholine and are named after nicotine which selectively binds to this type of cholinergic receptors instead of the muscarinic ones. As with all ligand-gated ion channels, opening of the nAChR channel pore requires the binding of a chemical messenger. Opening of the channel allows positively charged ions to move across it; in particular, sodium enters and potassium exits the cell membrane. The net flow of positively charged ions is inward. The nAChR is a non-selective cation channel, meaning that several different positively charged ions can cross through. It is permeable to Na^+ and K^+ , with some subunit combinations that are also permeable to Ca^{+2} . The reversal potential for nAChR is about 0 mV [40]. At the synaptic terminal, two molecules of acetylcholine are needed to bind to a nicotinic receptor in order to open the cationic channel. As a consequence the fraction of open cationic channels is $\frac{A^2}{K_d^2 + A^2}$, where A is the acetylcholine concentration and $K_d^2 = \gamma_A$ the dissociation constant. The value we choose for γ_A in (3.1) corresponds to [64], where K_d for nAChR is about 1.0 nM.

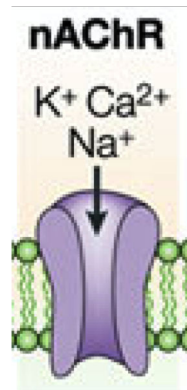


Figure 3.1: Schematic representation of a nicotinic cholinergic receptor (nAChR).

The evolution of the acetylcholine concentration is given by [12]:

$$A_t = -\mu A + \beta T_A(V) \quad (3.1)$$

where μ is the degradation rate in s^{-1} , β is the production rate for Acetylcholine in nM/s .

We model Acetylcholine's production mechanism as follows:

$$T_A(V) = \frac{1}{1 + \exp(-K_{ach}(V - V_0))} \quad (3.2)$$

where K_{Ach} and V_0 are the slope and inflection point of the sigmoid curve. The cholinergic current, received by a SAC from each of its neighbours is modeled as:

$$I_A = -g_A \frac{A^2}{A^2 + \gamma_A^2} (V - V_A) \quad (3.3)$$

where g_A is the maximal cholinergic conductance, V_A the reversal potential of nicotinic cholinergic receptors. Note that the second power of the acetylcholine concentration comes from the fact that we need 2 molecules of the neurotransmitter to bind to the nicotinic cholinergic receptor in order to open the channel.

As our modeling for Ach dynamics is based on Lansdell et al. [12], note the two

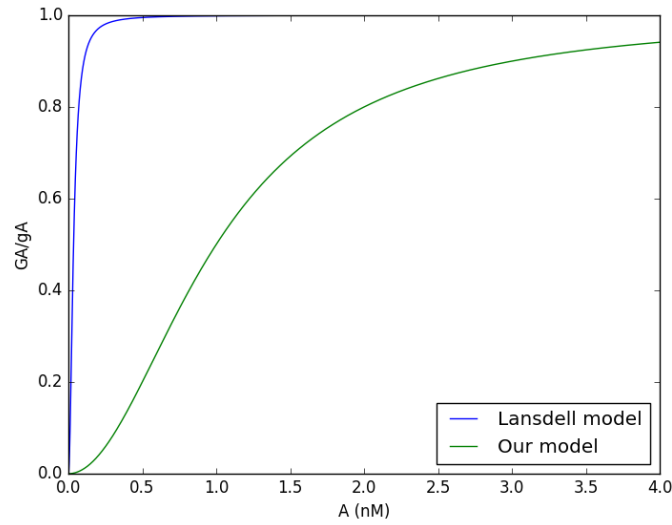


Figure 3.2: **Comparison between our and Lansdell et al. [12] Ach activation modeling curve.** We show that the normalized Ach conductance is a very steep function in the model of [12] compared to ours. In our model, the cholinergic conductance is not a switch-type but actually proportional to the Ach concentration A .

major differences between our Ach modeling: (i) We model direct synaptic interactions between cells, whereas these authors consider a volume diffusion of Ach. (ii) The value they choose for $K_d = \sqrt{\gamma A} = 0.035$ nM, is two orders of magnitude lower than our value. Their value makes the conductance function in (3.1) almost a Heaviside function, where the conductance is virtually constant except when Acetylcholine (Ach) concentration is lower than ~ 0.1 nM. This is not biophysically very accurate and also induces quite step dynamics in the system (see Fig 3.2) and requires robust numerical schemes to be treated correctly.

3.1.2 Full set of equations

To summarize, the full set of equations in our model with the 6 state variables V, N, C, S, R, A is the following:

$$\left\{ \begin{array}{l} C_m \frac{dV_i}{dt} = -g_L(V_i - V_L) - g_C M_\infty(V_i)(V_i - V_C) - g_K N_i(V_i - V_K) - g_{sAHP} R_i^4(V_i - V_K) \\ \quad - g_A(V_i - V_A) \sum_{j \in \mathcal{B}_i} \frac{A_j^2}{\gamma_A + A_j^2} \\ \tau_N \frac{dN_i}{dt} = \Lambda(V_i)(N_\infty(V_i) - N_i) \\ \tau_C \frac{dC_i}{dt} = -\frac{\alpha_C}{H_X} C_i + C_0 - \delta_C g_C(V_i)(V_i - V_C) \\ \tau_S \frac{dS_i}{dt} = \alpha_S(1 - S_i)C_i^4 - S_i \\ \tau_R \frac{dR_i}{dt} = \alpha_R S_i(1 - R_i) - R_i \\ \frac{dA_i}{dt} = -\mu A_i + \beta_A T_A(V_i). \end{array} \right. \quad (3.4)$$

where \mathcal{B}_i is the neighbourhood of the neuron i and i is the neuron index. Note that we represent neurons position in a $2D$ lattice by a single index (e.g. using lexicographic order) to avoid too heavy notations.

Parameters. The parameters used in the model are displayed in Table 3.1.

3.1.3 Tuning the parameters to fit experiments for acetylcholine dynamics

In order to tune biophysically the parameters associated to acetylcholine dynamics in the equation (3.1), we fitted experiments (see Fig 3.3) measuring the cholinergic post-synaptic currents evoked by acetylcholine puffs in [62]. Our hypothesis is that the exponential decay observed in Ach concentration after puff is due to degradation, so it allows us to measure the coefficient $\mu = 1.86 \text{ s}^{-1}$ in (3.1).

3.1.4 Bursting periods of immature SACs as a function of their biophysical parameters

The variability of the biophysical parameters across cells in a population or across different species is experimentally observed [30]. Using our modeling work, we would like to explore the role of relevant biophysical parameters of SACs on bursting characteristics, in order to first establish relationships between measurable features and second to extract possible underlying mechanisms for bursting.

The role of sAHP on bursting characteristics First, we compute how the inter-burst interval (IBI) depends on the parameters τ_S , directly related to the characteristic time of sAHP and g_{sAHP} , the sAHP conductance. We generally observe in Fig 3.4 a and b, that the IBIs increase monotonically while increasing the parameters τ_S and

Parameter	Physical value
C_m	22 pF
g_L	2 nS
g_C	$[3, 20] \text{ nS}$
g_K	$[1, 20] \text{ nS}$
g_{sAHP}	2 nS
g_A	$0 - 1.2 \text{ nS}$ per cell
V_L	$[-72, -70] \text{ mV}$
V_C	50 mV
V_K	-90 mV
V_A	0 mV
V_1	-20 mV
V_2	20 mV
V_3	-25 mV
V_4	7 mV
τ_N	5 ms
τ_R	8300 ms
τ_S	8300 ms
τ_C	2000 ms
μ	1.85 s^{-1}
β_A	5 nM/s
γ_A	1 nM^2
κ_A	200 V^{-1}
V_0	-0.04 V
δ_C	$10.503 \text{ nM pA}^{-1}$
α_S	$\frac{1}{200^4} \text{ nM}^{-4}$
α_C	4865 nM
α_R	4.25
H_X	1800 nM
C_0	88 nM

Table 3.1: Range of values for the parameters used in the model.

g_{sAHP} . The parameter τ_S , controls the characteristic time of the variable S , which controls the refractory period of the sAHP. By increasing τ_S , we almost directly increase the interburst intervals (IBI), and as we see the relationship between the two measures is approximately linear. The conductance g_{sAHP} has a more indirect effect on the bursting period of SACs. The maximal conductance of the sAHP is in fact the coefficient of the total sAHP conductance $g_{sAHP} R^4$. As we increase g_{sAHP} , we strengthen the effect of the variable R , which also controls the sAHP dynamics, along with variable S (see Chapter 2). However, as g_{sAHP} increases further, the variable R saturates at its maximum value and can not increase further, setting an upper bound on the effect on the period enlargement due to the increase of the sAHP conductance. This effect is illustrated in Fig 3.4 b, where we see that the IBI saturates as a function

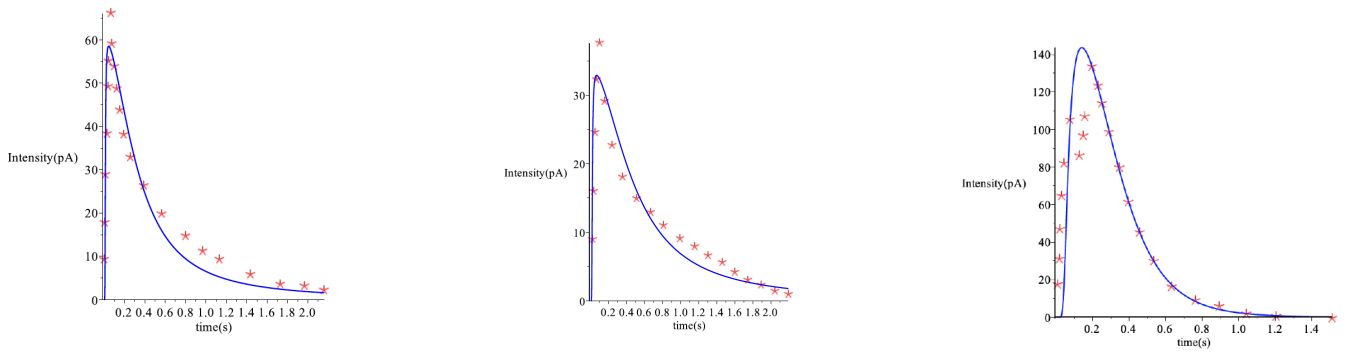
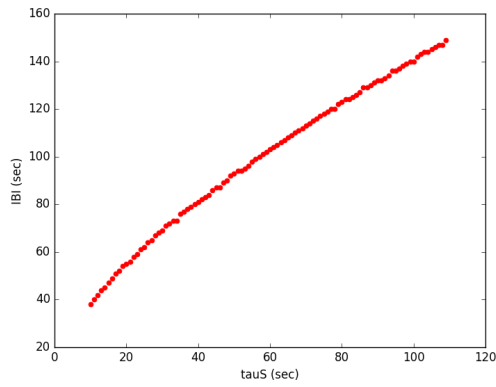
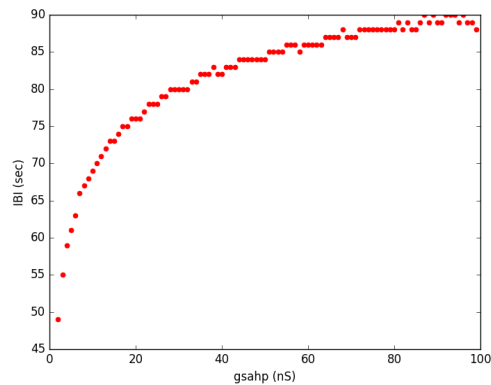


Figure 3.3: **Fitting the experimental curves of the cholinergic current temporal profile.** *Left, Middle:* Fit of the experiments in [62]. The red asterisks correspond to the experimental points (with $I \rightarrow -I$). In the left plot, $V_h = -75 mV$ and in the middle one $V_h = -45 mV$. *Right:* Fit for the dual patch clamp experiment shown in [62].

of g_{sAHP} .



(a)



(b)

Figure 3.4: a) and b) The interburst interval IBI in seconds as a function of the parameters τ_S and g_{sAHP} respectively.

The role of cholinergic coupling on bursting characteristics An important experimental feature reported in [63] deals with the increase of the interburst interval in the presence of acetylcholine. From this experiment, the authors measured the values of the bursting periods for two coupling strengths; i) in the uncoupled case where $g_A = 0$ where an antagonist cocktail is applied and ii) in the normal conditions case recording for which the exact value of the cholinergic coupling is not known. More precisely, in the presence of an antagonist cocktail which blocks the cholinergic synapses, bursts are observed with a mean interburst interval of $\simeq 15$ s (rabbit). In the absence of cocktail, in normal conditions, the interburst interval almost doubles $\simeq 28$ s.

Using our model, we are able to measure the average bursting period for several values of cholinergic coupling within a biophysical plausible interval of g_A , aiming to find how the bursting period depends on the coupling strength. In Fig 3.5, we report τ_{IBI} versus g_A for both a 2 and 4 cells configuration. For a vanishing value of g_A , the cells are independent. Because we are close to a bifurcation (saddle-node) [2], increasing of the noise fluctuations leads to a decrease of the mean interburst intervals. Here the noise level is constant, but the stronger g_A , the more a given SAC is sensitive to the source of fluctuations from its neighbors and the less is the τ_{IBI} . For higher values of g_A , the synchronization increase between SACs is concomitant with a strong increase of the mean interburst interval, because variable R increases. For even larger g_A , τ_{IBI} starts to decrease. This is explained below.

In order to match the experiment of [63], we observe in Fig 3.5, that there is a point where the period is doubled compared to the uncoupled case. This point corresponds to the maximum point in the bursting period curve. This observation possibly implies that the natural level of cholinergic coupling during stage II retinal waves, imposes a maximum interburst interval for immature SACs. This hypothesis has an important consequence on the spatiotemporal dynamics of waves, whose apparition is vastly controlled by the period refractoriness of SACs, during which no wave can be generated. However, we need to state that for this conjecture, we rely on the choice of our model parameters a lot, since we did not test its robustness with respect to parameters variations. As a result this hypothesis is weakened. It would be interesting though to explore also experimentally, if at this stage, immature SACs would choose to be tuned to their maximum refractoriness. Also, it would be interesting to compare this result across species in order to investigate whether maximum refractoriness during stage II retinal waves emerges as a universal property of the transient network of bursting SACs.

3.2 Bursting of an isolated cell and acetylcholine production.

We consider the evolution of Ach concentration during a SAC's burst in the noise driven bursting regime when (i) the SAC is isolated; (ii) cell 1 is coupled to another cell 2; When cell 1 bursts we write the conditions triggering a burst in cell 2. As cell 2 is bursting, it prolongates the bursting time of cell 1 and we compute the corresponding profile.

Rest state Let us first compute the rest state of all the state variables:

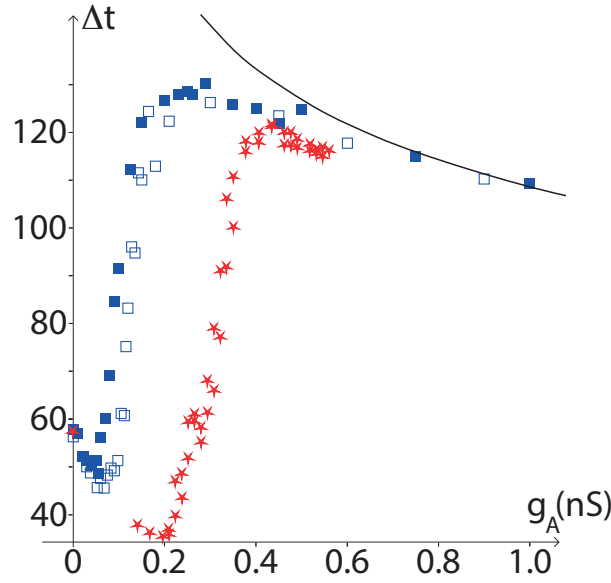


Figure 3.5: Numerical simulation showing the mean interburst interval τ_{IBI} versus cholinergic conductance g_A . The filled blue squares correspond to the 2 cells network, the unfilled blue squares to the 4 cells one. The red stars stands for the full 128×128 network, with 28 synaptic neighbors for each cell. The continuous black curve stands for the interburst interval of the periodic homogenous solution, in absence of noise ($I_{noise} = 0$).

$$\left\{ \begin{array}{l} V_i = \frac{g_L V_L + g_C V_C M_\infty(V_i) + g_K V_K N_i + g_{sAHP} V_K R_i^4 + g_A V_A \sum_{j \in \mathcal{B}_i} \frac{A_j^2}{1 + A_j^2}}{g_L + g_C M_\infty(V_i) + g_K \tilde{N}_i + g_{sAHP} R_i^4 + g_A \sum_{j \in \mathcal{B}_i} \frac{A_j^2}{1 + A_j^2}} \\ N_i = N_\infty(V_i); \\ C_i = \frac{H_X}{\alpha_C} [C_0 - \delta_C g_C(V_i)(V_i - V_C)]; \\ S_i = \frac{C_i^4}{1 + C_i^4}; \\ R_i = \frac{\alpha_R S_i}{1 + \alpha_R S_i}; \\ A_i = \beta_A T_A(V_i). \end{array} \right. \quad (3.5)$$

The rest state is the solution of a non linear equation:

$$\underline{V} = \underline{F}(\underline{V}),$$

where \underline{V} is the N -dimensional vector with entries V_i . In particular, when $g_A = 0$ (no coupling) this equation factorizes into N independent equations. There is always at least one solution (from Brouwer's theorem [65]), but, in general, several solutions (stable or unstable) can exist.

Acetylcholine concentration dynamics. The general solution of equation 3.1 is:

$$A(t) = A(t_0)e^{-\mu(t-t_0)} + \beta \int_{t_0}^t T(V(s))e^{-\mu(t-s)} ds, \quad (3.6)$$

where t_0 is the initial time. As V has fast fluctuations (quite faster than the time scale $\frac{1}{\mu}$), eq. (3.6) averages over these fluctuations with an exponential weight.

Acetylcholine concentration in the rest state. In the noise driven bursting regime voltage is at rest, with a value V_- independent of time. This gives

$$A(t) = A(t_0)e^{-\mu(t-t_0)} + \frac{\beta T(V_-)}{\mu} \left[1 - e^{-\mu(t-t_0)} \right].$$

If $t - t_0$ is large (larger than $\frac{1}{\mu}$) this is close to

$$A_- = \frac{\beta T(V_-)}{\mu}, \quad (3.7)$$

the asymptotic A concentration in the low state.

For our model's parameters value $\beta = 5 \text{ nMs}^{-1}$, $\mu = 1.86 \text{ s}^{-1}$, $V_0 = -40 \text{ mV}$, $\kappa_A = 0.2 \text{ mV}^{-1}$, $V_- = -60.5 \text{ mV}$, this gives $A_- = 0.044 \text{ nM}$.

Ach concentration during a burst. In the bursting regime, V exhibits fast oscillations. Taking $t_0 = 0$ (new time origin starting with the burst) we have:

$$A(t) = A_- e^{-\mu t} + \beta \int_0^t T(V(s))e^{-\mu(t-s)} ds,$$

where T is a sigmoid. This integral is difficult to obtain and we approximate it with the following ansatz. We replace $T(V(s))$ by a constant Ω and the inverse time scale μ by an inverse effective time scale μ' . This gives:

$$A(t) = A_- e^{-\mu t} + \frac{\beta \Omega}{\mu'} \left[1 - e^{-\mu' t} \right]. \quad (3.8)$$

where Ω, μ' are determined by fit. See figures 3.6 and 3.8 for a validation.

In the bursting regime $V(s)$ oscillates fast around an average value. In the simplest approximation (large fluctuations and/or steep function T) $T(V(s))$ is essentially a binary function which is 0 when $V(s)$ is low and 1 when $V(s)$ is high. Thus, we have to compute the integral $\int_{s, T(V(s))=1} e^{-\mu(t-s)} ds = \sum_{i=0}^{n(t)} \int_{\sigma_i}^{\tau_i} e^{-\mu(t-s)} ds + R$ where $n(t)$ is the number of time intervals $[\sigma_i, \tau_i]$ - within the time interval $[0, t]$ - where $V(s)=1$. R is a residual term depending on t and small compared to the sum. Thus the integral is $\frac{e^{\mu t}}{\mu} \sum_{i=0}^{n(t)} [e^{\mu \tau_i} - e^{\mu \sigma_i}] = e^{\mu t} f(t)$.

The integral is zero for $t = 0$ and it is upper bounded by $\int_0^t e^{-\mu(t-s)} ds = \frac{1}{\mu} [1 - e^{-\mu t}]$. So the simplest choice for $f(t)$ is $\Omega \frac{1}{\mu} [1 - e^{-\mu t}]$ where Ω is a constant roughly corresponding to the fraction of times where $T(V(s)) = 1$. Here, we add the possibility of modulating the rate μ , but most fit are very good with $\mu = \mu'$. The Ach concentration at the end of the burst of duration τ is therefore

$$A(\tau) = A_- e^{-\mu \tau} + \frac{\beta \Omega}{\mu'} \left[1 - e^{-\mu' \tau} \right]. \quad (3.9)$$

Ach concentration just after a burst. At time τ the burst stops. V decays rapidly, within a time scale of order τ_a , toward an hyperpolarized state V_h (which increases then slowly back to V_- , see next paragraph). The Ach production $T(V)$ drops rapidly from Ω to $T(V_h) \sim 0$ and we may write $T(V(s)) = -\frac{\Omega}{\tau_a}(s - \tau) + \Omega$, $s \in [\tau, \tau + \tau_a]$. Therefore, just, after the burst:

$$A(t) = A(\tau)e^{-\mu(t-\tau)} + \frac{\beta\Omega}{\mu} \left[-\frac{t-\tau}{\tau_a} + \left(1 + \frac{1}{\mu\tau_a}\right) \left(1 - e^{-\mu(t-\tau)}\right) \right], \quad t \in [\tau, \tau + \tau_a]. \quad (3.10)$$

We note $A_+ = A(\tau + \tau_a)$.

Ach concentration during the hyperpolarization phase. In this phase V varies very slowly (see lower branch of the bifurcation diagram 2.2), following R adiabatically: where:

$$V = \frac{g_L V_L + g_C M_\infty(V) V_C + V_K [g_K N_\infty(V) + G_S]}{g_L + g_C M_\infty(V) + g_K N_\infty(V) + G_S}, \quad (3.11)$$

where we have set $G_S = g_{sAHP} R^4$ for simplicity.

If we make the approximation that there is a very weak Ach production during hyperpolarization ($T(V(s)) < T(V_-) \sim 0$), $A(t)$ obeys

$$A(t) = A_+ e^{-\mu(t-\tau-\tau_a)} + A(R) \left[1 - e^{-\mu(t-\tau-\tau_a)} \right]. \quad (3.12)$$

where $A(R)$ slowly depends on R and converges to A_- as $t \rightarrow \infty$.

Numerical checks. We have checked these approximations numerically (Fig. 3.6).

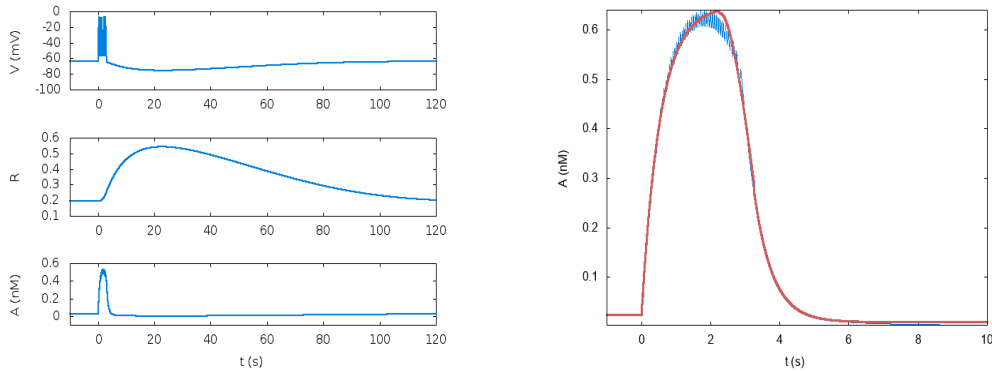


Figure 3.6: . Left: Evolution of voltage, R , and A during a burst in NIB regime. Right: Ach concentration profile during a burst (blue) and fit (red).

3.3 Bursting of 2 coupled cells.

In order to better understand the mechanisms involved in cells coupling we now study the case of two cells, before generalizing to a network with N cells. We consider two bursting cells, C_1, C_2 , coupled reciprocally to each other by cholinergic current of equal amplitude. Each cell follows its own proper bursting dynamics, which is controlled by the state variables and parameters.

Cells interaction. We consider now 2 cells in the noise driven bursting regime. The first cell C_1 starts to burst by a short clamp of current (+50 mV during 0.1 ms), and, if g_A is large enough, induces bursting to the second cell, C_2 . Then, C_2 generates an Ach current which prolongates the burst of C_1 . Both cells are mutually coupled until I_{sAHP} is large enough to stop bursting in both cells, not necessarily at the same time.

In Fig 3.7 we see the Ach concentration of cells 1 and 2 as a function of time. The main observations are: (i) the bursting of cell 2 prolongates the burst of cell 1; (ii) the interaction between bursts increases the peak in Ach production—as a consequence Ω in (3.8) depends on g_A when cells are coupled; (iii) Increasing Ach coupling favours the synchrony between cells.

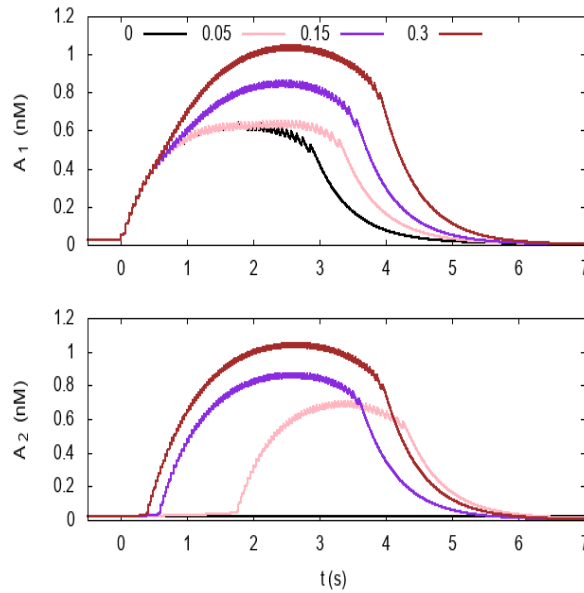


Figure 3.7: Evolution of coupled bursts for different values of g_A (0, 0.05, 0.15, 0.3 nS). Row 1 corresponds to cell 1 and row 2 to cell 2. Evolution of A during a burst in the noise driven bursting regime. Cell 1 bursts first due to a small pulse in V . Then cell 2 bursts due to the Ach current generated by 1. The Ach current generated by 2 prolongates the burst of 1.

Fitting the Ach profile. In the coupled case the Ach profile A_1 of cell 1 departs from section 3.2 because, in addition, there is an Ach current coming from cell 2, competing with sAHP, and prolongating the burst. As a consequence, in addition to the regimes (3.8), (3.10), (3.12), there is an intermediate regime, between the burst rising (3.8) and the rapid decay after the burst ((3.10)), where A_1 slowly varies. This results from the interaction of V_1, R_1 and the Ach current I_{A_2} due to the other cell.

As cell 1 is bursting V_1 has fast oscillations and we have not been able to compute the effect of these non linear fast oscillations on the other cell.

As an approximation we will assume that A is constant (plateau) in this regime. Results of this approximation are plotted in fig. 3.8. The plateau is visible for $g_A > 0.2$ nS.

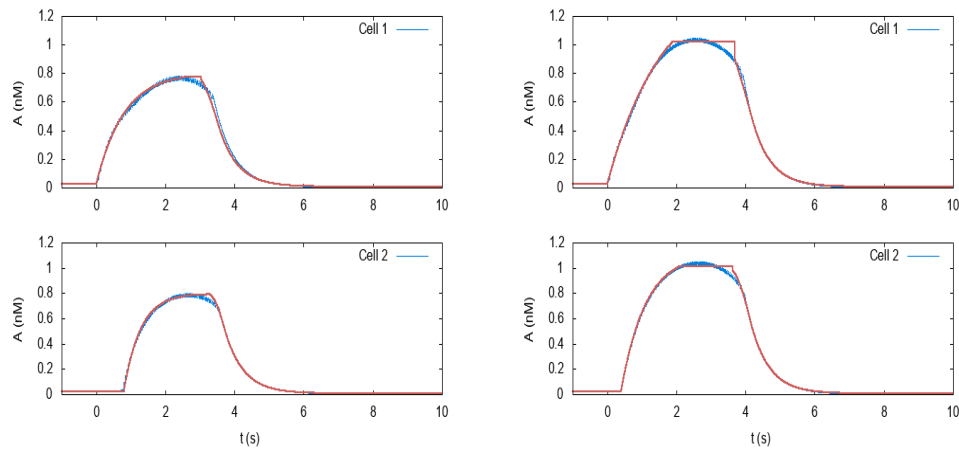


Figure 3.8: Ach profile (in blue) and fit (in red), for cell 1 and 2. Left: $g_A = 0.1$ nS; Right $g_A = 0.3$ nS.

The delay between bursts of cell 1 and cell 2. Here we compute numerically the time delay between the bursting time of cell 1 and the bursting time of cell 2. We consider 2 ways of defining the burst: (i) $I = I_{sAHP} + I_A$ crosses I_{SN} ; (ii) C , the calcium concentration crosses a critical value θ . In fig. 3.9 we have represented the time delay between the bursting time of cell 1 and the bursting time of cell 2 corresponding to these 2 ways as a function of g_A . The curves are slightly different although they have the same behaviour. The time t_B , delay corresponding to the first way (I crosses I_{SN}) is computed analytically in equation (3.17). This theoretical value is plotted as well.

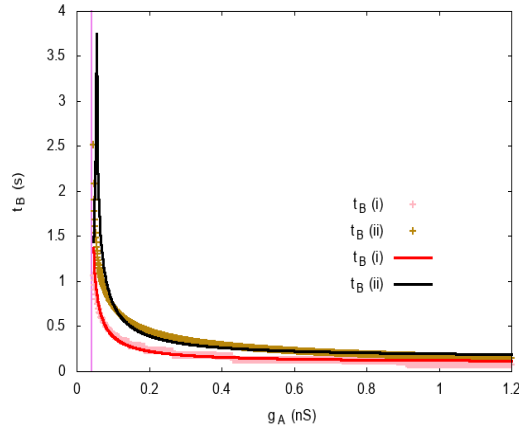


Figure 3.9: . Time delay t_B between the bursting time of cell 1 and the bursting time of cell 2. (i) corresponds to a definition of the burst when $I = I_{sAHP} + I_A$ crosses I_{SN} ; (ii) corresponds to C crossing a threshold. Red and black lines correspond to fit in case (i) and (ii). The pink, vertical line, corresponds to the limit value g_{A_m} given by (3.18).

Burst bifurcation. From the time scale separation and Morris-Lecar bifurcation analysis burst starts when the external current I crosses the Saddle-node bifurcation value I_{SN} . In this analysis, the external current is assumed to be slow, compared to the fast scale dynamics of V and N . However, the currents involved here, $I_A = -G_A(V - V_A)$, where $G_A \equiv g_A \sum_j \frac{A_j^2}{\gamma_A + A_j^2}$, or $I_S = -G_S(V - V_K)$, where $G_S = g_{sAHP}R^4$, have a slow component, the conductances, and a fast component, coming from the voltage. When considering the bursting transition of a rest cell, without noise, the fast component is constant, so the bifurcation is driven by the conductance. But, during bursting, where voltage fluctuations are fast, the bifurcation condition is more difficult to write because, one cannot apply the slow-dynamics condition $I < I_{H_c}$ on the fast $I_A + I_S$. A similar problem holds when there is noise, here, even for the starting burst condition, where the cell is in the rest state, because the noise induces fast fluctuations. In particular, one can check that crossing the value I_{SN} for the noisy current is not enough to trigger the burst. From Fig 3.10 the bifurcation conditions seems more on V than on I . One can indeed see that the bifurcations holds when V crosses the unstable middle branch.

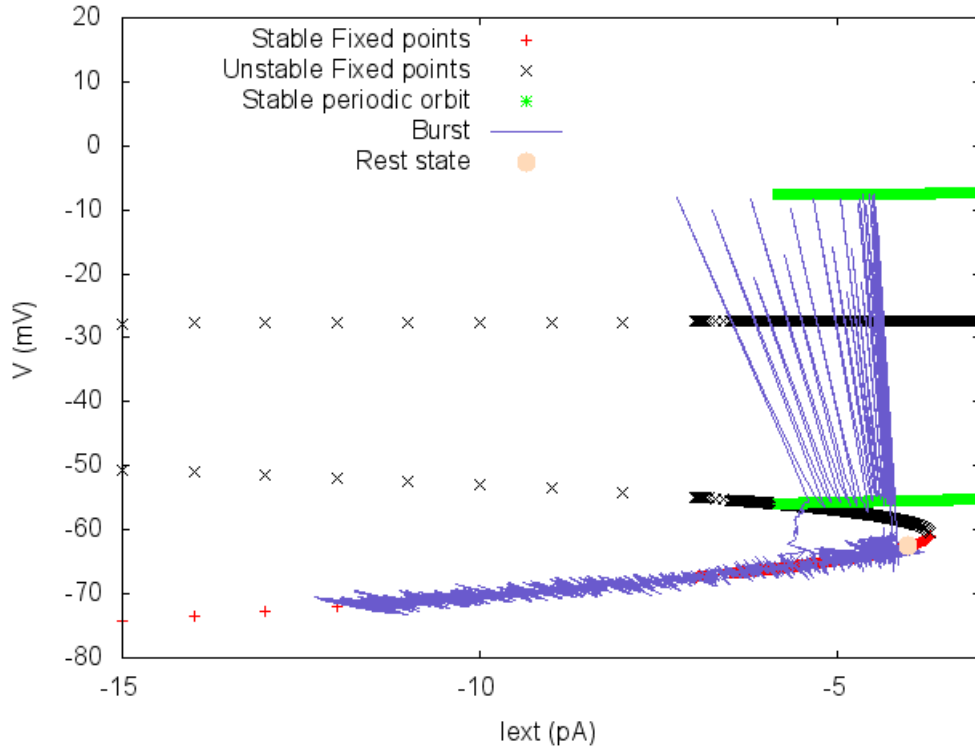


Figure 3.10: **Bifurcation diagram of the full dynamics.** The plot shows a representation of bursting in the plane $I_{ext} - V$ in relation with the bifurcation diagram of figure 2.2. Here we show the effect of a noisy trajectory (in blue) on the bifurcation diagram.

Numerically, it is safer to define the burst on the medium scale variable Ca , but the bifurcation condition is harder to write. Here, we focus on the bursting bifurcation when the cell is in the rest state V_- , without noise. The bursting condition reads:

$$-g_A \sum_j \frac{A_j^2}{\gamma_A + A_j^2} (V_- - V_A) - g_{sAHP} R^4 (V_- - V_K) = I_{SN}. \quad (3.13)$$

Piecewise linear approximation for U . We note $U(A) = \frac{A^2}{\gamma_A + A^2}$. We remark that $U(A)$ is a sigmoid that can be approximated by the piecewise linear function (Fig. 3.11 left):

$$U(A) \sim \begin{cases} \frac{1}{2\sqrt{\gamma_A}}, & 0 \leq A \leq 2\sqrt{\gamma_A}; \\ 1, & A > 2\sqrt{\gamma_A}. \end{cases} \quad (3.14)$$

In this approximation $U(A)$ is constant if all neighbours produce more Ach than $2\sqrt{\gamma_A} = 2K_d$.

We have computed the mean $\langle A \rangle$ and standard deviation σ_A of A , for two couples of values V_0, κ_A that fixes the Acetylcholine production function $T(A)$; namely $V_0 = -35 \text{ mV}, \kappa_A = 60 \text{ V}^{-1}$ and $V_0 = -40 \text{ mV}, \kappa_A = 200 \text{ V}^{-1}$. The results are shown in fig. 3.11. In general $\langle A \rangle$, as well as the maximum of A during its time-evolution, are well below $2\sqrt{\gamma_A}$, except for $V_0 = -35 \text{ mV}, \kappa_A = 60 \text{ V}^{-1}$ in the high stable fixed point regime (Fig. 3.11 left top). In this case $U(A)$ saturates to 1.

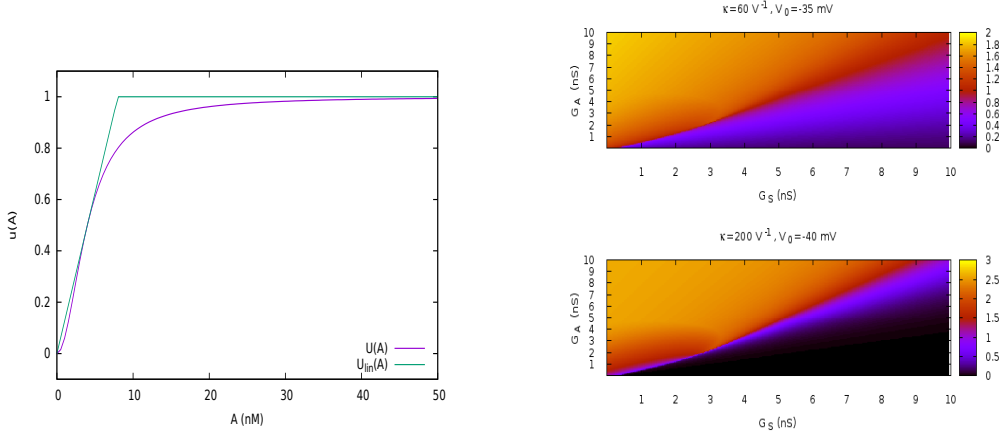


Figure 3.11: Left. Piecewise linear approximation for U with $\gamma_A = 1 \text{ nM}^{\frac{1}{2}}$. Right. Color map of the average Acetylcholine concentration as a function of G_S, G_A .

Average Ach current in the rising phase. From the piecewise linear approximation for $U(A)$ the Ach conductance generated, in the rising phase, by a bursting SAC is $\sim g_A \frac{\beta\Omega}{2\mu'\sqrt{\gamma_A}} [1 - e^{-\mu t}]$. Consider now a wave front in d dimension. A cell at rest receives an Ach current from bursting cells. We assume that there are n bursting cells and that they are synchronous¹ (they started to burst at the same time). Then, the Ach current viewed by this cell is, taking as time origin the time when the bursting neighbours started to burst:

$$I_A(t) \sim -g_A \frac{n\beta\Omega}{2\mu'\sqrt{\gamma_A}} [1 - e^{-\mu t}] (V_- - V_A) \quad (3.15)$$

and the total current is:

$$I(t) = -g_A \frac{n\beta\Omega}{2\mu'\sqrt{\gamma_A}} [1 - e^{-\mu t}] (V_- - V_A) - g_S R^4(t)(V_- - V_K).$$

Time of the next burst. Consider now 2 cells. C_1 is bursting and C_2 initially at rest. C_1 produces a G_A conductance which may induce C_2 bursting. This occurs if there is a time $t_B < \tau$ (τ is the time where the neighbours stop to burst) such that:

$$-g_A \frac{n\beta\Omega}{2\mu'\sqrt{\gamma_A}} [1 - e^{-\mu t_B}] (V_- - V_A) - g_S R^4(t_B)(V_- - V_K) = I_{SN}. \quad (3.16)$$

This gives:

$$t_B = -\frac{1}{\mu'} \cdot \log \left[1 + \frac{1}{g_A} \frac{2\mu'\sqrt{\gamma_A}}{n\beta\Omega} \frac{I_{SN} + g_S R^4(t_B)(V_- - V_K)}{V_- - V_A} \right]. \quad (3.17)$$

As we assumed that the neighbours cells started to burst at time 0, t_B is the time delay to have the next cell burst.

¹More generally n has to be replaced by the average number of neighbouring cells bursting within a time slot, i.e. this is $K\rho$ where K is the number of neighbours and ρ the density of bursting cells per time slot. When considering Calcium bursts, as done here, the time slot has to be faster than the Ca time scale and quite slower than the fast dynamics. Typically $100\text{ms} - 1\text{s}$.

Calcium burst. Numerically, it is safer and more natural to consider the condition where C crosses a threshold θ . However, the time where C crosses the threshold is delayed compared to the time when the burst starts, because C is a slow variable. As a consequence, one needs to add a time delay to (3.17) in order to obtain the calcium burst-time. One also needs to modify the time constant μ' and Ω in (3.17) (see Fig. 3.9).

3.3.1 Remarks on how the waves propagate and stop

1. $I_{SN} > 0$ in the noise driven bursting regime while $V_- - V_A < 0$. Therefore, if $\frac{I_{SN}}{V_- - V_A} < 0$, one needs a minimal Ach conductance to have a solution to (3.17). This minimal value is given by:

$$g_{Am} = -\frac{2\mu'\sqrt{\gamma_A}}{n\beta\Omega} \frac{I_{SN} + g_S R^4(t_B)(V_- - V_K)}{V_- - V_A} \quad (3.18)$$

g_A has to be larger than g_{Am} for a cell at the rest state in the NIB to start and burst. For our parameters value $g_{Am} = 0.041$ nS.

2. In general the condition (3.16) involves the sAHP current as well. That's why there is t_B in the right hand side of (3.17). Therefore, it might be that (3.16) holds at time τ_B and is then violated a few milliseconds after, if the excited cell is in a phase where R is growing (after hyperpolarization phase). Violating (3.16) does not mean that bursting stops though. For fast oscillations to stop we need $I(t) < I_{Hc}$. This arises either because:

- (a) sAHP is growing.
- (b) I_A is decreasing, because the neighbouring cells have stopped bursting. Then, the condition for the burst to stop is:

$$-g_A \frac{n\beta\Omega}{2\mu'\sqrt{\gamma_A}} A_+ e^{-\mu t} (V_- - V_A) - g_S R^4(t)(V_- - V_K) = I_{Hc} \quad (3.19)$$

Note that sAHP decays slower than Ach so, when a cell has stop to burst it cannot start to burst again just after.

3. Because of the competition between the 2 currents, a burst can therefore be quite short. Also, if the cell is hyperpolarized and if it bursts because of the neighbours, during bursting its V raises so R as well, making longer its hyperpolarization phase.

Analytic characterization of the propagation in a 1-dimensional chain. We consider a one dimensional wave starting from a bursting cell on the left and propagating to the right. If $g_A > g_{Am}$ the waves propagates ballistically. We compute the speed by a linear interpolation of the time delay (Calcium burst) between the bursting start of cell $k - 1$ and cell k (Fig. 3.12). Therefore, $v_B = \frac{1}{t_B}$ where t_B has a similar form as (3.17) i.e. for a Calcium burst:

$$v_B = \frac{1}{C - \frac{1}{\mu'} \cdot \log \left[1 + \frac{1}{g_A} \frac{2\mu'\sqrt{\gamma_A}}{n\beta\Omega} \frac{I_{SN} + g_S R^4(t_B)(V_- - V_K)}{V_- - V_A} \right]}, \quad (3.20)$$

for a Calcium burst. However, in comparison to the time delay between 2 cells computed above, we have here to adjust the parameters C, Ω by fit. This is due, for Ω to the fact that the Ach peak is higher in the chain than for 2 cells only.

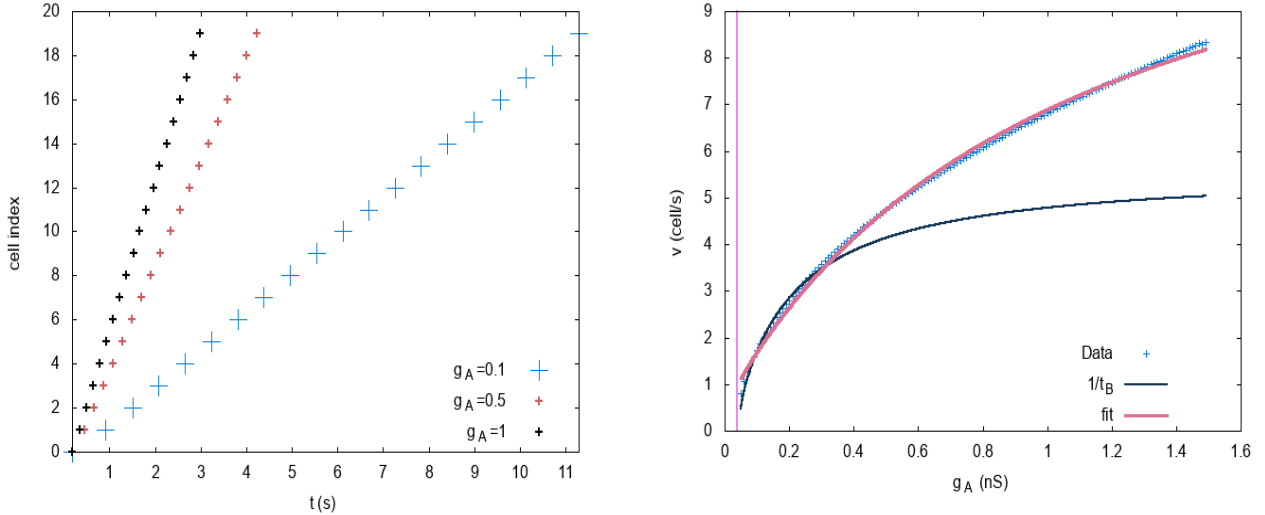


Figure 3.12: Left. Time delay between the burst of cell $k - 1$ and cell k . Right. Wave speed as a function of g_A and fit (pink curve) with $\frac{1}{t_B}$ where t_B is plotted in Fig. 3.9; (black curve) $\frac{1}{t_B}$ where t_B is given by eq. (3.17) and where parameters C, Ω have been adjusted by fit. .

3.4 Coupled Bursters in 1D (ring)

Before addressing the general two dimensional case of retinal waves, we conclude this chapter by addressing the dynamics of our system for a ring network of cells (see Figure 3.13). In the following, we will consider an one dimensional paradigm, simulating a network of 128 neurons, connected to their 6 nearest neighbours (3 per side) by acetylcholine coupling. The one dimensional numerical simulations are also less computationally costly and are guaranteed to converge faster compared to the 2D networks. These results will serve as a guide to study waves dynamics in the 2D network of SACs in the next chapter.

In the following parts, we are going to perform an analysis characterizing the two possible bursting regimes, namely the different triggering scenarios for bursting generation. In fact, the main difference between the two scenarios is the rest state of cells. For noise driven bursting, it is a fixed point, triggering a burst due to crossing the bifurcation point because of additive noise. For the dynamically driven bursting, cells are in an oscillating rest state (limit cycle) and therefore the triggering a burst is deterministic. In this case in our model, randomness comes from a background low-amplitude additive noise which breaks the bursting regularity. The switch between the two bursting scenarios is done by simply slightly change the value of V_L from $-70mV$ for dynamically driven bursting to $-72mV$ for noise induced bursting. To differentiate inbetween the two possible scenarios we need to address the question whether noise is fundamental for bursting triggering. However, experimentally it is not possible to perform such experiments with and without noise, since noise is de facto present in the cells. Attempting to validate physiologically one of the two scenarios, we will try

Ring network of N neurons

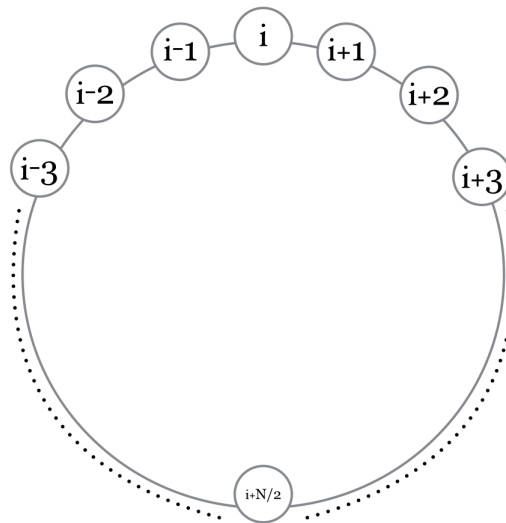


Figure 3.13: **Ring network with 6 nearest neighbours connectivity scheme.** The connections are cholinergic and birectional and neurons are identical

to characterize them with indirect measurements and try to map them to existing corresponding experimental observations.

3.4.1 Characterizing the dynamically driven bursting scenario in 1D

We simulate 128 SACs laid on a ring in the dynamically driven bursting regime for different values of cholinergic conductance g_A , corresponding to subcritical (weak) $g_A = 0.02nS$ per contact, critical (moderate) $g_A = 0.05nS$ and supercritical (strong) coupling $g_A = 0.06nS$. In Fig 3.14, we show the raster plots of the ring network, with a color code showing the cells activity, blue for low and red for high activity. Note that time evolves in the ordinate and space is represented in the abscissa. For weak coupling we observe that the cholinergic coupling is not enough to induce synchrony among cells, therefore there are no waves in this case, but only cells bursting at their own period. For moderate coupling, partial synchrony is achieved and at there are wave fronts of several distances. For the strong coupling, we observe that fuller synchrony is achieved. Nevertheless, there exist some domains within the wave able to propagate, revealing a characteristic length of the waves fronts. This effect is observed due to the combination of the characteristic time of the hyperpolarization of cells, therefore their incapability to be recruited, and the propagation time.

To quantify the characteristics of the observed wave fronts in these regimes of cholinergic coupling, we measure the probability distributions of the waves duration Fig 3.15 and size Fig 3.16 for several level of cholinergic coupling. We observe that for all values of g_A per contact the distributions tend to be exponentials. Also we don't observe zones of overlapping for waves, as it has however been observed experimentally by [36]. This is somehow expected, since the dynamics of all cells is deterministic therefore such zones are generated by the periodic deterministic bursting activity.

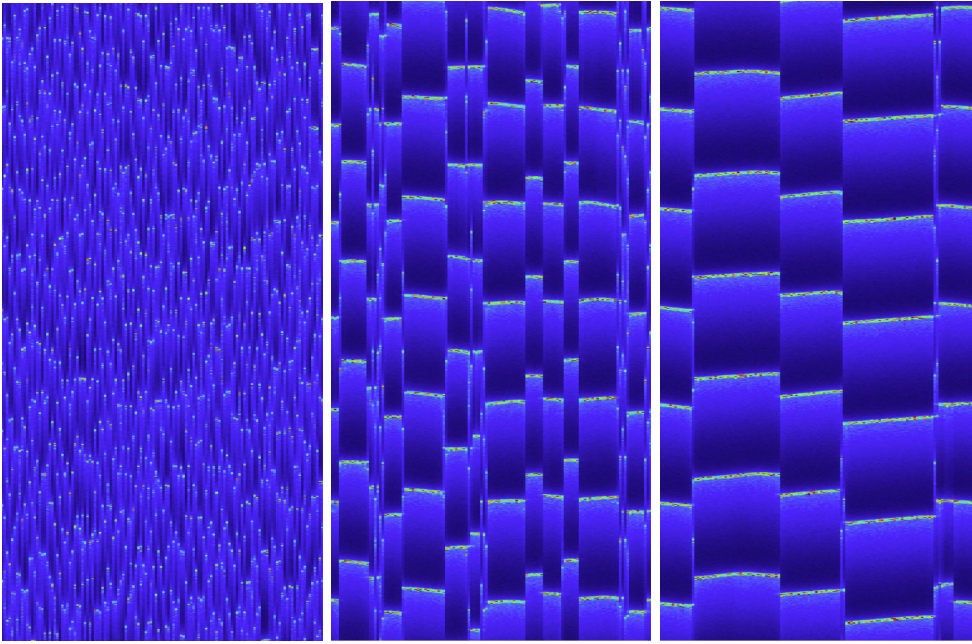


Figure 3.14: **Raster plots for the ring network of 128 cells.** Evolution in time is shown in the ordinate and space is represented in abscissa. From left to right the cholinergic coupling increases: weak $g_A = 0.02nS$ per contact, moderate $g_A = 0.05nS$ and strong coupling $g_A = 0.06nS$. The parameters regime corresponds to the dynamically driven scenario.

3.4.2 Characterizing the noise driven bursting scenario in 1D

We now simulate 128 SACs laid on a ring in the noise driven bursting regime for different values of cholinergic conductance g_A , corresponding to weak $g_A = 0.005nS$ per contact, moderate $g_A = 0.016nS$ and strong coupling $g_A = 0.02nS$. In Fig 3.17, we show the raster plots of the ring network. For weak coupling we observe that the cholinergic coupling is not enough to induce synchrony among cells, therefore there are no waves in this case, but only cells bursting at random due to noise. For the strong coupling, we observe that full synchrony is achieved, with almost waves at the size of the numerical box. In this case, a wave goes until the boundary unless it interacts with another wave. The critical value g_{Am} (see Eq 3.18) is raised because of R , so, either g_A is not strong enough and the 2 waves collide and stop; or it is larger and cells synchronize. Indeed, in Eq 1.19 g_{Am} depends on R which rises in the presence of waves. The most interesting case is the moderate coupling, where maximal variability of waves sizes is observed, revealing possible power-law signatures. This indicates that for the moderate coupling in the noise driven regime the network could be in a critical state, where variability is maximal. The observation of power-laws for waves characteristics in stage II, has been proposed experimentally and theoretically in [54], although the results are not thoroughly tested.

To quantify the characteristics of the observed wave fronts in these regimes of cholinergic coupling, we measure the probability distributions of the waves durations (top) and sizes (bottom) Fig 3.18 for several levels of cholinergic coupling. We observe that for all intermediate values of g_A per contact the distributions tend to be power-law like. For small and larger levels of coupling the distributions are exponential like. This means that there is a regime which is critical for the neural network, where the

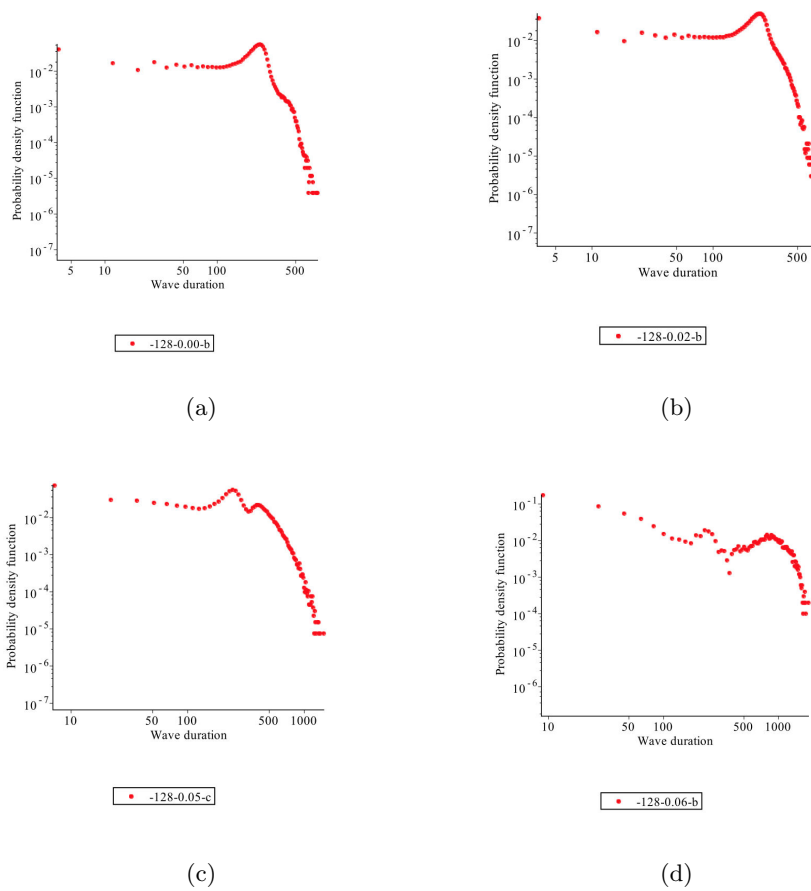


Figure 3.15: The probability density functions of the waves durations for different values of cholinergic coupling g_A . The scale is log-log and the corresponding values of conductances are 0, 0.02, 0.05, 0.06 nS per synaptic contact. The simulations are performed for 128 cells on a ring. The regime of parameters corresponds to the dynamically driven one, where bursting activity is triggered deterministically.

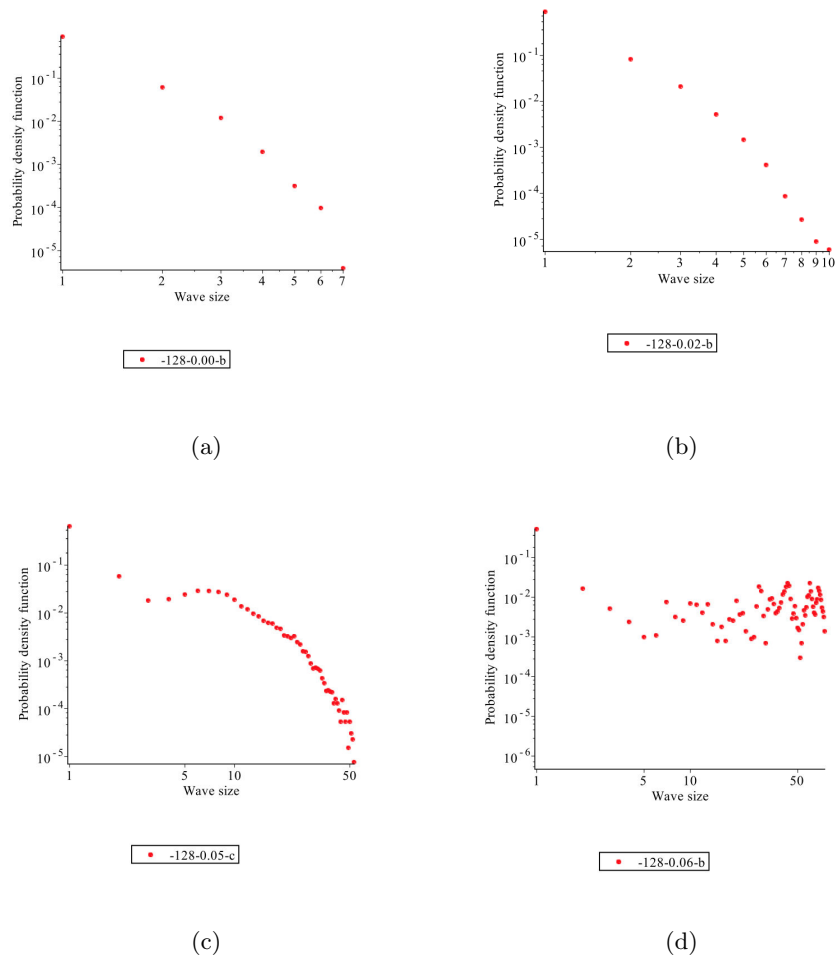


Figure 3.16: The probability density functions of the waves sizes for different values of cholinergic coupling g_A . The scale is log-log and the corresponding values of conductances are 0, 0.02, 0.05, 0.06 nS per synaptic contact. The simulations are performed for 128 cells on a ring. The regime of parameters corresponds to the dynamically driven one, where bursting activity is triggered deterministically.

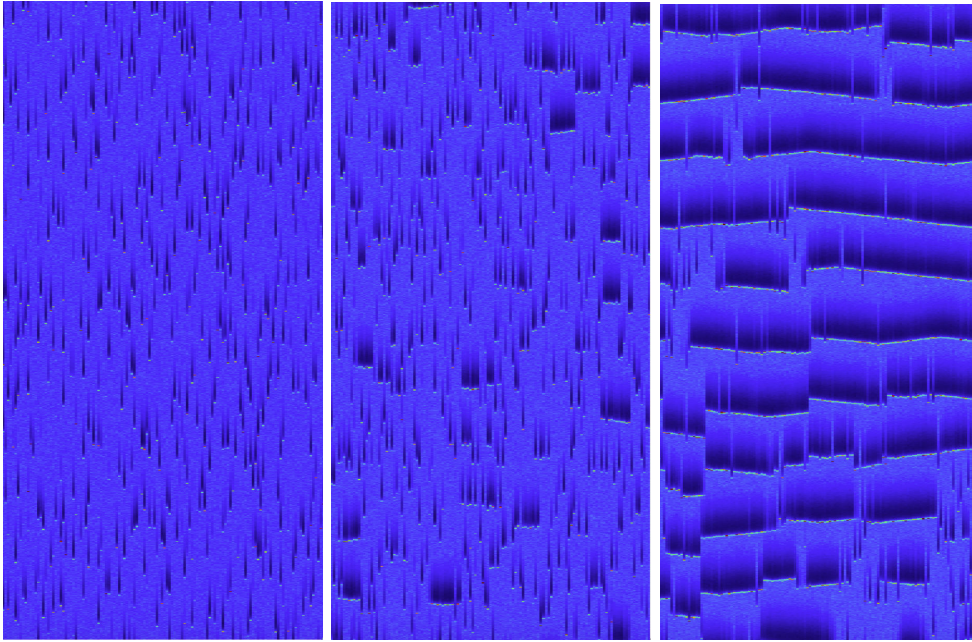
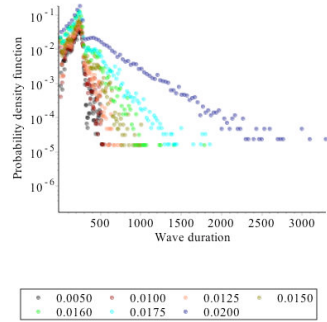


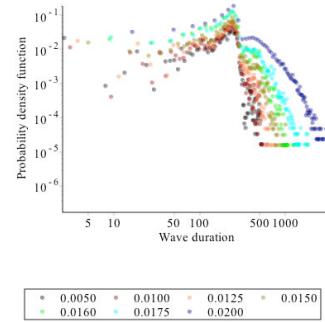
Figure 3.17: **Raster plots for the ring network of 128 cells.** Evolution in time is shown in the ordinate and space is represented in abscissa. From left to right the cholinergic coupling increases: weak, moderate and strong. The parameters regime corresponds to the noise driven scenario.

variability is maximal which is explained by the closeness to the critical point. Also in this bursting scenario, we observe zones of overlapping for waves, as it has been observed experimentally by [36].

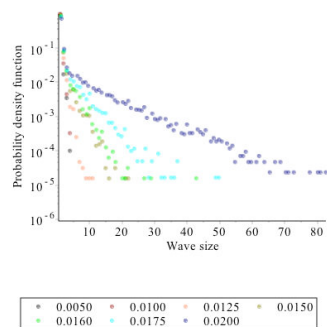
To sum up this section, we compute the correlations of the calcium activity with respect to distance for dynamically driven and noise driven regime as a function of distance. For the dynamically driven bursting regime we observe anticorrelations, indicating a characteristic length for the waves, measured in the units of neighbouring cells (see Fig 3.19).



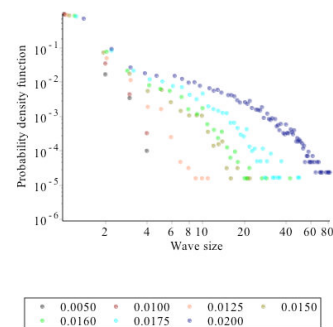
(a)



(b)



(c)



(d)

Figure 3.18: The probability density functions of the waves durations and sizes for different values of cholinergic coupling g_A . The scale is log-log and the corresponding values of conductances are 0, 0.02, 0.05, 0.06 nS per synaptic contact. The simulations are performed for 128 cells on a ring. The regime of parameters corresponds to the noise driven bursting regime.

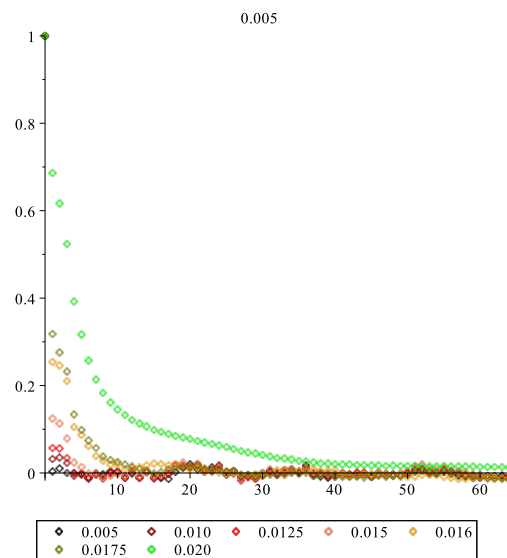
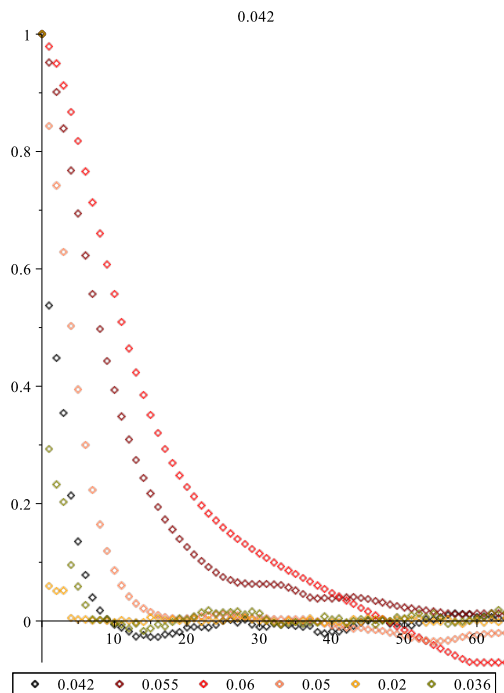


Figure 3.19: **Correlations for dynamically driven (top) and noise driven (bottom) regime as a function of distance.** The connections are cholinergic and birectional and neurons are identical. For the dynamically driven bursting regime we observe anticorrelations, indicating a characteristic length for the waves, measured in the units of neighbouring cells.

3.5 How do SACS synchronize upon cholinergic coupling?

As discussed in the previous chapter, individual cells bursting period is controlled by the slow dynamics of our system, namely the variables R, S . Especially, the bursting period of each individual SAC is controlled by two parameters, τ_R, τ_S , which are the characteristic times for sAHP currents. For reasons explained before concerning the variability of the cells period, we want to consider a paradigm where both cells have a different bursting period τ_1, τ_2 . More precisely, we compute the dependence of the ratio of the two bursting periods τ_1, τ_2 as a function of the parameter value τ_S (see Fig 3.20). Using this relation, we will be able to assign to each cell the desired bursting period, in order to test how SACS can synchronize in the following.

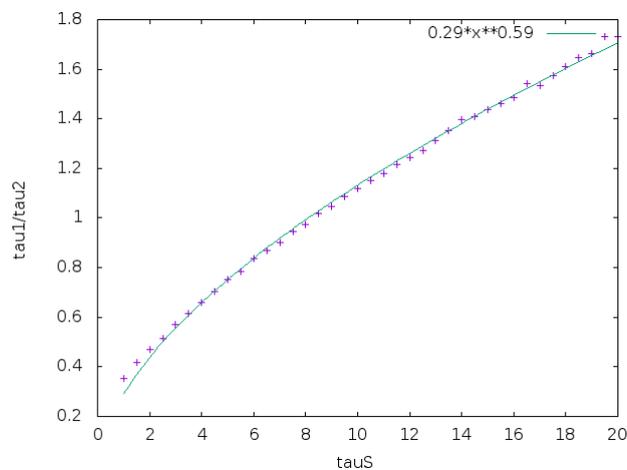


Figure 3.20: The dependence of the ratio of the two bursting periods τ_1, τ_2 as a function of the parameter value τ_S .

3.5.1 Mechanism for two bursting cells synchronization

Our following analysis is based on a general observation in physics that coupled oscillators have a tendency to synchronize, upon a sufficiently large coupling, even if their natural periods are not commensurable.

Synchronization and coupled oscillators. In a classical context, synchronization means adjustment of the periodic of the oscillators due to their interactions. Synchronization phenomena in large ensembles of coupled systems often manifest themselves as collective coherent regimes appearing via non-equilibrium phase transitions. For two oscillating cells, as in our case here, synchronization means that two nonidentical cells start to oscillate with the same frequency, which commonly lies between the frequency of the two oscillators [39]. Now, more particular, synchronization for bursters means a temporal overlap of the active phases of the cells. This synchrony could be partial or full. The synchronization of two bursters is largely dependent on the nature of their coupling. In the parameters plane of the bursters coupling and frequencies ratio, we can find regions where synchronization occurs. The overall picture for a broad range of forcing frequencies is presented by a family of triangular-shaped synchroniza-

tion regions touching the frequency axis at the rationals of the natural frequencies ration. These structures are widely known in the dynamical systems literature as *Arnold tongues* [48].

Synchronization in the dynamically driven bursting cells. We consider first the case of two non-coupled cells, for which we define the quantity $r = \frac{\tau_2}{\tau_1}$, called *rotation number*. Cell i enters into a burst each τ_i seconds. We consider that the two cells are $m : n$ *synchronized* if there exist two integers such that $m\tau_1 - n\tau_2 = 0$. It is easy to see that this corresponds to having r *rational*, with $r = \frac{m}{n}$. Then, if the two cells are bursting together at time 0 they will burst again together at time $m\tau_1 = n\tau_2$. Generically, the rotation number is irrational and cells are not synchronized although any irrational can be approximated, with any accuracy, by a rational (using Diophantine approximation) [48]. This means that if cells are bursting together at time 0, with an exact overlap, there will be a time (which can be quite long) where there bursts will, at least partly, overlap.

Now, in the presence of cholinergic synapses (more generally excitatory coupling) cells interact. If cell 1 is bursting whereas cell 2 is hyperpolarized, the excitatory current coming from 1 will accelerate the time for cell 2 to burst (see Fig 3.21). If the two cells are bursting together, the mutual interaction will prolongate their burst until their sAHP becomes large enough to stop bursting. When one cell stops bursting, its cholinergic current decay and the second cell, less and less simulated, will stop bursting thanks to I_{sAHP} growth. Thus, the cholinergic coupling mechanism has a tendency to synchronize cells.

As opposite to the uncoupled case though, cells are not expected to burst periodically anymore. It nevertheless makes sense to compute the time average bursting period of neuron i , τ_i and the rotation number $r = \frac{\tau_2}{\tau_1}$. Here, a rational rotation number $r = \frac{m}{n}$ means that, on average, cell 1 and 2 are bursting in synchrony after a time $m\tau_1 = n\tau_2$. Depending on the rotation number without coupling, and depending on the intensity of coupling, the synchronization of coupled oscillators is in general not 1 : 1 though. Having uncoupled oscillators with an irrational rotation number, oscillators tend, upon increasing coupling, to synchronize to the rational rotation number closest to r with the smallest numerator and denominator ². We observe a similar effect here: coupled cells synchronize clearly exhibiting *Arnold tongues* structure, shown in Fig 3.21. In abscissa we have the rotation number of the 2 cells when $g_A = 0$; in ordinate, we have g_A . Each color corresponds to a rational rotation number and define a structure called a "tongue". Thus, the tongue $\frac{m}{n}$ is a set of τ_S values where the two cells have $m : n$ synchronization upon Ach coupling when g_A is large enough. In other words, starting from a (generic) irrational rotation number, for large enough Ach coupling, the two cells synchronize in a rational rotation number.

This situation is represented by the red line in Fig. 3.21 corresponding to increasing g_A from 0 starting from an arbitrary rotation number. On the right, we have represented examples of bursting patterns. As we see, increasing g_A leads in general to the crossing of several tongues leading to a change in the rotation number. As we observed, large enough g_A leads to 1 : 1 synchrony, as the 1 : 1 Arnold tongue invades the whole diagram. Note that in coupled oscillators Arnold tongues overlap for a sufficiently large coupling and this situation corresponds to chaos [33]. As far as we have explored there

²More precisely, one can define a distance between rational and irrational, relevant for synchrony. This notion is related to Diophantine approximation and Farey sequences) [48]

is no chaos for 2 cells in our model.

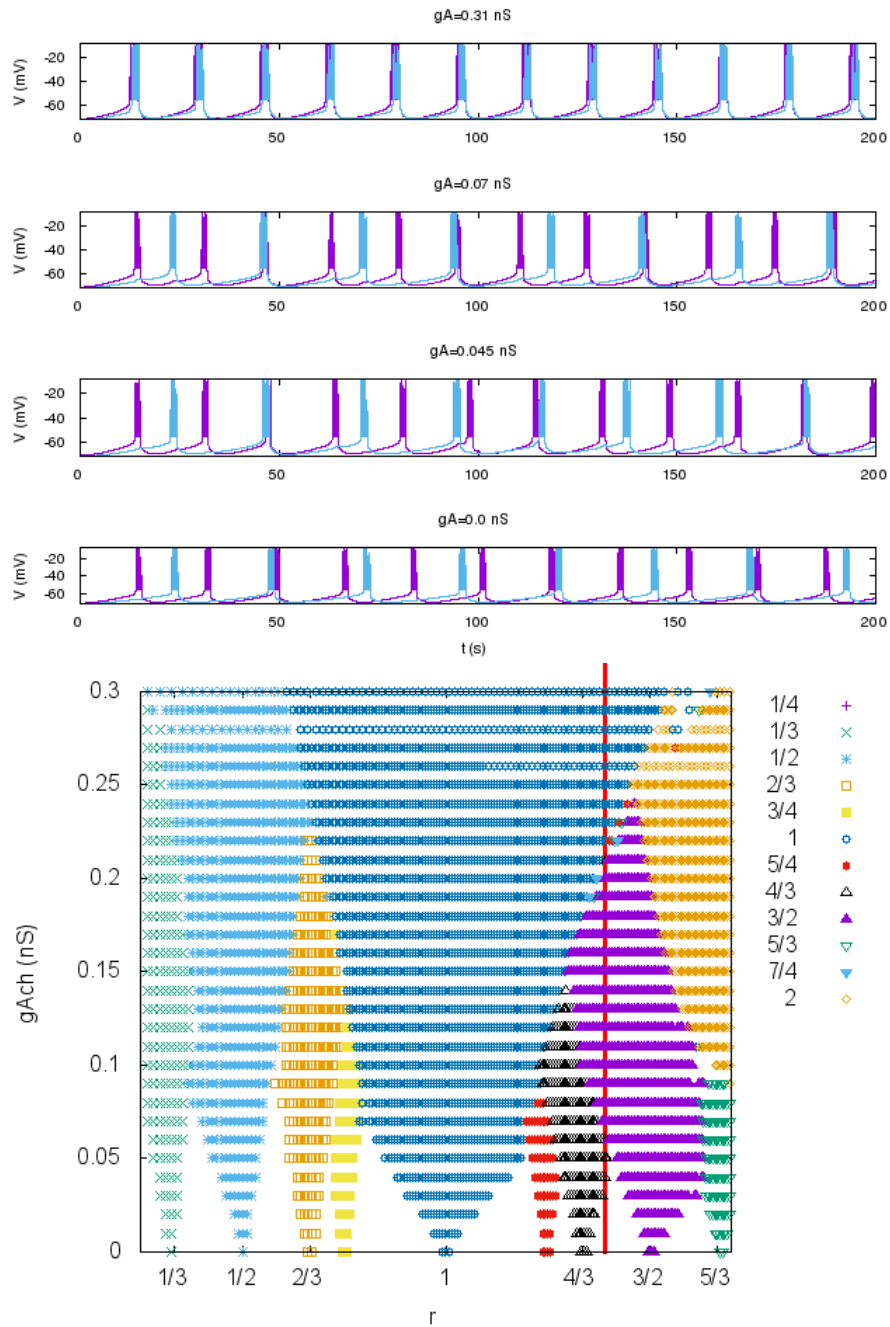


Figure 3.21: **Top.** $V(t)$ of two SACs with different bursting periods. As we increase the strength of the synaptic coupling cells tend to synchronize (bottom to top). **Bottom.** In abscissa we have the rotation number of the 2 cells when $g_A = 0$; in ordinate, we have g_A . Each color corresponds to a rational rotation number and define a structure called a "tongue". Thus, the tongue $\frac{m}{n}$ is a set of τ_S values where the two cells have $m : n$ synchronization upon Ach coupling when g_A is large enough

Synchronization in the noise driven bursting cells. To sum up this part let us briefly discuss the noise-driven bursting case. As we have seen the uncoupled cells are a in rest state corresponding to a stable fixed point. Upon noise they can burst (when crossing the SN_1 bifurcation point) and they return to the rest state. As the rest state is a sink where Jacobian has stable eigenvalues, it remains stable upon weak Ach coupling due to structural stability (Hartmann-Grobman theorem [45]). For large g_A this state can become unstable: this is because, even in the rest state Ach production is not strictly zero in the model, so, for a large enough g_A each cell experiences an increasing current which can destabilize it. When the rest state is stable, noise can trigger a burst on cell 1 say. If g_A is large enough it triggers a burst on cell 2; cells can then burst together until they return to their rest state (which occurs eventually by the mere assumption that rest state is stable). Now, the timing of bursts depends on noise intensity. If it is low, bursts occur rarely, and a neuron does not keep memory (via I_A, I_{sAHP}) of its previous state. On the opposite, if the frequency of noise triggered burst increases, cells have more tendency to synchronize. More generally the situation can be understood as follows. Fix σ and play with V_L or V_K so as to move continuously from the one bursting scenario (noise-driven) to the other (dynamically driven). Then, bursting patterns of the two cells will evolve, feeling more and more the influence of the dynamically bursting scenario and its Arnold tongue structure.

3.6 What is the probability that one cell induces bursting to its neighbour?

In the noise driven bursting regime we compute the probability that an isolated cell bursts due to noise in the presence of an Acetylcholine current $I_A = -G_A(V - V_A)$ where G_A is a free parameter. We also add an external current I_{ext} , corresponding, for example, to vary V_L by some amount δV_L around a reference value. As shown in Chapter 2, δV_L allows to tune the bursting period and to switch from noise induced to dynamically driven bursting regimes. The results presented here are preliminary as they have not been checked numerically.

3.6.1 Fluctuations about the rest state.

The cell is initially in the rest state of the Eq 3.4 given by:

$$\begin{cases} N^* &= N_\infty(V^*) \\ C^* &= \frac{H_X}{\alpha_C} [C_0 - \delta_C g_C M_\infty(V^*)(V^* - V_{Ca})] \\ S^* &= \frac{\alpha_S C^{*4}}{1 + \alpha_S C^{*4}} \\ R^* &= \frac{\alpha_R S^*}{1 + \alpha_R S^*} \end{cases} \quad (3.21)$$

where $G_S = g_{sAHP} R^{*4}$. We are characterizing noise fluctuations, around the rest state, until noise induces the burst bifurcation. As noise has a fast time scale we consider that C, S, R are constant, equal to the rest value. We focus therefore on the fast dynamics of V, N given by:

$$\begin{cases} C_m \frac{dV}{dt} &= -g_L(V - V_L) - g_C M_\infty(V)(V - V_C) - g_K N(V - V_K) \\ &\quad - G_S(V - V_K) - G_A(V - V_A) + I_{ext} + \sigma \xi \\ \tau_N \frac{dN}{dt} &= \Lambda(V)(N_\infty(V) - N) \end{cases} \quad (3.22)$$

Expanding around the rest state V^* , N^* by setting $V = V^* + \epsilon v$, $N = N^* + \epsilon n$, we obtain, to the first order in ϵ :

$$\begin{cases} C_m \frac{dv}{dt} = -g_L v - g_C [M_\infty(V^*) + M'_\infty(V^*)(V^* - V_C)] v \\ \quad - g_K [N^* v + n(V - V_K)] - G_S v - G_A v + \sigma \xi \\ \tau_N \frac{dn}{dt} = \Lambda(V) N'_\infty(V^*) v + \Lambda'(V^*) N_\infty(V^*) v. \end{cases} \quad (3.23)$$

As V^* has a low voltage we make the approximation that $N'_\infty(V^*), \Lambda'(V^*) \sim 0$ so that $n \sim 0$ to the first order. Then:

$$C_m \frac{dv}{dt} = -\mathcal{G}_0(G_S, G_A) v + \sigma \xi, \quad (3.24)$$

with:

$$\mathcal{G}_0(G_S, G_A) = g_L + g_C [M_\infty(V^*) + M'_\infty(V^*)(V^* - V_C)] + g_K N^* + G_S + G_A. \quad (3.25)$$

3.6.2 Ornstein-Uhlenbeck solution.

This equation holds true when fluctuations stay small (i.e. σ is not too big) so that the linear approximation holds. It characterizes a Ornstein-Uhlenbeck process whose solution is:

$$v(t) = \frac{\sigma}{C_m} \int_0^t e^{-\frac{(t-s)}{\tau_0}} \xi(s) ds,$$

where $v(0) = 0$ and where:

$$\tau_0 \equiv \tau_0(G_S, G_A) = \frac{C_m}{\mathcal{G}_0(G_S, G_A)}. \quad (3.26)$$

$v(t)$ is therefore Gaussian with mean zero and variance:

$$\Sigma_v^2(t) = \frac{\tau_0}{2} \frac{\sigma^2}{C_m^2} \left[1 - e^{-\frac{2t}{\tau_0}} \right] = \frac{1}{2} \frac{\sigma^2}{C_m \mathcal{G}_0} \left[1 - e^{-\frac{2t}{\tau_0}} \right] \quad (3.27)$$

3.6.3 Bursting bifurcation.

From the bifurcation diagram in the presence of noise (Fig 3.10) it is in principle possible to compute the probability that a burst starts, using the Ornstein-Uhlenbeck approximation. This is similar to the probability that an integrate and fire neuron in a rest state spikes under the influence of noise. This probability has been computed in [5]. The application of their result could give us the probability to start a burst, but we have not been able to finish this work (mathematical computation and numerical checks).

3.7 Conclusion and Discussion

In this section, we discussed in detail the modeling of the cholinergic interactions between SACs and how the parameters of the model affect the bursting characteristics of SACs. Moreover, we provided analytic results on the acetylcholine dynamics, leading to predicting analytically the critical value of the cholinergic conductance. We also show a complete one dimensional study of waves, characterizing them around as well as away from the critical regime. Before going to the next chapter, let us now discuss some points regarding the variability of cells in a network.

How identical cells can display variability in behaviour. One of the key result of this study is that SACs display bursting because they are close to a bifurcation point. As a consequence, the characteristics of bursting (IBI, amplitude) vary strongly upon tiny variations of physiological parameters such as $g_K, g_C, V_L, I_{ext} \dots$ and noise can induce huge fluctuations in their bursting period. In a network of SACs those parameters may fluctuate. Especially, the presence of acetylcholine inducing a cholinergic current impacts the bursting period as was experimentally observed by Zheng et al in [63] and confirmed by our model [2]. Therefore, a network of identical coupled SACs is expected to display a huge variability: SACs are not identical bursters. This variability has been invoked and modeled in a paper by Ford and Feller [37] where they show how it impacts the retinal waves dynamics and provide more realistic results than an homogeneous model. In their paper, inhomogeneity is inspired by recordings of several SACs exhibiting a vast variability in their bursting periods and modelled by a Gaussian distribution of IBIs and does not evolve in time.

In contrast we propose here that *(i) inhomogeneity purely results from the biophysical mechanisms leading SACs to burst; (ii) this heterogeneity evolves in space time depending on the collective dynamics (e.g. acetylcholine concentration varies in space and time and induces a variability in a given cell bursting period)*. In particular, one could have two populations of cells: one population acting as dynamically driven bursters with a well defined bursting period, and one population acting as noise induced bursters with a large variation of the period. Those populations would act in a different way on the collective dynamics of waves (see Chapter 4).

This propagation can be described, in our model, via a transport equation allowing to compute the wave characteristics (speed, size, duration) as well as the effect of sAHP on dynamics. Because of its slow time scale, quite slower than the characteristic time of the wave propagation, sAHP somewhat imprints the medium where the wave has to propagate leading to transient spatial structures observed in Ford et al. [30]. The full analysis of these aspects will be done in a forthcoming paper (see [3, 2] for a conference presentation). Already, some notions addressing this question are included in the next chapter.

Chapter 4

Modeling and simulating stage II Retinal waves in 2D

We now switch to the study of the whole system (3.4), in two dimensions. The goal of this chapter is to use our network model described by $6N$ equations, in order to address specific questions related to the underlying mechanisms of stage II retinal waves generation, propagation and disappearance. In general, the results in the current chapter are mainly theoretical, providing possible explanations for certain experimentally observed phenomena.

This work has been done in close collaboration with Lionel Gil, INPHYNI, UCA, France. Also, the numerical method for wave detection and characterization is a contribution made by Evgenia Kartsaki, Biovision team, Inria. For the model design we collaborated with O. Marre and S. Picaud, Vision Institute. This material is the subject of a journal paper '*Spontaneous emergence of spatio-temporal structure in the early retina*', which is currently under preparation.

4.1 Modeling a network of SACs

Let us define first, how we consider, the 2D modeling of a network of SACs.

4.1.1 Network structure

Stage II retinal waves propagate laterally across a network of Starburst Amacrine Cells. At this point of development the retinal circuitry is still immature and stage II waves are passively read out from the ganglion cells layer [56]. Neurons in the retinal structure are conveniently placed on horizontal lattices with lateral connections between same cell types and vertical connections inbetween different cell types layers. The layered structure of the retina, along with the immature circuitry, facilitates the topological modeling of the network of neurons.

In our modeling, we consider a single layer of cells with lateral connections. We do not consider a second layer of cells representing ganglion cells, in contrast to previous modeling work [36]. In [36], the authors needed a second layer of ganglion cells in order to filter the amacrine cells activity, accounting mainly for the difference between measured interwave intervals and the refractory period of SACs. In our model, a layer of ganglion cells would not bring anything fundamental, as the whole dynamics of burst, interburst, waves is controlled by SACs dynamics. We don't need a second

population of cells, as in [36], to tune the global activity. Furthermore, such a layer of passive ganglion cells, would not bring something fundamentally new to our analysis, except for the fact that waves on the ganglion cells layer would be a more realistic way to visualize them, if we consider that experiments with multielectrode arrays record from the ganglion cells layer. In fact, ganglion cells waves would be a subsampled projection of the wavy activity of SACs that would only be activated above a certain threshold of SACs activity, acting as a passive filter.

It is found that in the center of retina, the average distance between two distinct nearest SACs soma is about $\langle r \rangle \simeq 50 \mu m$ [21]. As the synaptic radius r_{syn} is about $300 \mu m$, the coverage factor, defined as the ratio between the synaptic surface and the hard core surface is about $\frac{\pi r_{syn}^2}{\pi \langle r \rangle^2}$. It means that each cell is in synaptic contact with about 36 neighbours, in good agreement with the experimental estimation in [63]. SACs are assumed to be fixed onto a square lattice (see Fig 4.1). In our simulations, we tested two types of connectivity:

1. The cells are in synaptic contact with 28 nearest network neighbours ¹.
2. The cells are connected to 4 nearest neighbours on a square lattice. Here the interest is to end up with a Laplacian, allowing to write a transport equation, similar to partial differential equations for waves in non linear media (see Section 5).

Furthermore, we considered a realistic type of boundary conditions with respect to the retina. In "realistic" boundary conditions, cells on the border are in synaptic contact with only those on the inner side of the lattice and any other connections in the borders are not allowed. In order to avoid boundary conditions effects, we consider a numerical box of a big size and we perform our numerical analysis in a smaller one. This way we avoid periodic boundary conditions, that could lead to artifacts with respect to wave dynamics. However, for theoretical reasons, some of our results were tested with periodic boundary conditions as well. First because they are very convenient to compute correlations, distributions of the durations and sizes of waves. Second, because it is the only way to prove that the observed pattern formation is an intrinsic non linear phenomena, not related to the retina borders. Finally, periodic boundary conditions are also very convenient for analytical investigations.

4.2 How waves are generated in the developing retina? A proposed mechanism for waves triggering

As we show in section 2.7, our model predicts two possible scenarios for the mechanism of the initial triggering of bursting; noise induced and dynamically driven bursting. In the following, we are going to analyse, the possible consequences of these two scenarios on the network and the waves triggering.

4.2.1 Scenario 1: Noise induced triggering.

For this triggering scenario, neurons are normally at rest, bursting periodically due to noise. Obviously, as in the previous case, when uncoupled, they burst independently.

¹We chose 28 neighbours instead of 36 as computed above, for geometrical reasons (see Fig4.1)

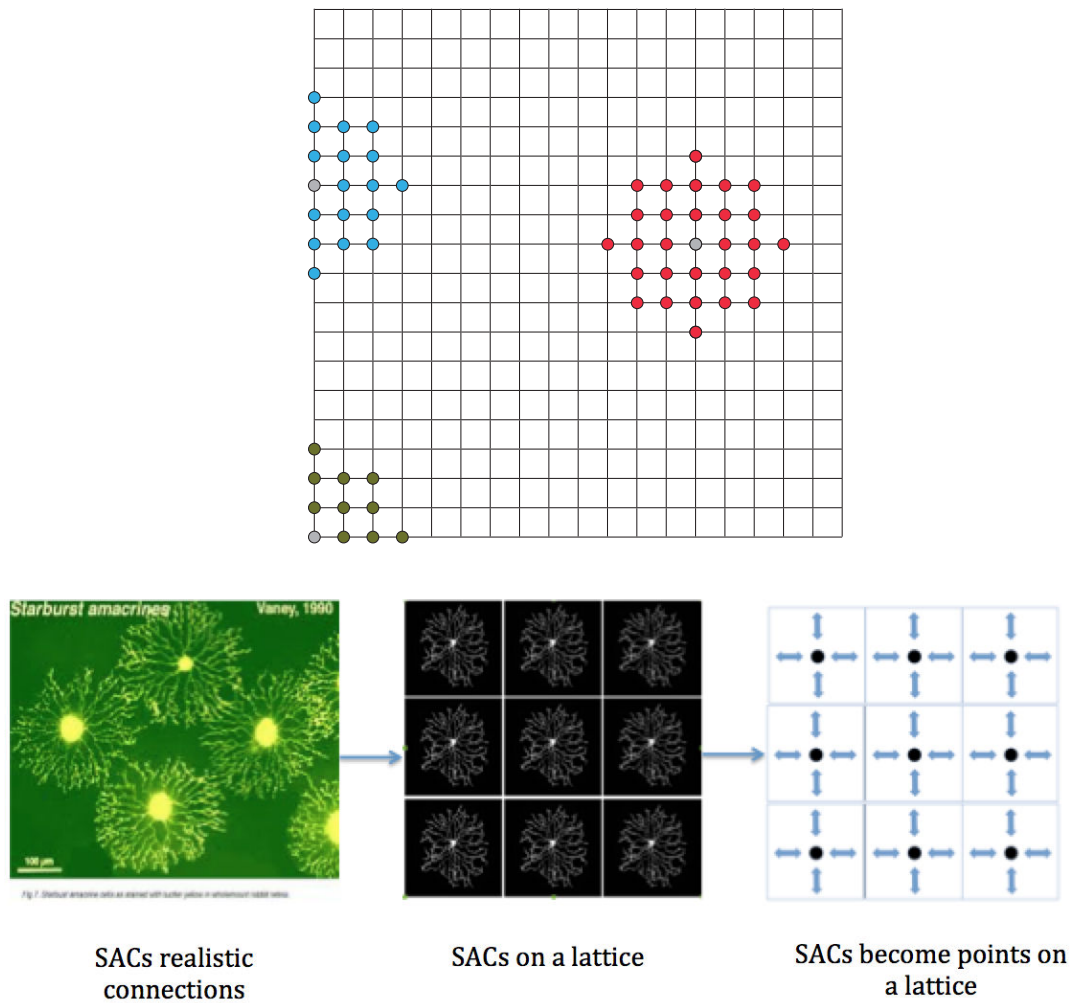


Figure 4.1: **The two connectivity schemes used in our simulations.** *Top.* Topology of the SACs network used in the numerical simulations where we used a square lattice. Also, either periodic or closed boundary conditions have been used. For the latter case, a bulk cell is in synaptic contact with its 28 closest neighbours (red), a border cell with 17 neighbors (blue) and a corner cell with 10 neighbors (green). *Bottom.* Schematic representation of how SACs realistic connectivity is modeled. In this connectivity scheme, they are connected to their 4 nearest neighbours. The strength of the coupling per contact is fixed so as cells receive the same current in both cases of connectivity a) and b).

However, when the cholinergic conductance is large enough a chain reaction is triggered when one or several neurons (neighbours) start to burst in the same period. They generate a cholinergic current which can induce bursting to their neighbours and so on. This mechanism is similar to a "forest-fire" type of modeling, studied by [54, 12] in the context of retinal waves, but also broadly studied in physics [46, 47]. This type of models are linked to critical systems, a point which has been discussed in more detail in chapter 3.

4.2.2 Scenario 2: Dynamically driven triggering.

In this case, we have N neurons which if uncoupled, burst independently. Note that their bursting characteristics are controlled by biophysical parameters of our model (mainly τ_S, τ_R) and could be considered identical or variable for each cell within a biophysically plausible interval. The role of such variability will be discussed in detail in Chapter 7.

We extend the notion of $m : n$ synchronisation introduced in section 3.5. We consider a group of R neurons, $R \leq N$. Let $m_i, i = 1 \dots R$, be integer (positive or negative) and call τ_i the bursting period of neuron i . We consider that these neurons are m_i synchronized if $\sum_{i=1}^R m_i \tau_i = 0$. This means that if these neurons were all bursting at

time t they will burst again after neuron k has bursted $m_k = \sum_{i=1; i \neq k}^R m_i \frac{\tau_i}{\tau_k}, k = 1 \dots R$.

As periods τ_i are random, with probability 1, there is no set of integers $m_i, i = 1 \dots R$ satisfying this condition. However, this condition can be loosely fulfilled, in the sense, that $\forall \epsilon > 0$ there is a set of integers $m_i, i = 1 \dots R$ such that $\sum_{i=1}^R m_i \tau_i < \epsilon$ [48]. This corresponds to approximate synchronization where neurons burst partially overlap. Thus, given a set of R *neighbouring* neurons, there will always be a time (which can be very long) after which these neurons will have overlapping bursts and therefore will be synchronized by chance.

Let us discuss now what happens when we couple the neurons in the network. After a certain time, neurons will tend to synchronize and generate a cholinergic current. The stronger the coupling, the easier neurons will produce the necessary cholinergic current to excite a sufficient number of neighbouring cells leading to synchrony and therefore wave generation.

4.3 How do waves propagate?

After studying the possible mechanisms of wave triggering, it is natural to address the question of waves propagation. It is not trivial to characterize the type of waves propagation i.e. ballistic, diffusive, singularly-diffusive etc. and for doing so, one needs to measure the relation of the instantaneous size of the wave with respect to time. The general form of a propagating wave mean radius $\langle \rho \rangle$ as a function of time reads as:

$$\langle \rho \rangle = \rho_0 + vt^z \quad (4.1)$$

where $\langle \rangle$ is the mean value, ρ_0 is the waves position of the starting wave at time $t = 0$, C is the wave velocity and z is the exponent showing the type of the propagation. For $z = 1$, we obtain a ballistic propagation, for $z = 0.5$ a normal diffusion, whereas for all other values of z we have an anomalous diffusion. In other words, a ballistic propagation means that the trajectory of the wave is linear as a function of time, whereas in normal diffusion, a wave would propagate as the square root of time. For the anomalous diffusion, the propagation is irregular and determined by the value of the exponent z . In the following, we are going to characterize the wave propagation, concluding on its type based on the value of this exponent z . Let us start by decomposing the problem in simple steps.

4.3.1 Propagation in a medium without friction

First, we consider a simple paradigm where only one cell is periodically bursting and the rest of the cells in the network are in a rest state. In this case, as soon as a wave is triggered all neurons are ready to be recruited to this wave, therefore, the propagation can be considered free in a medium with no 'friction', namely without the effect of the sAHP current (see Fig 4.2). In this paradigm, parameters are tuned so each subsequent wave is triggered after the end of the refractory period of all neurons ($\tau_S^* = 30s$, $V_L^* = -70mV$, $\tau_S = 60s$, $V_L = -72mV$). This way, we make sure that a new wave will not be stopped by refractory neurons. By this paradigm, we test the type of propagation of retinal waves in a simple scenario and compare how the type of propagation would change when the wave would propagate within a landscape profile of sAHP current.

Now, in order to quantify the type of propagation of waves in this paradigm, we compute the time dependent mean radius $\langle \rho \rangle$ accross several waves for several values of cholinergic conductances g_A . Here, since waves are radially symmetric, we perform all of our measurements along the projection of one single direction of the wave, since all of them are equivalent. More particularly, all waves start at a fixed point of the lattice and the mean radius of the wave $\langle \rho \rangle$ is computed as the distance of the wave front from the source at each time step. Note that all measurements are done for the variable C , the intracellular calcium concentration, since it is computationally more convenient to analyse the calcium dynamics, which follows a medium timescales dynamics, avoiding treating numerically the very fast time of V (order $\sim 5ms$). We simulate a square lattice of 4096 neurons for 1000s for a range of values of g_A .

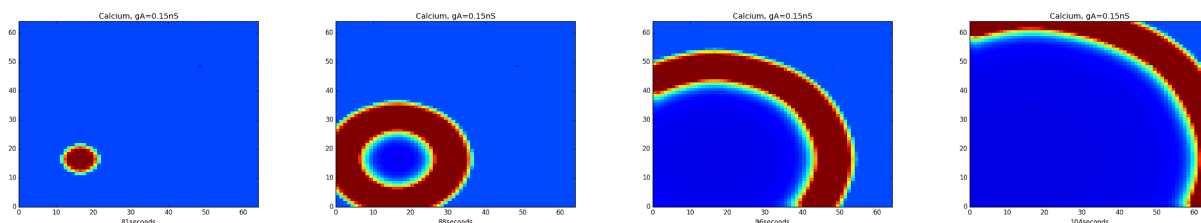


Figure 4.2: **A simulated Calcium wave, triggered every time by the same cell and propagating without interacting with sAHP profiles.** The colourbar is scaled to 0 – 500nM and the total time duration of this snapshot series is 20s.

In Fig 4.3, our numerical simulations show that the type of propagation in the network without friction changes upon the increase of g_A . Already in Eq 3.18, we predict an analytic form to estimate the critical value of g_{Am} above which waves start to emerge. This equation provides the dependence of this critical point g_{Am} , on the biophysical parameters of our model. For the 2D case g_{Am} is 0.07nS. Near the critical point g_{Am} , waves propagate more slowly and as we increase the coupling strength waves become faster. In order to quantify, how the waves speed and the type of propagation depend on the cholinergic coupling, we fit the numerically computed $\langle \rho \rangle (t)$, by the Eq 4.1, to estimate the speed v and the exponent z for each value of g_A .

In Fig 4.4, we see that indeed the speed increases upon the cholinergic coupling g_A increase. The form of this numerical curve is given by the analytic formula for the waves speed in the Eq 3.20.

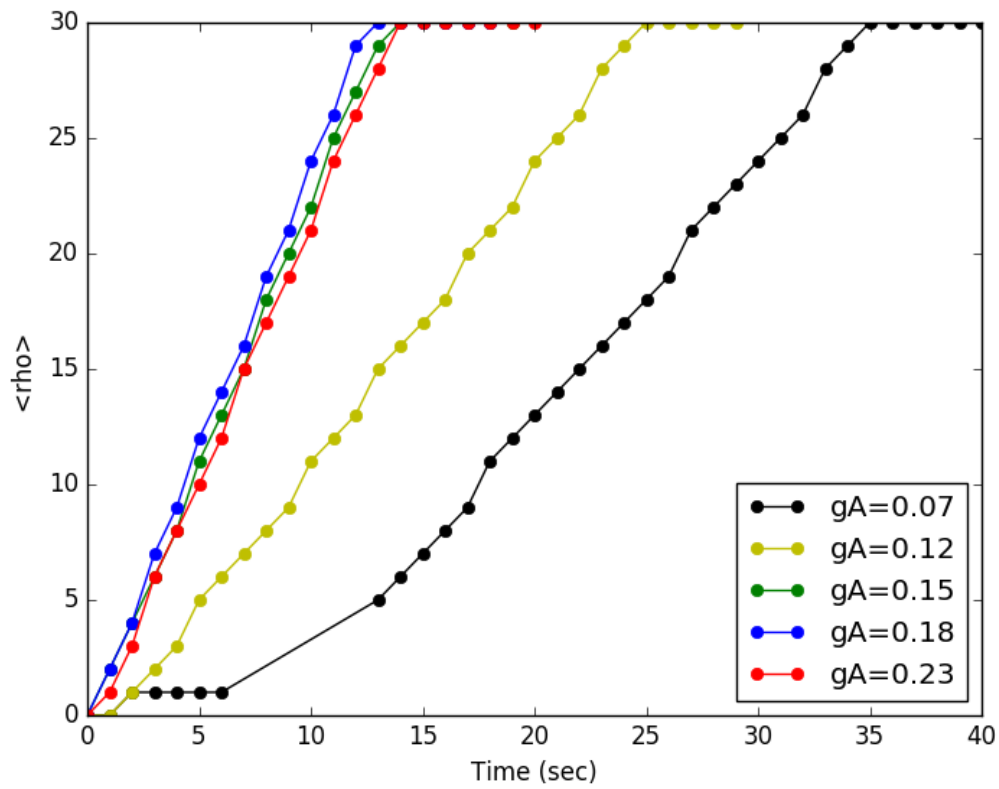


Figure 4.3: Mean radius $\langle \rho \rangle$ across several waves for several values of cholinergic conductances g_A . Waves increase their speed upon the increase of the cholinergic coupling g_A .

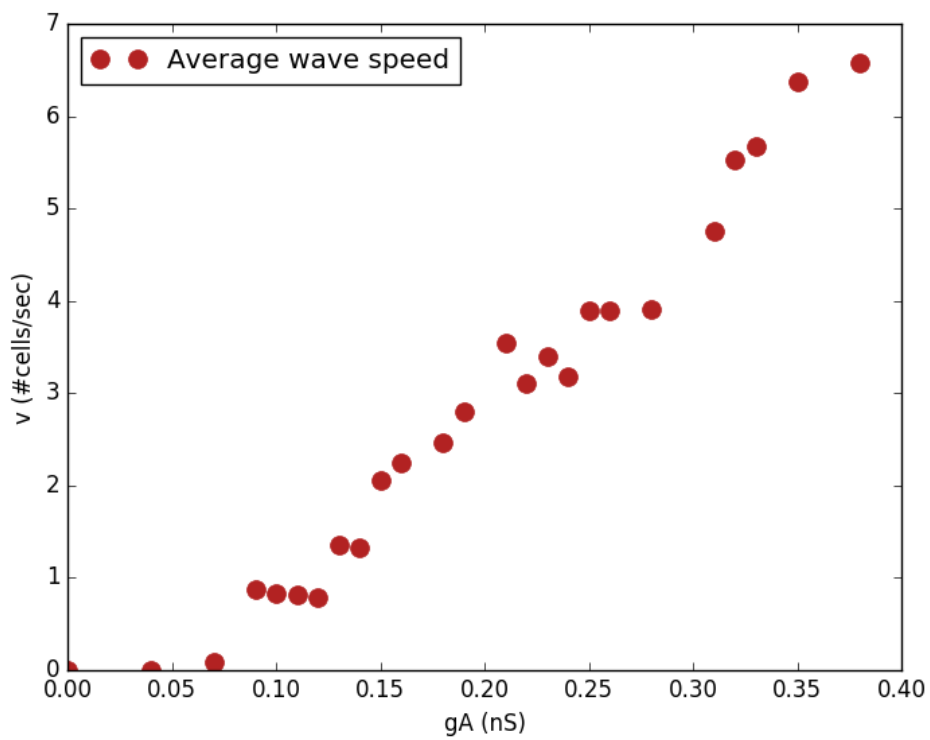


Figure 4.4: **The average speed of waves as a function of the cholinergic conductance g_A .** For $g_A < g_{Am}$ we see that there are no waves. For $g_A > g_{Am}$, we observe that the speed increases. (See also Eq 3.20 and Fig 3.12 for comparison.)

In Fig 4.5, we see that several zones of types of propagation are revealed in the parameters plane $z - g_A$. It is interesting, that around the critical point $g_{Am} = 0.07nS$, waves exhibit a super ballistic propagation, which is characterized by z exponents larger than 1. So, the propagation is faster than ballistic (super-ballistic). This means that the waves accelerate i.e. that it takes less and less time for a cell to activate its neighbours along the wave. For $z = 1$, the propagation is ballistic which means that the mean radius of the wave expands linearly with time. In the following there is a zone, corresponding to $0.2 < g_A < 0.35nS$, where waves propagate in an irregular way, exhibiting super diffusive (anomalous) propagation. Finally, the last zone, is observed for $g_A > 0.35nS$, where we have normal diffusion with z exponents around 0.5. Here the waves slow down although g_A is larger but it is not clear why. This might be due to the increase of τ_{IBI} upon the increase of g_A (as shown in Chapter 3). Please note that these results are preliminary and deserve more investigations.

It would be interesting to extend this analysis, for the full case of propagating waves within uncontrolled conditions, and it is currently under preparation. Based on this extension, we would be able to characterize the propagation of retinal waves as irregular, ballistic or diffusive, depending on the strength of the cholinergic synaptic coupling. This theoretical prediction could have a deep impact on the understanding of how waves propagate in reality. Each of these three types of propagation is linked with a different physical mechanism and elucidating this aspect would be the key to understand in more depth the underlying principles of the propagation of stage II retinal waves.

4.3.2 Propagation in a medium with an sAHP landscape

In the general situation a wave propagates in a substrate where previous waves have left a trace: after bursting SACs stay a long time in the hyperpolarized state. When a retinal wave reaches these cells it can be stopped or slowed down. Therefore, the image we have here is a wave propagation in a medium where the sAHP imposes propagation constraints. The medium has a memory and becomes non homogeneous due to its mere history. We want to analyze this effect starting from the simplest example where we control the shape of the landscape. This is also a way to check once again Eq 3.18 for the propagation speed, in a case where R varies with space. Now, we perform the same measurements regarding the mean radius $\langle \rho \rangle$ of waves for the case where we impose an sAHP landscape in the medium. Particularly, we define a radially symmetric sAHP spatial profile across the lattice (see Fig 4.6). The distance d of each point from the center is:

$$d = \sqrt{(x - x_0)^2 + (y - y_0)^2} \quad (4.2)$$

where x, y are the coordinates of a cell in the lattice and x_0, y_0 are the coordinates of the cell in the center.

All waves are generated by the cell in the center and the mean radius $\langle \rho \rangle$ is computed as the distance of the wave front from the center. By these measurements in this paradigm, we study the effect of the sAHP on how waves stop.

Based on the spatial profile of the sAHP of Fig 4.6, we define a landscape for the variable R which mainly controls the dynamics of the sAHP conductance. We remind that the sAHP conductance is given by: $G_{sAHP} = g_{sAHP}R^4$. For the R landscape, we choose to take it proportional to the $d^{1/4}$, in order to have a linear relation of the

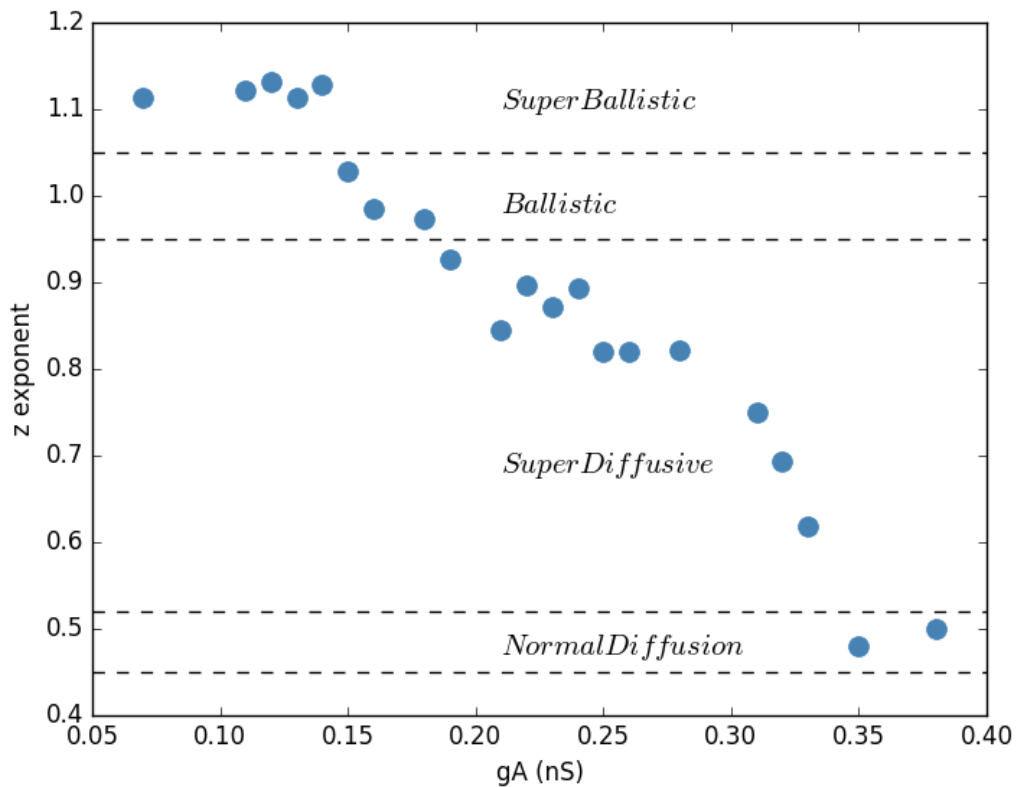


Figure 4.5: z exponent characterizing the type of the waves propagation. Around the critical point $g_{Am} = 0.07nS$, the propagation is *super ballistic*, since $z > 1$ in this regime. Then, for intermediate coupling $g_A > g_{Am}$, the propagation is *ballistic*. The next zone corresponds to a *super diffusive* propagation. For even larger values of g_A , we observe that $z = 0.5$, corresponding to *normal diffusion*.

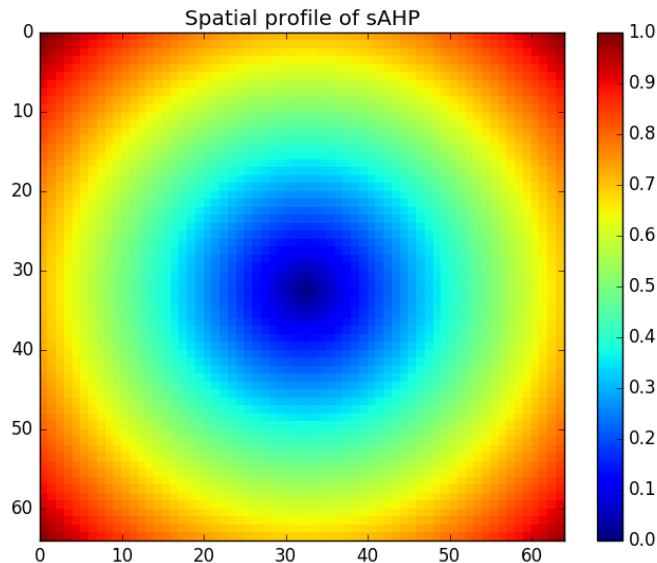


Figure 4.6: **The landscape of sAHP.** We consider a radial symmetry of the sAHP landscape where one neuron in the center is the only pacemaker of the network. The colour code corresponds to the normalized distance from the center with values from 0 to 1.

spatial profile and the sAHP conductance. Taken together, the spatial profile of the variable R is:

$$R_s = \alpha d^{1/4} \quad (4.3)$$

where d is the normalized radial distance given in Eq 4.2 and α is the coefficient of the sAHP profile taking values from 0 to 1. This parameter α will be varied in order to test the effect of sAHP on the waves propagation characteristics and shows the level of friction due to sAHP. For all the following simulations, we fixed the value of $g_A = 0.15nS$, corresponding to a ballistic regime of propagation.

In Fig 4.7, we see a series of snapshots of the evolution of the wave propagation in a linear landscape of sAHP current. The wave propagates until it reaches a characteristic length, which is controlled by the parameter α , the level of friction. Then for some time, the wave does not alter its size and therefore does not propagate further. This state changes eventually, the moment that the cells at the front of the wave, stop bursting, because they receive less current than those cells inside the wave. This cascade, continues so on and so forth, hence we have a sAHP wave propagating inwards, until it disappears completely.

In Fig 4.8, we see the mean radius $\langle \rho \rangle$ as a function of time, accross several waves for several values of sAHP friction α . As we mentioned already, we mainly distinguish three phases of the waves propagation: I) propagation phase up to a characteristic distance, II) no propagation with a wave front blocked at the characteristic distance and III) inward sAHP wave.

In Fig 4.9, we see a zoom of Fig 4.8, focusing on the regime of the wave propagation. We clearly observe that waves propagate more slowly as the parameter α increases.

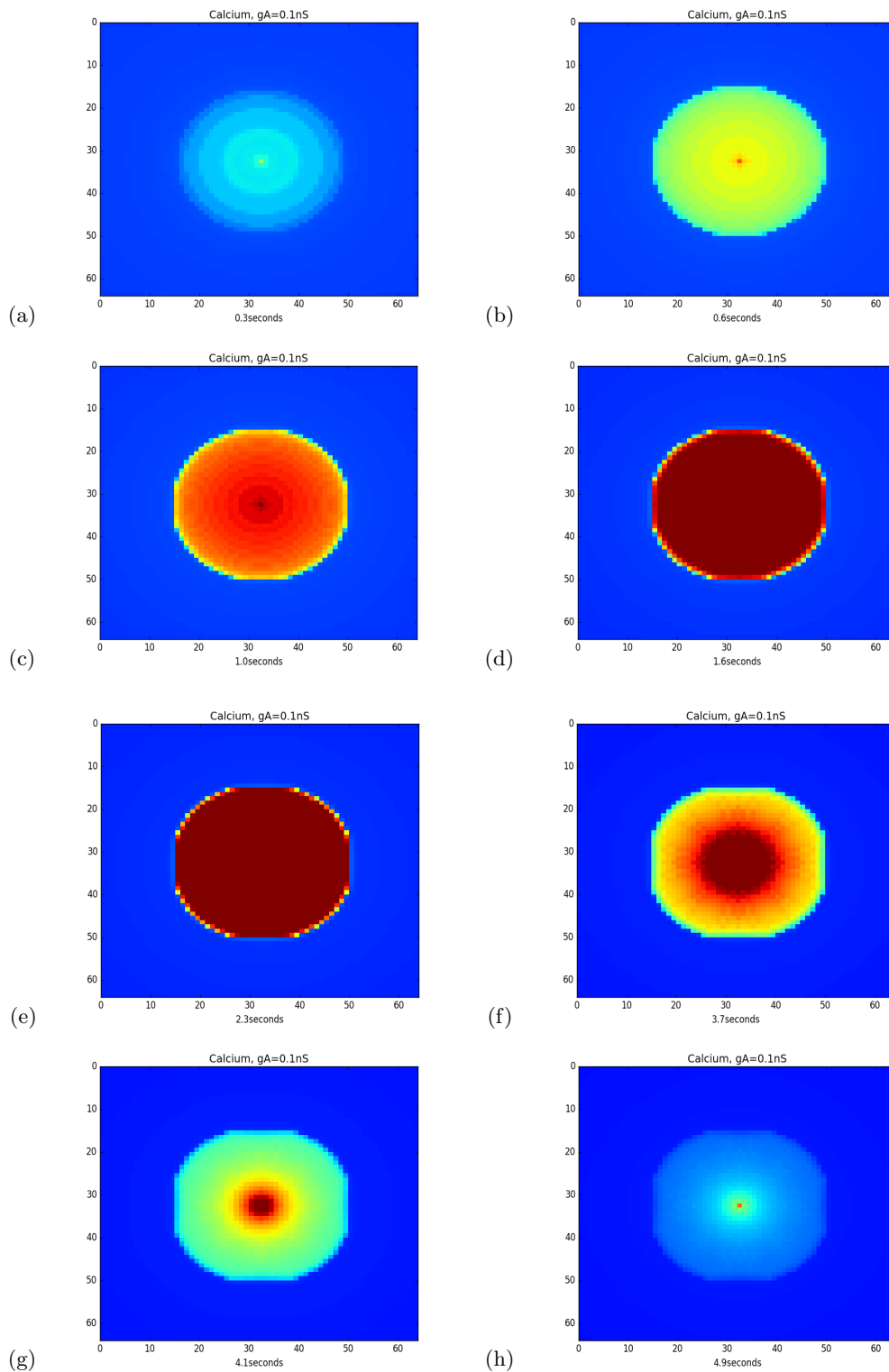


Figure 4.7: **Simulated Calcium Wave for $\alpha = 0.3$** The waves are triggered each time by the same cell and propagating while interacting with the sAHP spatial profile given by Eq 4.3. The colourbar is scaled to $0 - 500nM$ and the total time duration of this snapshot series is $5s$.

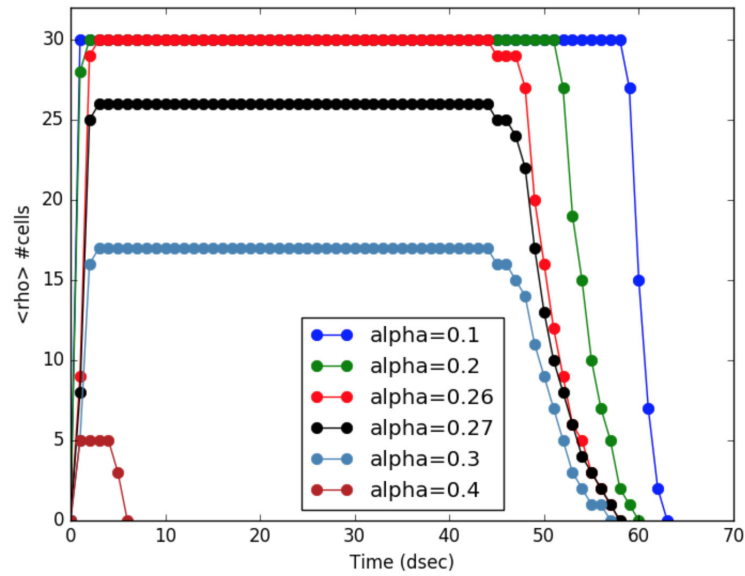


Figure 4.8: Mean radius $\langle \rho \rangle$ across several waves for several values of sAHP friction α . The radius is measured in number of cells and time in *dsec* ($1dsec = 0.1sec$).

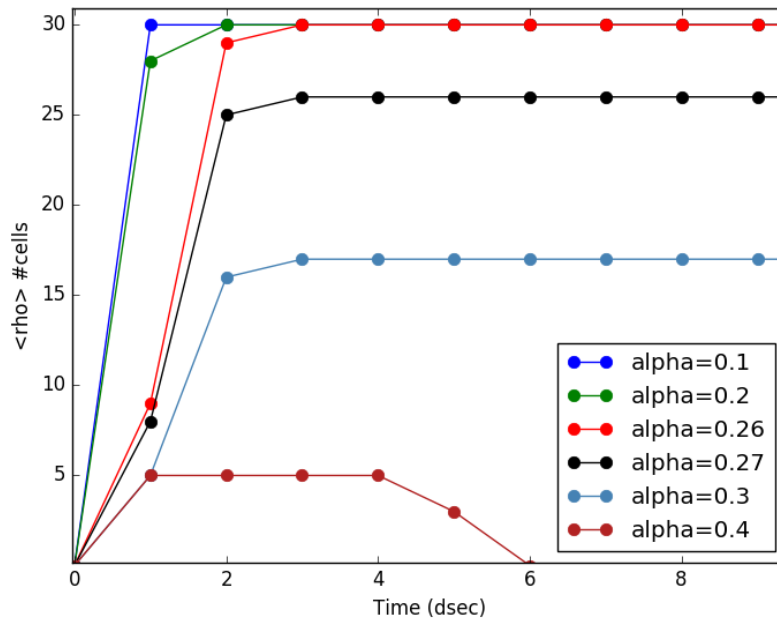


Figure 4.9: Mean radius $\langle \rho \rangle$ across several waves for several values of sAHP friction α . Waves become slower as we increase α .

In the following, we compute numerically the derivative of $\langle \rho \rangle$, from Fig 4.8, as a function of time. In Fig 4.10, we see the wave speed as a function of time for several values of the parameter α . We observe that during phase I of propagation, waves decelerate due to the effect of sAHP, and the strongest the sAHP, the fastest they

decelerate. During phase II, waves have zero speed, as they do not propagate, having reached their characteristic length. This phase is controlled by the equilibrated dynamics of the sAHP and the cholinergic coupling. When this equilibrium is lost, an inward wave starts to propagate, accelerating at first, reaching a maximum speed (negative because of the opposite direction) and decelerating until its complete disparition.

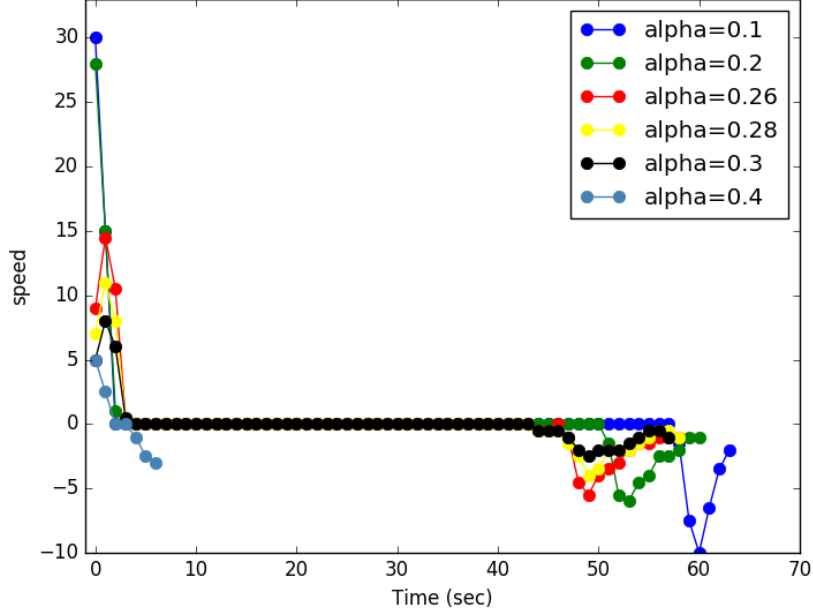


Figure 4.10: Mean speed $\langle v \rangle$ across several waves for several values of sAHP friction α .

We are currently working on the characterization of the type of propagation inside a linear sAHP profile.

Analytic characterization of the wave propagation in a sAHP profile. For a cell at position (x, y) with a R value $R(x, y)$ this means that its voltage $V(x, y)$ has to obey Eq3.11, 3.21. A way to achieve this state is to iterate the dynamics for some transient with $\frac{dR}{dt} = 0$.

In this situation we expect that $t_B(x, y)$ depends on x, y via the equation:

$$t_B(x, y) = -\frac{1}{\mu'} \cdot \log \left[1 + \frac{1}{g_A} \frac{2 \mu' \sqrt{\gamma_A}}{n \beta \Omega} \frac{I_{SN} + g_S R^4(x, y) (V_-(x, y) - V_K)}{V_-(x, y) - V_A} \right]$$

Especially, the wave stops ($t_B(x, y) \rightarrow \infty$) for those points x, y such that:

$$\frac{1}{g_A} \frac{2 \mu' \sqrt{\gamma_A}}{n \beta \Omega} \frac{I_{SN} + g_S R^4(x, y) (V_-(x, y) - V_K)}{V_-(x, y) - V_A} = -1,$$

i.e.

$$R^4(x, y) = -\frac{1}{g_S (V_-(x, y) - V_K)} \left(I_{SN} + \frac{n \beta \Omega g_A}{2 \mu' \sqrt{\gamma_A}} (V_-(x, y) - V_A) \right).$$

which requires, to have a solution, that $I_{SN} < -\frac{n\beta\Omega g_A}{2\mu'\sqrt{\gamma_A}} \frac{V_-(x,y)-V_A}{V_-(x,y)-V_K}$.

Remark. A useful approximation is to assume $V_-(x, y)$ constant.

Example: $R^4(x, y) = \alpha\rho$, with $\rho = \sqrt{(x - x_c)^2 + (y - y_c)^2}$ where x_c, y_c are the coordinates of the wave source cell. For our parameters values this gives:

$$\begin{aligned} \rho &= -\frac{1}{g_S (V_-(x, y) - V_K)} \left(I_{SN} + \frac{n\beta\Omega g_A}{2\mu'\sqrt{\gamma_A}} (V_-(x, y) - V_A) \right) \frac{1}{\alpha} \\ &\sim -\frac{1}{10 \times (-65 + 90)} \left(0.3 + \frac{2 \times 5 \times \Omega \times g_A}{2\mu'} (-65) \right) \frac{1}{\alpha} \\ \rho &\sim -\frac{1}{250} \left(0.3 - 325 \frac{\Omega}{\mu'} g_A \right) \frac{1}{\alpha} \end{aligned} \quad (4.4)$$

In a square lattice of edge length L the maximal value that ρ can reach is obviously $\rho = L$. As discussed already, due to the sAHP profile, waves have a maximal characteristic length $\rho_{max} < L$. We measure $\rho_{max} < L$ for each value of α to show how sAHP affect the maximal size of waves. Then, we fit the values of ρ obtained numerically with the analytic form in Eq 4.4. These results need further investigations as we obtain the right form of the curve but there is a multiplicative factor that we don't understand yet.

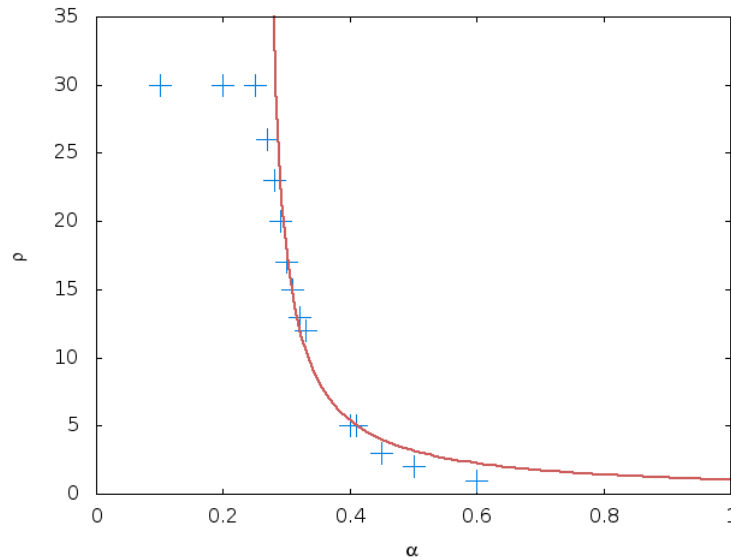


Figure 4.11: **Values of the maximum ρ obtained with $g_A = 0.15$ nS in a sAHP current growing linearly** with the distance to the waves source cell (center) (blue points) and fit with the analytic prediction (red line).

4.4 Distribution of waves near the critical point.

As we have seen before, there is a critical point for g_A before which waves cannot propagate. This is because the total current cannot exceed the bifurcation threshold. However, close to that point, in the presence of noise, noise fluctuations can trigger

the bifurcation and let the wave propagate. In addition, in the general case, wave propagates in a substrate of sAHP resulting from previous waves and acting on their propagation. Finally, when several propagate at the same time they can interact and collide. Here we want to study these effects in some details.

One wave. We begin with the case where the wave starts at the center and propagates in a flat R profile. Without noise, for $g_A < g_{A_c}$, there is no propagation, whereas, for $g_A > g_{A_c}$ the propagation is ballistic. If we add a bit of noise we expect the propagation to be non ballistic near the critical point g_{A_c} : for $g_A < g_{A_c}$ noise can favour the bursting of the next cell, whereas, for $g_A > g_{A_c}$, noise may delay the bursting of the next cell. Therefore, we expect, in general, a propagation of the form:

$$x(t) = v (t - t_0)^z + x_0, \quad (4.5)$$

In Fig 4.12 we show several examples of 1D waves generated this way, together with a fit of v, z . The main observation is that, near the threshold; wave stops at random points. Also, due to noise, waves can appear spontaneously. That's why, in Fig. 4.12 we choose a low level of noise, to avoid multiple waves.

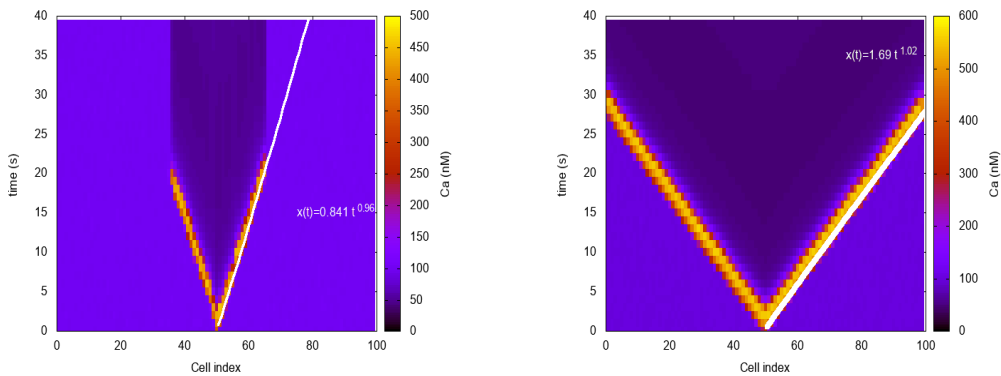


Figure 4.12: **Example of propagation near the g_A critical point, in the presence of noise.** In color is shown the calcium concentration. The white line corresponds to a fit of Eq 4.5 with linear regression on the log. Left: 100 cells, $g_A = 0.035$ nS, $\sigma = 4$ pA ms $^{-\frac{1}{2}}$; Right: , $g_A = 0.1$ nS, $\sigma = 3$ pA ms $^{-\frac{1}{2}}$. The critical point is $g_A \sim 0.04$ nS. .

Non direct interaction between waves. We then investigate the wave propagation near the critical point, and more generally, when g_A varies, for non interacting waves. To avoid waves interaction we take a low level of noise (to avoid spontaneous waves generation), $\sigma = 3$ pA ms $^{-\frac{1}{2}}$. We select a cell at random and inject a short (0.1 ms) pulse of voltage raise (50 mV). We do this every second until a wave starts. Then we let the wave propagate. At the end of the wave, we start again exciting randomly cells, until a new wave starts again, and so on. In this way, we are close to the "adiabatic" conditions of excitations used in SOC models. We record the activity after a transient of 200 s.

In fig. 4.13 we show the wave propagation for different values of g_A . The main observations are:

1. Due to noise, the symmetry left-right is broken. A wave can stop abruptly at some point.

2. Even if there is no direct wave interaction there is an interaction via the sAHP landscape. Especially, *even if we choose randomly uniformly the initial cell, wave is more likely to appear in regions where sAHP is lower. There is therefore a memory effect which lasts longer than the sAHP period.*

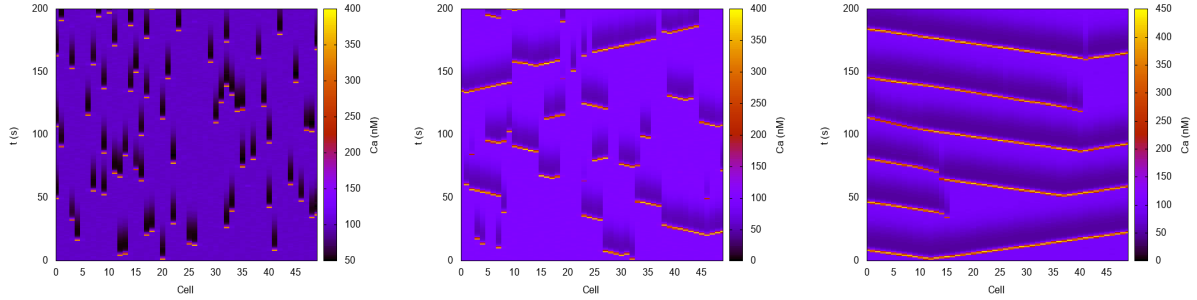


Figure 4.13: **Example of propagation for non interacting waves, near the g_A critical point, in the presence of noise ($\sigma = 3 \text{ pA ms}^{-\frac{1}{2}}$) for 50 cells.** Left: $g_A = 0.04 \text{ nS}$; Middle: $g_A = 0.06 \text{ nS}$; Right: $g_A = 0.1 \text{ nS}$.

For each wave we compute:

1. **Calcium correlation** between the central units 0 and the other units i , i.e.

$$C_{0,i} = \frac{\langle C(0,t)C(i,t) \rangle - \langle C(0,t) \rangle \langle C(i,t) \rangle}{\sigma_C(0)\sigma_C(i)}, \quad (4.6)$$

where $\langle \rangle$ denotes the time average, and $\sigma_C(i)$ is the mean square deviation of calcium concentration at cell i (see Fig. 4.14). We observe:

- (i) A breaking of symmetry left-right which presumably due to our procedure. Correlations here are computed on one trajectory and the sample (2000 s) is apparently not long enough.
- (ii) Correlation vanishes for low g_A values and then becomes negative. The point where it vanishes defines a correlation length ξ_C .

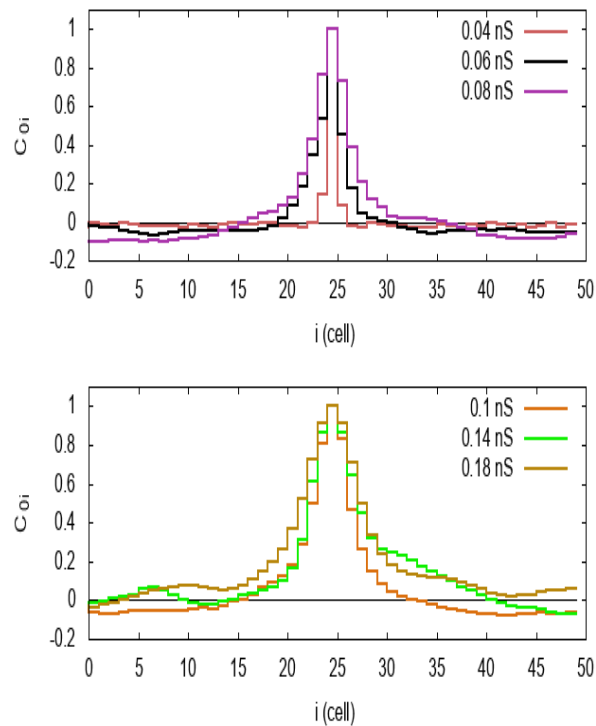


Figure 4.14: Calcium correlations as a function of distance for several values of g_A .

2. The Histogram of the total current during a burst (Fig. 4.15). We observe:

- (i) The current has a long negative tail (corresponding to the sAHP influence) and a peak near the maximum.
- (ii) The maximal value (also shown in Fig. 4.15) crosses I_{SN} for $g_A = 0.058$ close to the predicted critical point. This suggests that the bifurcation is driven by the maximum value of the current.
- (iii) This maximum grows like g_A^α with $\alpha \sim 1.56$.

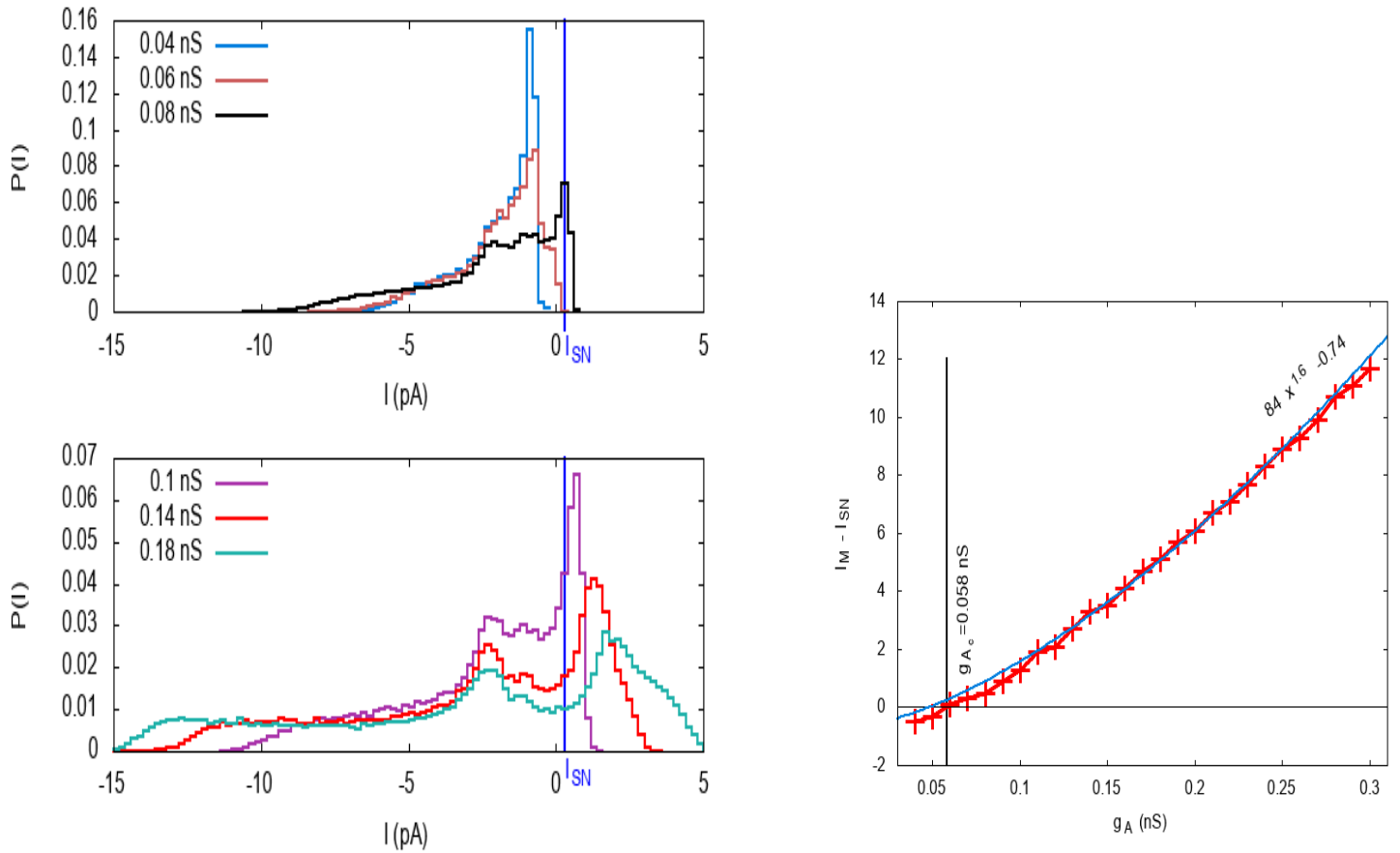


Figure 4.15: **Left.** Histogram of the total current within a burst. The vertical line is the value for I_{SN} . **Right.** Value of the maximum current during a burst minus I_{SN} .

3. The histogram of z and v where, for each wave involving more than 5 cells, we fit these quantities and compute their probability distribution. From this, we compute the mean and variance of z, v (Fig. 4.16). We observe:

- (i) The dynamical exponent is constant $z \sim 1.1$ (the value obtained at $g_A = 0.05$ might be not reliable as it corresponds to only one sample). It is slightly above ballistic transport.
- (ii) The speed v increases in agreement with eq. 3.20 provided one fits Ω and the constant C . Compared to the case with 2 bursting cells, we have a Ω smaller (0.05 compared to 0.2 in the 2 cells case).

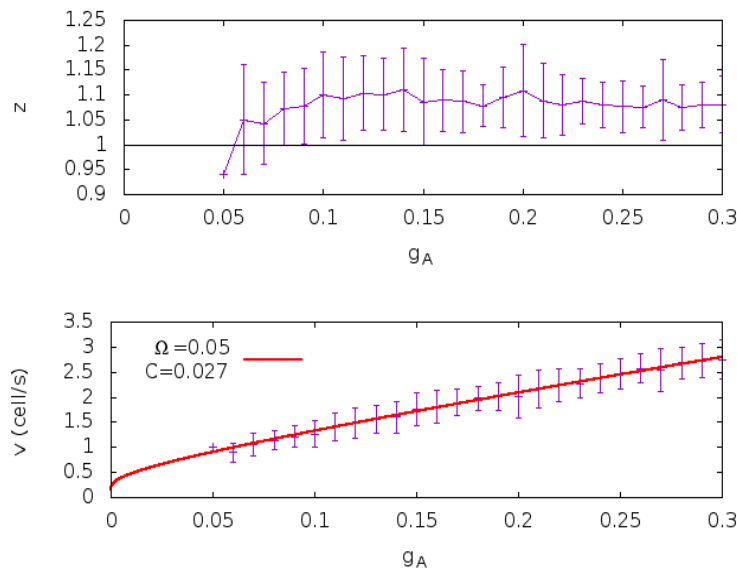


Figure 4.16: **Top.** Dynamical exponent z as a function of g_A . **Bottom.** Speed v as a function of g_A and fit with Eq (3.20).

4.5 Modeling the dynamical changes occurring within stage II retinal waves

4.5.1 How does the cholinergic conductance evolves during development?

As discussed already throughout this thesis, during development and especially in the case of retinal waves, transient processes occur, networks change their functionality and synapses that are no longer used get replaced. However, these transient processes change dynamically also within each stage of retinal waves, especially stage II. In this stage, the cholinergic excitatory connections between SACs degrade and eventually disappear around the onset of stage III waves [62]. This point in time, usually counted in postnatal days, varies across species but its existence is generic. In the work of [62], the authors measured the peak cholinergic responses of SACs, in rabbits, upon the application of acetylcholine puffs (1mM). Note that these recordings were made in the presence of 0.5-1mM of cadmium (Ca^{+2}), which blocks all Ca^{+2} dependent transmissions and therefore no external input would activate the nicotinic receptors. Consequently, this experiment measures the efficiency of the nicotinic receptors by measuring the induced cholinergic currents exclusively mediated by the acetylcholine puffs. It is shown in Fig 4.17 (Figure 3B in [62]) that the cholinergic current responses of SACs decline upon maturation. In particular, we observe that cholinergic nicotinic receptors are formed before birth and are already at their maximum efficiency before stage II phase starts (for rabbits this is around E29). We also see that cholinergic currents significantly decline around P6 in rabbits, coinciding with the loss of excitability of SACs. This is a strong signature of the switch occurring to the transient network of SACs functionality, in later stage waves.

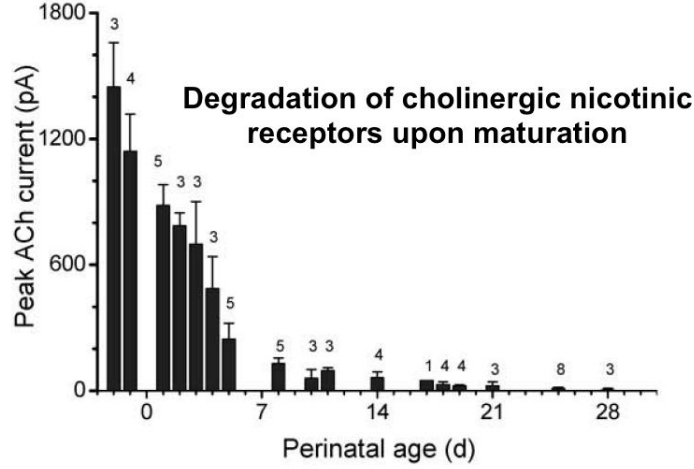


Figure 4.17: Age dependent decline of peak current responses of starburst cells to ACh puffs (1 mM) in the presence of $0.5 - 1mM Cd^{2+}$. The numbers of cells tested are shown above the histogram. (Figure 3B from [62])

In order to follow these dynamical changes, we use our model to estimate the evolution of cholinergic conductance based on the experiment of [62] as shown in 4.17. We assume that the fraction $\frac{A^2}{A^2 + \gamma_A^2}$, modeling the nicotinic receptors activation, is equal to 1, since during the puff of acetylcholine, receptors are considered to be saturated. Also, we make the assumption that the reversal potential $V_A = 0mv$ does not change upon maturation. After these two assumptions, the expression to describe the current response to cholinergic puffs reads as:

$$I_{A_{puff}} = -g_A V_{clamp} \quad (4.7)$$

Now if we assume that SACs are voltage-clamped during the puff at the rest state, then $\sim V_{clamp} = -70mV$. In order, to compute the evolution of the cholinergic conductance upon maturation, it suffices to extract the maximum peak values of the current responses from Fig 4.17 and multiply them by the potential. Assuming that the maximum cholinergic current response is $I_{A_{puff}}^{max} = 1400pA$, then $I_{A_{puff}}^{max} / V_{clamp} = g_{A_{max}}$, which gives $g_{A_{max}} = 0.017$ per synapse.

From this experiment and Eq 4.7 we are therefore able to roughly extrapolate the evolution of g_A during stage II. We now study how this evolution impact the retinal waves dynamics.

4.5.2 Different spatiotemporal patterns emerge within stage II retinal waves

In [53], a thorough study of the characteristics of retinal waves is performed for all three consecutive stages. In particular, in mice within stage II phase (P3-P10) exhibit a vast variability in waves characteristics such as size, duration, frequency and speed. This experimental observation suggests that *within* stage II, there exist underlying transient processes which result in this variability. In the biological literature, some of those processes are already known such as the degradation of nicotinic cholinergic

receptors upon maturation within stage II waves or the change in the excitability properties of SACs due to cellular mechanisms (see Chapter 1). However, it is not yet confirmed how these changes exactly affect waves within the stage II phase and what would be the implications on the way a transient network operates during a window in development and what could be the mechanisms explaining the wide variability of wave characteristics within stage II. This variability can of course result from the variability in the cells characteristics themselves. This was proposed by [30], where they introduce, in the Hennig et al. model [54], a distribution of sAHP time characteristics resulting in a variation in cells interbursts. They argue that this improves the model in reproducing experimental stage II retinal waves. However, this distribution appears quite ad hoc. Here we would like to propose a more natural mechanism for variability resulting directly from dynamics, in a network of perfectly identical cells.

In order to address this type of question, in our model we vary the strength of the cholinergic coupling by modifying the conductance g_A (see Fig 4.19). As we did in the previous section, but here in 2D, in the realistic conditions where waves interact and leave a trace of their propagation. For a large value of coupling strength spatiotemporal patterns appear to be larger covering the whole lattice. In this case cells tend to be more synchronized leading to the generation of larger waves. In contrast, when the coupling is very weak, the cells do not receive enough excitatory input to get synchronized and therefore no propagating waves are generated. Note that there is a threshold of g_A after which small local bumps of activity are formed without exhibiting propagation. We observe that there exists an intermediate regime for which waves exhibit a large variability of size leading to a mix of types of generated waves which corresponds qualitatively to the characteristics of the experimentally observed waves. In Fig 4.19, we show the different spatiotemporal patterns of the intracellular calcium concentration (variable C) that can be produced by our equations varying the strength of the coupling g_A . Note that in this simulation we use $N = 10000$ cells on a lattice and each cell has 28 neighbours.

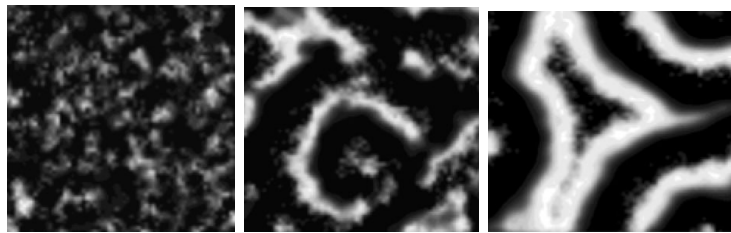


Figure 4.18: **Simulated Calcium waves** **Left.** Weak. **Center.** Moderate. **Right.** Strong Cholinergic coupling. The spatial resolution is 100x100.

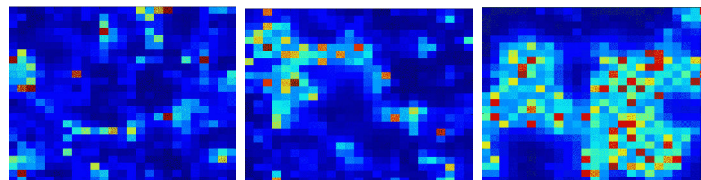


Figure 4.19: **Simulated retinal waves: Voltage patterns.** **Left.** Weak. **Center.** Moderate. **Right.** Strong Cholinergic coupling. The spatial resolution is 25x25.

4.5.3 Spatial Correlations reveal a characteristic size for stage II waves

In order to quantify the effect of different spatiotemporal patterns upon the variation of the cholinergic coupling we compute the spatial pairwise correlations averaged in time for several values of the cholinergic conductance g_A (see Fig 4.20) as follows:

$$C(d) = \frac{(\langle C(r, t)C(r + d, t) \rangle - \langle C(r, t) \rangle \langle C(r + d, t) \rangle)}{\sigma_r \sigma_{r+d}} \quad (4.8)$$

where C is the calcium concentration, r the radial coordinate (in polar coordinates), d the distance between cells, t time. $\langle \rangle$ corresponds to time average. σ_r is the mean standard deviation at point r .

We assume here rotation invariance, i.e. the cell located at r is far from the boundaries. This also implies that $r + d \ll L$ the lattice dimension.

As expected, for weak coupling spatial correlations extend to small distances which indeed result in local bumps of activity. For stronger coupling, we observe correlations that would reach the size of the lattice, explained by the large waves observed in this case. Interestingly, for the intermediate regime of coupling, we observe a positive correlation at short distances and a negative one at larger distances. That means that when certain neurons fire, the ones at a specific distance d where anticorrelations are observed are refractory. This observation gives a measure of the characteristic size of waves for a given strength of cholinergic coupling. These negative correlations mean that the waves stop where it encounters a refractory region (or collides with another wave). Hence, on average, the distance where correlation becomes negative gives the characteristic wave size. In our case, the characteristic size of stage II waves is shown to be ~ 15 cells. In order to compute the actual distance in mm we need to take into account the intercellular distance considered at $50\mu m$ so that would give $50 \times 15 = 750\mu m$. To have a rough estimation about the characteristic area of stage II retinal waves, if we assume radial symmetry, our model predicts a range of $\sim 0.56 - 1.68 mm^2$.

4.6 Characterizing the SACs population activity and the features of retinal waves

4.6.1 Possible phase transition on the population firing rate

In order to characterize the population activity, we are in need of an order parameter² of the network of SACs. In our case, we measure the average population firing rate with respect to the strength of cholinergic coupling. We use the calcium concentration, since it is a good indicator of the presence of a wave (actually used experimentally). For isolated spikes, the local calcium concentration slightly rises and falls with time. On the contrary, during the passage of a retinal wave, it reaches much more higher values, since the load of calcium increases when V stays longer on the upper branch, which happens during a wave. We introduce the state function of the SACs (i, j) as

$$B_{i,j}(t) = \begin{cases} 1, & \text{if } C_{i,j}(t) > C_{th}; \\ 0, & \text{otherwise.} \end{cases} \quad (4.9)$$

²An order parameter distinguishes two different phases, in physics.

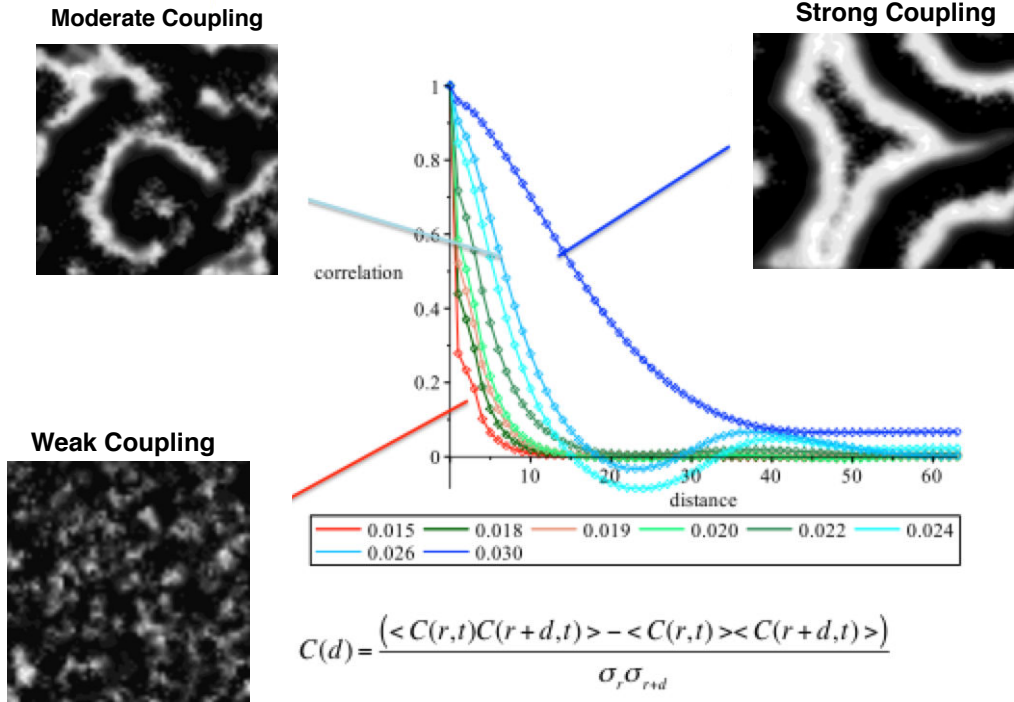


Figure 4.20: **Correlations with respect to cells distance for various values of the cholinergic conductance.** Three distinct regions are observed in the correlations linked with a different spatiotemporal pattern. *Insets.* Simulated calcium waves corresponding to each regime of coupling.

where C_{th} is an arbitrary threshold values that we select high enough to undoubtedly identify a wave $C_{th} = 2C_0$. Then:

$$FR_G(t) = \frac{1}{n} \sum_{i,j} B_{i,j}(t) \quad (4.10)$$

stands for the fraction of the total number of SACs which are involved in any retinal wave at time t and will be named "global firing rate". n is the number of cells. For long enough simulations, $FR_G(t)$ fluctuates around a constant, well defined average value $\langle FR_G \rangle_t$. Fig.4.21 displays the evolution of average global firing rate $\langle FR_G \rangle_t$ versus the coupling strength g_A . A transition zone is clearly evident, with a sharp increase of $\langle FR_G \rangle_t$ for $g_A \geq g_{Ac}$.

4.6.2 Distribution of waves size and duration, Power laws, Criticality

Waves statistical features

Having as a goal to quantify how the statistical features of waves change as upon the variation of the cholinergic coupling, in Fig 4.22 and 4.23, we report on the distribution of waves durations and waves sizes for various values of g_A . In this numerical experiment, because of the finite size of the observation window, some assumptions

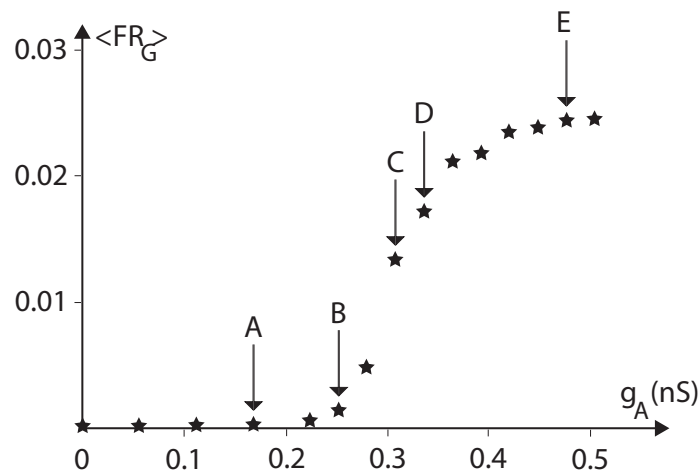


Figure 4.21: **Evolution of the average global firing rate ($\langle FR_G \rangle_t$) with the coupling strength g_A .** The capital letters (A,B,C,D,E) point to some selected values of g_A that we will focus on later. They correspond respectively to $g_A = 0.168, 0.252, 0.308, 0.336, 0.476$ nS per cell with 28 neighbours.

have to be done. For example, the features of waves that appear or disappear at the observation window without having finished, are impossible to compute. For this reason, here, we use periodic boundary conditions, leading to perfectly identification of our numerical waves. Waves durations are computed as the total time duration of wave followed from the beginning until its end. Waves sizes are computed as the total number of cells having participated in the wave during its duration. Splitting and merging waves are dealt with as events belonging to the same wave. Also, note that the following numerical simulations are done in the noise driven bursting regime.

In Fig 4.22 and 4.23, we observe that waves durations and sizes follow exponential distributions for the weak coupling regime *A*. For the moderate coupling regime *B* and *C*, we observe power-law like distributions, indicating that there might be a critical regime for the system. Also, the characteristic size area revealed by this analysis is $S^* = 200$ cells, which interestingly corresponds to the characteristic size found in Fig 4.20, where $d^* = 15$ cells leading to $S^* = d^{*2} = 225$ cells for a wave area. Note that, there has been a preliminary indication, of power-law distributions and critical regimes in the work of [54]. Finally, in the strong coupling regime *E*, we observe a mixed exponential and power law distribution for both waves durations and sizes.

4.7 Pattern formation in the dynamically driven bursting regime

We now study the structure of the spatio-temporal dynamics corresponding to the dynamically driven bursting scenario. In Fig 4.24, we display the instantaneous values of the variables involved in Eq 3.4. A first obvious remark is that the spatial patterns associated with the fast variables V and N are of smaller size than those of the other variables. This is because the instantaneous picture detects mainly the highest values associated with the spike activity, and is less sensitive to their time average. Note also

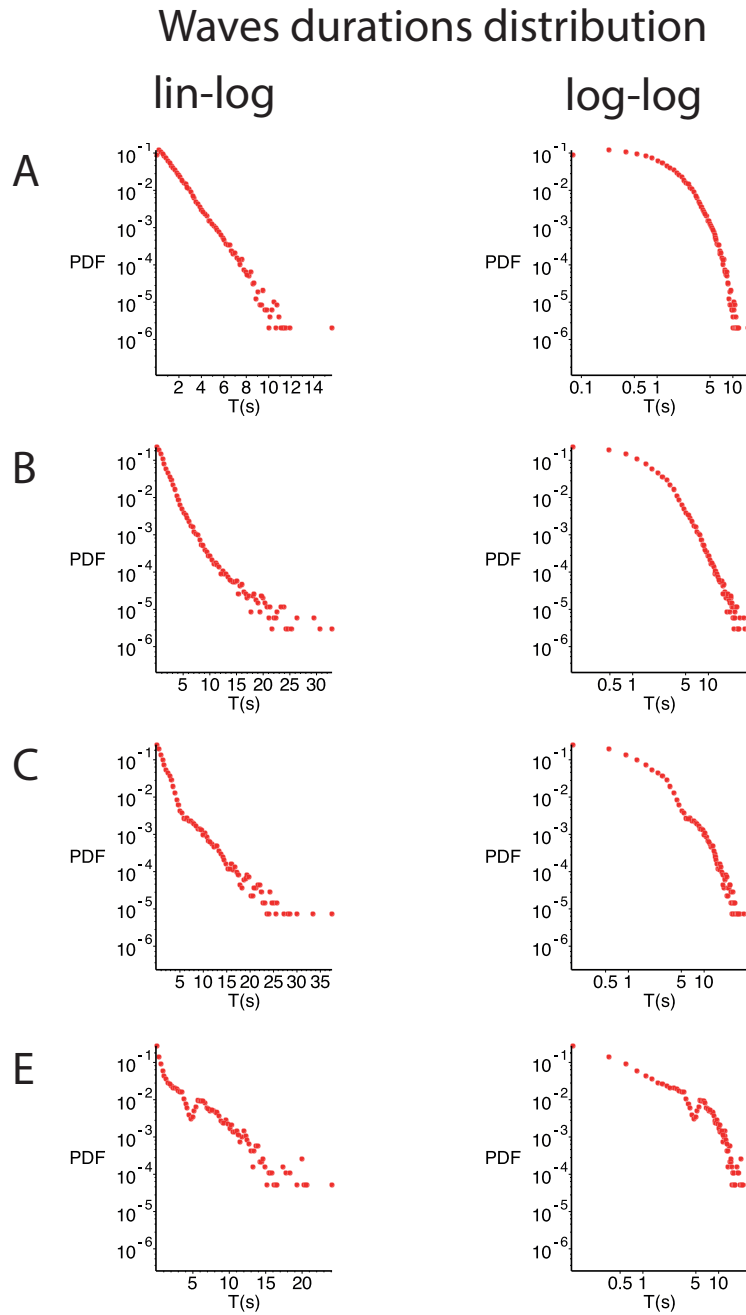


Figure 4.22: **Distribution of the waves durations, in linear-log plot (left column) and in log-log plot (right column).** The capital letters refer to the parameter regimes pinpointed in Fig 4.21.

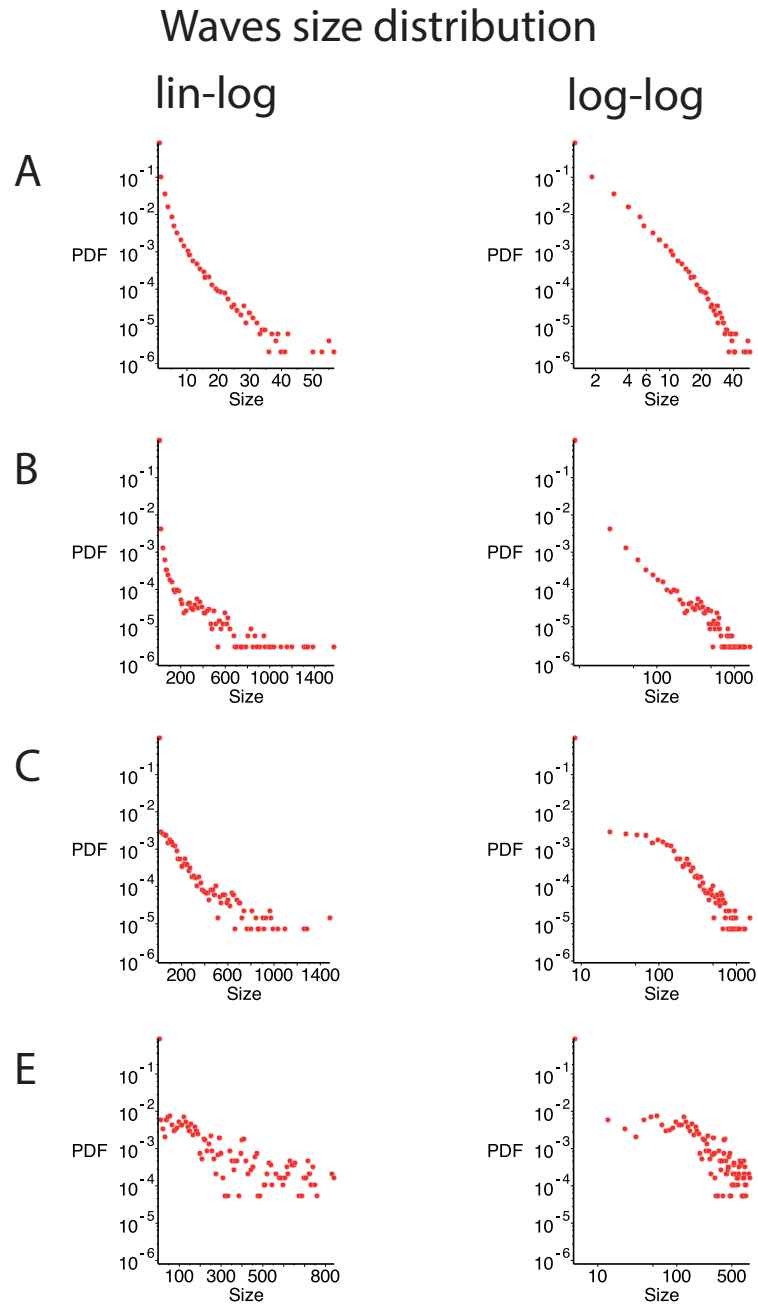


Figure 4.23: **Distribution of the wave size, in linear-log plot (left column) and in log-log plot (right column).** The capital letters refer to the parameter regimes pinpointed in Fig 4.21.

that the instantaneous spike activity is not homogeneous, but consists of clusters whose positions are clearly visible in the C and A plots. Finally R and S are associated with a spatial patchwork, whose elements, although irregular, seem to possess a well defined typical size. In Fig 4.25, the areas enclosed by the continuous white line (R and A) in Fig 4.24 are enlarged by a factor of 2. We first remark that high A activity and high value of C indeed correspond to *propagating waves* and not to other type of spatio-temporal patterns, such as bumps, standing waves etc. This analysis also reveals that propagating waves are clearly spatially bounded in specific areas, controlled by the blue R patches. This reveals, that there exist emerging spatio-temporal patterns, in which retinal waves are allowed to propagate.

We illustrate this, in Fig 4.26, where we show a typical time evolution: inside the continuous white line which surrounds an area of low R (not shown), waves start in two places ($t = 2.75$), propagate ($t = 5.50$) until they reach the border and disappear, leaving only a single wave ($t = 8.25$). Then this wave propagates ($t = 11.00, 13.75, 16.50$) until it reaches the border ($t = 19.25$) and disappear ($t = 22$). Then the whole sequence repeats itself almost identically starting from ($t = 0.00$). Therefore 3 spatial scales can be identified: the smallest one is associated with the spike activity (\simeq size of a cell), the medium with the spatial extension of the wave (\simeq size of a the excitable front), and finally the largest one with the sAHP dynamics (\simeq typical size of the R patchwork). The slowly varying R areas are natural candidate to play the role of the controlling the emerging domains.

A similar observation has been made in the one dimensional study of the dynamically driven regime, where in Fig 3.14, we see that 1D waves are bounded at a specific distance, especially for stronger coupling, which remains almost constant during a time scale of ~ 100 periods. We believe, that what we observe here, is an extension of the 1D case in the dynamically driven regime. We also believe, that the mechanism behind these patterns formation, is mainly the deterministic periodic dynamics of sAHP that create a mosaic of 'forbidden' areas for waves propagation leading to spatio-temporal patterns formation.

4.8 Conclusion and Discussion

In this section, we discussed in detail the two dimensional study of the spatio temporal dynamics of stage II retinal waves. Using our model, we were able to adress the questions on how waves propagate and stop, providing theoretical predictions on the mechanisms controlling the waves dynamics. We also show how wave dynamics depend on the variation of biophysical parameters, revealing the possible existence of critical regimes characterized by power-law distributions of the statistical features of retinal waves (sizes, durations). Already, we have performed stage II waves experiments in collaboration with Vision Institute, confirming as a preliminary result the power-law like behaviour for wave characteristics in normal conditions (see Chapter 6). The physical meaning of such a critical regime means that waves would exhibit maximal variability in their sizes and durations (definition of power law distributions). It would be interesting to explore what would be the functional reason behind the network's choice of such a regime, regarding waves.

We also predict the apparition of pattern, that spatially bound the propagating waves. Such patterns, despite the fact that have never been experimentally observed during stage II phase, are still interesting. For example, late waves (stage III) appear to be

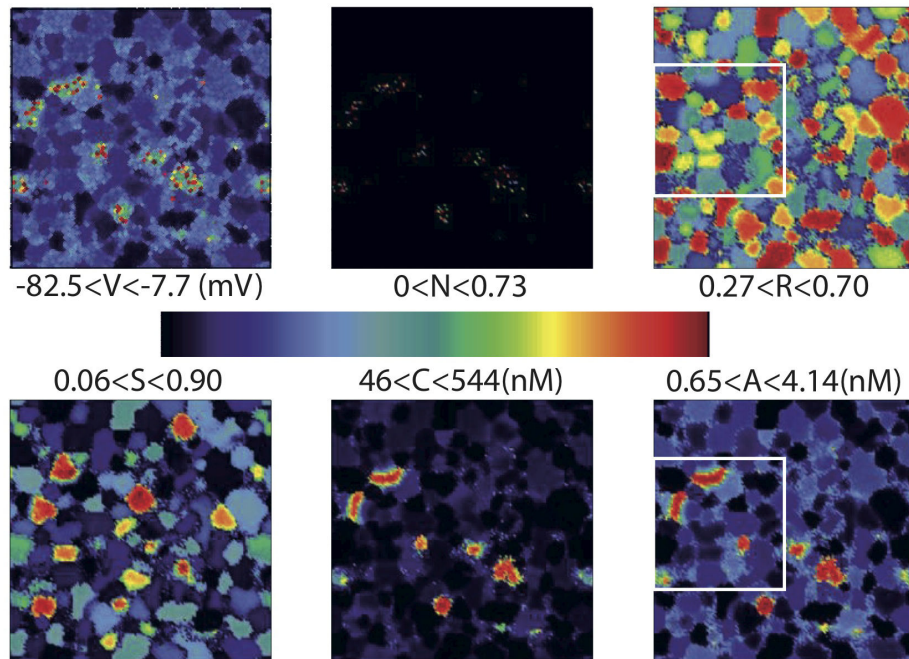


Figure 4.24: **Numerical simulation of Eq 3.4 with $g_A = 0.336 nS$** (case D in Fig 4.21). From top left to bottom right, the plot displays the instantaneous value of V, N, R, S, C and A versus i, j using the color code in the center of the figure. For each plot, the minimal and maximal values used to define the color code are explicitly indicated.

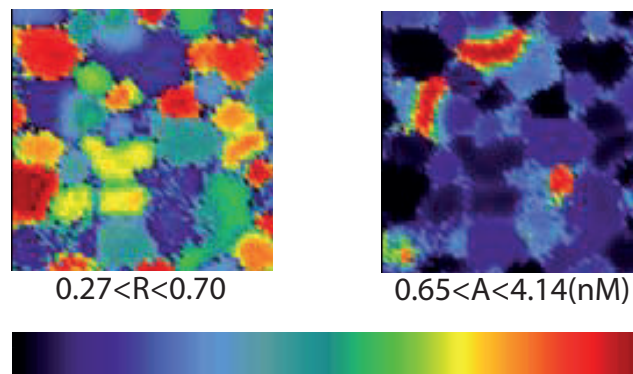


Figure 4.25: **Numerical simulation of Eq 3.4 with $g_A = 0.336 nS$** (case D in fig.(4.21)). The left (resp. right) plot displays R (resp. A) versus i, j using the color code in the center of the figure. For each plot, the minimal and maximal values used to define the color code are explicitly indicated. The two plots are an enlargement of the areas enclosed by the continuous white line in Fig 4.24.

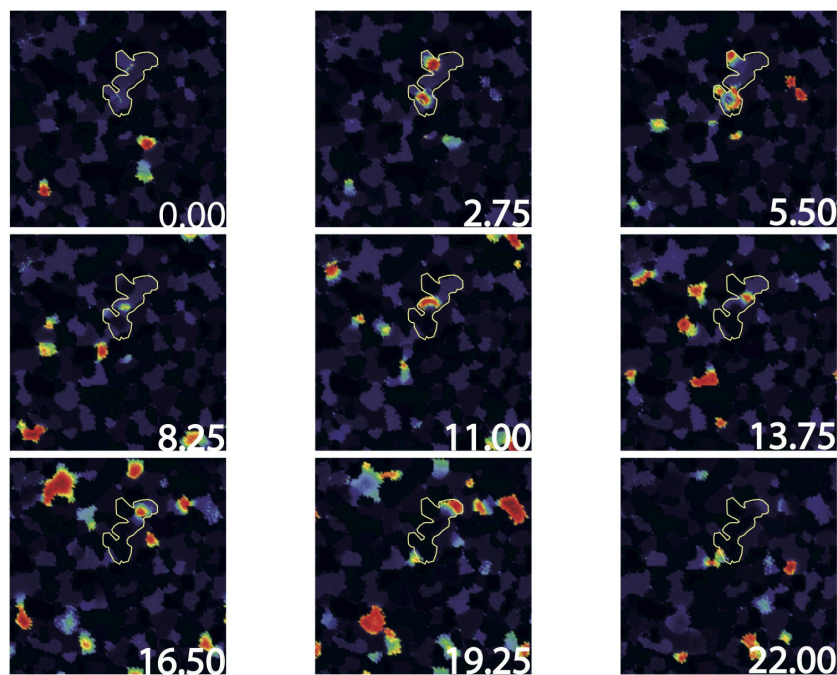


Figure 4.26: **Time evolution of the calcium concentration C with $g_A = 0.476 nS$** (case E in Fig 4.21). The color code is the same as in Fig 4.24. The time (in s) is displayed in the bottom right corner. The continuous close white line has been added manually to assist in the understanding (see text). The velocity of the front is above $120 \mu m s^{-1}$, while its width is $\simeq 240 \mu m$.

spatially bounded and more localised than stage II waves [53]. Those localized activity patterns, could potentially have a link with how receptive fields are formed before vision becomes functional. For studying the underlying mechanisms of such activity patterns, it would be interesting to use our theoretical framework.

In the following chapter, we are going to present a mesoscopic approach towards the description of waves, derived from the microscopic dynamics of the detailed biophysical equations.

Chapter 5

Towards a mesoscopic approach to analyse retinal waves

Our model features the elaborated dynamics of individual SAC and their cholinergic coupling. It is able to reproduce several experiments and to propose new ones. However at this stage it does not yet provide phenomenological equations for waves propagation and pattern formation. It is usual in physics to model waves by partial differential equations so here we attempt to follow the same approach. The goal is to better understand waves propagation, in particular, how they depend on parameters such as the cholinergic conductance g_A . Also, it is important to eliminate the fast dynamics to improve computational time during numerical investigations. In some sense, existing models of retinal waves, especially [12], attempt to propose such a mesoscopic description, but the proposed dynamics is not purely justified on biophysical grounds, where as in our model it was built based on the microscopic dynamics of individual SACs.

Using a fast-time averaging procedure we have been able to propose a partial differential equation for the propagation of Ach conductance upon SACs bursting and synchrony. This is a nonlinear equation, which is in a sense a generalisation of Kardar-Parisi-Zhang (KPZ) equation for surface growth [16]. In this approach, we consider a propagation of the conductance G_A , the total Ach conductance. This departs, already at this stage, from classical approaches, such as reaction-diffusion where one would consider instead directly the diffusion of Ach concentration. This approach has been followed by Lansdell et al. [12]. However, this requires a free diffusion of Ach, which is not what happens here. Ach is produced when the cell is bursting. This gives rise to a very original dynamics where activity propagates only when cells cross the threshold leading them to burst, in direct link with the bifurcation analysis of Chapter 2, and transport condition of Chapter 3. As we see in the next lines, it is easier to represent waves equation as a transport of conductance. In this approach, propagations occurs in a landscape shaped by the previous wave activity and most importantly, sAHP dynamics. As a consequence, this is a non linear PDE depending on the history of the system. Due to lack of time, we have not been able to study in full generality, but we have obtained analytic results about the waves speed and characteristic space and timescale. Especially, we found a condition whose dynamics is equivalent to a SOC sand pile [17, 18], hence implying power law distributions for waves. However, this case is very specific and has no reason to appear spontaneously in stage II retinal waves, unless an additional mechanism, such as homeostasis, stabilizes SACs, at this

very specific point. All this study is preliminary and requires further investigation.

5.1 Transport equation

5.1.1 Model and variables rescaling

We recall that the model equations are:

$$\left\{ \begin{array}{l} C \frac{dV_i}{dt} = -g_L(V_i - V_L) - g_C M_\infty(V_i)(V_i - V_C) - g_K N_i(V_i - V_K) - G_{sAHP}(R_i)(V_i - V_K) \\ \quad - G_A(A_{kk \in \mathcal{B}_i})(V_i - V_A) \\ \tau_N \frac{dN_i}{dt} = \Lambda(V_i)(N_\infty(V_i) - N_i) \\ \tau_C \frac{dC_i}{dt} = -\frac{\alpha_C}{H_X} C_i + C_0 - \delta_C g_C M_\infty(V_i)(V_i - V_C) \\ \tau_S \frac{dS_i}{dt} = \alpha_S(1 - S_i)C_i^4 - S_i \\ \tau_R \frac{dR_i}{dt} = \alpha_R S_i(1 - R_i) - R_i \\ \frac{dA_i}{dt} = -\mu A_i + \beta_A T_A(V_i), \end{array} \right. \quad (5.1)$$

where:

$$G_{sAHP}(R_i) = g_{sAHP} R_i^4, \quad (5.2)$$

is the sAHP conductance,

$$G_A(A_{kk \in \mathcal{B}_i}) = g_A \sum_{k \in \mathcal{B}_i} U(A_k), \quad (5.3)$$

is the Ach synaptic conductance, with:

$$U(A) = \frac{A^2}{\gamma_A + A^2}, \quad (5.4)$$

and where \mathcal{B}_i is the set of index of neurons connected to i .

We rescale conductances $\tilde{g}_X = \frac{g_X}{g_L}$ dividing by g_L to let the time scale $\tau_L = \frac{C}{g_L}$ appear in the equation of V . Also, we introduce $\tau_A = \frac{1}{\mu}$.

$$\left\{ \begin{array}{l} \tau_L \frac{dV_i}{dt} = -(V_i - V_L) - \tilde{g}_C M_\infty(V_i)(V_i - V_C) - \tilde{g}_K N_i(V_i - V_K) - \tilde{G}_{sAHP}(R_i)(V_i - V_K) \\ \quad - \tilde{G}_A(A_{kk \in \mathcal{B}_i})(V_i - V_A); \\ \tau_N \frac{dN_i}{dt} = \Lambda(V_i)(N_\infty(V_i) - N_i); \\ \tau_C \frac{dC_i}{dt} = -\frac{\alpha_C}{H_X} C_i + C_0 - \delta_C \tilde{g}_C M_\infty(V_i)(V_i - V_C); \\ \tau_S \frac{dS_i}{dt} = \alpha_S(1 - S_i)C_i^4 - S_i; \\ \tau_R \frac{dR_i}{dt} = \alpha_R S_i(1 - R_i) - R_i; \\ \tau_A \frac{dA_i}{dt} = -A_i + \frac{\beta_A}{\mu} T_A(V_i); \end{array} \right.$$

We rescale time at the time scale of Acetylcholine (which is close to Calcium time scale) by introducing a new medium time scale $t_m = \frac{t}{\tau_A}$. This gives:

$$\left\{ \begin{array}{l} \epsilon_V \frac{dV_i}{dt_m} = -(V_i - V_L) - \tilde{g}_C M_\infty(V_i)(V_i - V_C) - \tilde{g}_K N_i(V_i - V_K) - \tilde{G}_{sAHP}(R_i)(V_i - V_K) \\ \quad - \tilde{G}_A(A_{kk \in \mathcal{B}_i})(V_i - V_A) \\ \epsilon_N \frac{dN_i}{dt_m} = \Lambda(V_i)(N_\infty(V_i) - N_i) \\ \frac{\tau_C}{\tau_A} \frac{dC_i}{dt_m} = -\frac{\alpha_C}{H_X} C_i + C_0 - \delta_C g_C M_\infty(V_i)(V_i - V_C) \\ \frac{\tau_S}{\tau_A} \frac{dS_i}{dt_m} = \alpha_S(1 - S_i)C_i^4 - S_i \\ \frac{\tau_R}{\tau_A} \frac{dR_i}{dt_m} = \alpha_R S_i(1 - R_i) - R_i \\ \frac{dA_i}{dt_m} = -A_i + \frac{\beta_A}{\mu} T_A(V_i), \end{array} \right. \quad (5.5)$$

with $\epsilon_V = \frac{\tau_L}{\tau_A}$ and $\epsilon_N = \frac{\tau_N}{\tau_A}$.

5.1.2 Reduced dynamics

Fast dynamics of V, N

In eq. (5.5), ϵ_V and ϵ_N are small. N, V are fast variables and one can approximate their dynamics on the medium time scale by their steady state equations. This gives:

$$V_i^* = \frac{V_{ML}(V_i^*) + \tilde{G}_{sAHP}(R_i)V_K + \tilde{G}_A(A_{kk \in \mathcal{B}_i})V_A}{\tilde{g}_{ML}(V_i^*) + \tilde{G}_{sAHP}(R_i) + \tilde{G}_A(A_{kk \in \mathcal{B}_i})}. \quad (5.6)$$

where:

$$\begin{aligned} V_{ML}(V_i^*) &= V_L + \tilde{g}_C M_\infty(V_i^*)V_C + \tilde{g}_K N_\infty(V_i^*)V_K; \\ \tilde{g}_{ML}(V_i^*) &= 1 + \tilde{g}_C M_\infty(V_i^*) + \tilde{g}_K N_\infty(V_i^*), \end{aligned} \quad (5.7)$$

refer to Morris-Lecar (ML) terms.

Depending on parameters this equation has one, two or three solutions corresponding to branches of equilibria. The number of branches varies when saddle-node bifurcations (see Chapter 2).

We are here mainly interested in two parameters: the sAHP conductance $\tilde{G}_{sAHP}(R_i)$, where R_i is considered as a slow parameter and the Ach conductance \tilde{G}_A . Note that, V_i^* decreases when sAHP conductance increases, and it increases when Ach conductance increases, as expected.

Also remark that, in Eq (3.4) the effects of sAHP and Ach appears via a variation of conductance, i.e. via a current of the form $-g_X(V - V_X)$. As a consequence, the conductance appears both in the numerator and in the denominator of the rest potential. This is in contrast with an external current I_{ext} considered in Chapter 2, as a parameter, which appears only in the numerator. The two cases are similar, though, if the conductance is small compared to the other terms in the denominator.

Recall that if we consider V_i^* as a function of an external current I_{ext} then the saddle-node bifurcation SN_1 is given by $I_{ext} = I_{SN_1}$. Especially, (for $I_{ext} > I_{SN_1}$), there is one branch corresponding to the unstable fixed point inside the area delimited by a stable limit cycle.

Slow variables

Let us now return to the time rescaled equations (5.5). The ratios $\frac{\tau_S}{\tau_A}, \frac{\tau_R}{\tau_A}$ are large. Therefore, we may write the equation of S_i, R_i in (5.5) the form:

$$\frac{dS_i}{dt_m} = \epsilon_S [\alpha_S(1 - S_i)C_i^A - S_i] \sim 0; \quad \frac{dR_i}{dt_m} = \epsilon_R [\alpha_R S_i(1 - R_i) - R_i] \sim 0, \quad (5.8)$$

with $\epsilon_S = \frac{\tau_A}{\tau_S}, \epsilon_R = \frac{\tau_A}{\tau_R}$ small. Therefore, on the medium time scale, we can consider S, R as parameters, fixed in time.

Medium scale variables

C have the same time scale as A but it does not play a direct role in the equation of A . It only acts via R , acting on V , acting on A , but from the previous section, we consider R as a constant.

This approximation is fair, as soon as we want to consider propagation on the time scale of one wave, assuming that this time is quite smaller than the hyperpolarization time. In this approximation, the wave propagates in a "frozen" R landscape, in the spirit of the numerical experiments with one wave source cell done in Chapters 3 and 4.

On larger time scales (corresponding to having several waves) one has to consider a coupled dynamics between A and R where R evolves as well according to waves dynamics.

For A the equation becomes:

$$\frac{dA_i}{dt_m} = -A_i + \frac{\beta_A}{\mu} T_A(V_i^*(R_i, A_{k \in \mathcal{B}_i})), \quad (5.9)$$

where we made explicit the dependence of V_i^* in the variables R_i and A_k (Ach concentration emitted from presynaptic neurons).

5.1.3 Equation of transport for Ach

Approximations

Equation (5.9) relates the local concentration of Ach to the concentration of Ach emitted by presynaptic neurons. In this sense it characterizes how Acetylcholine propagates upon neurons activity. However, although this equation looks simple it hides several difficulties.

Mainly, the variable $V_i^*(R_i, A_{k \in \mathcal{B}_i})$ is not a continuous function of the sAHP variable (R_i) and presynaptic Ach concentration (A_k). This is because V_i^* has *jumps at bifurcation points*. In particular, when V_i^* jumps from the lower to the upper branch, its Ach production abruptly increases. There is therefore a thresholding mechanism leading to a singularity in the transport equation. From this point of view the transport equation is quite original and quite different from standard waves equations even in non linear systems. The only analogy we found is with models of self-organized criticality (see section ...) and the work of [14].

The second problem is that T is a nonlinear (sigmoidal function).

We propose now several approximation to help us having a tractable transport equation.

Ach production on the lower branch. We consider that V_i^* is so low on the lower branch that $T(V_i^*) = 0$. On the lower branch $V_i^* \in [-80, -60]$ mV, for $V_0 = -20$ mV, $\kappa_A = 0.2$ mV this gives $T(V_i^*) \in [6.10^{-6}, 0.00033]$. This justifies this approximation.

Ach production on the upper branch. We assume that V_i^* is almost constant for the range of currents it receives. Then, we replace $T(V_i^*)$ by a constant π_A . In our case, in the upper branch, $V_i^* \sim -30$ mV, giving $\pi_A \sim 0.12$.

Thresholding. In Chapter 3, we have defined a condition ensuring that a cell at rest starts to burst from the influence of bursting neighbours. This defines a threshold conditions depending on the local sAHP constrained by the variable R . We now rewrite this threshold condition by introducing the quantity $\Gamma_i(A_{k \in \mathcal{B}_i}) = \sum_{k \in \mathcal{B}_i} U(A_k)$. The

total Ach conductance is $G_A = g_A \Gamma_i$ and the threshold condition can we written as $\tilde{g}_A \Gamma_i > \Theta(R_i)$ where $\Theta(R_i)$ is a bursting threshold.

$\Theta(R_i)$ is derived the same way as Eq 3.18. However, in contrast with Eq 3.18, where we assumed that all neighbouring cells are synchronous, here they are not. Also, Eq 3.18, was derived assuming that a wave starts from a bursting cell and that all other cells are in a rest regime. If we want to generalize this computation to the case where the cells are not synchronous and the number of bursting cells can vary, we are led to a very complex problem. Indeed, e.g. the number of bursting cells, n , depends on dynamics, and dynamics on n .

A way to circumvent this problem is to use a naive mean-field approach. We replace n by its average value, $n \sim KF$, where K is the number of neighbours of a cell, and F the probability that a cell is bursting at a given time (computed in Section 3.6). We also replace $R(t_B)$ by its average. This gives us a threshold to replace 3.18 by the adequate equation. We call this a "naive" mean-field approach because it neglects the fluctuations of n and R around their mean.

The threshold conditions reads now as: $\tilde{g}_A \Gamma_i(A_{k \in \mathcal{B}_i}) > \Theta(R_i)$, where $\Theta(R_i)$ is the bifurcation threshold. Therefore, using the Heaviside function, we may replace the production term $T_A(V_i^*(R_i, A_{k \in \mathcal{B}_i}))$ in Eq (5.9) by $\pi_A H[\tilde{g}_A \Gamma_i(A_{k \in \mathcal{B}_i}) - \Theta(R_i)]$. Note that, for our parameters value (spontaneous bursting) $\Theta(R_i) < 0$. Therefore, there is Ach production even in the absence of coupling, but the cells do not interact together: the situation is as if there was Ach emission but no receptors.

Variable Γ . From now, we simplify the notation and remove the term in parentheses. The transport equation reads now:

$$\frac{dA_i}{dt_m} = -A_i + \frac{\beta_A \pi_A}{\mu} H[\tilde{g}_A \Gamma_i - \Theta(R_i)].$$

We have:

$$\begin{aligned} \frac{d\Gamma_i}{dt_m} &= \sum_{k \in \mathcal{B}_i} \frac{dU(A_k)}{dt_m} = \sum_{k \in \mathcal{B}_i} U'(A_k) \frac{dA_k}{dt_m} \\ &= \sum_{k \in \mathcal{B}_i} U'(A_k) \left(-A_k + \frac{\beta_A \pi_A}{\mu} H[\tilde{g}_A \Gamma_k - \Theta(R_k)] \right). \end{aligned}$$

Piecewise linear approximation. To simplify further this equation we replace U , a sigmoidal function, by its linear approximation (see Section 3.3) $U(x) = a_U + b_U x$, where $a_U = 0$ and $b_U = \frac{1}{2\sqrt{\gamma_A}} = \frac{1}{2K_d}$, provided $x \in [X_U^-, X_U^+]$. We have then $\sum_{k \in \mathcal{B}_i} U'(A_k) A_k = \sum_{k \in \mathcal{B}_i} b_U A_k = \sum_{k \in \mathcal{B}_i} (U(A_k) - a_U) = \sum_{k \in \mathcal{B}_i} U(A_k)$. Therefore $-\sum_{k \in \mathcal{B}_i} U'(A_k) A_k = -\sum_{k \in \mathcal{B}_i} U(A_k) = -\Gamma_i$ and:

$$\frac{d\Gamma_i}{dt_m} = \frac{\beta_A \pi_A b_U}{\mu} \sum_{k \in \mathcal{B}_i} H[\tilde{g}_A \Gamma_k - \Theta(R_k)]. \quad (5.10)$$

Recall that Γ_i is proportional to the Ach conductance. This equation tells that, when neurons are at rest (low branch), Γ_i has a steady state $\Gamma_i \approx 0$ i.e. each neighbour provides a conductance contribution 0. More generally, there is a source term proportional to the number of pre-synaptic neurons whose Ach conductance is larger than $\Theta(R_k)$.

Laplacian approximation. Here comes the interest of assuming cells distributed on a regular lattice with nearest neighbours interactions. We note a the lattice spacing. We locate the point i in the lattice by coordinates x_i, y_i but we assume that A is in fact a continuous field $A(x, y, t)$ that we sample at lattice points so that $A_i(t) \equiv A(x_i, y_i, t)$. Then, the Ach concentration in the four points of the neighbourhood \mathcal{B}_i of i is $A(x_i \pm a, y_i, t)$ and $A(x_i, y_i \pm a, t)$. Therefore:

$$\sum_{k \in \mathcal{B}_i} H[\tilde{g}_A \Gamma_k - \Theta(R_k)] \sim 2d H[\tilde{g}_A \Gamma_i - \Theta(R_i)] + a^2 \Delta H[\tilde{g}_A \Gamma_i - \Theta(R_i)], \quad (5.11)$$

with $\Gamma_i = \Gamma(x_i, y_i, t)$ and d the dimension of the system.

Singular diffusion. Here Δ is the Laplacian, and ΔH is a distribution. We recall that $H' = \delta$, the Dirac distribution. For a function $f(x, y, t)$ we have $\nabla H(f(x, y, t)) = \delta(f(x, y, t)) \nabla f$ and $\Delta H(f(x, y, t)) = \nabla(\delta(f(x, y, t)) \nabla f) = \delta'(f(x, y, t)) \|\nabla f\|^2 + \delta(f(x, y, t)) \Delta f$. Here $f(x, y, t) = \tilde{g}_A \Gamma(x, y, t) - \Theta(R)$, where R is a field characterizing the spatial variation of sAHP imprinted by the previous history of waves and it evolves slowly in time. Therefore $\nabla f = \tilde{g}_A \nabla \Gamma$ and:

$$\Delta H[\tilde{g}_A \Gamma - \Theta(R)] = \tilde{g}_A^2 [\delta'(\tilde{g}_A \Gamma - \Theta(R)) \|\nabla \Gamma\|^2 + \delta(\tilde{g}_A \Gamma - \Theta(R)) \Delta \Gamma]. \quad (5.12)$$

Let us interpret this equation. The Dirac distributions $\delta(\tilde{g}_A \Gamma - \Theta(R))$, $\delta'(\tilde{g}_A \Gamma - \Theta(R))$ weight the set of points x, y such that $\tilde{g}_A \Gamma(x, y, t) = \Theta(R)$. This is the set of neurons which are precisely at the bifurcation point (at time t). Typically this should be the front of the wave, what we call the critical front. If we assume that this set is a smooth curve $\mathcal{S}(t)$ with a length element dl , then, for a test function $\psi(x, y)$, $\langle \delta(\tilde{g}_A \Gamma - \Theta(R)), \psi \rangle = \int_{\mathcal{S}(t)} \psi(x, y) dl(x, y)$, the integral of ψ on the critical front. Therefore:

$$\langle \psi, \Delta H[\tilde{g}_A \Gamma - \Theta(R)] \rangle = \tilde{g}_A^2 \left[\int_{\mathcal{S}(t)} \nabla(\psi \|\nabla \Gamma\|^2) dl(x, y) + \int_{\mathcal{S}(t)} \psi \Delta \Gamma dl(x, y) \right].$$

In particular, taking $\psi(x, y) = 1$ in (5.12) we obtain, writing $\langle 1, f \rangle \equiv \langle f \rangle$ for simplicity:

$$\langle \Delta H [\tilde{g}_A \Gamma - \Theta(R)] \rangle = \tilde{g}_A^2 \left[\int_{\mathcal{S}(t)} \nabla (\|\nabla \Gamma\|^2) dl(x, y) + \int_{\mathcal{S}(t)} \Delta \Gamma dl(x, y) \right]$$

Current. The transport equation of Γ , considered now as a field, reads:

$$\frac{\partial \Gamma}{\partial t} = -\Gamma + 4a_U + \frac{\beta_A \pi_A b_U}{\mu} (4H [\tilde{g}_A \Gamma - \Theta(R)] + a^2 \Delta H [\tilde{g}_A \Gamma - \Theta(R)]), \quad (5.13)$$

where $n_i = 4$ in this graph configuration.

Equation (5.13) characterizes the transport of conductance through the network. In particular there is a current:

$$J_\Gamma = \frac{a^2}{\tilde{g}_A} \nabla H [\tilde{g}_A \Gamma - \Theta(R)] = a^2 \delta [\tilde{g}_A \Gamma - \Theta(R)] \nabla \Gamma, \quad (5.14)$$

such that eq. (5.13) reads as a continuity equation:

$$\frac{\partial \Gamma}{\partial t} + \tilde{g}_A \nabla J_\Gamma = -\Gamma + 4a_U + 4 \frac{\beta_A b_U \pi_A}{\mu} H [\tilde{g}_A \Gamma - \Theta(R)] \quad (5.15)$$

where the right hand side contains a loss term $-\Gamma$ and a source term $4a_U + 4 \frac{\beta_A b_U \pi_A}{\mu} H [\tilde{g}_A \Gamma - \Theta(R)]$.

The current has an interesting form. Indeed, it is non zero only on the "critical" manifold $\tilde{g}_A \Gamma - \Theta(R)$. On this manifold, it acts as a diffusion current. Therefore, Γ diffuses only on the critical manifold.

5.2 Discussion

Single neuron dynamics in the presence of a tunable sAHP and Ach currents We made the following experiment (Fig. 5.1). We simulate a single neuron dynamics replacing the sAHP conductance $g_S R^4$ by a fixed parameter G_S , and the Ach conductance $g_A \Gamma$ by a fixed parameter G_A . In other words, we consider a Morris-Lecar model in the presence of currents $-G_S(V - V_K)$ and $-G_A(V - V_A)$ where G_S and G_A are tunable parameters. We display the neuron activity in the figure 5.1. On the left we see a 3D plot of the average voltage value $\langle V \rangle$, whereas, on the right, we show the mean $\langle V \rangle$ (top) and the fluctuations $\sigma_V = \sqrt{\langle V^2 \rangle - \langle V \rangle^2}$ about the mean (bottom). When considering fluctuations, black regions correspond to zero fluctuations, hence to a fixed point dynamics. On the opposite, colored region correspond to a dynamical activity. In the colored region of Fig 5.1 right, bottom, there are oscillations whereas, below this region there is a low voltage fixed point, and, above, a high voltage fixed point. When increasing G_S these points merge at the end of the colored region via a saddle-node bifurcation.

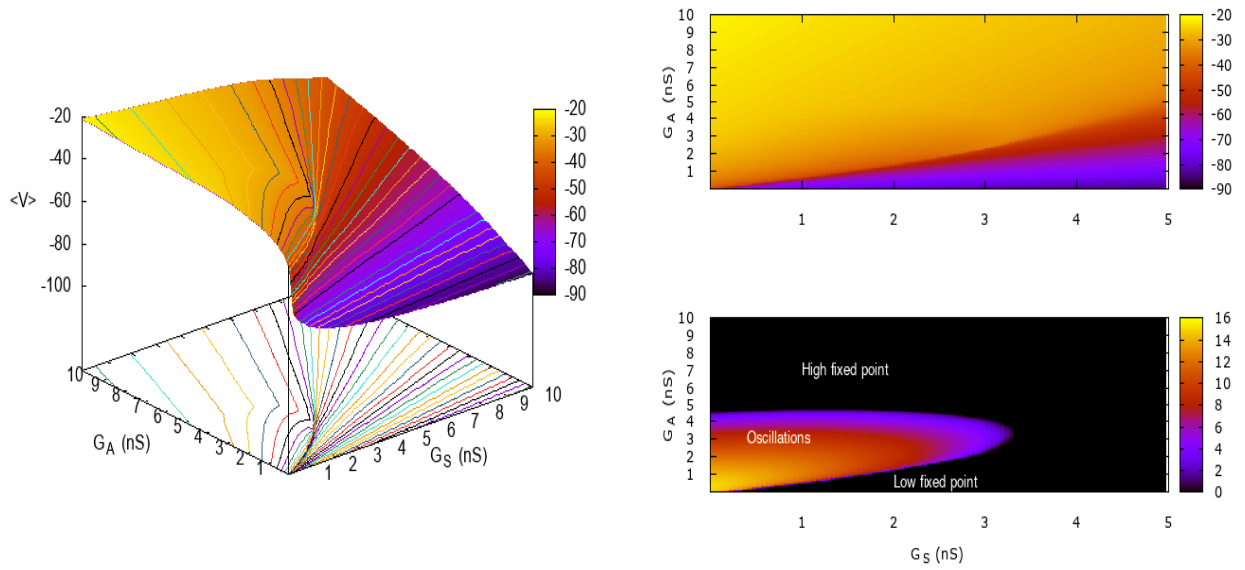


Figure 5.1: Left. 3D plot of the mean voltage $\langle V \rangle$ as a function of G_S, G_A . The lines on the surface and at the bottom are level lines. Right. Color map of the mean voltage $\langle V \rangle$ (top) and its standard deviation $\sigma_V = \sqrt{\langle V^2 \rangle - \langle V \rangle^2}$ (bottom).

It is interesting that in Fig 5.1 (bottom right), the numerical heat map plays the role of a two dimensional bifurcation diagram, characterizing the dynamics across the parameters plane $G_A - G_S$. This result provides us with information, on which regime in the parameters space, propagation is possible. What we miss for now, is how a propagating wave's trajectory moves in this parameter space, helping us to extract a mechanism for waves propagation. In Fig 5.2, we provide a simple sketch of a possible motion induced by a propagating wave, revealing a mechanism. Namely, propagation starts when G_A starts to increase. While G_A starts decreasing, G_S would start increasing, moving to the right in the parameters space, towards the regime of zero fluctuations. Inevitably the transition is crossed, and the dynamics are now described by a fixed point. The time for G_S to decrease is quite long and that controls the refractoriness. Finally, we reach a point where G_S is low enough and while G_A starts to grow, a propagating wave emerges again. Although this mechanism is hypothetical, it would be interesting to trace the real movement in the parameter space $G_A - G_S$, during a wave propagation.

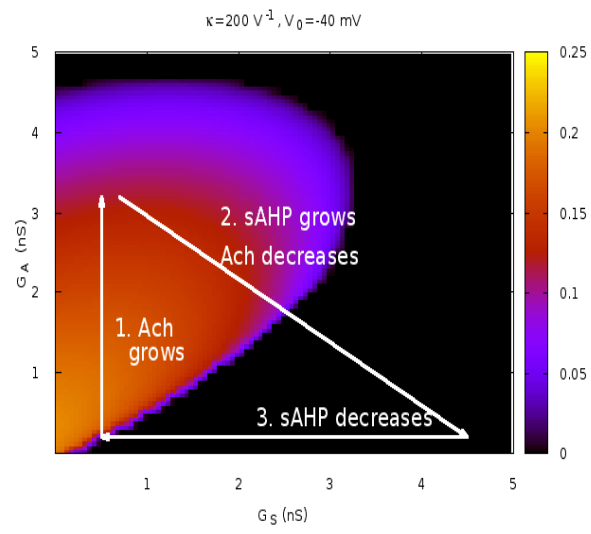


Figure 5.2: Color map of H and the schematic motion induced by a propagating wave.

Chapter 6

Confronting our model to experimental recordings

A short disclaimer

In this chapter, we include all our results related to experiments. As a physicist, I believe that every theory needs an experimental validation and during my thesis I was very lucky to collaborate closely with experts in experimental neuroscience and especially on retinal waves. Due to the lack of time, not all experiments we would have liked were done, and those who were, have not been fully analysed and their results are complementary to the main theoretical contributions of this thesis. However, I have found it magnificent to have learned a great deal about experiments during these three years and I would like to add a piece of what I learnt in the last chapter of my thesis. We explored two main questions with our collaborators: a) The role of potassium channels in waves characteristics with experiments performed by Evelyne Sernagor at University of Newcastle and b) the effect of the cholinergic transmission on the spatio-temporal patterns of stage II retinal waves experiments performed in the lab of Olivier Marre and Serge Picaud at Vision Institute, where I was hosted for two weeks to participate in experiments and analyse data. I would like to deeply thank them all for the opportunity to test some of our theoretical hypothesis in small pieces of the real world.

6.1 The role of potassium channels in waves characteristics

In order to characterize the role of potassium channels and especially sAHP current within stage II retinal waves, Evelyne Sernagor performed Multi Electrode Array (MEA 4096 electordes) recordings from stage II P6 mice. In this experiment, the goal was to manipulate the retinas pharmacologically and test the effect of this manipulations on waves characteristics and consequently compare to our theoretical results. In the experiment, E. Sernagor varied pharmacologically the intracellular K^+ concentration from $3nM$ to $6nM$ and $9nM$, changing the reversal potential of the voltage-gated K^+ channels to the following values respectively: $-67mV$, $-77mV$, $-90mV$ (see Fig 6.1). These values for V_K are computed using the Nernst voltage equation:

$$V_K = \frac{RT}{F} \ln\left(\frac{p_K[K^+]_o}{p_K[K^+]_i}\right) \quad (6.1)$$

where V_K is the reversal potential of K^+ , R is the universal gas constant, T is the temperature, F is the Faraday constant, p_K is the membrane permeability of K^+ , $[K^+]_{i,o}$ is the intra and extra-cellular concentrations of K^+ . For the calculation, we assume that the temperature is $T = 32$ C degrees and the $[K^+]_i = 115mM$.

As a result, the main effect of increasing potassium is the increase of firing frequency within bursts/waves, namely the population firing rate within waves increases. Waves also become larger and probably faster, at least for $V_K = -66mV$. These observations are intuitively explained by the fact that while increasing the reversal potential of K^+ , potassium related currents, such as sAHP and the fast voltage-gated K^+ , become less hyperpolarizing, leading to an increase in cells activity. It also explains why waves become larger and less complicated, since when a wave starts, it'll cover the bigger parts of the retina, as neurons are less hyperpolarized, facilitating the wave propagation in the medium. This observation once more confirms one of the important roles of the sAHP current on controlling the random boundaries of waves. In other words, the lesser the effect of the sAHP the more regular the waves appear to be.

Interestingly, at least in a qualitative point of view, there is no clear effect of varying V_K on the waves frequency, meaning that either sAHP is less instrumental at determining the wave frequency as we would expect or that interwave intervals are controlled by another biophysical parameter than the reversal potential V_K .

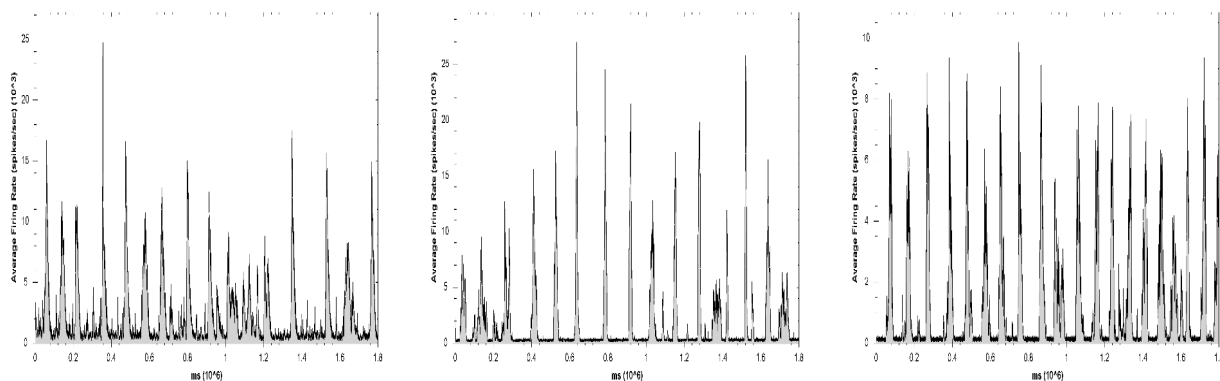


Figure 6.1: **Recording of the Average Population Firing Rate (spikes/sec) over time.** From left to right the average population firing for different values of V_K $-66, -77, -90mV$. Recording from 4096 electrodes on P6 mice (courtesy E. Sernagor). We observe that the firing rate increases as V_K increases and also waves become larger and more frequent. This result confirms the role of potassium channels in inhibiting retinal waves.

We simulate the same experimental conditions with our model. In our simulations, we vary directly the values of V_K to $-67, -77, -90mV$. We are able to qualitatively reproduce the experimental observations regarding the waves speed and frequency. In Fig 6.2, we also compute the average population firing rate for both dynamically and noise driven triggering scenario, by varying the value of V_L to $-70mV$ and $-72mV$ respectively.

It seems that our model is able to reproduce qualitatively the experimental results provided by Evelyne Sernagor but we can not make a quantitative statement yet on the similarities of the spatio-temporal patterns. Indeed in both numerical cases, upon

the increase of V_K firing rate increases within waves and there seems to be no dramatic effect on the waves frequency. However, we observe that for the dynamically driven bursting regime and for $V_K = -90mV$, in Fig 6.2, the baseline population activity when there is no wave is not zero, opposingly to the corresponding experiment where inbetween waves we see periods of silence in the network.

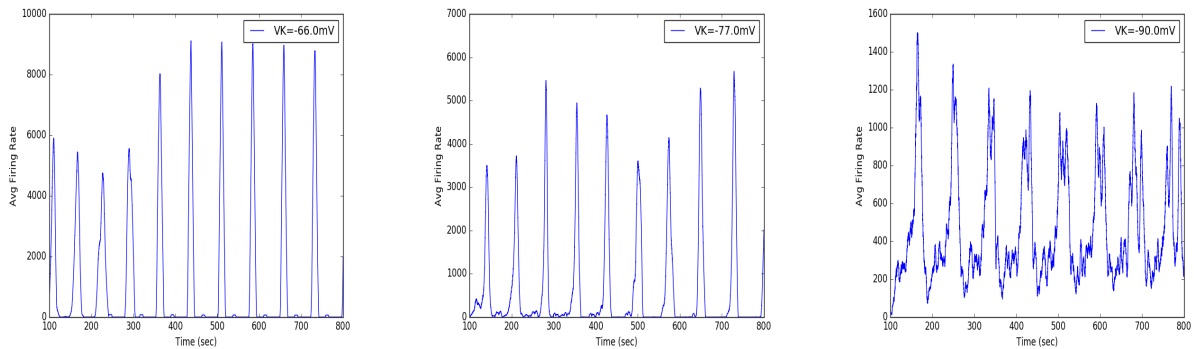


Figure 6.2: **Modeling with the Dynamically driven bursting scenario. Average Population Firing Rate (spikes/sec) over time.** From left to right the average population firing decreases for the different values of V_K $-66, -77, -90mV$. We observe that for the normal value of $V_K = -90mV$, the baseline population activity is not zero, opposingly to the corresponding experiment where inbetween waves we see periods of silence in the network.

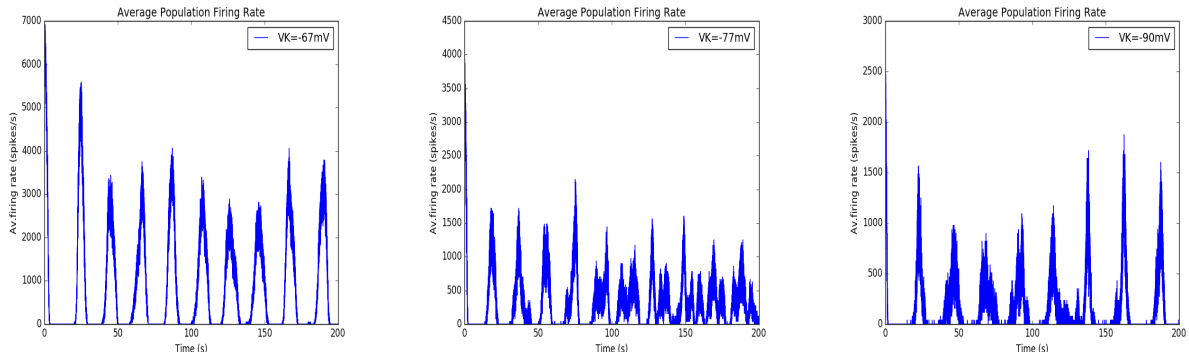


Figure 6.3: **Modeling with the Noise driven bursting scenario. Average Population Firing Rate (spikes/sec) over time.** From left to right the average population firing decreases for different values of V_K $-66, -77, -90mV$.

In order to explore the effect of the potassium channels on the spatiotemporal dynamics of stage II retinal waves, we compare the raster plots of the experiments with our simulations (here we show the case of the noise driven bursting regime). We observe that as we increase the V_K , we decrease the inhibition in the network, consequently leading to larger and more frequent waves (see Fig 6.4). These qualitative observations are well reproduced by our model (see Fig 6.5) where we also observe the same effect upon the decrease of inhibition. We also show series of snapshots of our simulated calcium waves for all three cases of V_K , illustrating better our conclusions (see Figs 6.6, 6.7, 6.8).

We have to note that in our model, we have two types of K^+ channels, the fast

voltage-gated K^+ channels and the slow Ca^{+2} -gated K^+ channels. The effects that we see here correspond to the role of the slow potassium channels, responsible for the sAHP current in stage II retinal waves, since the time scale of the effect is in the order of seconds and can not concern the fast ones whose dynamics evolve in several milliseconds. As explained above, upon the decrease of hyperpolarizing currents and therefore the effect of the sAHP currents, we observe that waves become more regular at their boundaries. This confirms the role of the sAHP in the randomness of the waves boundaries, since it acts like "walls" where waves are not allowed to propagate. This effect is also captured by our model (see Fig 6.5). However, in this case, our model is tuned to quite smaller bursting period, corresponding to our original parameters tuning, based on [63] with experiments on rabbits (interburst $\sim 20sec$), leading to smaller interwave intervals than the experimental data. As E. Sernagor's experiments were performed in mice (interburst $\sim 60sec$), the modeling parameter τ_S controlling the interburst and consequently the interwave interval should be adjusted accordingly.

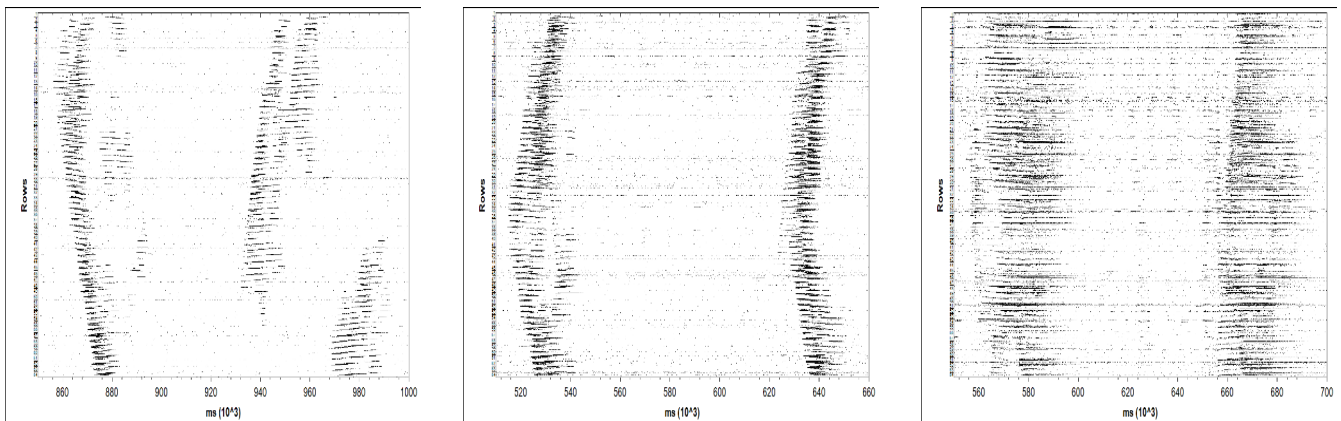


Figure 6.4: **Recording from stage II retinal waves (P6 mice)** From left to right the raster plot of the waves for different values of V_K $-90mV$, $-77mV$, $-66mV$. We observe that waves propagate more homogeneously as we increase V_K , verifying that potassium channels and especially sAHP plays a role in the irregular borders of waves.

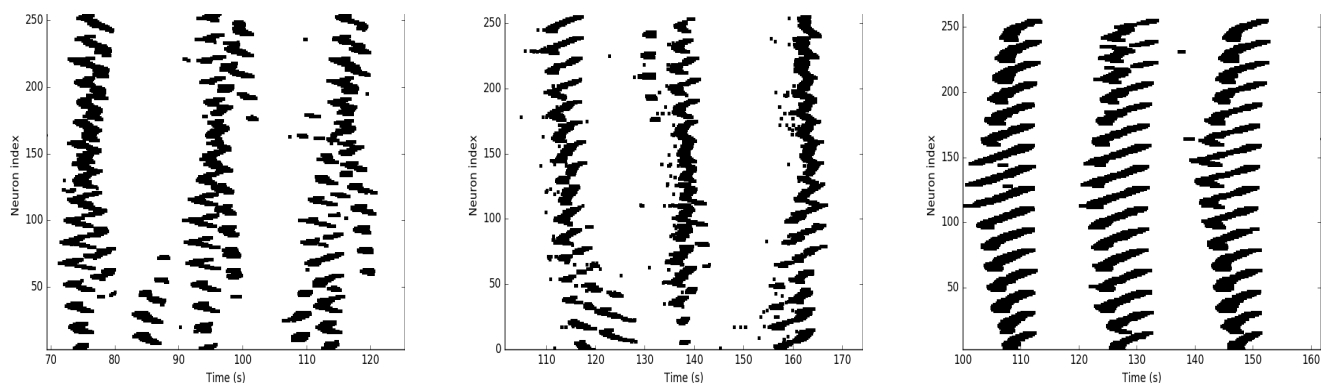


Figure 6.5: **Simulation of stage II retinal waves in the noise driven bursting scenario.** From left to right the raster plot of the waves for different values of V_K $-90mV$, $-77mV$, $-66mV$. Our simulated waves became larger, more frequent and more regular upon the decrease of the inhibition due to sAHP.

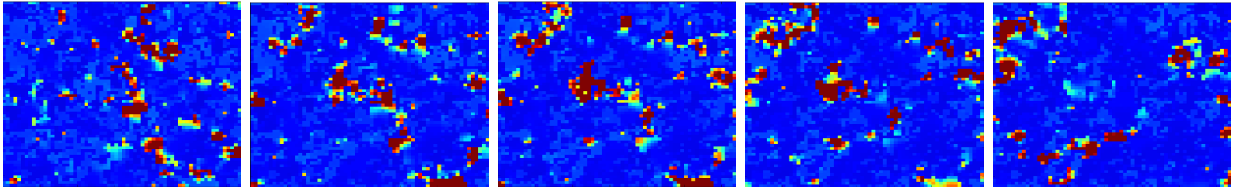


Figure 6.6: **Simulation of calcium stage II retinal waves for $V_K = -90mV$** From left to right, snapshots of propagating waves with total duration of all frames $20sec$.

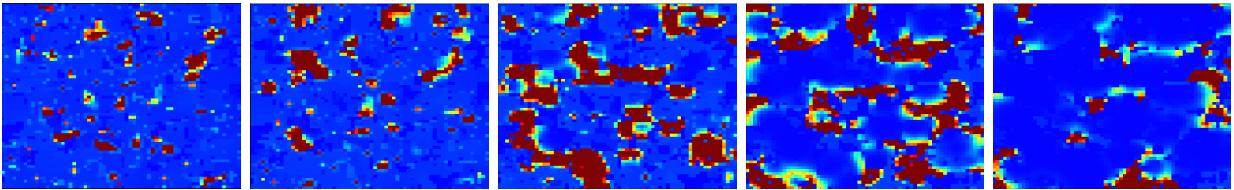


Figure 6.7: **Simulation of calcium stage II retinal waves for $V_K = -77mV$** From left to right, snapshots of propagating waves with total duration of all frames $20sec$.

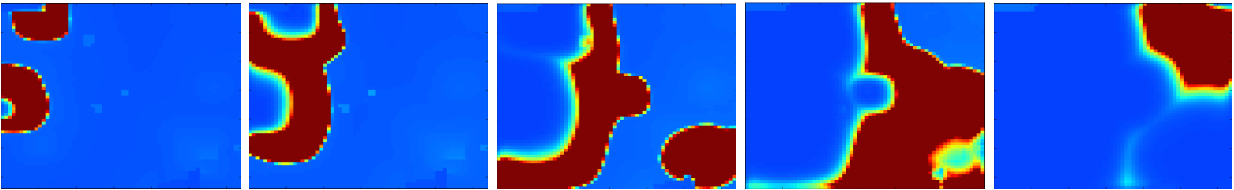


Figure 6.8: **Simulation of calcium stage II retinal waves for $V_K = -66mV$** From left to right, snapshots of propagating waves with total duration of all frames $20sec$.

After this qualitative analysis of the comparison between our model and experiments, it would be worth characterizing our simulated waves with respect to their sizes and durations and show in a more quantitative way the role of sAHP in stage II waves statistical characteristics. Due to the lack of time, this analysis has not been performed on the experimental data.

In Fig 6.9, by measuring the probability distribution functions of the waves sizes during our simulation of $1000s$, we confirm that indeed waves become larger upon the increase of V_K . Also, we should note that the shape of the distributions changes. However, our numerical method for wave detection, for the moment, treats waves that merge as the union of all of them, adding a bias towards larger waves which might be artificial. For that reason, to conclude on the exact shape of the distribution that has to be taken into account.

In Fig 6.10, by measuring the probability distribution functions of the waves durations during our simulation of $1000s$, we show that waves slightly become longer upon the increase of V_K . Also, we should note that the shape of the distributions changes but we can not conclude on the exact shape of the distribution with the current results.

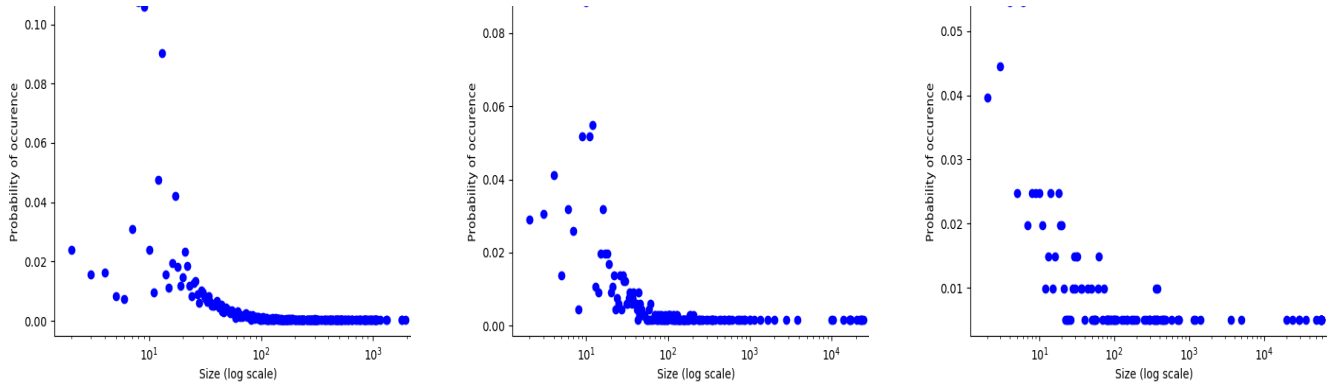


Figure 6.9: **Characterizing the sizes of stage II retinal waves in the noise driven bursting scenario.** From left to right the the probability distributions of the waves sizes for different values of V_K $-90mV$, $-77mV$, $-66mV$. Our simulated waves became larger (1 order of magnitude) upon the decrease of the inhibition due to sAHP.

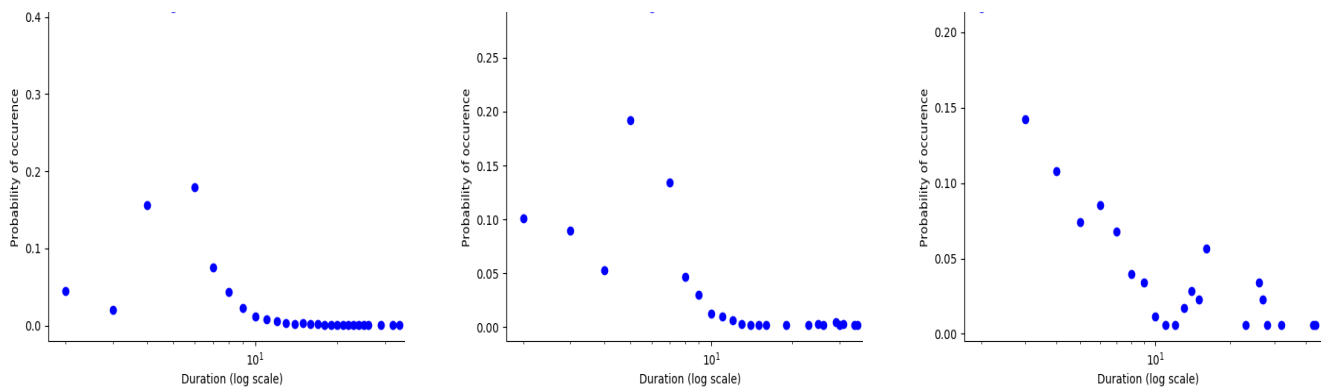


Figure 6.10: **Characterizing the durations of stage II retinal waves in the noise driven bursting scenario.** From left to right the probability distributions of the waves durations for different values of V_K $-90mV$, $-77mV$, $-66mV$. Our simulated waves became slightly longer upon the decrease of the inhibition due to sAHP.

6.2 Exploring the effect of the cholinergic transmission on the spatio-temporal patterns of stage II retinal waves

Objective of the experiment. Using our biophysical model of stage II retinal waves, we predict that the variation of the conductance of nicotinic cholinergic receptors g_A has a dramatic effect on the spatio-temporal patterns exhibited across the network of SACs (see Section 4.5.2). We show that weak connections lead to small bumps of activity, strong connections lead to large patterns that cover the whole numerical box and there is an intermediate regime where we observe the maximal variability in the spatiotemporal patterns. Also, we predict a change in the statistical characteristics of the spatio-temporal patterns upon the variation of the synaptic strength, such as the distribution of the waves size and duration.

In order to validate our theoretical prediction, we perform experiments on neonatal mice (P3-P7) at the laboratory of Olivier Marre and Serge Picaud at Vision Institute.

Pharmacology. We used *hexamethonium* in several concentrations to mimic the gradual blocking of the cholinergic transmission and test the effect on the characteristics of the spatiotemporal patterns. Hexamethonium is a nicotinic nACh receptor antagonist that acts in autonomic ganglia by binding mostly in or on the nACh receptor, and not the acetylcholine binding site itself.

It was not straightforward to find a pharmacological agent which would increase the efficiency of the cholinergic transmission. We tried *atropine* in several concentrations, which is found in the literature [61] to probably potentiate the nicotinic cholinergic receptors of the specific subunit β_2 , found also in SACs. Its pharmacological effects are due to binding to muscarinic acetylcholine receptors. However, it has been shown in [61], that atropine could potentiate the nicotinic nACh receptors (especially subunit β_2).

Tissue preparation. Experiments were performed in neonatal (P3-P7) mice. Mouse pups were sacrificed and eye balls enucleated prior to retinal isolation. The isolated retina was placed, RGC layer facing down, onto the MEA. Retinas were kept in a control Ames solution for about 1h before recordings, perfused with a pump. Hexamethonium and atropine were directly added to the perfusate. All experiments were performed by R. Caplette.

Recordings of retinal waves with MEA of 256 electrodes Extracellular recordings were performed on the MEA chip providing 256 square micro-electrodes with inter-electrode separation of $60\mu m$. The platform records at a sampling rate of 20kHz /electrode. Each data set generally consisted of 30 – 45min continuous recordings.

Analysis of the MEA recordings Our MEA recordings report the spike times for all electrodes. In order to consider a spike train to be a burst we set a threshold for the minimal duration 2sec [54]. Waves were detected as temporally overlapping groups of bursts using a sliding window of 1.5s length and a sliding step of 250ms. A supplementary criterion for waves detection was that the mean average rate over all electrodes has to be larger than 5 per cent. Here we use a different method for waves detection than in all previous chapters, based on the work of [70] and it provides us with a sufficiently good detection and characterization of waves as a first approach.

However, this method relies the wave detection largely on the average firing rate which is a parameter characterizing the network, meaning that two separate but co-existing waves in the recording will be regarded as one while characterizing the waves size. In the future, it would be interesting to analyse these data with our more elaborate method for waves detection (see Chapter 4), where we are able to follow each wave independently.

6.2.1 The effect of hexametonium in early stage II retinal waves

Hexametonium as a pharmacological agent is typically used as an antagonist of the nicotinic cholinergic receptors and it is considered to be very specific. Thus, applying hexametonium in several concentrations, allows us to gradually decrease the strength of the cholinergic coupling. In Fig 6.16, we show the average population firing rate over time for control data (P3) and several hexametonium concentrations $1\mu M$, $10\mu M$, $100\mu M$. The main effect of applying hexametonium in increasing concentrations, is the decrease of waves sizes leading eventually to their disparition for $100\mu M$ of hexametonium. This experimental observation validates our theoretical prediction (see section 4.5.2), concerning the decrease of waves sizes upon the decrease of cholinergic coupling.

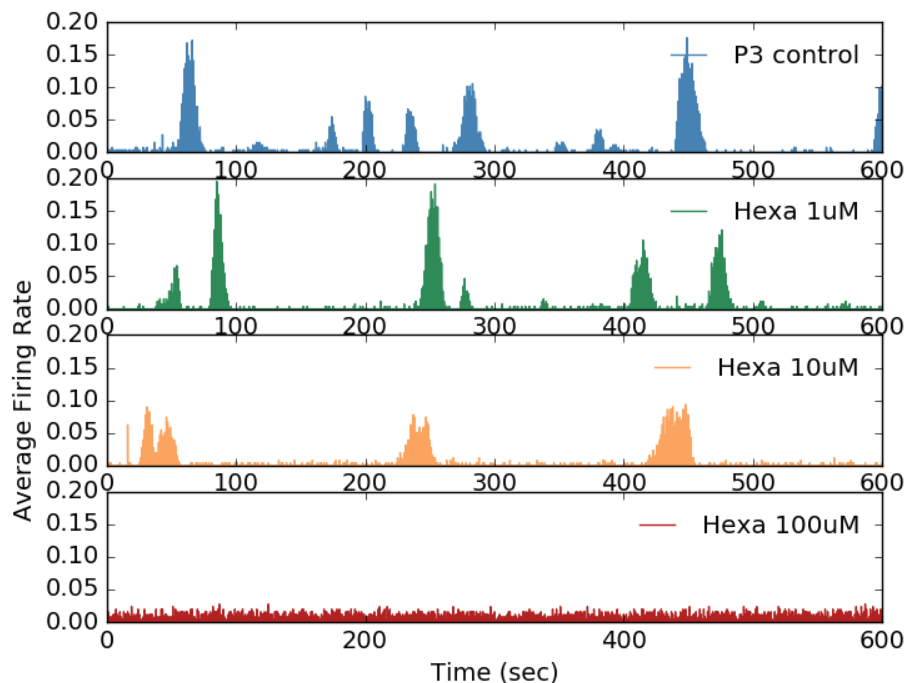


Figure 6.11: **How the average population firing rate changes upon hexametonium induction in P3 mouse retina.** The time shown here corresponds to 600sec. *Blue.* Control P3 waves. *Green.* Hexametonium concentration $1\mu M$. *Orange.* Hexametonium concentration $10\mu M$. *Red.* Hexametonium concentration $100\mu M$.

Also, upon the gradual pharmacological decrease of the cholinergic coupling, waves appear slightly less frequent (see Fig 6.12), indicating that the cholinergic coupling plays a role in the interwave intervals. Note also, that around half of the electrodes

(~ 120), exhibit regular activity, participating in a wave with a period fluctuating around $100 - 200 \text{ sec}$. In Fig 6.12, very high values of interwave intervals mean that those electrodes rarely participated in waves during this recording. As a convention, an $IWI = 0$, means that no wave was recorded from the specific electrode, either by chance or due to faulty electrodes.

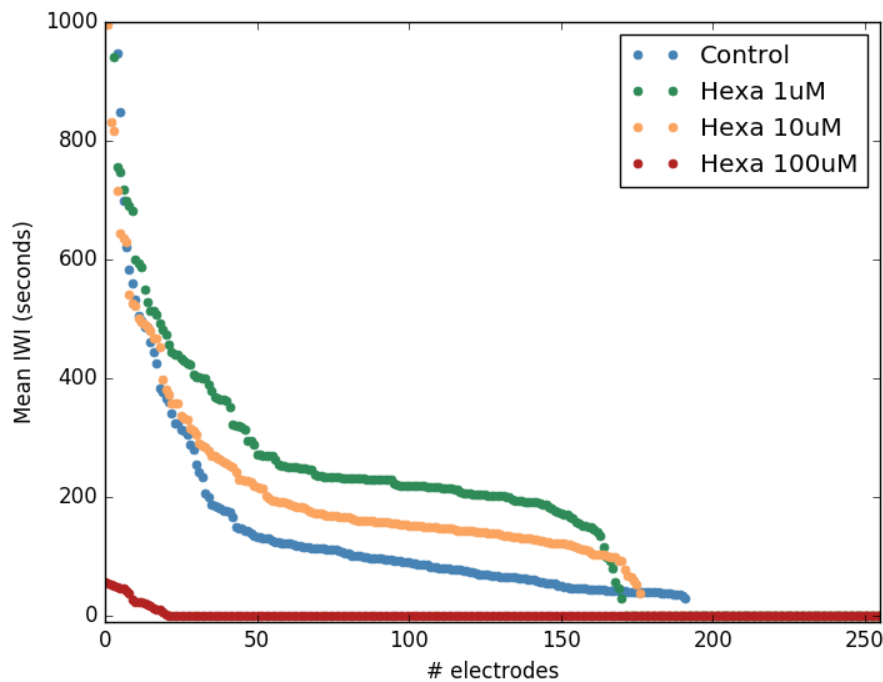


Figure 6.12: **Interwave intervals (IWI) profile for all electrodes, sorted in decreasing order for different concentrations of hexametonium.** The interwave intervals increase upon the induction of hexametonium in concentrations such as $1, 10\mu M$, the waves become less frequent. For $100\mu M$, waves disappear completely.

In an attempt to quantify the effect of hexametonium on the waves sizes, we measure the probability distribution of the waves sizes for control data and two hexametonium concentrations, 1 and $10\mu M$. We define as the waves size, as the number of electrodes participating in a wave. For $1\mu M$, the shape of the waves distribution and the maximum waves sizes do not differ from the control data (compare Figs 6.13,6.14). However, $10\mu M$ of hexametonium has a dramatic effect on the shape of the distribution of waves sizes and their maximum value, since the waves size decreases 50 per cent compared to the control data. As mentioned above, $100\mu M$ completely diminishes wavy activity.

In order to fully characterize the effect of hexametonium, it would be essential to measure several concentrations of hexametonium, aiming to construct a tuning curve for the waves size as a function of several hexametonium concentrations. For this, one would need to slightly increase each time the concentration of the solution and repeat at least 20 times from 0 to $100\mu M$ for a good resolution of the curve. These pharmacological manipulations must be done always in an increasing order, since in the laboratory we checked that if we decrease the concentration of the solution (decreasing order), the results are not coherent and hexametonium does not act like it should. In

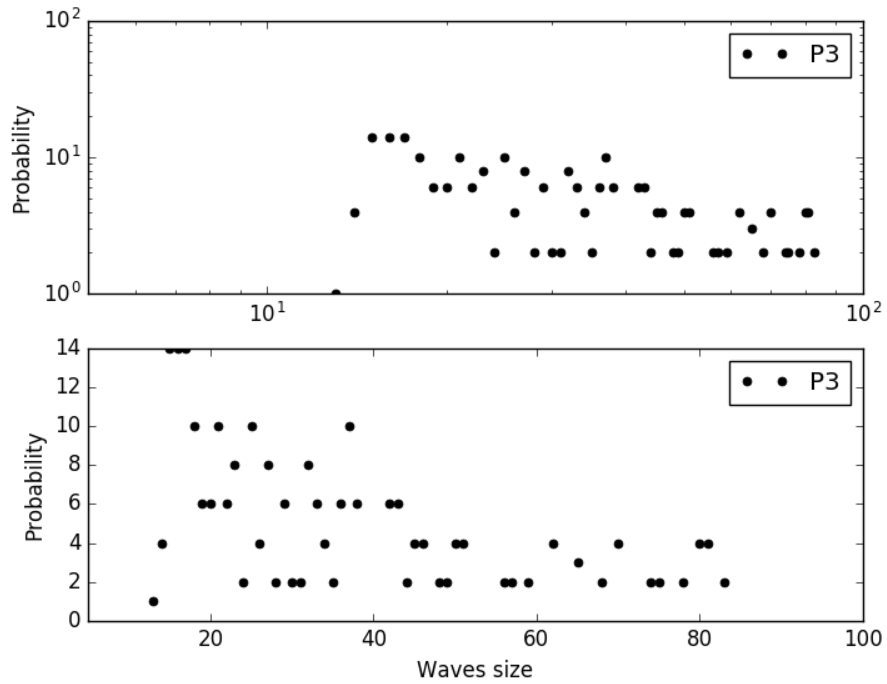


Figure 6.13: **Probability distribution of waves sizes in control waves in a P3 mouse retina.** *Top.* PDF in lin-log scale. *Bottom.* PDF in lin-lin scale.

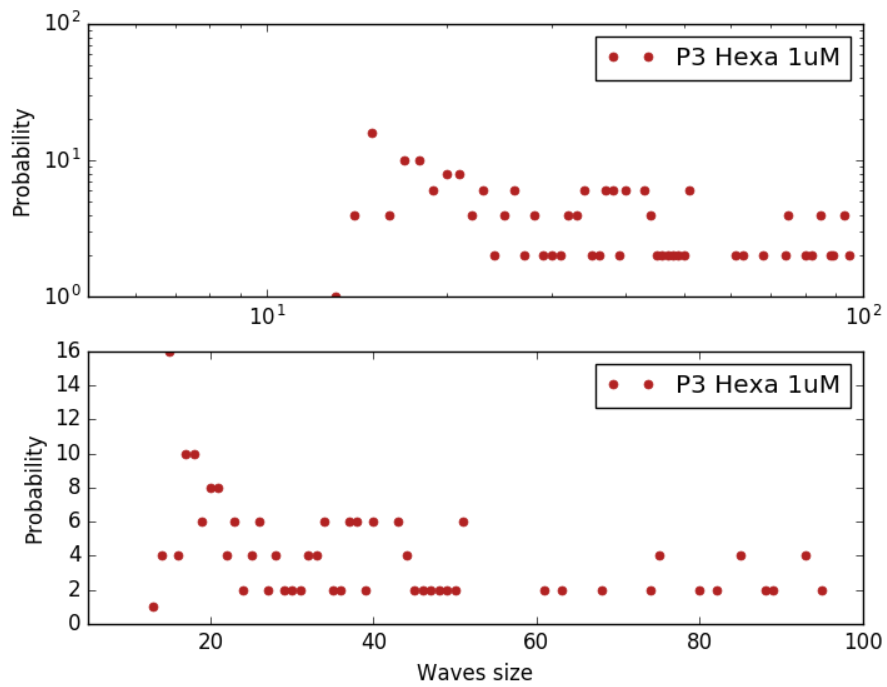


Figure 6.14: **Probability distribution of waves sizes with $1\mu\text{M}$ hexametonium in a P3 mouse retina.** *Top.* PDF in lin-log scale. *Bottom.* PDF in lin-lin scale.

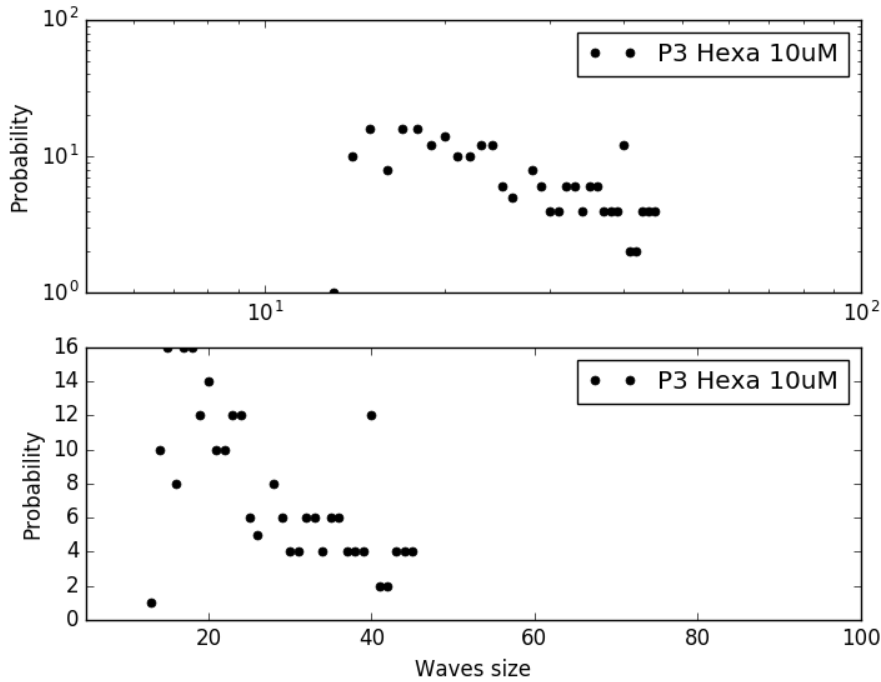


Figure 6.15: **Probability distribution of waves sizes with $10\mu M$ hexametonium in a P3 mouse retina.** *Top.* PDF in lin-log scale. *Bottom.* PDF in lin-lin scale.

other words, we concluded that the two directions, increasing and decreasing, are not equivalent. In order to fully characterize the effect of hexametonium on stage II retinal waves, further experiments are required.

6.2.2 The effect of atropine in early stage II retinal waves

As explained above, atropine as a pharmacological agent is widely used as a muscarinic cholinergic receptor blocker and in principle has no effect on the nicotinic receptors. Nevertheless, we tested its effect due to the result of [61] on nAChR subunit β_2 potentiation. We found that waves size seems to remain unaltered upon the atropine application. Nevertheless, slight alterations in activity characteristics were still observed due to atropine. In Fig 6.16, we show the average population firing rate over time for control and several atropine concentrations $1\mu M$, $10\mu M$, $100\mu M$. We observe that as the concentration of atropine increases, spontaneous activity (not participating in a wave) is eliminated almost completely, especially for concentrations larger than $10\mu M$ (see Fig 6.16). Moreover, the increase of the atropine leads to slightly less frequent waves (see Fig 6.17). We conclude that atropine most probably can not potentiate the nAChR subunit β_2 found in SACs.

In an attempt to quantify the effect of atropine on the waves sizes, we measure the probability distributions of the waves sizes for control data and two atropine concentrations, 1 and $10\mu M$. We use the same method as above. We again confirm that waves size is not affected by atropine (compare Figs 6.18, 6.19, 6.20). However, note that waves sizes in Fig 6.18 seem quite smaller due to the high spontaneous activity

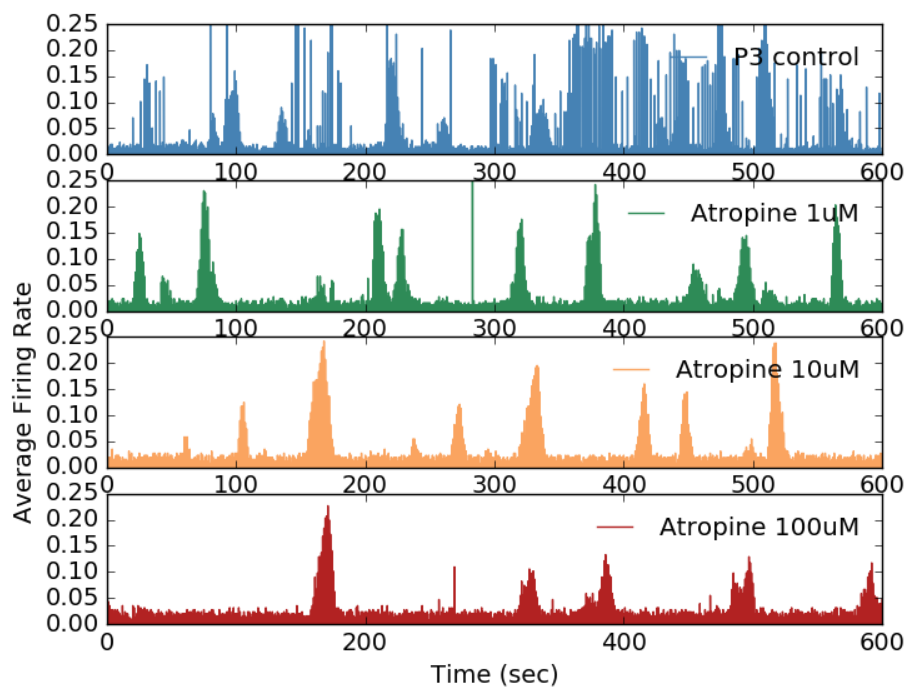


Figure 6.16: **How the average population firing rate changes upon atropine induction in P3 mouse retina.** The time shown here corresponds to 600sec. *Blue.* Control P3 waves. *Green.* Atropine concentration $1\mu M$. *Orange.* Atropine concentration $10\mu M$. *Red.* Atropine concentration $100\mu M$.

6.2. EXPLORING THE EFFECT OF THE CHOLINERGIC TRANSMISSION ON THE SPATIO-TEMP

of this retina in the control condition, introducing a bias to our numerical method of wave detection.

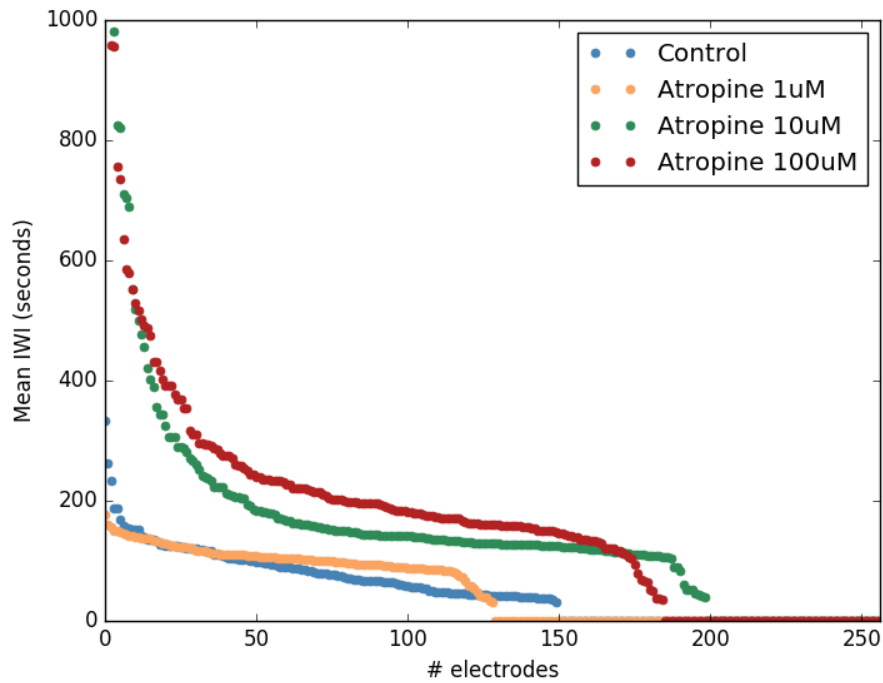


Figure 6.17: **Interwave intervals (IWI) profile for all electrodes, sorted in decreasing order for different concentrations of atropine.** The interwave intervals increase upon the induction of atropine in concentrations such as 1, 10, 100 μ M, the waves become less frequent.

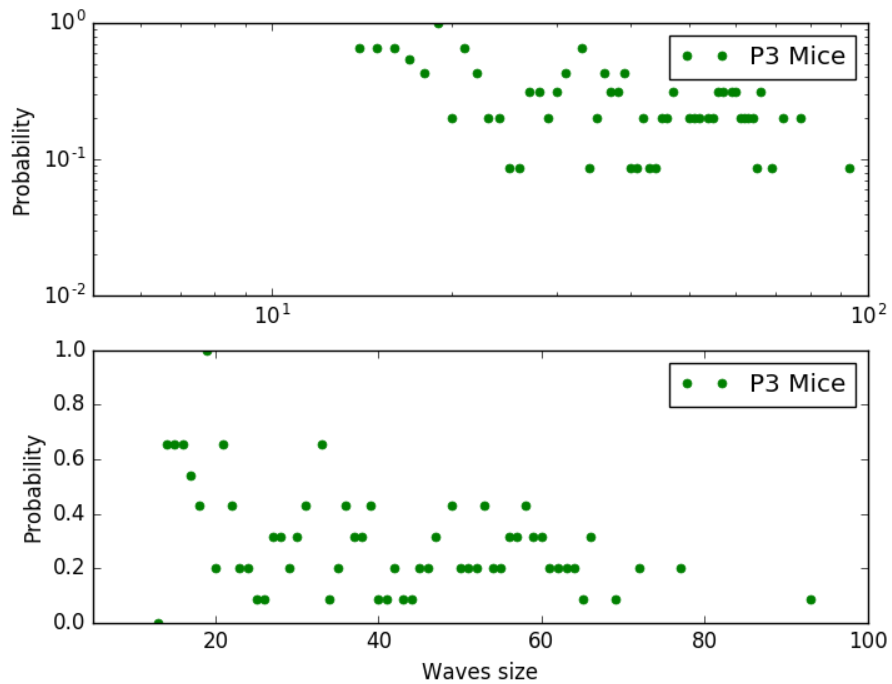


Figure 6.18: **Probability distribution of waves sizes in control waves in a P3 mouse retina.** *Top.* PDF in lin-log scale. *Bottom.* PDF in lin-lin scale.

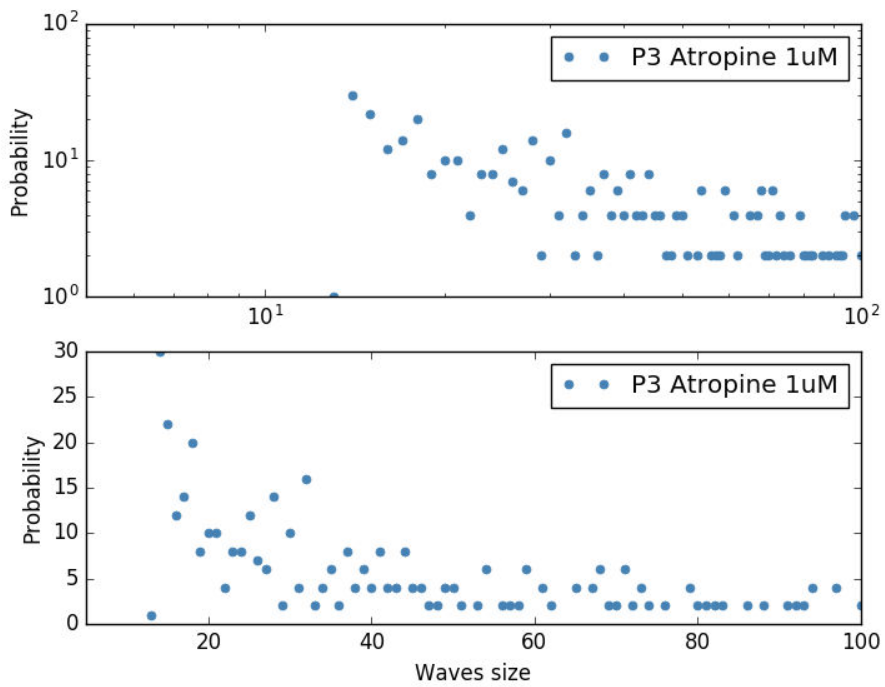


Figure 6.19: **Probability distribution of waves sizes with $1\mu M$ atropine in a P3 mouse retina.** *Top.* PDF in lin-log scale. *Bottom.* PDF in lin-lin scale.

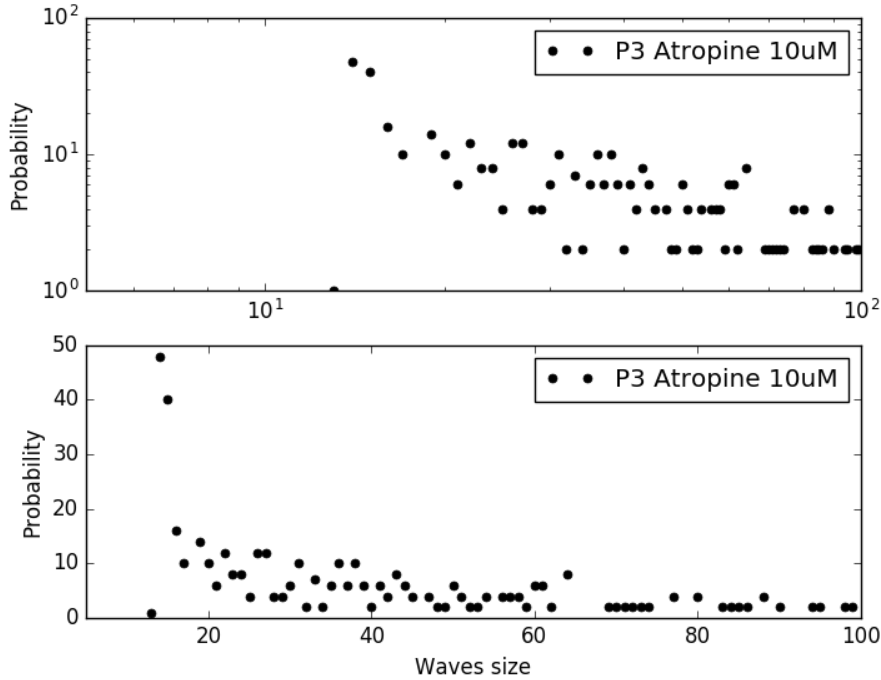


Figure 6.20: **Probability distribution of waves sizes with $10\mu M$ atropine in a P3 mouse retina.** *Top.* PDF in lin-log scale. *Bottom.* PDF in lin-lin scale.

6.2.3 Power laws and criticality in experimental recordings of retinal waves

We would like now to compare the distributions of waves size for both our simulations and experimental data obtained at Vision Institute. In order to perform a statistical analysis on the waves size and more particularly conclude on the shape of their probability distribution we need a quite large sample. The recordings described in section 6.2, were not long enough ($\sim 35min$) in order to provide us with a large number of waves for our analysis. For this reason, we used another dataset of control $P5$ waves from mice for over an $1h$ in total, from Vision Institute (256 electrodes).

In Fig 6.21, we show that the distribution of waves size in $P5$ mice is power-law like. This means that sizes could exhibit maximal variability, indicating that the system is critical in control conditions. It is interesting to see that experiments confirm our theoretical prediction, where we show that there exists a regime in the parameters space of our model, where power-law distribution is observed for the waves size (see Fig 4.23 (regime B) and section 4.6.2). Away from this regime, no power-law like distributions are observed for the waves characteristics in our model. Note that the same regime B, corresponds also to the sharp transition in the population firing rate in Fig 4.21. It is very interesting that the critical regime corresponds to the normal stage II waves, possibly meaning that the neural network of SACs chooses to be close to this state. Therefore, it means that the network is governed by an underlying mechanism that ensures that the system remains in the critical state, which is not yet identified neither theoretically or experimentally.

In Fig 6.22, we illustrate the agreement of theory and experiments on the power-law

like distribution of waves size.

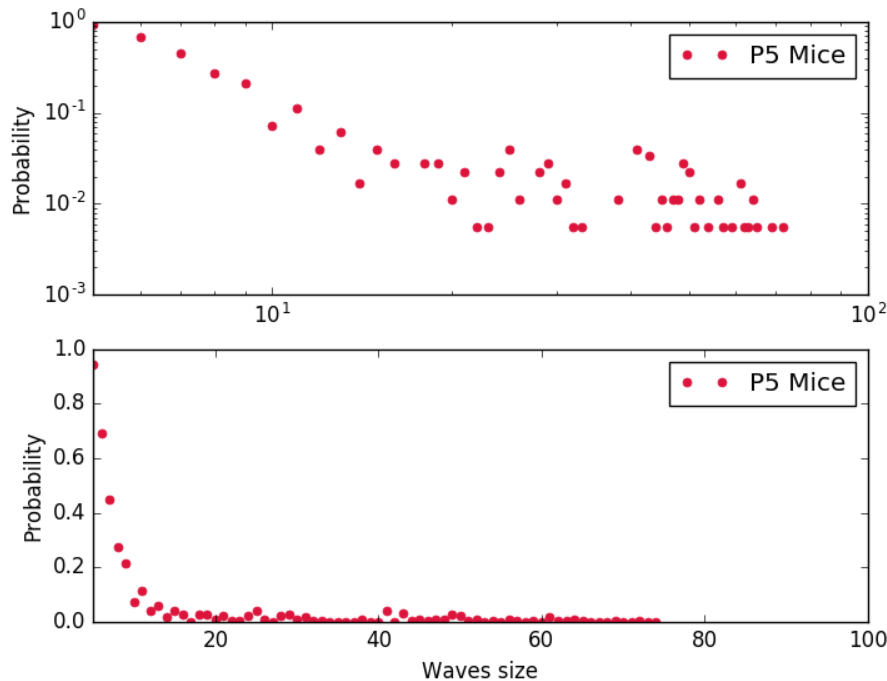


Figure 6.21: **Probability distribution of waves sizes in a P5 mouse retina is power-law like.** This indicates a link to criticality for the network of SACs.

6.3 Conclusion and Discussion

In this chapter, we confronted some of our model's predictions to certain preliminary experiments with the goal to validate our hypothesis. Through this analysis, we were able to enhance our claim that our equations are biophysically valid and robust with respect to parameter tuning. Our equations are able to reproduce the effect of the sAHP and cholinergic coupling on waves spatiotemporal dynamics and predict their effect on the statistical characteristics of waves. We also confirm experimentally our theoretical prediction of power-law like distributions for wave characteristics and made a link with critical systems. According to our modeling, we observe power laws at a very specific regime of our parameters space, meaning that dynamics needs tuning to reach that particular point (tune for example g_A as shown in section 4.6.2). However, if we accept criticality for stage II waves, the network of SACs manages to self-tune to this very regime. Consequently, we assume that there exists an homeostasy-like mechanism which controls the self tuning of the network to the critical state. For the moment, the cellular mechanisms of an homeostatic control have not been yet identified. However, a first indication comes from the work of [57], where they showed in experiments that there is an homeostatic control of spontaneous retinal activity maintaining specific network dynamic properties in an age-dependent manner. They also show that the possible underlying mechanism is linked to $GABA_A$ signaling. An extension of our model is possible, in order to account for the effect of $GABA_A$

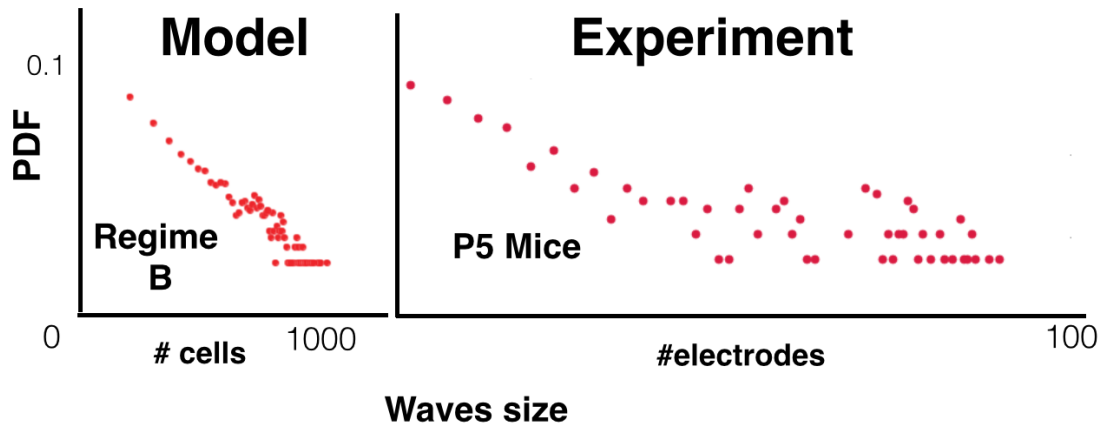


Figure 6.22: **Comparison of simulated and experimental data measuring the distribution of stage II retinal waves.** *Left.* Power-law like PDF of simulated waves size in the regime B (see section 4.6.2). The size of the network is 10000 neurons. *Right.* Power-law like PDF of simulated waves size in the regime B (see 4.6.2). We record from 256 electrodes. Note that the maximum waves sizes, if normalized with respect to the size of the network, correspond to ~ 0.1 for the model and ~ 0.23 for the experiment.

signaling, by adding a term describing the *GABAergic* current. In order to elucidate the possibility of such a homeostatic mechanism, further experimental and theoretical work is essential. Note that notable theoretical work on homeostatic mechanisms of other neural networks such as motor networks in *Drosophila* larvae [32], showing a mechanism behind the self-regulation, linked with the relative characteristic times between neighbouring populations. Also, another regulatory mechanism was studied in the context of the stomatogastric ganglion (STG) neuron of *Cancer borealis* in [41], showing that several calcium dependent pathways are used to regulate the maximal conductances of membrane currents in an activity dependent manner.

Chapter 7

Conclusions and Perspectives

During my thesis, we built a biophysical model of the spontaneous bursting activity of immature starburst amacrine cells, first at the individual neuron and then at the network level. This model, is able not only to reproduce experimental observations, but it proposes a quantitative mechanism for SACs activity, leading to experimentally testable predictions, such as the wide variability in the bursting periods observed across species [1]. We performed the mathematical analysis of the model using dynamical systems and bifurcations theory, allowing us to identify a few key biophysical parameters, which control the features of waves. We also provide analytic and numerical results revealing mechanisms on how waves start, propagate and stop, making a link also with critical systems. On top of our theoretical work, we collaborated with experimentalists, in order to test the model's predictions on the effect of pharmacological manipulations on the characteristics of waves Chapter 6. Through this thesis, we have been able to build a framework, which includes mathematical tools, numerical simulators and experimental procedures to understand the mechanisms that generate retinal waves during development.

Let us now reflect on some possible extensions of this work.

7.1 Reflecting on possible theoretical extensions

Synaptic coupling versus volume diffusion. It is still not clear what is the exact mechanism of cholinergic transmission during stage II retinal waves. In [37] it is proposed that a possible explanation for the widespread effects of Ach during waves, is that Ach is released by volume transmission, the diffuse release of neurotransmitter in the absence of pre- and postsynaptic specializations. In other words, in volume neurotransmission ACh reaches the extrasynaptic space, as opposed to remaining confined to the synaptic cleft in the case of the synaptic neurotransmission [24]. Indeed cholinergic retinal waves are present prior to the formation of conventional synapses, as identified in [26]. Clearly this means, that retinal waves are controlled by immature nicotinic cholinergic synapses that are less spatially specialized than those in the adult retina. Now the question is how this effect could be biophysically modeled and what would be the actual different consequences on waves characteristics in the cases of volume diffusion and synaptic transmission.

In their paper, Lansdell et al. [12] considered only volume diffusion and added to equation (3.1) the term $D_A \nabla^2 A$, where ∇^2 is the Laplacian and A is the Ach concentration. On mathematical grounds, the main consequence is to end up with a very standard

model in non linear physics: a reaction diffusion model. Here, standard methods (heteroclinic connections) allow for example to compute the propagation speed of a wave (it was done numerically by Lansdell et al because their model is a bit more complex than the standard setting for this type of computations). Note however that their diffusion mechanism is a phenomenological and not a literal diffusion process based on the net Brownian motion of molecules.

In contrast, in our model, cholinergic transmission is modeled as synaptic, with parameters such as Ach degradation time and production rate, directly fitted from experiments in [62], in order to match the characteristics of immature cholinergic synapses. So we have a clear biophysical interpretation of the parameters. The model we end up with is not a reaction diffusion model because of the presence of a threshold in the Laplacian. It renders the analysis more complex, but it allows direct comparison with experiments. To explore the nature of the transmission mechanism of Ach during development, it would be needed to construct a model describing the exact biophysical process for volume diffusion, characterize the waves it would produce and then compare them with those generated by synaptic transmission in our work.

The role of variability in SACs on waves generation. Variability is de facto present in biological systems and one can not claim that cells are identical. For example, in [63], the authors show that only 60 per cent of SACs were found to be bursters, whose bursting characteristics also exhibit a vast variability. However, one could ask, whether the variability of cells is fundamental to the mechanisms generating retinal waves. Throughout this thesis, we have shown that identical cells are able to produce biologically realistic retinal waves, meaning that maybe variability per se is not necessary to produce them. Nevertheless, it would be very interesting to explore what is the role of the observed variability in SACs' biophysical parameters such as their bursting periods, their cholinergic conductances and their ability to burst.

An interesting numerical experiment, addressing the effect of variable bursting periods of SACs on waves characteristics, is to start from an homogeneous network, except for one neuron (and then several) with different bursting periods and/or conductances than the rest of the network. This would test the role of bursting period heterogeneity and the fact that some neurons could be 'leaders' in wave triggering. Preliminary results which are not shown in this manuscript, show that cells with stronger coupling and shorter bursting period impose their own dynamics to the network by initiating waves. However, experimentally waves initiation sites are found to be homogeneously distributed across the retina [36]. This means that all SACs should be virtually eligible to become 'leaders' and initiate waves, rather than have special cells which are predefined in the network. A possible mechanism to explain that is noise. If noise is responsible for driving SACs to start bursting (noise driven bursting scenario), and this noise is Gaussian, then all SACs would be equally probable to start a wave. Noise would make at random and opportunistically all SACs to become virtual leaders, namely having the strongest coupling or shortest bursting period at a given point in time compared to their neighbours. Another possibility is that time scales play a role here. On the time scale of a few waves, there is a memory (larger than sAHP time) which imprints the medium and make cells temporary leaders. On larger scales (hours) the leaders may move and we may end with a uniform distribution on these time scales. It would be very interesting to test this hypothesis numerically with our model where we can control all conditions.

In the literature, variability in SACs has been modeled in [37], by imposing a randomness at the value of a parameter i.e. neuron i has a characteristic time τ_{S_i} following a Gaussian distribution. This introduces another level of randomness in their model, of a different nature than noise. Whereas the noise acting on voltage is renewed at each time step ("annealed disorder"), the parameters τ_{S_i} are fixed during the evolution (more generally, they evolve on a time scale quite smaller than the largest characteristic time in the model). Physicists are used to call this type of randomness "quenched disorder" (see e.g. the spin glasses literature [27]).

Extending our model towards a generic dynamical system for retinal waves

All stages of retinal waves are mediated by transient networks of cells with different pharmacological signatures. However, macroscopically, in spite of the fact that dramatic changes undergo in the immature retina circuitry, waves characteristics remain largely unaltered [15]. In fact, in [15], it is shown that two coordinated transitions occur in the excitatory drive for retinal waves: one from a fast cholinergic to a fast glutamatergic input and the other from a nicotinic to a muscarinic system. They show that Ach changes its functional role via a switch between two completely different classes of receptors for the same neurotransmitter and that the cholinergic system plays a critical role not only for early but also late retinal waves. These observations have led to the hypothesis that spontaneous rhythmic activity is mainly controlled by homeostatic mechanisms. In the same work, it is stated that it is possible that the spontaneous activity relies on an overall excitatory input from certain neurotransmitters and not on the detailed type or circuitry of the excitatory input, meaning that the drastic transition from a cholinergic to a glutamatergic network may not actually alter significantly the overall input in the network leading to similar spontaneous patterns of activity. For the moment, as mentioned in 6, the cellular mechanisms of an homeostatic control in retinal waves have not been yet identified. However, a first indication comes from the work of [57], showing $GABA_A$ signaling is involved.

In this thesis, we developed a detailed biophysical model especially tailored to describe the dynamics of SACs during stage II retinal waves. However, taking into account the above, it would be possible to extend it by taking into account the minimal necessary ingredients to generate retinal waves for all 3 stages: i) fast excitatory drive (lateral and vertical) and ii) a mechanism for inhibition. Using our equations as a starting point, we could construct a minimal model, which by the mere variation of parameters could follow the evolution of retinal waves dynamics during development. Then it has to be an equation like the transport equations (Chapter 5) where we have smoothed many biological specificities (e.g. type of neurotransmitters) to end up with a canonical equation.

7.2 Can we use retinal waves to restore plasticity in pathological retinas?

The following project was submitted to L'Oreal/UNESCO competition for Scholarships Women in Science 2017 Awards, category Rising stars and received an excellence certificate, ranking in the top 10 per cent of the applications.

Around 285 millions of people around the world suffer from retinal degenerative

diseases at varying degrees of vision loss including complete blindness. In the recent years, a new hope towards the dream of reversing vision loss is growing with techniques such as gene therapy, stem cells transplants and retinal prostheses, developed and tested by research labs and biotechnology companies. In order to make those therapeutic techniques valuable to patients in need, it is important to consider the risks, cost and comfort of the methods. For this reason it is essential to work towards solutions requiring minimal invasiveness and maximal safety of a patient. In this context, it is interesting to study retinal waves, a natural mechanism of the shaping of the visual system, as a possible mechanism to use for vision restoration in pathological retinas.

In a healthy retina, during development, visual pathways are shaped naturally by retinal waves, which are spontaneous bursts of activity propagating across the immature retina and disappear when vision is functional [10]. In the pathological case, these synapses could change completely, depending on the type of degenerative retinal disease [42]. So far, both experimental and theoretical studies, have provided a deeper understanding on the cellular mechanisms generating retinal waves during development. Moreover, based on our biophysical model of retinal waves, [3] provides a classification of the observed waves activity with respect to their features, using dynamical systems tools. On the other side, researchers in the lab of Serge Picaud at Vision Institute, Paris, were able to restore wavy activity pharmacologically, in the adult mouse retina [20]. This possibility of waves restoration in the mature retina circuitry brings up the necessity to characterize the pharmacologically restored waves (size, duration, frequency) and compare them with developmental ones in normal and pathological cases. We propose the construction of a robust method to reinitiate retinal waves in adult retinas (both healthy and degenerated), with the same characteristics as the ones during development, establishing the necessary framework to test the effect of the restored activity on neural plasticity in the future.

As an extension of this thesis, it would be interesting to study the pharmacologically induced waves in the adult retina bridging the gap between paradigms from healthy retinas and pathological ones.

This project would be the continuation of the results of my thesis work both on the theoretical and experimental side. On the mathematical and numerical side, one could extend our existing model [1, 2] to capture the pharmacological manipulation presented in [20] for mature starburst amacrine cells, as well as enhance our existing numerical methods and develop new (Python and Brian2 simulator) to simulate and validate the modeled cellular dynamics. On the experimental side, new Multi Electrode Array (MEA) experiments on perinatal and adult mice would be necessary, to test our model's predictions on pharmacologically induced waves. The goal of this project would be twofold: 1. Adapt the mathematical model so as to describe the mature amacrine cells dynamics 2. Perform experiments guided by our model on healthy and pathological adult mouse retinas to restore and characterize retinal waves. In more detail, on the mathematical aspect, one could extend our biophysical model in [1, 2] by adding additional currents to mimic the inputs from other cell types in the mature circuitry and also adjusting the parameters to capture the activity observed in adult mouse retinas. Through simulations and mathematical analysis, it would be possible to identify the key mechanisms that restore bursting activity in mature starburst amacrine cells, taking into account the experimental work of [20] on wave restoration. Based on this extension of our model, it will give a theoretical guidance

7.2. CAN WE USE RETINAL WAVES TO RESTORE PLASTICITY IN PATHOLOGICAL RETINAS?

for the experiments, to validate testable predictions on restored waves in adult retina, as already done for developmental waves. The predicted pharmacological manipulations for the wave restoration will be done on healthy and pathological adult mouse retinas. Finally, the characterization of the pharmacologically restored waves in both aforementioned cases would be necessary, using our existing numerical methods and consequently, comprising both natural and pharmacologically induced waves.

Such a study could elucidate how plasticity could be restored for certain pathologies. In the visual system at an adult age, it was demonstrated in [23] that plasticity could be restored, following retinal ganglion cells axonal regrowth after optic nerve damage, upon the right stimulus. It is natural to consider as a following step, that this wave-like propagation of the elicited bursting activity could be the right stimulus to restore plasticity in the pathological retina. Furthermore, so far, the existing methods attempting to restore vision to blind patients have a common shortcoming; they do not take into account that a degenerating retina may trigger synaptic remodeling [42], resulting in unconventional synaptic connections, making it hard for the network to function. Being able to establish a rigorous classification of developmental and pharmacologically induced waves, in the future, would allow us to possibly control restored retinal waves leading to new experimental protocols in pharmacological treatments. Consequently, under strong interdisciplinary studies and collaborations between theoreticians, biologists, and clinical doctors, pharmacologically restored waves could be used for therapeutic purposes for blind patients.

Bibliography

- [1] D. Karvouniari, L. Gil, O. Marre, S. Picaud, B. Cessac A biophysical model explains the spontaneous bursting behavior in the developing retina Nature Scientific Reports, under review, January 2018
- [2] D. Karvouniari, L. Gil, O. Marre, S. Picaud, B. Cessac Following stage II retinal waves with a biophysical model Bernstein Conference, Gottingen, 2017
- [3] D. Karvouniari, L. Gil, O. Marre, S. Picaud, B. Cessac Mathematical and experimental studies of retinal waves ICMNS Conference, selected talk, Juan-les-pins, 2016
- [4] Ozaita A., Petit-Jacques J., Volgy B., Ho C. S., Joho H., S. A. Bloomfield, and B. Rudy. A unique role for kv3 voltage-gated potassium channels in starburst amacrine cell signaling in mouse retina. The Journal of Neuroscience, 33(24):7335–7343, 2004.
- [5] Jonathan Touboul, Olivier Faugeras B. Rudy. The spikes trains probability distributions: A stochastic calculus approach Journal of Physiology, 200
- [6] Fried SI, MÃ¼nch TA, Werblin FS. Mechanisms and circuitry underlying directional selectivity in the retina. Nature, 2002.
- [7] Tsumoto K., Kitajima H., Yoshinaga T., Aihara K., Kawakami H., Bifurcations in Morris-Lecar neuron model, Neurocomputing 69 (2006) 293-316.
- [8] Marder E., Goaillard J.M., Variability, compensation and homeostasis in neuron and network function, Nat. Rev. Neurosci., 2006, 7, 563 - 574
- [9] Xu H-P , Burbridge T. J. , Ye M. , Chen M. , Ge X. X. , Zhou Z. J., Crair M. C. , Retinal Wave Patterns Are Governed by Mutual Excitation among Starburst Amacrine Cells and Drive the Refinement and Maintenance of Visual Circuits, The Journal of Neuroscience, March 30, 2016, 36(13): 3871-3886
- [10] Firth S. et al Retinal waves: mechanisms and function in visual system development Cell Calcium, 2004.
- [11] H. J. Abel, J.C.F. Lee, J. C. Callaway, R. C. Foehring. Relationships between intracellular neocortical pyramidal neurons calcium and afterhyperpolarizations in neocortical pyramidal neurons. J Neurophysiol, 2004.
- [12] Lansdell B, Ford K, and Kutz JN. A reaction-diffusion model of cholinergic retinal waves. PLoS Computational Biology, 10(12):1–14, 2014.
- [13] Morris C and Lecar H. Voltage oscillations in the barnacle giant muscle fiber. BIOPHYS. J., 35:193–213, 1981.
- [14] Cessac B., Blanchard Ph., KrÃ¼ger T. Lyapunov exponents and transport in the Zhang model of Self-Organized Criticality. Phys. Rev. E., Vol. 64, 016133, (2001)..
- [15] Z. Jimmy Zhou and Dichen Zhao Coordinated Transitions in Neurotransmitter Systems for the Initiation and Propagation of Spontaneous Retinal Waves Journal of Neuroscience, 1 September 2000, 20 (17) 6570-6577
- [16] Mehran Kardar, Giorgio Parisi, and Yi-Cheng Zhang Dynamic Scaling of Growing Interfaces Phys. Rev. Lett., 56, 889, 3 March 1986
- [17] Per Bak, Chao Tang, and Kurt Wiesenfeld Self-organized criticality: An explanation of the 1/f noise Phys. Rev. Lett., 59, 381, 27 July 1987
- [18] Daniel O. Cajueiro and R. F. S. Andrade Controlling self-organized criticality in sandpile models Phys. Rev. E, 81, 015102(R), 19 January 2010

- [19] Vanessa I Pinto Thesis, DLX HOMEBOX TRANSCRIPTIONAL REGULATION OF CRX AND OTX2 GENE EXPRESSION DURING VERTEBRATE RETINAL DEVELOPMENT University of Toronto, 2015, DOI10.13140/RG.2.1.3341.7766
- [20] Djilas M. et al. Pharmacologically induced wave-like activity in the adult retina IOVS, 2012
- [21] M. Tauchi, R. H. Masland. The shape and arrangement of the cholinergic neurons in the rabbit retina Proc. R. Soc. Lond. B 1984
- [22] Goodman DFM and Brette R, The Brian simulator Front Neurosci, 2009
- [23] de Lima S. et al., Full-length axon regeneration in the adult mouse optic nerve and partial recovery of simple visual behaviors Proc Natl Acad Sci USA, 2012
- [24] Sarter M, Parikh V, Howe WM., Phasic acetylcholine release and the volume transmission hypothesis:time to move on. Nature Reviews. Neuroscience, 2009
- [25] W.R. Taylor and R.G Smith The role of starburst amacrine cells in visual signal processing Vis Neurosci, 2012 Jan
- [26] W.R. Taylor and R.G Smith Histogenesis of the ferret retina Exp Eye Res., 33(3):315-32., Sep 1981
- [27] M. Mezard and G. Parisi and M.A. Virasoro Spin-glass theory and beyond World scientific Singapore, 1987
- [28] Starburst Amacrine Cells <http://wiki.eyewire.org>
- [29] Robert Clewley. Hybrid models and biological model reduction with pydstool. PLoS Computational Biology, 2012.
- [30] Ford, Kevin J. and Felix, Aude L. and Feller, Marla B. Cellular Mechanisms Underlying Spatiotemporal Features of Cholinergic Retinal Waves The Journal of Neuroscience, 850-863, 2012.
- [31] Sernagor E., Eglon S.J., and O'Donovan M.J. Differential effects of acetylcholine and glutamate blockade on the spa- tiotemporal dynamics of retinal waves. The Journal of Neuroscience, 20:RC56, 2000.
- [32] Julijana Gjorgjieva, Jan Felix Evers, and Stephen J. Eglon Homeostatic Activity-Dependent Tuning of Recurrent Networks for Robust Propagation of Activity The Journal of Neuroscience, 20:RC56, 2000.
- [33] R.S. Mackay and C. Tresser Transition to topological chaos for circle maps Physica D, 1986
- [34] DA Butts, MB Feller, CJ Shatz, DS Rokhsar Retinal waves are governed by collective network properties Journal of Neuroscience , 1999
- [35] M. Iwata, S. Shinichi Theoretical analysis for critical fluctuations of relaxation trajectory near a saddle-node bifurcation Phys. Rev. E, 82, 011127 (2010)
- [36] Marla B. Feller, Daniel A. Butts, Holly L. Aaron, Daniel S. Rokhsar, and Carla J. Shatz. Dynamic processes shape spatiotemporal properties of retinal waves. Neuron, 19(2):293 – 306, 1997.
- [37] Kevin J. Ford and Marla B. Feller. Assembly and disassembly of a retinal cholinergic network. Visual Neuroscience, 29:61–71, 1 2012.
- [38] Keith B Godfrey and Nicholas V Swindale. Retinal wave behavior through activity-dependent refractory periods. PLoS Comput Biol, 3(11):e245, 11 2007.
- [39] Arkady Pikovsky and Michael Rosenblum Synchronisation Scholarpedia,2007, doi:10.4249/scholarpedia.1459
- [40] Lassignal, N L and Martin, A R Effect of acetylcholine on postjunctional membrane permeability in eel electroplaque. The Journal of General Physiology, 23-36, 1977.
- [41] Zheng Liu, Jorge Golowasch, Eve Marder, and L. F. Abbott A Model Neuron with Activity-Dependent Conductances Regulated by Multiple Calcium Sensors The Journal of Neuroscience, 1998
- [42] Haq W. et al. Synaptic remodeling generates synchronous oscillations in the degenerated outer mouse retina Front Neural Circuits, 2014
- [43] Michael Graupner. A theory of Plasma Membrane calcium pump function and its consequences for presynaptic calcium dynamics. PhD thesis, Master's thesis, TU Dresden, Dresden, 2003.

- [44] Michael Graupner, Frido Erler, and Michael Meyer-Hermann. A theory of plasma membrane calcium pump stimulation and activity. *Journal of biological physics*, 31(2):183–206, 2005.
- [45] J. Guckenheimer and Ph. Holmes. *Non linear oscillations, dynamical systems, and bifurcation of vector fields*. Springer-Verlag, 1983.
- [46] Bak, P., Chen, K. and Tang, C. *A forest-fire model and some thoughts on turbulence*. *Phys. Lett. A* 147, 297-300
- [47] Drossel, B. and Schwabl, F. *Self-organized critical forest-fire model*. *Phys. Rev. Lett.* 69, 1629-1632
- [48] Arnold, V.I. *Supplementary chapters of the theory of ordinary differential equations..* [1978] S Nauka, Moscow, 304 pp
- [49] E.M. Izhikevich. *Dynamical Systems in Neuroscience: The Geometry of Excitability and Bursting*. The MIT Press, Cambridge, MA, 2007.
- [50] Godfrey K, Eglén S Theoretical models of spontaneous activity generation and propagation in the developing retina *Molecular BioSystems*, 2009.
- [51] Julijana Gjorgjieva and Stephen J. Eglén Modeling developmental patterns of spontaneous activity *Curr Opin Neurobiol.*, 2011
- [52] Kaneda M, Ito K, Morishima Y, Shigematsu Y, and Shimoda Y. Characterization of voltage-gated ionic channels in cholinergic amacrine cells in the mouse retina. *J Neurophysiol*, 2007.
- [53] A. Maccione, M. Hennig M., M. Gandolfo, O. Muthmann, J. van Coppenhagen, S. Eglén, L. Berdondini, and E. Sernagor. Following the ontogeny of retinal waves: pan-retinal recordings of population dynamics in the neonatal mouse. *J Physiol*, 485:1545–1563, 2014.
- [54] Hennig MH, Adams C, Willshaw D, and Sernagor E. Early-stage waves in the retinal network emerge close to a critical state transition between local and global functional connectivity. *J Neurosci*, 2009.
- [55] E. Sernagor and N. Grzywacz. Spontaneous activity in developing turtle retinal ganglion cells: Pharmacological studies. *J Neuroscience*, 19, 1999.
- [56] Evelyne Sernagor and Matthias Hennig. *Retinal Waves: Underlying Cellular Mechanisms and Theoretical Considerations*. Elsevier, 2012.
- [57] Matthias H. Hennig, John Grady, James van Coppenhagen, and Evelyne Sernagor *Age-dependent Homeostatic Plasticity of GABAergic Signaling in Developing Retinal Networks* *Journal of Neuroscience*, 2011.
- [58] Dhooze A., Govaerts W., Kuznetsov Y.A. *MATCONT: A MATLAB Package for Numerical Bifurcation Analysis of ODEs*. *Acm Transactions on Mathematical Software* 29 (2): 141-164, 2003
- [59] A. L. Hodgkin and A. F. Huxley *quantitative description of membrane current and its application to conduction and excitation in nerve* *J Physiol*, 117(4): 500-544, 1952
- [60] Yoshida K, Watanabe D, Ishikane H, Tachibana M, Pastan I, Nakanishi S. A key role of starburst amacrine cells in originating retinal directional selectivity and optokinetic eye movement. *Neuron*, 2001.
- [61] Ruud Zwart and Henk P. M. Vijverberg Potentiation and Inhibition of Neuronal Nicotinic Receptors by Atropine: Competitive and Noncompetitive Effects *Molecular Pharmacology*, November 1997.
- [62] Ji-jian Zheng, Seunghoon Lee, and Z. Jimmy Zhou. A developmental switch in the excitability and function of the starburst network in the mammalian retina. *Neuron*, 44(5):851–864, 2004.
- [63] Jijian Zheng, Seunghoon Lee, and Z. Jimmy Zhou. A transient network of intrinsically bursting starburst cells underlies the generation of retinal waves. *Nat Neurosci*, 9(3):363–371, 2006.
- [64] Marritt, Andrea M. and Cox, Brandon C. and Yasuda, Robert P. and McIntosh, J. Michael and Xiao, Yingxian and Wolfe, Barry B. and Kellar, Kenneth J. Nicotinic Cholinergic Receptors in the Rat Retina: Simple and Mixed Heteromeric Subtypes *Molecular Pharmacology*, 1656-1668, 2005.
- [65] Katok, Anatole and Hasselblatt, Boris and Mendoza, Leonardo Collaborateur Introduction to the modern theory of dynamical systems *Cambridge university press*, 1995

- [66] C. Park and J.E. Rubin. Cooperation of intrinsic bursting and calcium oscillations underlying activity patterns of model pre-Botzinger complex neurons *J. Comp. Neurosci.*, 2013
- [67] Jung Min Han , Akihiko Tanimura, Vivien Kirk, James Sneyd A mathematical model of calcium dynamics in HSY cells *PLOS Comp Bio*, 2017
- [68] Hannah Choi, Lei Zhang, Mark S. Cembrowski, Carl F. Sabottke, Alexander L. Markowitz, Daniel A. Butts, William L. Kath, Joshua H. Singer, Hermann Rieke Intrinsic bursting of AII amacrine cells underlies oscillations in the rd1 mouse retina *Journal of Neurophysiology*, 2014
- [69] Warland DK, Huberman AD, Chalupa LM. Dynamics of spontaneous activity in the fetal macaque retina during development of retinogeniculate pathways. *Journal of Neuroscience*, 2006
- [70] Ben K. Stafford, Alexander Sher, Alan M. Litke, David A. Feldheim, Spatial-Temporal Patterns of Retinal Waves Underlying Activity-Dependent Refinement of Retinofugal Projections *Neuron*, 2009
- [71] Z. Jimmy Zhou. Direct Participation of Starburst Amacrine Cells in Spontaneous Rhythmic Activities in the Developing Mammalian Retina. *J. Neurosci.*, 18(11):4155–4165, June 1998.
- [72] Fredlin, M.I., Wentzell, A.D Random Perturbations of Dynamical Systems *Springer*, Grundlehren der mathematischen Wissenschaften, vol. 260, 1998
- [73] Strogatz, Steven H. Nonlinear Dynamics and Chaos : with Applications to Physics, Biology, Chemistry, and Engineering. *Boulder, CO*, Westview Press, a member of the Perseus Books Group, 2015. Print.
- [74] Henri Poincaré. L'Equilibre d'une masse fluide animee d'un mouvement de rotation *Acta Mathematica*, vol.7, pp. 259-380, Sept 1885.